Nuclear magnetic ordering in simple metals at positive and negative nanokelvin temperatures

A. S. Oja* and O. V. Lounasmaa

Low Temperature Laboratory, Helsinki University of Technology, FIN-02150 Espoo, Finland

This paper is a comprehensive review of almost twenty years of research on nuclear magnetic ordering, first in copper and later in silver and rhodium metals. The basic principles of nuclear magnetism and the measurement of positive and negative spin temperatures are discussed first. Cascade nuclear refrigeration techniques, susceptibility and nuclear-magnetic-resonance (NMR) measurements, and arrangements for neutron-diffraction experiments at nanokelvin and picokelvin temperatures are described next. Comprehensive magnetic-susceptibility and neutron-diffraction measurements on copper, which led to the discovery of at least three antiferromagnetic phases, one displaying the novel $(0\ \frac{2}{3}\ \frac{2}{3})$ spin structure and the other two showing the type-I order of the fcc system, are then described in detail. NMR data on silver, at $T>0$ and $T<0$, are presented next leading to the observation that silver orders antiferromagnetically at positive spin temperatures and ferromagnetically at negative spin temperatures. The authors discuss recent neutron-diffraction measurements that show that the antiferromagnetic structure at $T>0$ is in a single-**k** type-I state. NMR data on rhodium at $T>0$ and $T<0$ are also described. Results obtained on Tl, Sc, $AuIn_2$, and metallic Pr compounds and on insulators like CaF_2 are then discussed briefly. The paper is concluded by an extensive theoretical section. Calculations of conduction-electron mediated exchange interactions are described, and the mean-field theory of nuclear magnetic ordering is presented. The role of thermal and quantum fluctuations is then discussed, particularly in the selection of the antiferromagnetic ground state. Finally, theoretically calculated magnetic phase diagrams and ordered spin structures of copper and silver are presented in detail and compared with experimental results. The overall agreement is good, affirming the value of nuclear magnets in Cu and Ag as realizations of simple physical models. [S0034-6861(97)00301-2]

CONTENTS

*Present address: VTT Automation, Measurements Technology, P.O. Box 1304, FIN-02044 VTT, Finland. Fax: 358-9-451-2969. Electronic address: Aarne.Oja@vtt.fi

LIST OF SYMBOLS

Most of the specialized notation is defined where it is needed in the text. This list collects for ready reference the notation used throughout the paper.

$B_{\rm loc}$	The average strength of the local fluctuating field [Eq. (29)].
$\mathbf{B}_i$	Molecular field at site i due to interactions with neighboring spins [Eq. (75)].
$\mathbf{d}_i$	Amplitude of the antiferromagnetic modulation corresponding to the ordering vector $\mathbf{k}_i$ [see, for example, Eqs. (111) and (160)].
D	Demagnetizing factor. It is assumed that the demagnetizing tensor is diagonal and that D is the component of interest, usually the one parallel to the external magnetic field.
L	Lorentz constant $L=\frac{1}{3}$ [see, for example, Eq. (34)].
p	Nuclear-spin polarization $p=\langle \mathbf{I}_i\rangle/I$ [Eq. (76)].
R	Strength of the exchange interaction with respect to the dipolar force [Eqs. (6) and (66)].
T	Temperature of nuclear spins.
T_e	Temperature of conduction electrons.
$T_{\rm Z}$	Temperature of the Zeeman reservoir (see Sec. II.B.).
$T_{\rm ss}$	Temperature of the spin-spin interaction reservoir (see Sec. II.B).
$\lambda_n(\mathbf{k})$	Eigenvalue, or eigenenergy, of the Fourier transform of the interaction matrix $\underline{A}(\mathbf{k})$ [see Eq. (83)].
$\lambda_{\rm max}$	The largest eigenvalue $\lambda_{\rm max}=\max_{\mathbf{k},n}\{\lambda_n(\mathbf{k})\}$, sometimes denoted as λ. See Eqs. (87) and (88).
θ	Weiss temperature $\theta=C(R+L-D)$ in $\chi=C/(T-\theta)$ [see Eq. (34)].

I. INTRODUCTION

This paper reviews two decades of research on nuclear magnetic ordering, first in copper and later in silver and rhodium metals. The focus, in the experimental section, is on research carried out by the authors and their colleagues in Helsinki, as well as on joint projects in the Risø National Laboratory (Denmark) and at the Hahn-Meitner-Institut (Berlin), in the course of which at least three antiferromagnetic phases were discovered and several low-temperature world records broken at both positive and negative sides of the absolute zero. This work is set in the context of the broader effort to understand spin structure and to measure magnetic phases in a variety of metals, metallic compounds, and insulators.

Nuclear spin assemblies in simple metals are good model systems of magnetism, a fact that has motivated a large body of theoretical work. We review this work in the last third of the paper. Our emphasis is on copper, silver, and rhodium, particularly on copper, in part because of our own experience with these systems and in part as a reflection of the huge body of experimental and theoretical work that has been produced on these metals.

The review is organized as follows. In Sec. I.A. we briefly survey the historical background and in I.B the theory of nuclear ordering studies. Section I.C. discusses the early susceptibility measurements and NMR experiments using continuous-wave techniques. Neutron-diffraction measurements on copper followed (Sec. I.D), and then experiments on silver and rhodium (Sec. I.E) and other metals (Sec. I.F). Section II describes the principles of nuclear magnetism that are important in the study of metals. This completes the background portion of the paper.

Three experimental techniques are treated next: susceptibility measurements (Sec. III), measurement of nuclear-spin temperatures (Sec. IV), and neutron-diffraction techniques (Sec. VI). The data obtained by these methods on copper are discussed in Secs. V and VII. Results on silver (Secs. VIII and IX) and rhodium (Sec. X) are then presented. Other NMR studies of copper and silver, not directly related to nuclear ordering, are described in Sec. XI. Recent nuclear ordering experiments on other elements and materials such as thallium, scandium, gold-indium, praseodymium compounds, and insulators are reviewed in Secs. XII–XIV.

The longest single section, amounting to about one-third of the review, is Sec. XV, which treats in detail the theoretical work on spontaneous nuclear ordering in simple metals. Its length is also an indication of the appeal that the subject holds for researchers. See the beginning of Sec. XV for a more detailed description of its contents.

In Sec. XVI we summarize what has been learned to date about magnetic ordering in the three best-studied simple metals, copper, silver, and rhodium, giving magnetic phase diagrams for each. We also mention some possible directions that future studies of nuclear ordering could take.

A. Historical comments

Electronic magnetism exhibits a wide spectrum of different ordering phenomena over a temperature range that extends from room temperature and above in iron

to a few millikelvins in cerium magnesium nitrate. Because nuclear magnetic moments are three orders of magnitude smaller than their electronic counterparts and because the interactions between spins are proportional to the magnetic moment squared, spontaneous ordering phenomena can be expected to occur in the nuclear-spin system only at microkelvin temperatures and below. Solid ^{3}He is an exception owing to the strong quantum-mechanical exchange force, enhanced by the large zero-point motion (Roger *et al.*, 1983; Cross and Fisher, 1985), and so are Van Vleck paramagnets, such as $PrNi_5$, in which considerable hyperfine enhancement of the magnetic field at the nucleus occurs (Andres and Lounasmaa, 1982).

Copper is probably the best material for studies of nuclear ordering, since cooling by adiabatic nuclear demagnetization of this metal is relatively easy owing to its favorable thermal and magnetic properties. Progress in cooling techniques has recently made it possible to carry out similar experiments on silver and rhodium. The opportunity to make detailed comparisons with theoretical predictions is the most important driving force for experiments on spontaneous nuclear ordering in simple metals. Such metals offer several theoretical advantages: the spins are well localized, the magnetic degrees of freedom do not couple to lattice distortions, and the spin-spin interactions are well defined. Simple metals can be exchange-dominated magnets, such as silver and rhodium, or magnets with equally strong dipolar and exchange forces, such as copper.

The pioneering experiments of Nicholas Kurti and coworkers established, in 1956, the feasibility of the nuclear-demagnetization method (Kurti *et al.*, 1956; Hobden and Kurti, 1959). In spite of the limitations imposed by cryogenic techniques available at that time, the Oxford group succeeded in reaching 1 μK. The first studies of nuclear cooperative phenomena, on insulators like CaF_2 and LiH, were made by Abragam and Goldman and co-workers at Saclay 13 years later (Chapellier *et al.*, 1969; Abragam and Goldman, 1982). The Helsinki work on copper (Ehnholm *et al.*, 1980; Huiku *et al.*, 1986, and references therein) was begun as early as 1974 but, due to many experimental difficulties, only since the spring of 1982 has spontaneous nuclear order been observed below the Néel temperature $T_N = 58$ nK. As a culmination point of this research, in 1984 the magnetic field vs entropy diagram (see Fig. 1) of the nuclear-spin system in copper was constructed, with the external field in the crystallographic [001] direction of the single-crystal sample; three antiferromagnetic phases were found.

In 1987, a Danish-Finnish-German group, working at the Risø National Laboratory near Copenhagen, succeeded in observing, by means of neutron scattering, the (1 0 0) Bragg reflection from a nuclear-ordered single-crystal ^{65}Cu specimen (Jyrkkiö, Huiku, Lounasmaa, *et al.*, 1988). This study resolved the spin order in two of the antiferromagnetic phases. In 1989, the nature of the third phase was determined by observing a strong neutron peak at the $(0\ \frac{2}{3}\ \frac{2}{3})$ Bragg position (Annila *et al.*, 1990).

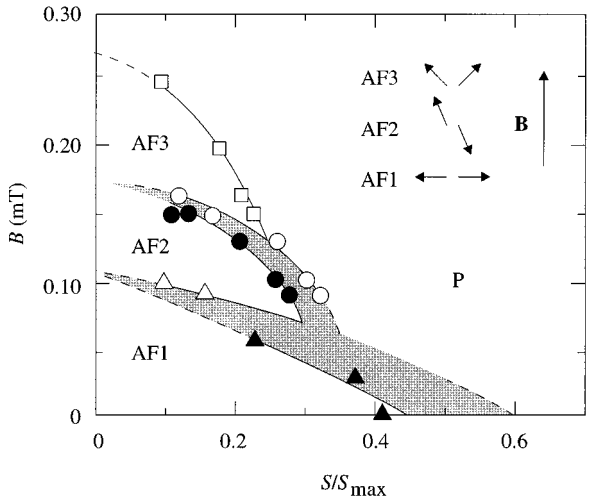

FIG. 1. External magnetic field vs entropy diagram for nuclear spins in copper. The three antiferromagnetic phases are denoted by AF1, AF2, and AF3; P stands for the paramagnetic phase and the shaded areas indicate regions where first-order phase transitions take place. The upper right corner of the figure shows the schematic spin arrangements that were originally proposed. The suggested structure for AF2, which consists of two sublattices, is, however, inconsistent with later neutron-diffraction experiments (see Fig. 3). In addition, AF1 and AF2 can, in fact, consist of four sublattices rather than two. From Huiku *et al.* (1986).

Experiments on silver were begun in Helsinki in 1987. Because of the relatively small magnetic moment of the Ag nuclei, an ordering temperature much lower than that observed in copper was expected. The NMR measurements indicated a transition to an antiferromagnetic state at $T_N = 560$ pK. The long spin-spin relaxation time of silver made it possible to produce negative nuclear-spin temperatures and look for nuclear ordering at $T < 0$. The measurements showed that the same interactions that produced antiferromagnetism at positive temperatures ordered the nuclear-spin system of silver ferromagnetically above $T_C = -1.9$ nK. These experiments have been described in several papers (see, for example, Oja, Annila, and Takano, 1990; Hakonen and Yin, 1991; Hakonen, Nummila, Vuorinen, and Lounasmaa, 1992; Steiner, Metz, Siemensmeyer, *et al.*, 1996).

Most recently the Helsinki group has investigated nuclear ordering in rhodium (Hakonen, Vuorinen, and Martikainen, 1993). The spin-spin interactions in this metal are slightly weaker than in silver. So far rhodium nuclei have been cooled to 280 pK; this is the current world low-temperature record. In the negative temperature regime, $T = -750$ pK has been reached, which is, in a sense, the highest temperature obtained so far. That is, the energy of a spin system is larger at a negative temperature than at, say, an infinite positive temperature (see Sec. II.D). In spite of these records, nuclear ordering in rhodium has not yet been observed.

B. Theoretical survey

At very low temperatures it is meaningful to speak about two distinct temperatures in the same specimen, at the same time: the nuclear-spin temperature, denoted in this paper by T, and the common conduction-electron and lattice temperature T_e. The nuclei reach local thermal equilibrium among themselves in a time characterized by τ_2, the spin-spin relaxation time (150 μs in copper and 10 ms in silver and in rhodium), whereas the approach to equilibrium between nuclear spins and conduction electrons is governed by the spin-lattice relaxation time τ_1. At low temperatures, $\tau_2 \ll \tau_1$; this makes a separate nuclear-spin temperature meaningful (Goldman, 1970). In experiments on copper, silver, and rhodium, T_e and T may differ by several orders of magnitude. Nevertheless, thermal isolation between the conduction electrons and the nuclei is sufficient for the spin system to be treated by equilibrium thermodynamics.

Nuclear ordering can be studied by using several cooling techniques, described in many review papers and monographs (Huiskamp and Lounasmaa, 1973; Lounasmaa, 1974; Betts, 1976; Abragam and Goldman, 1982; Andres and Lounasmaa, 1982; Pickett, 1988; Pobell, 1992a, 1992b). Among them, the "brute force" method, applicable to metallic samples, is the most straightforward. In this technique, the nuclear spins are first polarized using a high initial magnetic field B_i (6–9 T) at a low starting temperature T_i (10–20 mK) and then adiabatically demagnetized to a small final field B_f. Under ideal conditions, the temperature then decreases according to the relation $T_f = T_i B_f / B_i$, provided that B_f is clearly larger than the local internal field of the material. Further cooling can be achieved by cascading two nuclear-demagnetization stages. If demagnetization is started from a sufficiently low spin entropy, and if B_f is small enough, it can be expected that spin-spin interactions will produce spontaneous magnetic order in the assembly of nuclei. This ordering is analogous to phenomena observed in electronic systems at much higher temperatures. All investigations of nuclear magnetism in copper, silver, and rhodium have been carried out using the brute force cascade-demagnetization technique. It should be noted that nuclear-spin order is not influenced by the temperature of the conduction electrons.

This review is devoted to experiments on and theory of nuclear ordering in Cu, Ag, and Rh. Data on thallium, scandium, $AuIn_2$, and praseodymium compounds will be discussed only briefly. In Cu, Ag, and Rh the spin Hamiltonian is

$$\mathcal{H} = \mathcal{H}_D + \mathcal{H}_{RK} + \mathcal{H}_Z \,. \tag{1}$$

The first term is the dipole-dipole interaction

$$\mathcal{H}_D = (\mu_0 \hbar^2 / 4\pi) \sum_{i<j} \gamma_i \gamma_j r_{ij}^{-3} [\mathbf{I}_i \cdot \mathbf{I}_j - 3 r_{ij}^{-2} (\mathbf{I}_i \cdot \mathbf{r}_{ij})(\mathbf{I}_j \cdot \mathbf{r}_{ij})] \,, \tag{2}$$

where μ_0 is the permeability of free space, γ_i is the gyromagnetic ratio of the nucleus at the lattice site i, $\mathbf{r}_{ij}$ is the lattice vector from i to j, $\mathbf{I}_i$ is the nuclear spin, and the summation is to be taken over all pairs i,j. The second term in Eq. (1) is the Ruderman-Kittel (RK) coupling (Ruderman and Kittel, 1954)

$$\mathcal{H}_{RK} = -\sum_{i<j} J_{ij} \mathbf{I}_i \cdot \mathbf{I}_j \,, \tag{3}$$

where J_{ij} is the coupling constant between spins at sites i and j. The RK interaction is usually the largest contribution to the indirect exchange force. In copper, anisotropic exchange is also significant although clearly smaller than the RK force (see Sec. XV.A.2). The last contribution in the Hamiltonian of Eq. (1) is the Zeeman term

$$\mathcal{H}_Z = -\hbar \gamma \mathbf{B} \cdot \sum_i \mathbf{I}_i \,, \tag{4}$$

where $\mathbf{B}$ is the applied magnetic field.

While the dipolar and Zeeman forces are accurately known, exchange interactions must be inferred either from experiments or from theoretical calculations. In the free-electron approximation, J_{ij} assumes the form

$$J_{ij} = \eta (\mu_0 / 4\pi) \hbar^2 \gamma^2 r_{ij}^{-3} f(2 k_F r_{ij}) \,, \tag{5}$$

where $f(x) = \cos(x) - \sin(x)/x$ and the parameter η describes the strength of the RK interaction. Theoretical values for J_{ij} in copper and silver, more reliable than those obtained using the free-electron approximation, have been deduced recently from band-structure calculations (Lindgård *et al.*, 1986; Frisken and Miller, 1986, 1988b; Miller and Frisken, 1988; Oja *et al.*, 1989; Harmon *et al.*, 1992).

Experimentally, the relative magnitudes of the RK interaction and the dipolar forces are often described by the parameter

$$R = \sum_j J_{ij} / (\mu_0 \hbar^2 \gamma^2 \rho) \,, \tag{6}$$

where ρ is the number density of spins. The R parameter has the value –0.42 for copper, –2.5 for silver, and –1.4 for rhodium. In an fcc lattice, with one conduction electron per atom, the corresponding η parameters in Eq. (5) are –0.71, –4.3, and –2.4, respectively ($R = 0.587\eta$). The negative signs of R and η imply that the interactions have an antiferromagnetic character. Thus we see that copper is in the region where the dipolar and RK interactions are of comparable strength, while silver and rhodium are exchange dominated.

The gyromagnetic ratios of the two stable isotopes of these elements, ^{63}Cu and ^{65}Cu in copper and ^{107}Ag and ^{109}Ag in silver, differ by 7% and 13%, respectively. Rhodium has only one stable isotope, ^{103}Rh. The various γ's are given in Table I. There are no nuclear quadrupolar interactions in silver or rhodium because all stable isotopes have a spin $I = \frac{1}{2}$. Neither is there a quadrupolar force in an undistorted lattice of copper ($I = \frac{3}{2}$) owing to fcc symmetry. The Hamiltonian of Eq. (1) should thus describe the nuclear-spin systems in these metals rather well in a carefully prepared specimen.

TABLE I. Properties of stable Cu, Ag, and Rh isotopes, important for nuclear ordering experiments.

	Isotopic abundance (%)	I	$\gamma/2\pi$ (kHz/mT)
^{63}Cu, ^{65}Cu	69.1, 30.9	$\frac{3}{2}$, $\frac{3}{2}$	11.29, 12.09
^{107}Ag, ^{109}Ag	51.8, 48.2	$\frac{1}{2}$, $\frac{1}{2}$	1.723, 1.981
^{103}Rh	100	$\frac{1}{2}$	1.340

C. Susceptibility and nuclear-magnetic-resonance (NMR) experiments on copper

The main nuclear ordering results on copper were obtained either by means of ac susceptibility measurements at low frequency or by NMR experiments using continuous-wave techniques. The NMR studies were unusual in that the resonant frequencies were low because the measurements were made either in zero field or in a small external field. The interesting range of frequencies was typically from 0.5 to 20 kHz in copper and even lower in silver and rhodium, from 10 to 200 Hz. In principle, the NMR experiment was just an ac susceptibility measurement in which the response of the spin system was monitored in two components, separated by a 90-degree phase angle, and the frequency was swept across the maximum of the absorption signal to observe the resonance. The static susceptibility $\chi'(0)$ was calculated from the measured NMR absorption peak by using the Kramers-Kronig relation. The ac susceptibility experiments, at a sufficiently low frequency, give $\chi'(0)$ quite accurately, too. Therefore, in the terminology of this review, static susceptibility data on copper were, in fact, the results of low-frequency ac susceptibility measurements.

The first NMR results on copper were obtained in 1978 (Ehnholm, Ekström, Jacquinot *et al.*, 1979; Ekström *et al.*, 1979): The nuclear spins reached about 50 nK in zero field, but no clear evidence for a magnetic phase transition was seen (Kurti, 1982). However, several important results were deduced, among them the magnitude and sign of the RK exchange interaction. The value $R=-0.42$ was obtained in two ways: from the relative magnitudes of the separate ^{63}Cu and ^{65}Cu NMR absorption lines and from a 2-kHz shift downwards of the second harmonic in the NMR peak. According to a calculation based on the mean-field theory (Kjäldman and Kurkijärvi, 1979), the RK interaction with $R=-0.42$ should have ordered copper nuclei to an antiferromagnetic state as early as 230 nK, far above the lowest temperatures reached in the measurements. This discrepancy between experiment and theory remained a problem for several years, although calculations showed that fluctuations can substantially decrease the ordering temperature from its mean-field value (Kumar *et al.*, 1980; Kjäldman *et al.*, 1981; Niskanen and Kurkijärvi, 1981, 1983; Niskanen *et al.*, 1982).

The main problem in these early experiments was the short spin-lattice relaxation time, about 10 minutes, which caused the entropy of the nuclear-spin system to increase rapidly after demagnetization. In the next series of measurements (Ehnholm *et al.*, 1980), started in 1979, T_e was decreased further, which resulted in a somewhat longer relaxation time. It was then observed, after demagnetization to zero field, that the susceptibility was saturated during the first few minutes in a longitudinal measuring geometry but not in a transverse geometry. Subsequent studies suggested that the plateau in the longitudinal susceptibility had been caused by an experimental artifact (Huiku and Soini, 1983). However, an unexplained difference between the longitudinal and transverse zero-field susceptibilities remained.

Finally, in 1982, the Helsinki group unambiguously saw ordering in copper at $T_c=58$ nK (Huiku and Loponen, 1982; Huiku, Jyrkkiö, and Loponen, 1983); the nuclear-spin system was cooled to the at-that-time record low temperature of 25 nK. A polycrystalline specimen of thin foils was used. Two critical modifications finally led to experimental success: the preparation of the sample by selective oxidation and the construction of a new nuclear cooling stage made of a bulk piece of copper. These improvements resulted in an order-of-magnitude increase of the spin-lattice relaxation time. Simultaneously, indications of two different ordered regions were found by recording the static susceptibility $\chi'(0)$ during warmup after demagnetization to different final fields below the critical value $B_c=0.25$ mT.

Experiments on a single-crystal specimen were begun in 1984 (Huiku, Jyrkkiö, *et al.*, 1984; Huiku *et al.*, 1986). The static susceptibility was measured in the three Cartesian directions. Below B_c, three different antiferromagnetically ordered regions were distinguished at low entropies. Using a simple two-sublattice model for the transverse and longitudinal susceptibilities, provisional spin arrangements were obtained for the ordered states. The B-S phase diagram, illustrated in Fig. 1, was constructed.

The experimental result was analyzed in several theoretical calculations (Kjäldman and Kurkijärvi, 1979; Oja and Kumar, 1984; Kumar *et al.*, 1985, 1986; Viertiö and Oja, 1987; Frisken and Miller, 1988a; Lindgård, 1988a). However, it was not possible to test the proposed spin structures against experiments, since measurements of static susceptibility do not yield sufficiently detailed information. In studies of electronic magnetism, neutron diffraction has been the tool for determining ordered spin structures. The basic principles of nonmagnetic and magnetic Bragg reflections are illustrated in Fig. 2. In the case of nuclear magnets, the use of neutron diffraction is based on the spin-dependent part of the neutron-nucleus scattering amplitude, which results from the strong interaction between a neutron and a nucleus. In particular, long-range antiferromagnetic order gives rise to additional Bragg reflections, yielding directly the translational symmetry of the spin system.

D. Neutron-diffraction measurements on copper

Previously, the ordered structures of purely nuclear systems had been determined by neutrons in only a few

cases and never in simple metals. The first measurements were made on LiH in 1978 by Abragam and Goldman and their co-workers at Saclay (Roinel *et al.*, 1978; Abragam and Goldman, 1982).[1] Neutron studies of this insulator are feasible because of the very large spin-dependent scattering amplitude of protons. These experiments revealed antiferromagnetic and ferromagnetic nuclear structures at $T>0$ and $T<0$, respectively. The ordering temperatures could not be determined from the experimental data. Benoit *et al.* (1985) were able to perform neutron-diffraction experiments on ordered solid ^{3}He and to verify the previously proposed (Osheroff *et al.*, 1980) up-up-down-down order in the low-field phase. Even though the transition temperature is as high as 1 mK, other experimental difficulties, such as the need to grow the ^{3}He crystal *in situ* and the enormous neutron absorption by the ^{3}He nuclei, kept the counting statistics rather low. Nuclear-spin ordering has also been observed around 1 mK by neutron diffraction in several hyperfine-enhanced systems (Benoit *et al.*, 1981; Nicklow *et al.*, 1985).

Before the Risø work on copper was begun in 1986 (Jyrkkiö, Huiku, Clausen, *et al.*, 1988), neutron-diffraction studies had not been performed on a purely nuclear magnet with a full dipolar and exchange interaction between the spins. As metallic copper provides such a system, the study paved the way for an understanding of ordering in this metal as well as in nuclear magnets more generally. The large amount of information obtained earlier by the susceptibility measurements in Helsinki provided a good basis for subsequent investigations with neutrons. The Risø study was performed on an isotopically enriched ^{65}Cu single crystal. As the ordering took place at 58 nK, these measurements opened a totally new temperature range for neutron-diffraction experiments.

Reaching low nanokelvin temperatures in quiet surroundings is a difficult undertaking in any case, but the task is even more complicated in a reactor environment. The presence of numerous pieces of equipment in the experimental hall tends to increase the heat leak into the cryogenic system. A new and significant problem is warming of the specimen by the neutron beam. The low-temperature requirements must be taken into account in the design of the diffractometer as well. A special feature, not encountered in standard neutron-scattering experiments, is that only limited mechanical movements of the spectrometer are allowed during actual measurements, again because of heating problems.

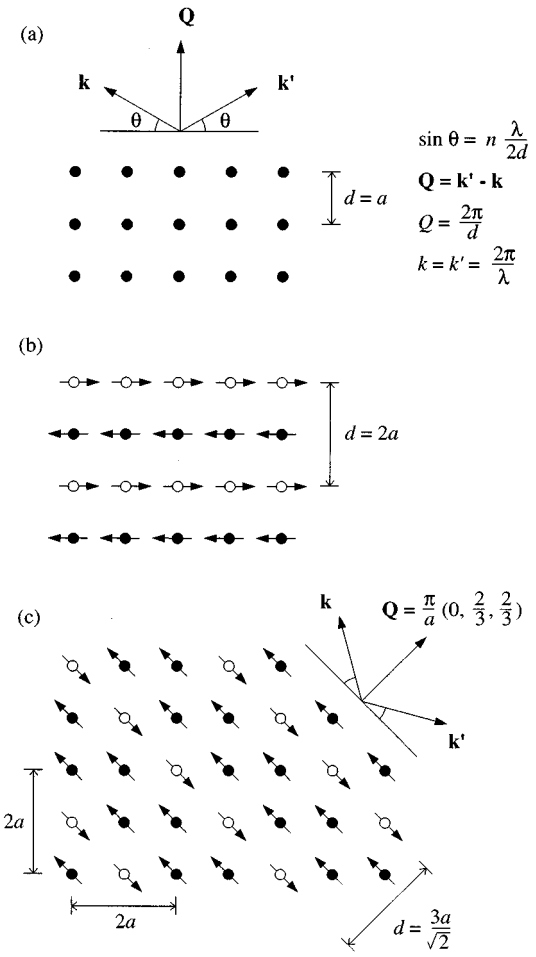

FIG. 2. Illustration of basic principles of Bragg reflection. (a) $\mathbf{k}$ and $\mathbf{k}'$ are the wave vectors of the incident and reflected neutron beams, respectively. $\mathbf{Q}=\mathbf{k}-\mathbf{k}'$ is the scattering vector. The scattering angle 2θ is determined by the distance between the lattice planes, as described by the equation at right. (b) In the presence of antiferromagnetism, there will be additional Bragg reflections resulting from the magnetic structure. For a simple two-sublattice structure, the fundamental antiferromagnetic reflection corresponds to an interplanar distance $d=2a$, where a is the lattice constant. Such a two-sublattice state produces the antiferromagnetic (1 0 0) Bragg reflection in an fcc lattice. (c) Illustration of the antiferromagnetic $(0\frac{2}{3}\frac{2}{3})$ Bragg reflection in an fcc lattice. The spin configuration is the up-up-down pattern depicted in three dimensions in Fig. 3(c). Here, all spins have been projected onto the scattering plane, i.e., the plane spanned by $\mathbf{k}$ and $\mathbf{k}'$. The period of the magnetic structure $d=3a/\sqrt{2}$.

The Risø group enjoyed its first significant success in the fall of 1987, when the antiferromagnetic (1 0 0) Bragg reflection from nuclear-ordered copper was detected (Jyrkkiö, Huiku, Lounasmaa *et al.*, 1988). The signal corresponded to type-I ordering in the fcc lattice; the observation was consistent with theoretical predictions (Kjäldman and Kurkijärvi, 1979). In the simplest case, a type-I antiferromagnetic spin configuration consists of alternating ferromagnetic sheets. Such a structure is illustrated in Fig. 2(b).

[1]In the studies of insulators by the Saclay group, nuclear order was produced in the rotating frame of reference, under a high magnetic field, by the so-called truncated part of the dipolar interaction, i.e., the part that commutes with the Zeeman term (see Sec. XIV.C). For dynamic polarization, a small concentration of paramagnetic impurities was introduced into the sample. The ordering temperatures in these insulators were in the range 0.3–0.6 μK according to theoretical estimates.

Comprehensive neutron-diffraction measurements were then made of the magnetic-field dependence of the scattered-neutron intensity (Jyrkkiö *et al.*, 1989). The data, shown in Fig. 3, indicated the existence of at least two different antiferromagnetic phases, both producing the (1 0 0) Bragg reflection. These spin structures were found in the low- and high-field regions. In intermediate fields, the (1 0 0) reflection nearly vanished, and the nature of the spin structure there remained unclear.

In the fall of 1989 the puzzle was solved: another Bragg reflection at $(0\ \frac{2}{3}\ \frac{2}{3})$ was discovered in the intermediate-field region (Annila *et al.*, 1990). This kind of ordering had not been observed before in any fcc antiferromagnet. Once again, calculations were important in finding the antiferromagnetic reflection (Lindgård *et al.*, 1986; Lindgård, 1988a). Theoretical work identified the $(0\ \frac{2}{3}\ \frac{2}{3})$ structure with an up-up-down spin configuration in fields where the Bragg reflection was strongest (Viertiö and Oja, 1990a). The spin structure and the resulting Bragg reflection are illustrated in Fig. 2(c).

In the low intermediate-field region, both the $(0\ \frac{2}{3}\ \frac{2}{3})$ and the (1 0 0) reflections were observed. Although this can be attributed to the presence of two different types of domains, there is theoretical evidence for a more exotic type of ordering in which a single magnetic domain displays, at the same time, both reflections. The calculated spin structures in the various regions of the B-S plane are illustrated in Fig. 3. The phase diagram obtained from the neutron-diffraction measurements is in good overall agreement with the diagram constructed previously from magnetic-susceptibility measurements (see Fig. 1).

The most recent series of neutron-diffraction experiments at Risø (Annila *et al.*, 1992) were performed by varying the direction of the external magnetic field with respect to the crystalline axis. It was found that the intensities of the $(0\ \frac{2}{3}\ \frac{2}{3})$ and the (1 0 0) Bragg reflections depended sensitively on the alignment of the field. These measurements provided stringent tests of the theoretically proposed spin structures. The data showed, indeed, the characteristic features of the predicted spin structures (Viertiö and Oja, 1987, 1990a, 1990b). Unexpectedly, however, in high fields aligned close to the [111] crystalline axis, no (1 0 0) Bragg reflection was observed. It is likely that there is yet another type of antiferromagnetic order present in this field region, to be found in future studies.

E. Experiments on silver and rhodium

Measurements of nuclear magnetism in silver were begun in Helsinki in 1986. The main difficulty in these experiments was achieving high enough initial nuclear polarization, i.e., low enough spin entropy, before demagnetizing the sample to zero field. The equilibrium polarization at $B=7$ T and at $T=200$ μK is 91.4% (the corresponding entropy is $0.26\mathcal{R}$ ln2, where $\mathcal{R}$ is the gas constant), while in copper it would be 99.9%. Furthermore, polarization of silver nuclei is a relatively slow process: the spin-lattice relaxation time in a high magnetic field is 14 h at $T_e=200$ μK (τ_1 would be 2 h for Cu).

In the first sets of experiments (Oja, Annila, and Takano, 1990, 1991), the nuclear-spin entropy of the specimen was reduced to $0.50\mathcal{R}$ ln2, corresponding to polarizations up to 78%. Evidence for antiferromagnetic ordering was obtained at the lowest entropies by observing saturation of the static magnetic susceptibility. Conclusive data on antiferromagnetic ordering were obtained, however, only after improved precooling of the sample. In this second set of experiments spin polarizations up to 94% were reached (Hakonen, Yin, and Lounasmaa, 1990; Hakonen and Yin, 1991; Hakonen, Yin, and Nummila, 1991; Hakonen, Nummila, and Vuorinen, 1992; Hakonen, Nummila, Vuorinen *et al.*, 1992; Hakonen and Vuorinen, 1992). The ordering temperature in zero field was determined to be $T_N=560$ pK; this is the lowest ordering temperature ever measured.

The boundary for antiferromagnetic order was traced in the B-S plane. The phase diagram is illustrated in Fig. 4. Interestingly, the critical entropy for ordering increased with B in small fields. Only one ordered state could be singled out, although some features of the NMR spectra indicated the presence of two phases. Definite conclusions were difficult to make because the sample was polycrystalline.

An important new feature in the investigations on silver was that it was possible to study nuclear magnetism at negative spin temperatures as well (Oja, Annila, and Takano, 1991). Unlike the spins in insulators studied by the Saclay group (Abragam and Goldman, 1982), nuclear spins in silver interact through the full dipolar force, which, together with exchange interactions, produces ordering in the laboratory frame in low external fields. There are several ways to generate negative spin temperatures. In silver this regime was achieved by quickly reversing the direction of the external magnetic field, in less than $\tau_2=10$ ms, so that the spins did not have time to redistribute themselves among the energy levels. At negative temperatures, the population of spins among the Zeeman levels is given by the usual Boltzmann factor, $\exp(-\mu B/kT)$ as at positive temperatures, but with $T<0$. Only the highest energy level is populated when $T\rightarrow -0$. Therefore, the energy of a nuclear-spin system is maximized when absolute zero is approached from the negative side. It can be shown that, at $T<0$, the thermodynamic equilibrium state corresponds to the *maximum* of the Gibbs free energy (see Sec. II.D.3).

Measurement of NMR absorption at $T<0$ is actually a measurement of NMR emission, since $\chi''(f)<0$. Static susceptibility can still be obtained using the Kramers-Kronig relation, that is, by integrating over $\chi''(f)/f$. Therefore, $\chi'(0)$ is negative as well. Nuclear-spin temperatures can be determined by directly applying the second law of thermodynamics, using the same procedure as at $T>0$ (see Sec. IV). The $\chi'(0)$ data showed that silver orders ferromagnetically at $T=-1.9$ nK (Hakonen, Nummila, Vuorinen, and Lounasmaa, 1992). Al-

though it may, at first, seem surprising that a system with antiferromagnetic interactions can order ferromagnetically, this is exactly according to theoretical expectations for a spin system at $T<0$: Maximum energy for antiferromagnetic interactions presumably corresponds to ferromagnetic order. Such a situation, antiferromagnetism at $T>0$ and ferromagnetism at $T<0$, has also been found for LiH in a coordinate frame rotating at the Larmor frequency about the external magnetic field (Roinel *et al.*, 1980). According to theoretical calculations (Viertiö and Oja, 1992), the ferromagnetic structure in silver is a novel kind of domain configuration. The measured value of the susceptibility in the ferromagnetic state is consistent with the proposed structure. The phase diagram of silver at $T<0$ is illustrated in Fig. 4.

NMR measurements alone cannot verify details of the spin configuration in silver. Experiments employing scattering of polarized neutrons are again necessary for this purpose. Tuoriniemi, Nummila *et al.* (1995) have recently observed long-range nuclear antiferromagnetic order by neutron diffraction in a single crystal of silver. The observed antiferromagnetic (0 0 1) Bragg peak decisively proved spontaneous long-range ordering. In a magnetic field along the [001] direction, a single-**k** state with $\mathbf{k}=(\pi/a)(0,0,1)$ developed. A structure with this ordering vector remained stable in zero field. Domains with the other equivalent **k**-vectors did not appear within the available experimental time, as was deduced from the lack of (0 0 1) intensity in measurements with $\mathbf{B}\|[010]$. The results support the theoretically predicted structure for low magnetic fields along the [001] axis, but no evidence for a proposed triple-**k** state in higher fields was seen (Viertiö, 1992; Heinilä and Oja, 1993a). In 50 μT ($\approx B_c/2$), the (0 0 1) reflection was observed when **B** was aligned within a cone of 110° opening around the [001] axis, in partial agreement with Monte Carlo simulations. The phase diagram based on neutron-diffraction data closely resemble the earlier NMR results on a polycrystalline sample of natural silver.

The spin dynamics of silver nuclei have been investigated extensively as well. Studies of cross relaxation (Oja, Annila, and Takano, 1990) between the Zeeman temperatures of the two isotopes ^{107}Ag and ^{109}Ag provide a clear demonstration of the theoretical prediction (Goldman, 1970) that mutual flips of unlike spins, which become effective once the two isotopic NMR lines overlap, do not lead to an equalizing of temperature. Equilibrium between the two Zeeman reservoirs is achieved only through the energy reservoir of spin-spin interactions via single spin flips, which become frequent in low fields. The observed cross-relaxation rate also gives a measure for the strength of the RK interaction in silver. Values for R were obtained from the relative intensities of the ^{107}Ag and ^{109}Ag NMR-absorption lines at a high spin polarization in a low field, both at $T>0$ and at $T<0$ (Hakonen, Nummila, and Vuorinen, 1992). The data were consistent with the early NMR work at high temperatures (Poitrenaud and Winter, 1964), with susceptibility measurements (Hakonen and Yin, 1991), and with band-structure calculations (Harmon *et al.*, 1992).

During the past four years the Helsinki group has investigated nuclear magnetism in rhodium metal, which is an $I=\frac{1}{2}$ fcc system like silver (Hakonen, Vuorinen, and Martikainen, 1993, 1994). The R parameter [see Eq. (6)] was found to be –1.4, implying that interactions are exchange dominated but not so strongly as in silver. Although the nuclear magnetic moment of rhodium is 30% smaller than in silver, nuclear-spin polarizations up to 83% were reached in experiments at $T>0$ and –60% at $T<0$. These values correspond to spin entropies that in silver were low enough to produce magnetic order. In rhodium, however, no ordering was observed in spite of the record-low and record-high temperatures of 280 pK and –750 pK.

Nevertheless, susceptibility measurements showed that rhodium nuclei tend to order antiferromagnetically at both positive and negative spin temperatures, which can be understood if the nearest-neighbor and next-nearest-neighbor exchange interactions are competing, as the NMR measurements suggest. It is then possible that the observed structure at $T>0$ is a type-I antiferromagnet, as in copper and silver, while the ground state at $T<0$ is an fcc antiferromagnet of the type II.

The spin-lattice relaxation of rhodium showed an interesting feature: τ_1 was clearly longer at $T<0$ than at $T>0$ (Hakonen, Vuorinen, and Martikainen, 1994). Such an effect had not been seen in similar measurements on silver. The observation was explained by the presence of iron impurities in the sample, at the level of 10 ppm. It was concluded that the large susceptibility of Rh nuclei modifies the scattering of conduction electrons by the impurities and leads to changes in τ_1.

F. Studies of other metals

Before beginning a thorough discussion of experimental and theoretical results on copper, silver, and rhodium, we should like to mention some interesting recent results on nuclear magnetism in other metals (see Sec. XII for a more detailed discussion). The Bayreuth group has made extensive measurements on the properties of the metallic compound $AuIn_2$ at low temperatures in fields above the critical field for superconductivity (Herrmannsdörfer and Pobell, 1995; Herrmannsdörfer, Smeibidl, Schröder-Smeibidl, and Pobell, 1995). Data on nuclear specific heat, magnetic susceptibility, and the measured NMR spectra gave strong evidence for a ferromagnetic transition at $T_C=35$ μK. The magnitude of T_C was unexpectedly large, perhaps by an order of magnitude. The magnetically ordering spins in $AuIn_2$ are the In nuclei, which form a simple cubic lattice. Unlike Cu, Ag, and Rh, ordered nuclei of $AuIn_2$ are in thermal equilibrium with the conduction electrons.

Possible indications of a transition to an ordered state have been reported in scandium (Suzuki *et al.*, 1994; Koike *et al.*, 1995). The quadrupolar interaction is important in this metal. As a result, Sc is a good example of a three-dimensional Ising model in a hexagonal lattice, so that the spin Hamiltonian is qualitatively differ-

ent from that in the noble metals. It seems clear that new data will be forthcoming, but it is too early to discuss these systems in detail at present. Interesting NMR results on highly polarized thallium nuclei have been obtained by Eska and Schuberth (1987) and Leib *et al.* (1995).

Several short reviews on nuclear ordering in metals have been published earlier (Oja, 1987; Lounasmaa, 1989; Hakonen, Lounasmaa, and Oja, 1991; Oja, 1991; Hakonen and Vuorinen, 1992; Hakonen, 1993; Ramakrishnan and Chandra, 1993; Hakonen and Lounasmaa, 1994; Pobell, 1994; Steiner, Metz, Siemensmeyer, *et al.*, 1996).

II. BASIC PRINCIPLES OF POSITIVE AND NEGATIVE SPIN TEMPERATURES IN NUCLEAR MAGNETISM

A. Spin temperature

The idea of spin temperature originates from the work of Casimir and Du Pré (1938). Their work was extended by Bloembergen and Wang (1954), who suggested that there may be two temperatures within the spin system, one, T_Z, relating to the distribution of the Zeeman energy, and the other, T_{ss}, relating to the energy of spin-spin interactions. When $T_Z = T_{ss}$ it is meaningful to speak of a common spin temperature; otherwise a distinction between T_Z and T_{ss} should be made. A large number of experiments have verified theoretical predictions based on the concepts of T_Z and T_{ss}. Comprehensive reviews have been written on spin temperature and its implications (Goldman, 1970; Wolf, 1979; Abragam and Goldman, 1982). We also refer the reader to the paper by Van Vleck (1957), in which the basics of positive and negative spin temperatures are discussed in a clear and simple way.

1. Zeeman temperature

The meaning of the Zeeman temperature T_Z, associated with the Hamiltonian $\mathcal{H}_Z = -\hbar\gamma\mathbf{B}\cdot\Sigma_i\mathbf{I}_i$, can be illustrated using an energy-level diagram. Since the nuclei are well localized in their lattice sites, Boltzmann statistics is appropriate for a description of the spin system. The energy-level diagram for a spin $I=\frac{1}{2}$ assembly is shown in Fig. 5(a) in the case when the Zeeman energy dominates over spin-spin interactions. The number of nuclei in the different energy levels $E_m = -\hbar\gamma m B$, $m = -I \ldots +I$, is proportional to $\exp(-E_m/k_B T_Z)$. At positive temperatures, the number of nuclei in a higher level of energy is always smaller than that in a lower energy level.

2. Temperature of the interaction reservoir

The temperature of the interaction reservoir T_{ss} can be understood in a similar way. Let us consider the situation in high external fields, where spin-spin interactions are but a small perturbation to the Zeeman Hamiltonian. In the energy-level diagram, interactions split each Zeeman level into a number of sublevels. The characteristic width of the splitting is on the order of the spin-spin interaction energy, and the number of sublevels is proportional to $(2I+1)^N$, which in practice is infinite (N is the number of spins).

Mathematically, the meaning of T_{ss} as the temperature of the interaction reservoir $\mathcal{H}'_{ss}$ is described by the distribution function (i.e., the density matrix)

$$\rho = \exp(-\mathcal{H}_Z/k_B T_Z)\exp(-\mathcal{H}'_{ss}/k_B T_{ss}). \tag{7}$$

Thus the distribution of the nuclei in the sublevels of each Zeeman level is determined by the same T_{ss}. In general, T_{ss} can differ from T_Z. Such a situation is illustrated in Fig. 5(b). In thermal equilibrium, however, $T_{ss} = T_Z$, as in Figs. 5(a) and 5(c).

The detailed form of $\mathcal{H}_{ss}$ in the density matrix is a subtle point. $\mathcal{H}'_{ss}$ is that part of the full spin-spin interaction $\mathcal{H}_{ss}$ which conserves the Zeeman energy, i.e., commutes with $\mathcal{H}_Z$. When the Zeeman and interation reservoirs are not in mutual thermal equilibrium, $\mathcal{H}'_{ss}$ must be used in the density matrix, as is written into Eq. (7). However, in thermal equilibrium $T_{ss} = T_Z$, and the full $\mathcal{H}_{ss}$ is the appropriate quantity; then $\rho = \exp[-(\mathcal{H}_Z + \mathcal{H}_{ss})/k_B T]$. Exchange forces of the form $\mathbf{I}_i\cdot\mathbf{I}_j$, such as the Ruderman-Kittel interaction [see Eq. (3)], commute with $\mathcal{H}_Z$, while the dipolar Hamiltonian does not. This has the important consequence that there will be thermal contact, so-called thermal mixing, between the Zeeman and interaction reservoirs.

B. Heat reservoirs, spin-lattice relaxation, and thermal mixing

The various parts of the spin Hamiltonian can be thought of as thermal reservoirs with a certain heat capacity and temperature. Figure 6(a) schematically illustrates the situation in which the Zeeman and interaction reservoirs are in mutual thermal equilibrium. This is typically the case for fields that are low or comparable to the local field B_{loc}. A single temperature then describes the spin system. The lattice vibrations and conduction electrons form a heat reservoir at the temperature T_e.

Equalization of T_e and T_Z is obtained via a relaxation process,

$$d(T_Z^{-1})/dt = \tau_1^{-1}(T_e^{-1} - T_Z^{-1}), \tag{8}$$

where τ_1 is the spin-lattice relaxation time. In metals, τ_1 is obtained from

$$\tau_1 = \kappa/T_e, \tag{9}$$

where κ is the Korringa constant (Korringa, 1950). This equation is valid for fields much higher than B_{loc} and for not too large values of B/T_e. In low B, spin-lattice relaxation becomes faster. The situation can still be described by Eq. (9) if a field dependency is incorporated into the Korringa constant through

$$\frac{\kappa(B)}{\kappa_\infty} = \frac{B^2 + B_{loc}^2}{B^2 + \alpha B_{loc}^2}. \tag{10}$$

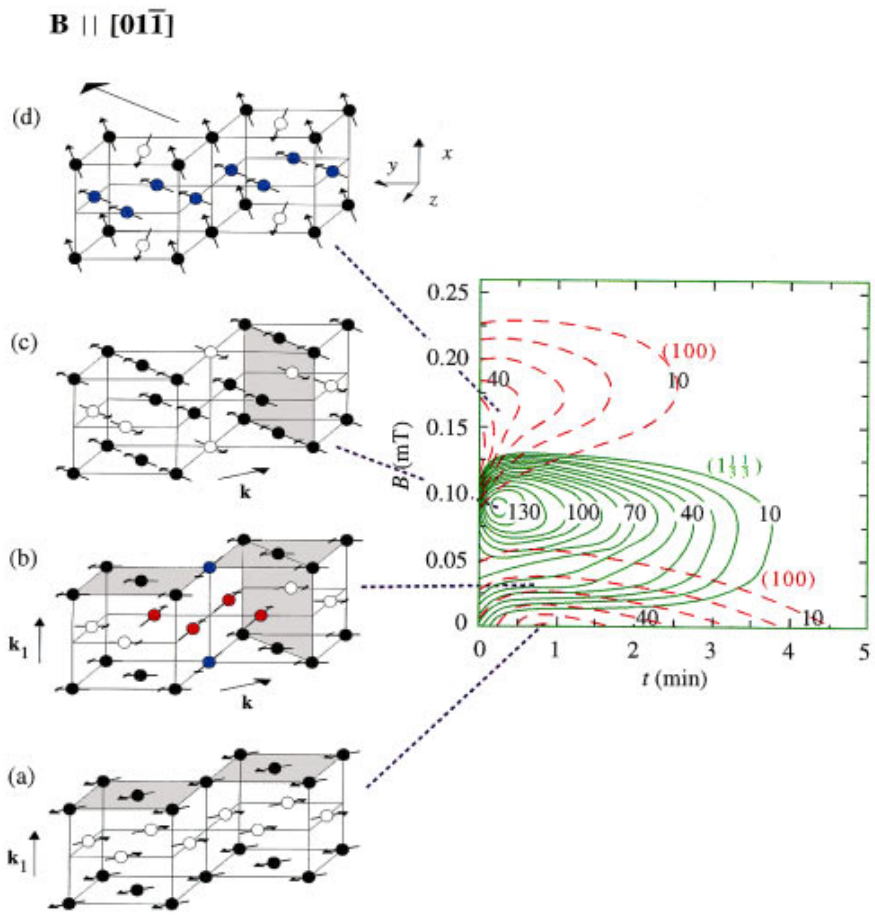

FIG. 3. At right: Neutron-intensity contour diagram of copper for the Bragg reflections, as a function of time and the external magnetic field: (solid curves), (1 $\frac{1}{3}$ $\frac{1}{3}$); and (dashed curves) (1 0 0). The number of neutrons collected per second is marked on the contours. From Annila *et al.* (1990). At left: Spin structures of copper for the [011] alignment of the magnetic field, as given by Eqs. (159) and (140). (a) B=0: antiferromagnetic $\mathbf{k}_1=(\pi/a)(1,0,0)$ structure consisting of alternating ferromagnetic planes. (b) $0<B<B_c/3$: structure with ordering vectors $\mathbf{k}_1=(\pi/a)(1,0,0)$ and $\pm\mathbf{k}=\pm(\pi/a)(0,\frac{2}{3},\frac{2}{3})$, illustrated for $B=0.17B_c$; (0 $\frac{2}{3}$ $\frac{2}{3}$) and (1 $\frac{1}{3}$ $\frac{1}{3}$) reflections are equivalent under fcc symmetry. (c) $B=B_c/3$: the up-up-down structure with $\pm\mathbf{k}=\pm(\pi/a)(0,\frac{2}{3},\frac{2}{3})$ order. (d) High-field state with three ordering vectors $(\pi/a)(1,0,0)$, $(\pi/a)(0,1,0)$, and $(\pi/a)(0,0,1)$. The spin structures, which are consistent with the neutron-diffraction data, were taken from theoretical calculations by Viertiö and Oja [1990a (structures a–c), 1987 (structure d)].

According to measurements as well as theoretical calculations, the constant α varies in the range $\alpha=2$–3 (Goldman, 1970). Spin-lattice relaxation is also faster than that given by Eq. (9) at large B/T_e (Jauho and Pirilä, 1970; Bacon *et al.*, 1972; Shibata and Hamano, 1982).

In high fields, thermal contact between the Zeeman and interaction reservoirs is weak. It is therefore usually more appropriate to describe the spin system in terms of the block diagram illustrated in Fig. 6(b). As was mentioned above, the interaction reservoir now consists of those interactions which commute with $\mathcal{H}_Z$.

The relaxation of $\mathcal{H}_Z$ and $\mathcal{H}'_{ss}$ towards T_e is determined by different time constants, τ_1 and τ_{1ss}. The former is described by the usual high-field Korringa constant, Eq. (9). The relaxation time τ_{1ss} is not of practical importance for experiments discussed in this paper.

The direct thermal contact between $\mathcal{H}_Z$ and $\mathcal{H}'_{ss}$ is called thermal mixing, and the corresponding time constant τ_m is the thermal mixing time. Thermal mixing is caused by spin-spin interactions that do not conserve the Zeeman energy. Usually τ_m is determined by the dipolar interaction. Processes that contribute to thermal mixing are single spin flips (terms $I_i^+ I_j^z$ and $I_i^- I_j^z$) and double spin flips ($I_i^+ I_j^+$, $I_i^- I_j^-$; see Sec. XI.A.2 for definitions). An isotropic exchange interaction commutes with $\mathcal{H}_Z$ and therefore does not cause thermal mixing.

The constant τ_m depends strongly on the magnetic field, becoming exceedingly long at high B. The reason for this is easy to understand. The energy must be conserved during the relaxation process. If the change in the Zeeman energy is large, it cannot be counterbalanced easily by a corresponding but opposite change in the interaction energy. Various theoretical models predict, approximately, $\tau_m \approx \tau_0 \exp(B^2/b^2)$ or $\tau_m \approx \tau_0 \exp(B/b)$, where the constant b is on the order of B_{loc} and τ_0 is on the order of the spin-spin relaxation time τ_2 (Goldman, 1970). An experiment in which the field dependence of

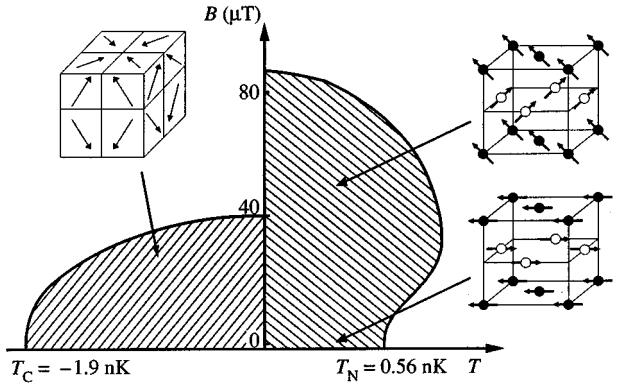

FIG. 4. Right half: Phase diagram of nuclear spins in silver at $T>0$ in the magnetic field vs temperature plane. "Inside" the full curve the spin system is antiferromagnetically ordered. The phase boundary is drawn on the basis of measurements by Hakonen, Yin, and Nummila (1991), assuming that its shape is the same as in the magnetic field vs entropy plane. The spin configurations at right represent a two-sublattice, type-I antiferromagnet in $B=0$ (lower structure) and in a finite field (higher structure). These configurations, with the ordering vector parallel to the external magnetic field, are consistent with the neutron-diffraction data of Tuoriniemi, Nummila, *et al.* (1995) and with theoretical predictions in low fields but not in high fields (Viertiö, 1992; Heinilä and Oja, 1993a). The external magnetic field is pointing down. Note that the gyromagnetic ratio of silver nuclei is negative and therefore spins $\mathbf{I}_i$ align antiparallel to $\mathbf{B}_{\rm ext}$ at $T>0$. Left half: Phase diagram at $T<0$. The solid curve shows the boundary between the ferromagnetic domain state (inside) and the paramagnetic region. From Hakonen, Nummila, Vuorinen, and Lounasmaa (1992). One of the possible domain configurations predicted by Viertiö and Oja (1992) is also shown.

τ_m was measured for silver will be discussed in Sec. XI.A.

C. Demagnetization to the ordered state

We discuss next the process during which a sample is demagnetized into the magnetically ordered state. The nuclear-spin system is first polarized in a high field and a low temperature to decrease its entropy below the critical value for magnetic ordering. After the equilibrium polarization with $T_Z=T_e$ has been reached, the sample is demagnetized down to $B=0$, or to a low field, to produce spontaneous nuclear ordering. The demagnetization is performed in a time much shorter than τ_1 to avoid warmup of the spin system caused by spin-lattice relaxation.

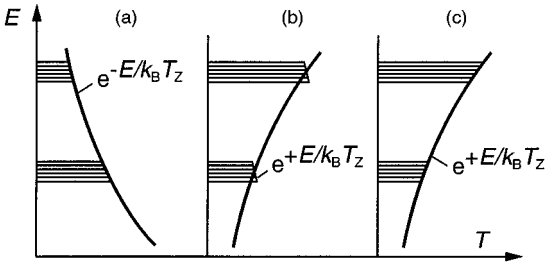

FIG. 5. Equilibrium distribution of nuclei in the various Zeeman levels: (a) at a positive spin temperature T_Z for a spin $I=\frac{1}{2}$ system. Splitting into sublevels is due to spin-spin interactions. (b) Situation when $T_{ss}>0$ and $T_Z<0$. (c) Equilibrium at a negative $T_{ss}=T_Z$.

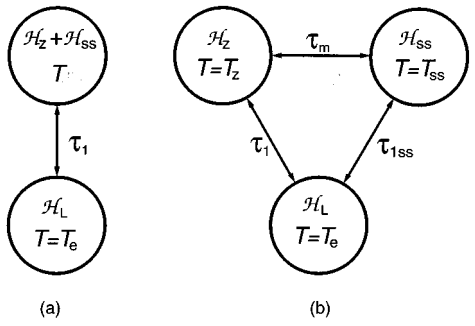

FIG. 6. Schematic illustration of the Zeeman ($\mathcal{H}_Z$), spin-spin-interaction ($\mathcal{H}_{ss}$), and conduction-electron ($\mathcal{H}_L$) heat reservoirs. The various thermal relaxation times, τ_1, τ_m, and τ_{1ss}, are indicated. (a) In low fields, $\mathcal{H}_Z$ and $\mathcal{H}_{ss}$ form a single heat reservoir, but (b) in high fields they are decoupled.

Let us first neglect, for simplicity, the spin-lattice relaxation. When we change from the high initial field to a low, so-called mixing field B_m, we see that the only effect of the demagnetization is to decrease the Zeeman temperature, so that the ratio B/T_Z remains constant. At $B=B_m$, the thermal mixing time τ_m becomes sufficiently fast compared to the rate of the field sweep that there will be thermal contact between the Zeeman and interaction heat reservoirs. As a result, thermal equilibrium with $T_Z=T_{ss}$ is achieved. It is only now that the interaction reservoir is cooled. Before the mixing process it remained at the initial precooling temperature.

Thermal mixing is necessarily a nonadiabatic process, since the cold Zeeman temperature has to cool down the hot interaction reservoir. The degree of adiabaticity is characterized by the factor

$$B_m^2/(B_m^2+B_{\rm loc}^2), \tag{11}$$

which is derived in Sec. IV.F. The closer to one this factor, the more adiabatic will be the thermal mixing. It is obvious that it would be desirable to perform mixing in the highest possible B_m. In practice, however, thermal mixing is too slow a process to occur in fields much larger than $B=B_{\rm loc}$.

On the other hand, nuclear ordering also takes place in fields on the order of $B_{\rm loc}$. One may wonder whether the non-occurrence of nuclear ordering after demagnetization to a certain low field might simply be because thermal mixing has not yet taken place. This does not seem to be the case. Measurements on silver, for example, show that $B_m\approx 10B_{\rm loc}=0.3$ mT while the critical field for nuclear ordering is $B_c\approx 3B_{\rm loc}=0.1$ mT. Thus the final cooling necessary for nuclear ordering takes place in a field three times larger than the critical field.

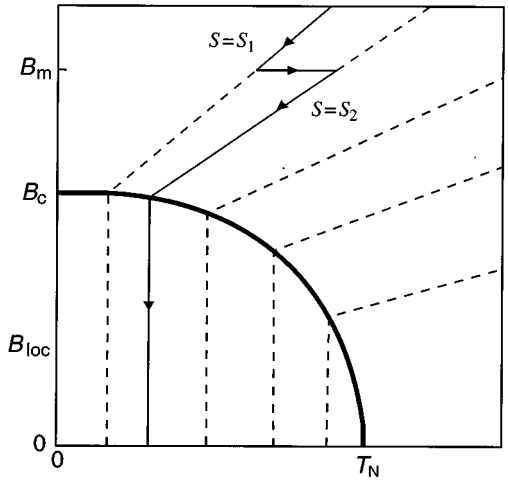

FIG. 7. Demagnetization into the antiferromagnetically ordered state along isentropes in the magnetic field vs temperature plane. Thermal mixing takes place in the field $B=B_m$, larger than the local field B_{loc}. In silver, $B_m \approx 0.25$ mT, $B_c=0.1$ mT, $B_{loc}=0.035$ mT, and $T_N=560$ pK.

Theoretical estimates and actual measurements show that the nonadiabaticity associated with thermal mixing is on a few-percent level and that it is not prohibitive for nuclear ordering. A more detailed explanation is given in Sec. IV.F. The present discussion is, of course, an oversimplification in that thermal mixing is, in reality, a gradual process, which proceeds in a range of fields during demagnetization. The steep field dependence of τ_m, however, makes the steplike process a good approximation.

The form of the isentropes in the ordered state is an important question. Mean-field calculations, to be discussed in Sec. XV.B.5. for antiferromagnetic type-I spin structures or more generally for the so-called permanent spin structures show that isentropes in the ordered state are vertical in the magnetic field vs temperature plane, as shown in Fig. 7. The temperature T then stays constant during demagnetization in the ordered state. Figure 7 also depicts the entropy increase due to thermal mixing at $B=B_m$.

D. Negative spin temperatures

The main ideas associated with negative spin temperatures can again be illustrated conveniently by an energy-level diagram. For the sake of simplicity, we consider a diagram for a noninteracting $I=\frac{1}{2}$ spin system in an external magnetic field. The same ideas can be applied readily to interacting spin assemblies in an arbitrary field.

At the absolute zero, $T=+0$, all nuclei are in the ground state with $\vec{\mu}=\hbar\gamma\mathbf{I}$ parallel to $\mathbf{B}$. As the temperature is increased, keeping B constant (see Fig. 8), nuclei begin to flip into the upper energy state and, at $T=+\infty$, there is an equal number of spins in both levels. If the energy is increased further, the reversed distribution of nuclear spins can still be described by the Boltzmann factor but now with $T<0$. Finally, when approaching zero from the negative side, $T\rightarrow -0$, eventually only the highest energy level is populated.

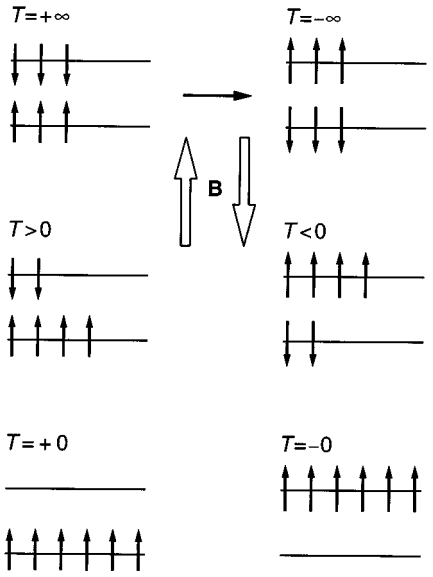

FIG. 8. Energy-level diagram of nuclear spins ($I=\frac{1}{2}$) in silver or rhodium at selected temperatures when B=constant. Spin populations in the $I_z=\frac{1}{2}$ and $I_z=-\frac{1}{2}$ levels are shown at both positive and negative absolute temperatures. Rapid reversal of the external magnetic field **B** interchanges the energy levels and produces a negative spin temperature.

As Fig. 8 shows, the transition from positive to negative spin temperatures is smooth and takes place via $T=\pm\infty$. The positive and negative infinite temperatures correspond to the same spin arrangement.

Since heat has to be added to the spin system at $T>0$ to reach a state with $T<0$, negative temperatures are actually hotter than positive ones. If two spin assemblies, one at $T>0$ and the other at $T<0$, are brought into thermal contact, heat will flow from the latter to the former.

1. Production of negative temperatures

Purcell and Pound (1951) first produced negative temperatures in the nuclear-spin system of LiH. Their experimental procedure was, in fact, a simple one. If the direction of the external magnetic field is reversed so fast that spins do not have time to redistribute among their energy levels, the spin assembly enters a state that can be described by a negative temperature. After the field flip, there are more nuclear moments antiparallel to the field than parallel to it. In terms of the energy-level diagram, the spin populations at the $I_z=\frac{1}{2}$ and $I_z=-\frac{1}{2}$ levels are exchanged.

A sufficiently rapid field reversal is fast in comparison with the spin-spin relaxation time τ_2, which is the approximate length of time between successive spin flips in low external fields. If the field change is slower, the spins are able to follow adiabatically the field reversal, and

negative temperatures will not result. Demagnetization would just be followed by remagnetization to the positive starting temperature.

To estimate the rate of field change needed to produce negative temperatures one may assume that only the low-field region $\mathbf{B}=+B_{\rm loc}\mathbf{z}\rightarrow -B_{\rm loc}\mathbf{z}$ has to be passed in a time much shorter than τ_2. On the other hand, τ_2 is approximately the Larmor period of the spins in the local field $B_{\rm loc}$ created by neighboring nuclei. Thus the critical field sweep rate is on the order of

$$\frac{\Delta B}{\Delta t}\approx\frac{\gamma B_{\rm loc}^2}{2\pi}\,. \tag{12}$$

In fact, during the quick field flip the Boltzmann distribution of the spins breaks down and, for a short moment, the spin system cannot be assigned a temperature.

Once the spins have been brought to the $T<0$ state, they remain there for a long time. The spin system relaxes towards the positive lattice temperature through a passage via $T=\mp\infty$, at a rate determined by the relatively long τ_1.

Only the Zeeman temperature is reversed in the field flip; the temperature of the interaction reservoir is not. See Fig. 5(b) for an illustration of such a situation. An irreversible entropy increase results when $\mathcal{H}_Z$ warms the interaction reservoir to negative temperatures, producing the equilibrium depicted in Fig. 5(c). This thermal mixing process is similar to that described earlier (see Sec. II.B). A more detailed discussion is presented in Sec. IV.G.

Other methods for producing negative spin temperatures will be discussed in Secs. XIV.A and XIV.D.

2. Thermodynamics at $T<0$

Some of the fundamental aspects of negative temperatures have been described by Ramsey (1956). Our discussion draws mostly from his text.

From the thermodynamic point of view, an essential requirement for the existence of a negative temperature is that the entropy S not be a monotonically increasing function of the internal energy U. In fact, whenever $(\partial S/\partial U)_B<0$, $T=1/(\partial S/\partial U)_B<0$ as well. At negative temperatures an increase in U corresponds to a decrease in S, while the reverse is true when $T>0$ (see Fig. 9). For negative temperatures to occur, there must be an upper limit to all allowed energy states of the system, otherwise the Boltzmann factor $\exp(-E_m/k_{\rm B}T)$ does not converge for $T<0$. Nuclear spins satisfy this requirement, since there are $2I+1$ Zeeman energy levels. In addition, the elements of the assembly must, of course, be in thermodynamic equilibrium among themselves so that the system can be described by the Boltzmann distribution and thereby assigned a temperature. The thermal equilibrium time τ_2 among the nuclear spins themselves must be short compared to the time τ_1 of appreciable "leakage" of energy to or from other systems. In silver, for example, $\tau_1=14$ h at $T_e=200$ μK while $\tau_2=10$ ms.

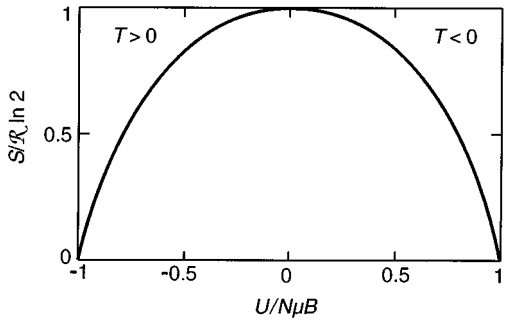

FIG. 9. Entropy S as a function of the internal energy U for the two-level system of Fig. 8. Negative slope of the $S/\mathcal{R}$ ln2 vs $U/N\mu B$ curve corresponds to a temperature $T<0$.

Nuclear-spin assemblies are different from some more common systems for which the temperature in Kelvins describes the average energy. Consider, for example, the kinetic energy E. When the temperature is raised towards infinity, E increases without an upper limit. Therefore the crystalline lattice or conduction electrons cannot be brought to a temperature $T<0$: the energy of the system would be infinite.

At $T<0$ the second law of thermodynamics, $T=\Delta Q/\Delta S$, can just as well be used for thermometry (see Sec. II.E). In this case, $\Delta Q<0$ when the entropy increases and the system radiates energy at the Larmor frequency of the nuclei, while the populations of the two energy levels tend to equalize.

At $T=+0$ and at $T=-0$ there is complete but opposite order, i.e., the entropy is zero in both cases. When $T=\pm\infty$, S has its maximum value $\mathcal{R}$ ln2 for the spin $I=\frac{1}{2}$. At $T<0$, adiabatic demagnetization heats the spin system instead of cooling it, as happens when $T>0$. Similarly, for experiments on polarized nuclei at $T<0$, the spin system must be heated to the hottest negative temperature to achieve maximum polarization, while at positive temperatures the spins must be cooled.

The difficulty of heating a "hot" system at negative temperatures is analogous to the problems of cooling a cold system at positive temperatures. An NMR absorption experiment at $T>0$ becomes an NMR emission experiment at $T<0$. This effect was observed with the ^{7}Li nuclei by Purcell and Pound (1951), and it provided the key proof that negative spin temperatures actually had been produced in the nuclear-spin system: the emission peaks at $T<0$ gradually became weaker until, at $T=\pm\infty$, the emission and absorption canceled out because of equal populations of the energy levels. Slowly increasing absorption spectra were then observed as the spin system "cooled" towards room temperature.

When two systems are brought into thermal contact, heat always flows from the hotter to the colder body. The order of temperatures on the absolute Kelvin scale, from the coldest to the hottest, is thus +0 K, ... +300 K, ... $\pm\infty$ K, ... −300 K, ... −0 K. The system cannot become colder than +0 K since it is not capable of giv-

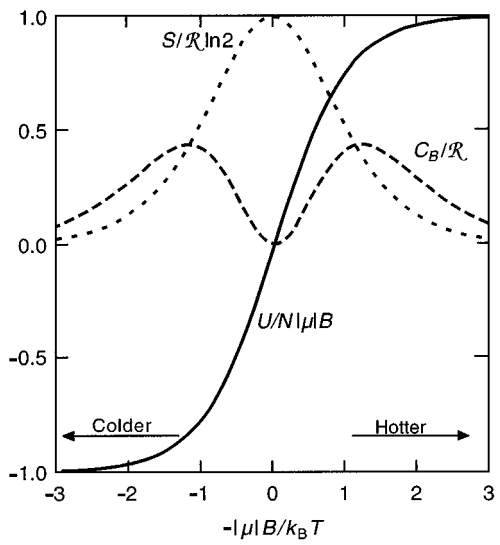

FIG. 10. Entropy (dotted curve), internal energy (full curve), and specific heat (dashed curve) plotted as a function of $-|\mu|B/k_BT$ for a nuclear-spin system of two energy levels ($I=\frac{1}{2}$, as for Ag and Rh, and $|\mu|=\frac{1}{2}\hbar|\gamma|$).

ing up more of its energy; likewise, it cannot become hotter than -0 K because the system is unable to absorb more energy.

Near the absolute zero, $1/T$ or $\log T$ is sometimes used as the temperature function but, when $T<0$, $\log T$ is not suitable. However, on the inverse-negative scale where $\beta=-1/T$, the coldest temperature, $T=+0$, corresponds to $\beta=-\infty$, and the hottest temperature, $T=-0$, to $\beta=+\infty$. On this scale the algebraic order of β and the order from cold to hot are identical; the system passes from positive to negative Kelvin temperatures through $\beta=-0\rightarrow+0$. The choice of the function, $\beta=-1/T$, ensures that a colder temperature is always to the left of a hotter one. This inverse-negative scale thus runs in an "orderly" fashion from the coldest to the hottest. The third law of thermodynamics emerges "naturally" by the impossibility of reaching the positive or negative ends of the β axis.

The theorems and procedures of statistical mechanics, such as the use of the partition function or the quantum-mechanical density matrix, apply equally to systems at negative temperatures. By examining the statistical theory by which the Boltzmann distribution is derived, we see that there is nothing objectionable *a priori* in the parameter $1/k_BT$ being negative; $T<0$ simply means that the mean energy of the system is higher instead of being lower than that corresponding to equal populations among the energy levels at $T=\pm\infty$.

Figure 10 illustrates the entropy S, the internal energy U, and the specific heat C_B of a two-level spin assembly (see Fig. 8) as a function of $\beta=-1/T$ in units of $k_B/|\mu|B$, calculated in the usual way [see Eqs. (25a) and (26a)]. The entropy has its maximum value $S=\mathcal{R}\ln 2$ at $\beta=\pm 0$ because both energy levels are equally populated (the spin polarization $p=0$). The specific heat C_B is zero at $\beta=-\infty$ and at $\beta=+\infty$ since all spins occupy their lowest or highest energy level and no more heat can be removed or absorbed, respectively. At $\beta=\pm 0$, $C_B=0$ as well because a very large change occurs in T for a very small change in the spin configuration. The internal energy has its minimum value at $\beta=-\infty$ $(T=+0)$ and its maximum at $\beta=+\infty$ $(T=-0)$.

Although systems at negative temperatures can be treated without difficulty by thermodynamics and statistical mechanics, albeit with certain modifications to the Kelvin-Planck formulation of the second law of thermodynamics (Ramsey, 1956), the occurrence of systems at $T<0$ is infrequent because of the rather restrictive requirements for a thermodynamic assembly to be described by a negative temperature. Population inversion alone is not sufficient. A Boltzmann distribution of the particles among the energy levels, i.e., internal thermal equilibrium, is needed before a temperature can be assigned to the assembly. Lasers do not operate at negative temperatures. Laser beams, however, have been used to achieve very low temperatures, for example, 100 nK in an assembly of sodium atoms (Kasevich and Chu, 1992).

3. Nuclear ordering at $T<0$

At $T=+0$ an isolated nuclear-spin assembly has the lowest, and at $T=-0$ the highest, possible energy. This feature can be put into a more general thermodynamic basis. As the external magnetic field B is reduced towards $B_{\rm loc}$ and ultimately even to $B=0$, the dipole-dipole and exchange forces gradually take over, and the spin order begins to change from that forced by **B** to an arrangement determined by mutual interactions. During this spontaneous adjustment of spins the entropy increases, according to the general principles governing thermodynamic equilibrium, until S reaches a maximum, while the magnetic enthalpy $H=U-BM$ stays constant.[2] One must thus consider the variation of entropy under the restriction of a constant enthalpy, i.e., seek an extremal value of $S+\beta H$ where β is a Lagrange multiplier. By differentation, $dS+\beta dH=0$, so that $\beta=-dS/dH=-1/T$. Therefore, one finds $S-H/T=-G/T$ for the thermodynamic potential reaching an extremum; G is the Gibbs free energy. When $T>0$, $G=H-|T|S$, and the extremum is a minimum, since S assumes its maximal value at equilibrium. When $T<0$, $G=H+|T|S$, and the Gibbs free energy obviously reaches a maximum.

The tendency to maximize rather than to minimize the energy is the basic difference between negative and positive temperatures. This produces a profound effect on the spin structure into which a system spontaneously orders below the transition temperature when $T>0$ or

[2]Enthalpy, which is the sum of the internal and magnetic energies, is constant since the system is isolated. In terms of the microscopic Hamiltonian, Eq. (1), this would mean $\langle\mathcal{H}\rangle=$constant.

"above" it when $T<0$. In silver, for example, the nearest-neighbor antiferromagnetic Ruderman-Kittel exchange interaction favors antiparallel alignment of the nuclear magnetic moments and thus produces antiferromagnetism when $T>0$. At $T<0$, since the energy now must be maximized, the very same interactions cause ferromagnetic nuclear order.

E. Thermometry with nuclear spins

Measurements of the temperature of a nuclear-spin system are based on the second law of thermodynamics, $T=\Delta Q/\Delta S$. This relation can be used equally well at positive and negative temperatures. A practical way to administer a small heat pulse ΔQ on the spin system is to expose it to an alternating magnetic field of a suitable frequency f for a time Δt. Then $\Delta Q \propto B_1^2\chi''(f)\Delta t$, where B_1 is the amplitude of the alternating field. The crucial difference between the behavior at $T>0$ and that at $T<0$ is that in the former case spins absorb energy from the alternating field whereas in the latter case spins *emit* energy to this field. Hence at $T<0$, $\Delta Q<0$ when the entropy increases. This is borne out also by the fact that $\chi''(f)>0$ at positive temperatures while the opposite is true for negative temperatures. The common feature at $T>0$ and at $T<0$ is that, when exposed to an alternating magnetic field of the resonant frequency, the populations of the two energy levels tend to equalize.

Measurements of ΔS ensuing from the heat pulse are usually made by relating S to the spin polarization p before and after the pulse; p can be determined from the area of the NMR peak.

Thermal conductivity within the nuclear-spin system in a metal is such that, over atomic distances, equilibrium is reached quickly. However, on a macroscopic scale thermal diffusion is very slow. This means that in any experiment all parts of the sample must be subjected to similar treatment so that different regions of the specimen will be at the same spin temperature.

A thorough discussion of nuclear-spin thermometry on copper, silver, and rhodium is given in Sec. IV.

III. EXPERIMENTAL TECHNIQUES FOR SUSCEPTIBILITY MEASUREMENTS

A. Principle of brute force nuclear cooling

The basic principle of nuclear cooling is the same as that for paramagnetic salts (de Klerk, 1956), but there are very significant differences in practice. Because nuclear magnetic moments are about 2000 times smaller than their electronic counterparts, it is more difficult to produce significant changes in the entropy of the nuclear-spin system by external means. For example, to reduce the entropy by 5%, one must start from an initial temperature $T_i=10$ mK and an initial magnetic field $B_i=6$ T, if copper is used as the working substance; for paramagnetic salts the corresponding values are 1 K and 1 T. Fortunately, the starting conditions for nuclear cooling today can be reached rather easily with dilution refrigerators and superconducting magnets (Lounasmaa, 1974).

The main advantage of nuclear cooling is, of course, the very low temperature that can be reached. Nuclei align spontaneously, owing to their mutual interactions, well below 1 μK. Because spontaneous ordering is the limit of any cooling process, temperatures in the submicrokelvin region can be reached by nuclear-demagnetization. The current record, 280 pK, was obtained by demagnetizing a rhodium specimen in a cascade nuclear-demagnetization process (Hakonen, Vuorinen, and Martikainen, 1993). For cerium magnesium nitrate, the weakest paramagnetic salt, the ordering temperature is slightly below 2 mK.

The technique of nuclear cooling consists of first magnetizing the sample isothermally from zero to $B_i \geqslant 5$ T at a low initial temperature $T_i \leqslant 20$ mK. The mixing chamber of the precooling dilution refrigerator and the nuclear stage are then thermally isolated from each other by means of a superconducting heat switch, and the magnetic field is reduced to a low final value B_f adiabatically. The nuclear sample is thereby cooled to

$$T_f=(T_i/B_i)(B_f^2+B_{\rm loc}^2)^{1/2}\,, \tag{13}$$

where $B_{\rm loc}$ is 0.36 mT for copper, 35 μT for silver, and 34 μT for rhodium and represents the effective interactions between the nuclei. The exact definition of $B_{\rm loc}$ will be given by Eq. (29). Thus, for example, if one starts from $B_i=8$ T and $T_i=16$ mK and demagnetizes to $B_f=0$, the final temperature is 0.7 μK using copper nuclei.

The basic equations of brute force nuclear cooling will be discussed here only briefly; for more detail we refer the reader to other publications (Huiskamp and Lounasmaa, 1973; Lounasmaa, 1974; Betts, 1976; Andres and Lounasmaa, 1982; Pickett, 1988; Pobell, 1992a, 1992b), which also describe dilution refrigeration and other relevant cryogenic techniques in detail.

In an external magnetic field B, the $2I+1$ equidistant nuclear energy levels are given by $E_m=-\mu_N g_N B m=-\hbar\gamma B m$, where $\mu_N=5.05\times10^{-27}$ Am^2 is the nuclear magneton, $g_N=\mu/I$ is the nuclear g factor, and m runs from $-I$ to $+I$, with I denoting the nuclear spin. The partition function of the system is

$$Z=\left[\sum_m \exp(-E_m/k_{\rm B}T)\right]^{nN_{\rm A}}, \tag{14}$$

where n is the number of moles of the sample, $k_{\rm B}$ is Boltzmann's constant, and $N_{\rm A}$ is Avogadro's number; $nN_{\rm A}$ is thus the number of magnetic nuclei in the specimen. The population of the mth energy level is given by

$$P(m)=nN_{\rm A}\exp(-E_m/k_{\rm B}T)/\sum_m \exp(-E_m/k_{\rm B}T)\,. \tag{15}$$

In the approximation $E_m \ll k_{\rm B}T$, the entropy $S=k_{\rm B}\partial(T\,\ln Z)/\partial T$ becomes

$$S=n\mathcal{R}\,\ln(2I+1)-n\Lambda B^2/2T^2\,, \tag{16}$$

where the nuclear Curie constant per mole $\Lambda = N_A I(I+1)\mu_N^2 g_N^2/3k_B$. In a constant field, the nuclear heat capacity $C_B = T(\partial S/\partial T)_B$ is then, in the same approximation, given by

$$C_B = n\Lambda B^2/T^2 . \quad (17)$$

Equation (14) shows that Z and therefore also $P(m)$, S, and C_B are functions of B/T only for all values of B and T. During adiabatic demagnetization ($\Delta S = 0$) from B_i and T_i to B_f, S remains constant, and therefore $B_i/T_i = B_f/T_f$; the final temperature is then given by

$$T_f = T_i B_f/B_i . \quad (18)$$

If demagnetization is carried out to a low or zero field, B_f must be replaced in this equation by $(B_f^2 + B_{\rm loc}^2)^{1/2}$; we then obtain Eq. (13). Similarly, if Eq. (17) is to be used in low fields, B must be replaced by $(B^2 + B_{\rm loc}^2)^{1/2}$.

After demagnetization, the nuclear-spin system begins to warm up owing to the unavoidable external heat leak $dQ/dt = \dot{Q}$. By observing that $\dot{T} = \dot{Q}/C_B$, one can calculate the time Δt during which the nuclear spins warm from T_f to a higher temperature T. The result is

$$\Delta t = (n\Lambda B_f^2/\dot{Q})(T_f^{-1} - T^{-1}) , \quad (19)$$

where Eq. (17) has been employed. The relation shows that $1/T$ is a linear function of time, provided that $\dot{Q}$ is constant. It should be noted that Δt is proportional to B_f^2; demagnetization should not be carried out to fields lower than is necessary to reach the desired temperature T_f.

The rate at which equilibrium is established between nuclear spins and conduction electrons is governed by the spin-lattice relaxation time τ_1, defined by Eq. (8). For most metals τ_1 is on the order of seconds at 10 mK; for insulators τ_1 is days or even weeks. It is thus clear that metals must be used for brute force nuclear refrigeration. The lattice heat capacity, proportional to T^3, is totally negligible below 10 mK. One may therefore assume that T_e represents the common conduction-electron and lattice temperature.

The short spin-lattice relaxation time in metals is due to conduction electrons that act as intermediaries between the nuclear spins and the lattice. Only electrons near the Fermi surface contribute; their number is proportional to T_e making τ_1 proportional to $1/T_e$. This results in Eq. (9), $\tau_1 = \kappa/T_e$ (Korringa, 1950). As was discussed in Sec. II.B, the Korringa behavior is modified in fields comparable to $B_{\rm loc}$ and for high B/T_e. In practice, among the elemental metals, only copper, indium (Symko, 1969), silver, thallium (Angerer and Eska, 1984; Eska and Schuberth, 1987), scandium (Suzuki *et al.*, 1994; Koike *et al.*, 1995), and rhodium have been used for brute force nuclear cooling.

The unavoidable external heat leak $\dot{Q}$ into a conduction-electron system has an important effect on the equilibrium between T_e and T. If $\dot{Q}$ is large, the spin-lattice relaxation process is not sufficiently rapid for cooling the conduction electrons adequately, and $T_e - T$ will be large. One can derive the equation

$$(T_e/T) - 1 = \kappa\dot{Q}/n\Lambda(B_f^2 + B_{\rm loc}^2) \quad (20)$$

starting from the equations governing spin-lattice relaxation, Eqs. (8) and (9) (Lounasmaa, 1974).

To obtain significant refrigeration of conduction electrons, one should not carry out nuclear demagnetization all the way to $B_f = 0$ but should stop at some intermediate field value. In fact, the lowest T_e is reached by demagnetizing to

$$B_f({\rm opt}) = (\kappa\dot{Q}/n\Lambda)^{1/2} ; \quad (21)$$

in this case $T_e/T = 2$. In the derivation of this result it has been assumed that $B_f \gg B_{\rm loc}$.

The very lowest temperatures have been obtained by means of cascade nuclear magnetic cooling techniques. In cryostats of this type, the first nuclear stage acts as a precooler for the much smaller second stage. Three cascade refrigerators, namely, those at Helsinki (Ehnholm, Ekström, Jacquinot *et al.*, 1979; Ehnholm *et al.*, 1980; Huiku *et al.*, 1986), at Risø (Jyrkkiö *et al.*, 1989), and at the Hahn-Meitner-Institut in Berlin (Tuariniemi, Nummila, *et al.*, 1995), were employed in the experiments to be described in detail in this review. Other machines of the cascade type have been built in Jülich (Mueller *et al.*, 1980), Tokyo (Ishimoto *et al.*, 1984), and Bayreuth (Gloos *et al.*, 1988); in these cryostats the aim is usually to cool conduction electrons or ^{3}He. For useful reviews, see Huiskamp and Lounasmaa (1973); Pickett (1988); and Pobell (1988).

B. Helsinki cryostat

The main parts of the Helsinki cryostat are schematically illustrated in Fig. 11 (Ehnholm, Ekström, Jacquinot *et al.*, 1979; Ehnholm *et al.*, 1980). The apparatus consists of a dilution refrigerator and two nuclear stages, operating in series. During its active life of nearly two decades, the cryostat has naturally undergone many modifications (Huiku *et al.*, 1986; Hakonen and Yin, 1991; Oja, Annila, and Takano, 1991).

The dilution unit in this apparatus was designed to be used as the precooling stage of a nuclear-demagnetization cryostat. The main objectives in its construction were therefore a rigid structure and a high cooling power down to about 10 mK. The home-made refrigerator was able to reach 7 mK without an external heat load and to cool the nuclear stage in an 8-T field down to 10 mK. Between the mixing chamber and the first nuclear stage there is a superconducting heat switch made of a piece of bulk tin.

In the first design of the apparatus (Ehnholm, Ekström, Jacquinot *et al.*, 1979; Ehnholm *et al.*, 1980), the upper nuclear stage was assembled from 10 moles of copper wire, 0.5 mm in diameter and insulated with fiberglass. The early version of the second nuclear stage, i.e., the sample, was made of 2000 copper wires, 0.04 mm

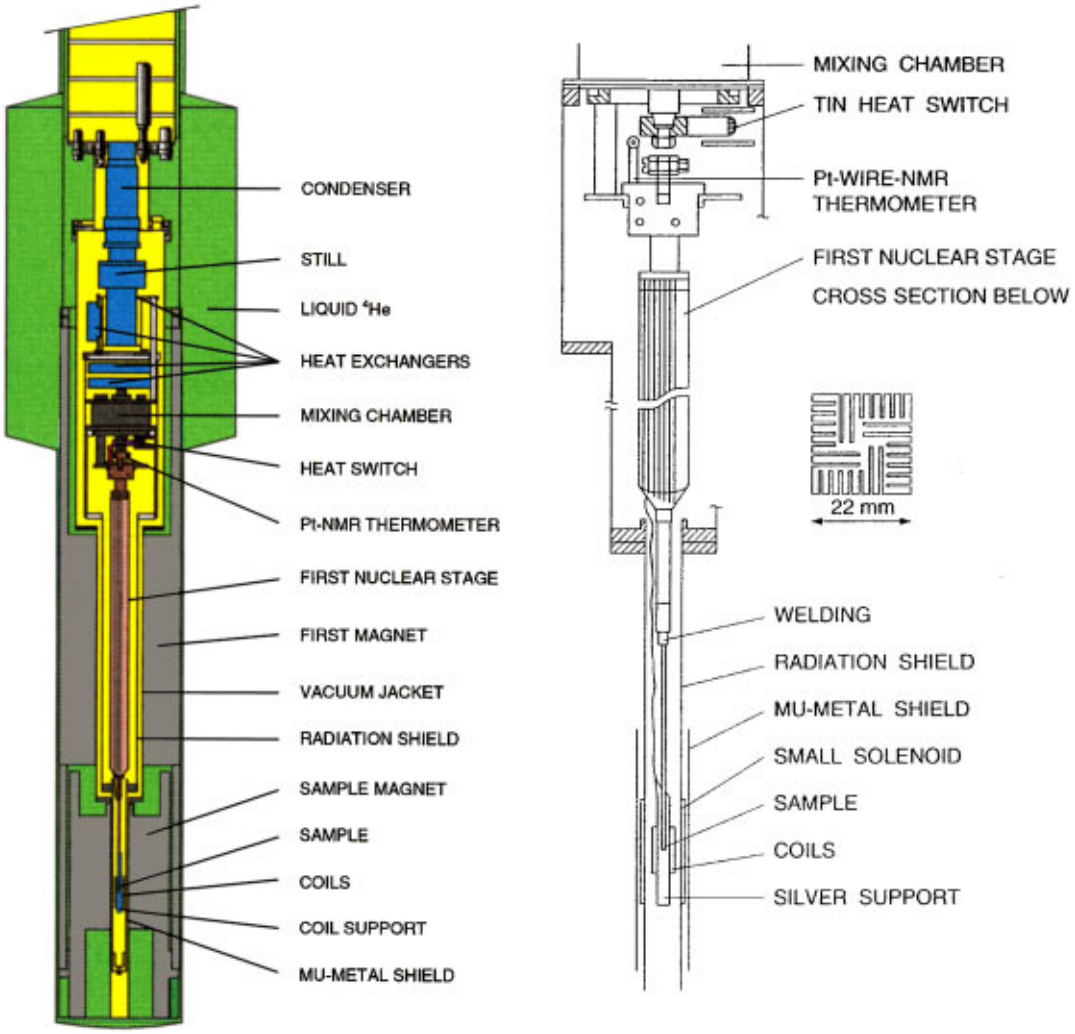

FIG. 11. Cascade nuclear-demagnetization cryostat in Helsinki. The main parts below the mixing chamber of the dilution refrigerator, inside the vacuum jacket, are shown in more detail at right. The second nuclear stage is also the sample; it is connected to the first stage by welding. From Ehnholm *et al.* (1980) and Huiku *et al.* (1986).

in diameter and insulated by oxidation; the measured residual resistivity ratio RRR=200.[3] This wire was chosen because its spin-lattice relaxation time had previously been measured (Aalto *et al.*, 1972). The weight of the sample was 2 g. At their upper ends, the thin copper wires were welded together and connected to the first nuclear stage by means of copper foils, without any heat switch. Therefore, thermal contact between the conduction electrons in the two nuclear stages was good.

The electronic temperature T_e in the sample was determined by the temperature of the large upper nuclear stage, by the thermal conductivity between the two nuclear stages, and by the heat leak $\dot{Q}$ to the second stage [see Eq. (20)]. $T_e = 250$ μK was reached, corresponding to $\dot{Q} = 0.3$ nW to the sample. The heat input to the first nuclear stage was 3 nW.

The magnetic fields for operating the nuclear stages were generated by two superconducting solenoids. The upper stage could be magnetized to a maximum field of 8 T. The magnet had field-compensated volumes at both ends; the upper low-field region was at the location of the heat switch and the mixing chamber, and the lower low-field region was at the site of the second nuclear stage. The effective amount of copper in the 8-T field was $n_{\rm eff} = 2.5$ mol; this early version of the first stage was thus relatively small compared with other nuclear demagnetization cryostats built in Helsinki (Gylling, 1971; Veuro, 1978) or elsewhere. In later versions of the apparatus, $n_{\rm eff}$ was increased.

The superconducting magnet surrounding the lower nuclear stage produced a maximum field of 7.3 T. It also had two field-compensated regions: the upper one at the joint between the two nuclear stages, so that a heat switch could have been assembled there if desired, and the lower one starting 110 mm below the center of the magnet, at the site of the SQUID that was used for measurements of the nuclear susceptibility. Inside the 7.3-T solenoid, there is a mu-metal tube to reduce the effect of the field trapped in the superconducting magnet after the current has been removed.

[3] RRR=ρ(300 K)/ρ(4.2 K).

The difficulty in the first experiments (Ehnholm *et al.*, 1980) was the short spin-lattice relaxation time, 10–20 min, which caused the system to warm up rather rapidly and apparently prevented the observation of nuclear ordering. To remedy this problem, the upper wire bundle was replaced in 1981 with a solid copper rod, 22×22 mm^2 cross section and 30 cm long, designed by P. Roubeau (Huiku *et al.*, 1986). To reduce eddy-current heating during demagnetization, 0.6-mm wide slits, spaced 1.6 mm apart, were cut on each side of the square rod (see Fig. 11). The mass of the new nuclear stage was 1.1 kg, which corresponded to an effective size of 10 mol of copper in the operating magnetic field of 8 T. The advantages of a bulk copper nuclear stage are that (l) it is rigid, (2) it is relatively easy to make, (3) it is a good conductor of heat, (4) all kinds of thermal contacts can be made to it, (5) it is devoid of insulating materials needed in a wire bundle to eliminate eddy currents during demagnetization, and (6) it is easy to handle.

Two essential improvements were observed (Huiku *et al.*, 1986) after replacing the old ''wire bundle'' first nuclear stage by the bulk copper rod: the conduction-electron temperature was lowered from 250 to 50 μK, and the minimum heat leak to the first nuclear stage was reduced from 2 to 0.5 nW. A drawback of the bulk nuclear stage was an enhanced time-dependent heat leak: the low 0.5 nW level was reached after the cryostat had been kept below 4 K for 6 weeks; two days after cooldown the heat leak was still 10 nW. Time-dependent heat leaks have been discussed by several authors (Loponen *et al.*, 1981; Zimmermann and Weber, 1981; Pobell, 1982, 1992a; Schwark *et al.*, 1983; Kolac *et al.*, 1985).

Conduction-electron temperatures were measured by monitoring the susceptibility of platinum wires using pulsed NMR techniques (Lounasmaa, 1974; Pobell, 1992a). The design of the thermometer (Huiku *et al.*, 1986; Hakonen and Yin, 1991) was similar to that used by the Jülich group (Buchal, Hanssen *et al.*, 1978). Commercial NMR electronics were employed (PLM-4, RV-Electronics, Veromiehentie 14, 01510 Vantaa, Finland). The static field for the thermometer was produced by a small, unshielded, and end-compensated solenoid made of multifilamentary NbTi wire. The Pt signal was calibrated against the superconducting transition temperatures of Be and W samples in a fixed-point device (Soulen and Dove, 1979). All thermometers were installed on top of the first nuclear stage.

In experiments on silver and rhodium, reaching sufficient initial polarization of the sample was a much more difficult task than it was with copper. This is due to the smallness of the magnetic moments of silver and rhodium nuclei as well as to their long spin-lattice relaxation times. To solve these problems, an even more massive version of the first nuclear stage was made, with $n_{\rm eff}=21$ mol (Oja, Annila, and Takano, 1991), and the rigidity and heat conductivity of the thermal link between the two nuclear stages was improved (Hakonen and Yin, 1991).

C. Experimental procedure

In studies of nuclear magnetism of copper the experimental procedure, illustrated in Fig. 12, was as follows (Huiku *et al.*, 1986). After the superconducting heat switch had been turned on,[4] the first nuclear stage was magnetized to 8 T. The dilution refrigerator then precooled, in about 40 h, the $n_{\rm eff}=10$ mol copper stage to about 10–12 mK, after which the heat switch was turned off to isolate the nuclear stages from the dilution unit.

Next, the second nuclear stage was magnetized, in 40 min, to 7.3 T and, starting simultaneously, the first stage was demagnetized to $B_f=0.1$ T in about 5 h, with a rapidly decreasing dB/dt towards the end of demagnetization. This procedure was possible because the heat of magnetization of the small second stage could be absorbed easily by the first nuclear stage at 0.1 T. In principle, it would have been preferable to do the precooling with the second-stage field on, but the magnet could not operate in the persistent mode. This resulted in a large boiloff from the ^{4}He bath when the magnet was operated at the full current.

After waiting for 1.5 h at the 0.1-T field, demagnetization of the first stage was continued to $B_f=20$ mT, producing a temperature $T_e=50-100$ μK in the conduction-electron system of the sample. The second nuclear stage was then demagnetized rather rapidly. A typical time from 7 T to zero field was 20 min; this kept polarization losses in the sample low, 0.5–1.5% during the field sweep.

After demagnetization of the lower magnet, the conduction-electron temperature of the copper specimen remained constant for several hours because of the high cooling capacity of the large first nuclear stage. Furthermore, the low heat resistance (3–6 K^2/W) in the thermal link between the specimen and the first stage and the small external heat leak ($\leqslant$30 pW) to the sample guaranteed a constant T_e along the whole second nuclear stage and thus a constant relaxation time τ_1 of the nuclei while they warmed up.

The residual trapped field in the 7.3-T solenoid surrounding the sample was a serious problem in the very first measurements. A too high field would keep the sample above B_c even at $B_{\rm ext}=0$. In addition, the slow relaxation of the trapped field increased noise in the measuring system. In tests it was found that immediately after demagnetization the residual field could be as high as 1 mT, decreasing only slowly, in about 20 min, to ±0.1 mT. Outside the center of the magnet even stronger fields were measured. The problem was overcome by surrounding the specimen with a mu-metal tube whose permeability, after heat treatment, was 40,000 at room

[4]This means that a current was allowed to flow in the small superconducting solenoid surrounding the switch; the magnetic field so produced forced tin into the normal state, where it conducts heat well. When the current was switched off, the strip of tin returned to its superconducting state, at which it conducts heat very poorly; the switch was then in its off state.

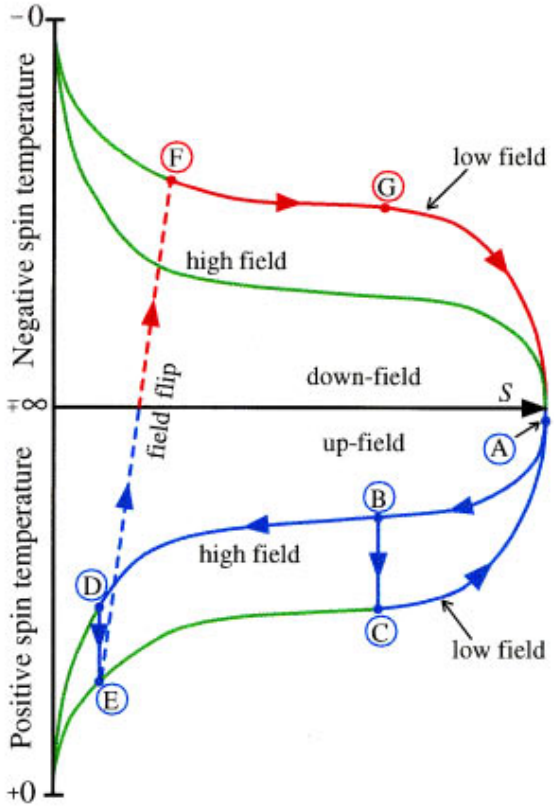

FIG. 12. Schematic illustration, on a temperature vs entropy diagram, of the cascade nuclear-demagnetization procedure for cooling an assembly of silver or rhodium nuclei to positive or negative nanokelvin temperatures. (A → B) Both nuclear stages are cooled to $T_i = 15$ mK by the dilution refrigerator and, simultaneously, the first stage is polarized in a strong magnetic field $B_i = 8$ T. (B → C) The nuclei of the first stage, made of 20 mol of copper, are adiabatically demagnetized to $B_f = 100$ mT, which produces a low temperature $T_f = T_i(B_f/B_i) \approx 200$ μK. Towards the end of demagnetization, the second nuclear stage, that is, the silver or rhodium sample, is magnetized to 8 T. (B → D) The 2-gram specimen of thin polycrystalline foils cools in the field $B = 8$ T, by thermal conduction, to $T_f \approx 200$ μK. (D → E) The specimen is demagnetized from 8 T to 400 μT, whereby the spins cool into the low nanokelvin range [$T \approx (400\ \mu\text{T}/\ 8\ \text{T})\ 200\ \mu\text{K} = 10$ nK], thermally isolated by the slow spin-lattice relaxation ($\tau_1 = 14$ h) from the conduction electrons, which are anchored to 200 μK by the first nuclear stage at C. When demagnetization of the specimen was then continued to zero field (not shown in the illustration), the record temperature of 280 pK was reached in rhodium. In silver, dipole-dipole and exchange interactions produced antiferromagnetic order at the Néel temperature $T_N = 560$ pK. (E → F) A negative temperature can be produced in the spin system of silver or rhodium nuclei by reversing, instead of demagnetizing to zero, the 400-μT magnetic field in about 1 ms. The rapid field flip causes some loss of polarization (that is, increase of entropy). When demagnetization was continued to zero field, the record temperature of −750 pK was reached in rhodium (not shown in the diagram). In silver, dipole-dipole and exchange interactions produce ferromagnetic order at the Curie temperature $T_C = -1.9$ nK. (F → G → A) The system starts to lose its negative polarization, crossing in a few hours, via infinity, from negative to positive temperatures. (C → A) The first nuclear stage warms slowly, under the $B_f = 100$ mT field, from $T_f = 200$ μK towards 15 mK. A new experimental sequence can then be started.

temperature. In high magnetic fields, the mu-metal saturates and has no effect, whereas in low fields, even immediately after demagnetization, it shields the sample effectively against external fields less than 8 mT. With the tube in place, the residual field decreased below 0.05 mT in 1 min, and in 2 min it was below 0.02 mT. For measurements on silver and rhodium, in which the critical field is lower than in copper, an additional magnetic shield was installed on the outer surface of the vacuum can. This decreased the remanent field to 2–5 μT.

After demagnetization of the lower magnet, the sample was in a field of 10 mT, generated by a small superconducting solenoid inside the mu-metal tube. A wait of about 1 min allowed the noise in the SQUID system to decrease sufficiently for final demagnetization to the low field, usually between 0 and 0.3 mT, in which nuclear ordering was to be investigated. The spin system was thereby cooled below 50 nK in copper, while the conduction electrons remained at 50 μK.

In experiments on silver and rhodium, polarizing the sample was slower than with copper. The cooling procedure was therefore modified. After the first nuclear stage had been demagnetized down to a low field, typically 65 mT, which produced $T_e = 100$–150 μK, the sample was polarized in the 7.3-T field for about 20 h. Polarizations up to 94% were obtained in silver (Hakonen and Yin, 1991). Even longer times were needed to polarize the rhodium sample. The first-stage demag-

netization was then continued down to 35–45 mT while the sample was kept in 8.3 T, produced by a new second-stage magnet, for 30 h. Polarization of 83% was thereby reached in rhodium (Vuorinen, Hakonen, Yao, and Lounasmaa, 1995). Longer polarizing times were prevented by the need to refill the ^{4}He bath of the dewar. Demagnetization of the silver and rhodium samples down to zero field produced spin temperatures well below 1 nK.

D. Sample preparation

The samples used for studies of nuclear ordering by the Helsinki group have usually been polycrystalline. A specimen made of several thin foils or wires gives a stronger NMR signal than a bulk single crystal because the electromagnetic field is screened by the skin effect in bulk material. In addition, eddy-current heating, when the sample is being demagnetized, is a less severe problem in thin foils and wires. The specimen should obviously be as pure as possible so that impurities will not affect the ordering process. It is difficult, however, to know *a priori* what is the purity needed, and in practice the best available samples were always used. The purity affects the low-temperature thermal and electrical conductivity, which are proportional to each other according to the Wiedemann-Franz law. In spite of increased eddy-current heating, high thermal conductivity is desirable so that the heat of magnetization, created when the sample is polarized in a high field and low temperature, can efficiently be conducted away. In practice, however, this is not very critical in reasonably pure (99.99+%) copper and silver, nor in 99.96+% pure rhodium owing to its relatively small nuclear magnetic moment. The sample was usually made of thin foils rather than wires, since good thermal contacts are easier to achieve with foils. A further important aspect of impurities is their effect on the spin-lattice relaxation time.

1. Quenching of magnetic impurities by internal oxidation

During the early years of the Helsinki investigations on copper (Ehnholm, Ekström, Jacquinot *et al.*, 1979; Ehnholm *et al.*, 1980) it was observed, by measuring the spin-lattice relaxation time τ_1, that below 2 mT magnetic impurities speed up the relaxation process. The high-field relaxation time $\tau_1(15\ \mathrm{mT})$ was longer, by a factor between 4 and 7, than the experimentally important zero-field relaxation time $\tau_1(0)$. This effect, together with the fact that the conduction-electron temperature was as high as 250 μK, presumably prevented definite observation of nuclear ordering.

Several approaches were tried to increase $\tau_1(0)$. The final success grew out of the dismaying observation (Huiku, Loponen *et al.*, 1984) of an anomalously rapid spin-lattice relaxation in a very pure copper specimen. An impurity analysis, using atomic absorption techniques, showed that this material had less than 1.3 ppm of magnetic contaminants: Mn<0.1, Cr=0.3, Fe=0.8, and Ni<0.1 ppm. The ratio $r=\tau_1(B_{\mathrm{high}})/\tau_1(0)$, with $B_{\mathrm{high}}=15\ \mathrm{mT}\gg B_{\mathrm{loc}}(\mathrm{Cu})=0.36\ \mathrm{mT}$, at first was as large as 100 but, after the sample had been prepared by oxidizing it at 950 °C for 3 h under a pressure of 0.1 μbar of dry air, the spin-lattice relaxation rate became much slower in low fields; the new ratio $r=2.6$ was essentially the same as the calculated value for a spin system with no impurities (Goldman, 1970).

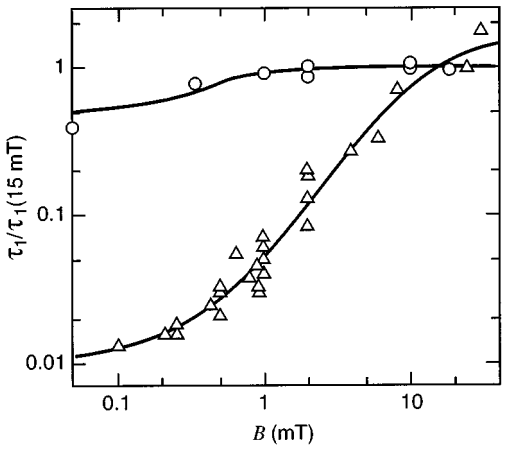

FIG. 13. Spin-lattice relaxation time of a high-purity copper sample: △, before selective oxidation; ○, after selective oxidation. From Huiku *et al.* (1986).

Therefore the effect of magnetic impurities, which aid in the relaxation process at low fields, can be quenched by a suitable heat treatment that changes the magnetic impurities into their nonmagnetic oxides; Fig. 13 illustrates the spin-lattice relaxation time for the new specimen as a function of the external magnetic field, after normal annealing and after internal oxidation. The effect is dramatic and was of crucial importance for observing nuclear ordering in copper.

After having observed the effect of internal quenching on the low-field spin-lattice relaxation time, the Helsinki group routinely applied the oxidation technique to all samples studied for nuclear ordering. It is likely that the effect has its origin in the same processes that typically led to improved low-temperature electrical conductivity in oxygen-annealed copper, as had been found previously by many authors (Fickett, 1974). Measurements on several samples carried out in Helsinki over a long time suggest that there can be a correlation between the RRR and the low-field spin-lattice relaxation rate $\tau_1(B_{\mathrm{low}})^{-1}$, but the effect is not clear from Fig. 14.

It has been emphasized (Fickett, 1974) that oxygen annealing lowers the *chemical* purity although its effects can usually be described by an improvement of *electrical* purity. Recent studies (Shigematsu *et al.*, 1992) on ultrapure copper (99.99999%) show, indeed, that oxygen annealing can be very harmful to the low-temperature electrical conductivity when the copper matrix is extremely pure. By analogy, one may speculate that such heat treatment could shorten τ_1 at low fields in an ultrapure metal.

Oxygen annealing has also been observed to increase the RRR of silver (Ehrlich, 1974). Anticipating that annealing would increase τ_1 in low fields, the Helsinki

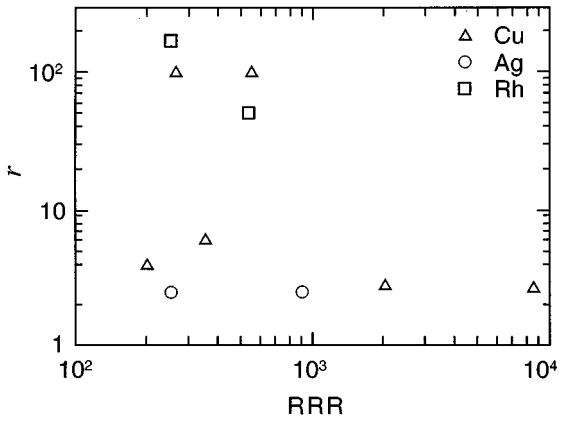

FIG. 14. Ratio of the spin-lattice relaxation times measured in high and low fields, $r=\tau_1(B_{\rm high})/\tau_1(B_{\rm low})$, for samples of copper, silver, and rhodium with different residual resistivity ratios (RRR). Data are from Huiku, Loponen *et al.* (1984) and from Jyrkkiö *et al.* (1989) for Cu, from Hakonen and Yin (1991) and Oja, Annila, and Takano (1991) for Ag, and from Hakonen, Vuorinen, and Martikainen (1994) for Rh.

group selectively oxidized all silver samples prepared for nuclear ordering experiments. A typical treatment took 18 h at 750 °C in an oxygen atmosphere of 0.2 μbar. The temperature during the heat treatment was somewhat lower than for copper because of the higher vapor pressure of silver. The annealing resulted in RRR's up to 900 for 25-μm thick foils and up to 1500 for 125-μm thick foils, both of 99.99+% nominal purity (Hakonen and Yin, 1991; Oja, Annila, and Takano, 1991). Measurements of the spin-lattice relaxation rate of the 25-μm thick foils showed that $r=\tau[B\gg B_{\rm loc}({\rm Ag})=35\ \mu{\rm T}]/\tau_1(0)$ was within the expected value between 2 and 3 for pure material.

In rhodium, effects due to impurities could not be fully removed by internal oxidation. The annealing procedure for 25-μm thick foils was 16 h at 750 °C in an oxygen atmosphere of 0.4 μbar (Hakonen, Vuorinen, and Martikainen, 1993, 1994). The first sample contained about 100 ppm of iron, and its Korringa constant decreased from $\kappa=10$ sK to 0.06 sK in small magnetic fields, i.e., $r=170$. The second sample had a nominal purity of 99.96+% and the total quantity of magnetic impurities was less than 15 ppm. It had $r=50$, which was sufficient for carrying out extensive zero-field susceptibility measurements. The RRR's were 250 for the first sample and 530 for the second. From these values the effective iron contents were estimated as 14 ppm and 6 ppm, respectively.

2. Thermal contact

A problem closely connected with sample preparation is joining the specimen to the thermal link between the sample and the first nuclear stage. Several different techniques have been used for this purpose: tungsten-tip inert-gas (TIG) welding (Ehnholm *et al.*, 1980), diffusion welding (Huiku *et al.*, 1986), and electron-beam welding (Hakonen and Yin, 1991; Oja, Annila, and Takano, 1991). Conventional TIG welding produces low contact resistances between similar metals after annealing (Muething *et al.*, 1977). TIG welding is, however, unsuitable for joining foils and dissimilar metals owing to alloy formation.

Diffusion welding is particularly convenient with foils. To join two pieces of copper, for example, a preliminary joint is first made at a low temperature (400 °C) by pressing the foils together with a stainless-steel clamp. Once the pieces stick together, the clamp is removed and the final diffusion welding is done at a high temperature (1000 °C), perhaps simultaneously with oxygen annealing. Diffusion welding of dissimilar materials is possible, for example, between copper and aluminum (Bunkov, 1989), but the procedure can be difficult if the melting temperatures T_m of the two metals are very different. One can then coat the material of higher T_m with a thin layer of the metal having the lower melting temperature. Thermal joints between silver and rhodium foils have been made this way (Vuorinen, Hakonen, Yao, and Lounasmaa, 1995) by first sputtering a 0.2 μm layer of silver on rhodium and then making the diffusion weld between the silver foil and the sputtered surface of the rhodium foil.

Electron-beam welding is practical if the foils to be joined are not too thin; together the two pieces should be at least 1 mm thick. Good thermal joints between copper and silver are easily achieved; a contact resistance of 0.55 $\mu\Omega$ mm^2 has been measured for a joint between these metals (Yin and Hakonen, 1991). To release welding stresses, the joint was annealed for 3 h at 750 °C; the contact resistance then decreased to 0.2 $\mu\Omega$ mm^2. The thickness of the alloyed layer at the joint was studied by an electron microscope using backscattering, and the layer was found to be 1–30 μm thick, depending on the position. The layer is thus rather thin in comparison with the typical spot size of 0.5 mm of the electron beam, making it possible to obtain a low contact resistance.

The actual setup for nuclear ordering experiments on silver, depicted in Fig. 15, illustrates many of the aspects discussed above. The sample consists of 48 silver foils 25 μm thick. The foils were folded into U shapes and grouped together with other foils as shown, in order to increase the rigidity of the structure. The foils were electrically insulated from each other by sprinkling them with a 7-μm layer of SiO_2 powder. The sample was connected to a thermal link made of silver by a diffusion weld, which was further improved by electron-beam welding. The link was machined into the shape of a cross, again to increase the mechanical rigidity of the whole structure. This is important for reducing vibrational heat leakage in high magnetic fields, as well as for decreasing the noise during susceptibility measurements. The link was connected to the first nuclear stage by electron-beam welding.

We have discussed sample preparation in great detail because it was of crucial importance for the success of the experiments.

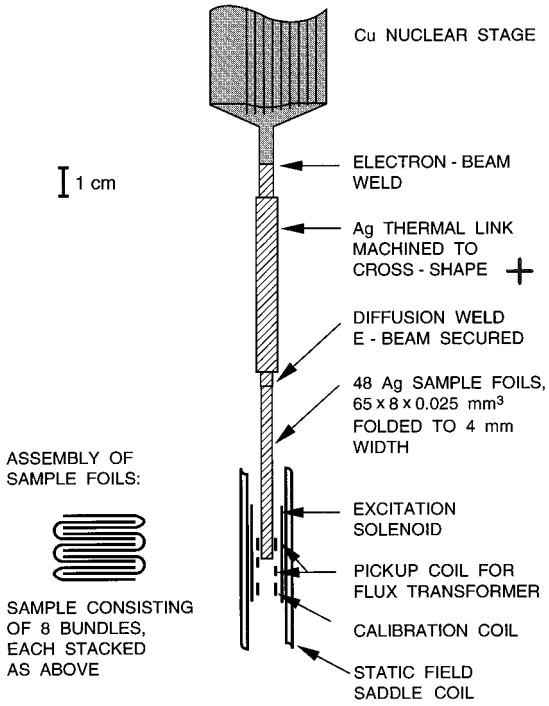

FIG. 15. Schematic view of the silver sample and its connection to the copper nuclear-demagnetization stage. The NMR coils are located over the lower end of the sample. From Hakonen and Yin (1991).

E. SQUID measurements of the NMR signal and the low-frequency magnetic susceptibility

Apart from the neutron-diffraction data on copper and silver (see Secs. VII and IX), all experiments on nuclear ordering in copper, silver, and rhodium are based on measurements of the dynamic magnetic susceptibility $\chi(f)=\chi'(f)-i\chi''(f)$, where $\chi'(f)$ is the dispersion at frequency f and $\chi''(f)$ is the absorption.[5] In high fields, $\chi''(f)$ and $\chi'(f)$ are usually referred to as the NMR absorption and dispersion. In low fields, when the width of the $\chi''(f)$ signal becomes comparable to the frequency at the maximum of $\chi''(f)$, description of $\chi''(f)$ as the nuclear-magnetic-*resonance* absorption does not correspond to the conventional picture, and it is better to call $\chi''(f)$ the absorptive part of the dynamic susceptibility. It is both fortunate and important that measurements of the dynamic susceptibility alone give information not only on the magnetic behavior but also on the thermodynamics of the nuclear-spin system, which is isolated sufficiently well from the conduction electrons.

The NMR measurements on copper, silver, and rhodium were made by using a superconducting quantum interference device (SQUID). In this type of study, SQUID NMR has several advantages over conventional

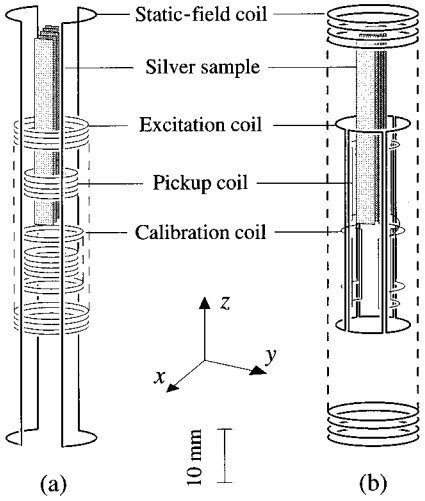

FIG. 16. Coils used in the NMR measurements in (a) horizontal and (b) vertical external fields. The dashed vertical lines indicate sections to which (a) the excitation and (b) the static field coils extend. From Oja, Annila, and Takano (1991).

NMR techniques based on a field-effect-transistor (FET) preamplifier. SQUIDs offer greater sensitivity at low frequencies because a SQUID magnetometer measures directly the change in the magnetic flux caused by changes in magnetization, whereas the conventional method responds to $d\mathbf{M}/dt$, where $\mathbf{M}$ is the magnetization. In particular, for NMR on metals at low temperatures, working at low frequencies is advantageous from the point of view of penetration depth and eddy-current heating of the sample by the rf field. SQUID NMR is ideal for studying systems that have long spin-lattice relaxation times and short spin-spin relaxation times, i.e., fast dephasing times. The bandwidth of a system employing a SQUID can be made very large. As an example, in the apparatus of Chamberlin *et al.* (1979), the same instrument could be used both for NMR down to 10 kHz and for low-field electron paramagnetic resonance up to 1 GHz. Meredith *et al.* (1973) and Webb (1977) have discussed the basic principles of SQUID NMR and have presented typical applications. For a more recent review on the use of SQUIDs in low-frequency applications, see Ryhänen *et al.* (1989).

Ehnholm *et al.* (1980) introduced and developed the SQUID NMR technique for investigations of nuclear ordering on copper. The methods employed in later measurements of Cu, Ag, and Rh were variants of this original scheme. The measuring system consists essentially of a pickup coil connected to an rf SQUID, which works as a sensitive preamplifier over a large frequency range. The dynamic susceptibility is recorded by varying the excitation frequency rather than the external field. During some measurements in high fields, however, corresponding to Larmor frequencies close to 200 kHz, the conventional field-sweep method was employed.

A typical coil assembly for measuring the magnetic response of the sample is shown in Fig. 16 (Oja, Annila, and Takano, 1991), which illustrates two systems, one longitudinal, the other transverse, for detecting different

[5]Here $\chi(f)$ refers to a diagonal component of the matrix $\chi(f)$, which, in most cases, is perpendicular to the external magnetic field.

components of the susceptibility. The longitudinal-coil arrangement, Fig. 16(a), is used for measuring the NMR signal in horizontal static fields, created by a saddle coil in the xy plane, whereas the transverse system, Fig. 16(b), is employed when the static field is vertical.

In the longitudinal measuring geometry, the vertical pickup coil consists of two 4-mm high, seven-turn solenoids, which were wound in opposite directions, with an 11-mm separation to reduce direct feedthrough of the excitation signal. The inductance of the pickup coil was matched to the 2-μH input inductance of the SQUID. The excitation field was generated by a small solenoid outside. For calibrating the SQUID response, a small solenoid was wound on the lower half of the pickup coil below the sample.

In the horizontal geometry, Fig. 16(b), the transverse, saddle-shaped 30-mm-long figure-of-eight pickup coil was made of four loops. Two transverse excitation coils were wound, one coaxial with the pickup coil and the other at a right angle to it. A transverse saddle-shaped calibration coil was also wound on the lower half of the pickup loop.

The crossed-coil system can be employed only in nonzero fields, where the macroscopic magnetization rotates around $\mathbf{B}\|\mathbf{z}$. In zero field, when there is no longer any preferred axis, the response of the spins vibrates in the direction of the excitation and thus no signal is detected if the excitation and pickup coils are crossed. Therefore the zero-field measurements were made with a coaxial coil system. Another possibility would be to use a rotating excitation, generated by feeding into the two crossed excitation coils currents with $\pm 90°$ phase shift. The response to positive and negative frequencies could then be measured separately (Ehnholm *et al.*, 1980).

All coils in the setup of Fig. 16 were wound on a cylindrical support of 10 mm diameter, made of Stycast 1266. The coil system was mounted inside the mixing-chamber radiation shield surrounding the sample region so that the support did not make any contact with the specimen. In earlier experiments on copper, the measuring coils were wound on a cylindrical coil former made of silver and thermally anchored to the first nuclear stage. The advantage of this scheme is a better filling factor. This design was abandoned, however, in the measurements on silver and rhodium, since a clearance between the sample and the coil former guaranteed that no heat could leak to the specimen, which has a very small thermal capacity.

The pickup coils were usually wound of normal-metal wire, such as insulated silver or copper, rather than superconducting material. The advantage of a resistive pickup wire is that the input circuit of the SQUID, which is shown schematically in Fig. 17, then forms a high-pass filter and noise below the cutoff frequency is attenuated, so that it is easier to maintain the operational position of the SQUID; the quality of the signal is improved as well. In practice, by a suitable choice of pickup wire, the cutoff frequency $f_L = R_p/(2\pi L_s)$ can be chosen between 10 Hz and 1 kHz with a typical $L_s = 2$ μH inductance of the signal coil in the SQUID.

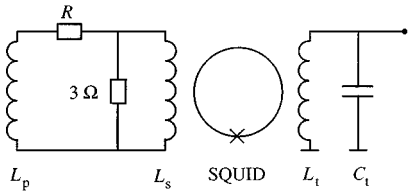

FIG. 17. Low-temperature parts of a SQUID-NMR measuring system. L_p and L_s are the inductances of the pickup and signal coils, respectively. R is the resistance of the pickup coil. A 3-Ω resistor protects the signal coil of the SQUID from high-frequency disturbances. Components forming an LC resonant circuit, the so-called tank circuit, are shown on the right.

10 Hz is slightly below the important frequency range for NMR on silver and rhodium, while $f_L \approx 1$ kHz is suitable for copper. The upper cutoff frequency of the detection system could be adjusted by a small shunt resistor across the signal coil of the SQUID.

Pickup loops made of superconducting wire were tried as well, but with variable degrees of success. In some setups flux jumps in the superconducting pickup wire were suspected of introducing much noise, although in other cases a superconducting pickup coil made of 70-μm multifilamentary NbTi wire in a CuNi matrix worked without problems (Huiku and Loponen, 1982). A superconducting pickup loop would also allow a direct measurement of the dc magnetization of the sample. This possibility was tried in the very first studies on copper, but the noise was several orders of magnitude larger than the expected signal.

The dynamic susceptibility $\chi(f)$ was measured using frequency sweeps across the resonance in a constant external magnetic field. The block diagram of the measuring system is shown in Fig. 18. Detection of the NMR spectra was controlled by a computer. When measuring a spectrum, an oscillator was set to sweep through the frequency range of interest. The ac output was fed into the excitation and compensation coils and to the refer-

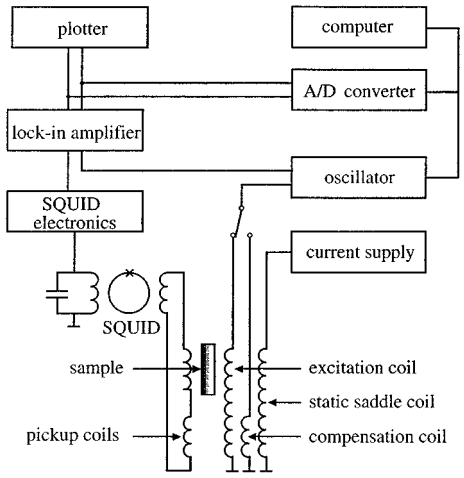

FIG. 18. Computer-controlled SQUID-NMR measuring system. The experimental procedure is explained in the text.

ence input of the biphase lock-in analyzer. The in- and out-of-phase signals of the SQUID electronics were measured by a lock-in amplifier. The two phases were monitored by a digital voltmeter and a recorder.

When the measuring frequencies were low, the SQUID was used in the flux-locked mode.[6] This technique made it possible to employ higher excitation levels, over half a flux quantum, which improved the signal-to-noise ratio. During measurements in the 100-kHz frequency range the SQUID was not operated in the feedback mode, but the voltage across the tank circuit was monitored directly (Ehnholm, Ekström, Loponen *et al.*, 1979; Ekström *et al.*, 1979).

As the stability of the SQUID response during measurements is important, possible changes in the gain or phase of the detection system were checked after every recorded NMR spectrum by feeding a small current into the calibration coil below the sample. This coil was also used to measure the overall frequency dependence of the gain and the phase. In a metallic sample an extra phase shift is caused by eddy-current shielding (Chapman *et al.*, 1957).

In practice, a limitation on the accuracy of the measurements was not intrinsic to the SQUID but due to other sources of noise. This is not surprising considering the fact that the pickup coil was supposed to measure small magnetic signals at a location that had been in an 8-T field half an hour earlier. The noise level usually increased permanently after the 8-T solenoid had been energized for the first time after cooldown to 4.2 K. Several sources of degraded performance were identified in the various setups: (1) The noise in the measuring system, as well as the lowest temperatures achieved, were sensitive to the level of external vibrations. (2) After demagnetization, the mu-metal tube around the sample relaxed slowly and produced noise during the first few minutes. (3) The remanent field of the 8-T sample magnet drifted for several hours after the end of demagnetization. This effect, and the remanent field itself, could be reduced by feeding a small opposite current to the 8-T solenoid after demagnetization. In addition, this procedure accomplished some degaussing in the mu-metal shield. (4) When a superconducting pickup wire was used, movements of trapped flux caused noise for several hours after demagnetization. (5) In some setups, the SQUID sensors were operated at 0.7 K, although their performance had been optimized for use at 4 K; this caused a small increase of noise. (6) In many cases, transfer of liquid helium to the main dewar warmed the SQUID to the normal state owing to its poor thermal anchoring to 4.2 K. When the SQUID returned to its superconducting state it trapped magnetic flux, generated by the field of the first-stage magnet, and the noise level of the sensor became very large. The problem was solved by heating the SQUID to the normal state just before the final demagnetization of the sample. During this phase of the experiment the first-stage field was so low that it did not disturb the SQUID. (7) In most setups the SQUID was mounted close to the top plate of the vacuum can so that the pickup wires had to pass through the first-stage field, which had to be low to avoid increasing the noise in the measuring system.

[6]In the flux-locked mode, the flux penetrating the SQUID ring is kept constant. This is achieved by compensating for any changes in the external flux by the use of a feedback circuit and a coupling coil. There is a linear relationship between the feedback current (or voltage) and the external flux. For more details, see Lounasmaa (1974).

IV. MEASUREMENT OF NUCLEAR-SPIN TEMPERATURE

To compare theoretical calculations with experimental data, one must know the temperature of the spin system. When the nuclei are not in equilibrium with the conduction electrons, one cannot measure T by using an external thermometer. The thermal isolation of nuclear spins makes it possible, however, to obtain the spin temperature directly from the second law of thermodynamics, viz.,

$$T=\Delta Q/\Delta S\ . \tag{22}$$

The experimental problem is then reduced to giving a heat pulse ΔQ of known magnitude and measuring the resulting change in entropy ΔS. A heat pulse to nuclear spins can be administered through NMR absorption. When an alternating magnetic field $B_1(t)=B_1\sin(2\pi ft)$ is applied for a time Δt, the energy absorbed by the spins is

$$\Delta Q=\pi f B_1^2\chi''(f)\Delta t/\mu_0\ , \tag{23}$$

where $\chi''(f)$ is the absorptive part of the complex susceptibility. To measure ΔS one needs to know the entropy before and after the pulse. Entropy can be determined by using adiabatic sweeps between the field where the temperature is measured, which is usually zero, and a high field. Here this means a field considerably stronger than $B_{\rm loc}$ so that one can use the known equations for noninteracting spins. The details of the actual procedures used were somewhat different in the various measurements on copper, silver, and rhodium. Our discussion in the following emphasizes the more recent measurements on silver and rhodium.

A. Calibration of polarization and entropy

The measurement of the polarization p is based on the fact that in a sufficiently high field, $B=B_{\rm calib}\gg B_{\rm loc}$, p is proportional to the integrated area of the NMR absorption signal,

$$p=A\int_0^\infty \chi''(f)df\ , \tag{24}$$

where A is a calibration constant. In practice, $B_{\rm calib}$ was 1.0 mT in Cu (Huiku *et al.*, 1986), 0.19 mT in Ag (Hakonen and Yin, 1991), and 0.40 mT in Rh (Hakonen, Vuorinen, and Martikainen, 1993).

The constant A can be determined by first producing an equilibrium polarization in a field on the order of 7 T

at a relatively high electronic temperature around $T_e = 1$ mK. T_e was measured using the pulsed NMR technique on platinum wires (Lounasmaa, 1974; Pobell, 1992a, 1992b). Around $T_e = 1$ mK, it is possible to equilibriate nuclear spins with the conduction electrons and to avoid thermal gradients between the sample and the Pt-NMR thermometer attached to the first nuclear stage. A commercial Pt-NMR electronics unit was employed (PLM-4, RV-Electronics, Veromiehentie 14, 01510 Vantaa, Finland). The platinum thermometer was calibrated against the superconducting transitions of tungsten and beryllium at $T_c = 15.7 \pm 0.1$ mK and 22.6 $\pm$ 0.1 mK, respectively. The calibrated W and Be samples were supplied by Dr. R. J. Soulen of the U.S. National Bureau of Standards. The fixed-point device was similar to that described by Soulen and Dove (1979).

Polarization of the nuclear-spin system in the 7-T field can be calculated from

$$I = \tfrac{1}{2}: \; p = \tanh u \quad (\mathrm{Ag},\ \mathrm{Rh}), \tag{25a}$$

$$I = \tfrac{3}{2}: \; p = \tfrac{1}{3}(4\ \coth 4u - \coth u) \quad (\mathrm{Cu}), \tag{25b}$$

where $u = \gamma\hbar B/2k_B T$. These equations are valid for noninteracting spins, since interactions can be ignored in the 7-T field. As soon as the polarization is known, the entropy can be calculated from the equations

$$I = \tfrac{1}{2}: \; S/\mathcal{R} = \ln 2 - \tfrac{1}{2}[(1-p)\ln(1-p) + (1+p)\ln(1+p)] , \tag{26a}$$

$$I = \tfrac{3}{2}: \; S/\mathcal{R} = u(\coth u - 4\ \coth 4u) + \ln(\sinh 4u/\sinh u) . \tag{26b}$$

For $I = \frac{3}{2}$ one has to eliminate u from the coupled equations (25b) and (26b).

Finally, the sample is adiabatically demagnetized from the field $B = 7$ T to the field $B = B_{\mathrm{calib}}$ used for monitoring p. However, a correction must be made for the loss of polarization due to spin-lattice relaxation during demagnetization. This can be done by watching the decay of $\int \chi''(f)\,df$, as shown in Fig. 19, and then extrapolating the signal back to the midpoint of demagnetization. This gives the area corresponding to the initial polarization with good accuracy.

B. Calibration of susceptibility

To calculate the magnitude of the heat pulse [see Eq. (23)], one has to know $\chi''(f)$ in absolute units. Calibration of the polarization alone yields only the product $A\chi''(f)$. To find $\chi''(f)$ one can use the Kramers-Kronig relation

$$\chi'(0) = (2/\pi)\int_0^\infty (\chi''(f)/f)\,df , \tag{27}$$

where $\chi'(0)$ is the measured static susceptibility. Here we assume the usual situation in which the field $B = B_{\mathrm{calib}}$ is applied along the z direction and the magnetic response [$\chi'(0)$ or $\chi''(f)$] is monitored using a coaxial measuring system in the y direction. Both y and z are further assumed to be along the principal axes of

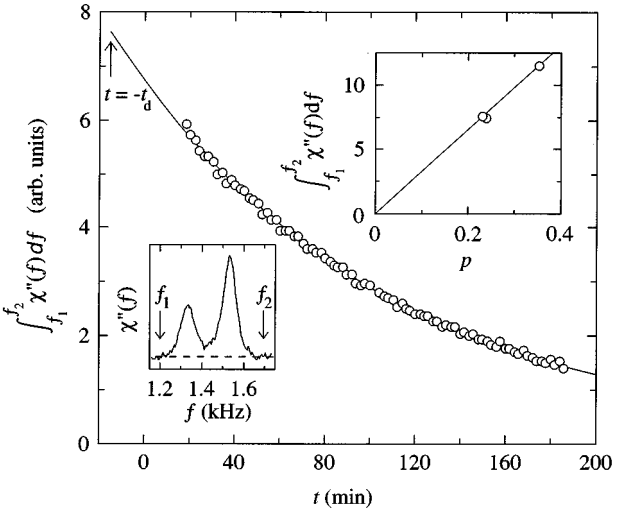

FIG. 19. Decay of $\int \chi''(f)\,df$ after demagnetization of the silver nuclear spins to $B = B_{\mathrm{calib}}$ had ended at $t = 0$. In this experiment $B_{\mathrm{calib}} = 0.77$ mT. The equilibrium value of the polarization in $B = 7$ T and at $T_e \approx 1$ mK can be obtained by extrapolating the signal to the midpoint of demagnetization ($t = -t_d$). The inset in the lower left corner shows a typical NMR signal consisting of ^{107}Ag and ^{109}Ag resonances. The signal was integrated from f_1 to f_2 to obtain p. The inset in the upper right corner displays the data points that, together with the origin, fixed the polarization scale. From Oja, Annila, and Takano (1991).

the demagnetizing tensor of the sample. The signal is then related to the polarization through the equation

$$\chi'(0) = \mu_0 p M_{\mathrm{sat}}/[B + \mu_0(D_y - D_z)p M_{\mathrm{sat}}] , \tag{28}$$

where M_{sat} is the saturation magnetization and μ_0 is the permeability of free space. D_y and D_z are the demagnetizing factors of the sample in the y and z directions, respectively; they can be estimated from the dimensions of the specimen. The term containing $D_y - D_z$ typically affects the calibration of $\chi'(0)$ by only a few percent.

C. Local field

The local field B_{loc} is an important quantity in nuclear thermometry. This is highlighted by Eq. (13), which directly yields the spin temperature after adiabatic demagnetization to zero field if the starting conditions and B_{loc} are known. B_{loc} describes the average strength of the local fluctuating field that is felt by a nucleus. Therefore, it determines the entropy reduction at high temperatures in the disordered phase [see Eq. (35)].

The local field is defined by

$$B_{\mathrm{loc}}^2/B^2 = \mathrm{Tr}\{\mathcal{H}_{\mathrm{ss}}^2\}/\mathrm{Tr}\{\mathcal{H}_{\mathrm{Z}}^2\}, \tag{29}$$

where $\mathcal{H}_{\mathrm{ss}}$ describes the spin-spin interactions $\mathcal{H}_{\mathrm{Z}}$ is the Zeeman term, and the trace $\mathrm{Tr}\{\ldots\}$ is taken over spin states. Assuming dipolar and isotropic interactions, where $\mathcal{H}_{\mathrm{ss}} = \mathcal{H}_{\mathrm{D}} + \mathcal{H}_{\mathrm{RK}}$, given by Eqs. (2) and (3), one finds

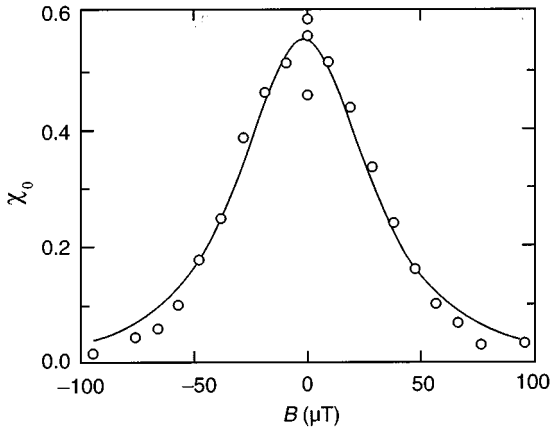

FIG. 20. Reduced longitudinal susceptibility χ_0 of silver vs B at $p=0.50$ [see Eq. (34) and its discussion]. The solid line displays a fit to the theoretical curve $\chi_L \propto (1+B^2/B_{\rm loc}^2)^{-3/2}$, which yields $B_{\rm loc}=44$ μT. The small shift of the symmetry axis from zero gives 1.4 μT for the remanent field. Modified from Hakonen and Yin (1991).

$$B_{\rm loc}^2 = B_{\rm loc,D}^2 + B_{\rm loc,RK}^2 , \tag{30a}$$

where

$$B_{\rm loc,D} = \frac{\mu_0}{4\pi}\hbar\gamma\left[I(I+1)\sum_j r_{ij}^{-6}\right]^{1/2}, \tag{30b}$$

$$B_{\rm loc,RK} = \left[\tfrac{1}{2}I(I+1)\sum_j J_{ij}^2\right]^{1/2}/\hbar\gamma. \tag{30c}$$

The dipolar sums $\Sigma_j r_{ij}^{-6}$ have been tabulated for cubic lattices (see p. 226 in Goldman, 1970).

There is an intimate connection between $B_{\rm loc}$ and the width of the NMR absorption line. Roughly speaking, both quantities are determined by the randomly fluctuating local field. Details depend, however, on the particular mixture of magnetic isotopes present in the system (Van Vleck, 1948). Various NMR measurements at high temperatures, above $T=1.5$ K, have yielded $B_{\rm loc}$ in several materials, as reviewed by Oja (1987).

$B_{\rm loc}$ can also be deduced by measuring the field dependence of the adiabatic susceptibility. According to theory (Anderson, 1962, and references therein), there is the relationship

$$\chi_L \approx \chi_T/(1+B^2/B_{\rm loc}^2) \tag{31}$$

between the longitudinal χ_L and transverse χ_T adiabatic susceptibilities; possible modifications caused by zero-frequency absorption have been neglected (Anderson, 1962; Huiku and Soini, 1983). If this result is applied in the high-T limit, one may use the Curie law $\chi_T=C/T$ and Eq. (13) to obtain the field dependence of the temperature. One then finds $\chi_L \propto (1+B^2/B_{\rm loc}^2)^{-3/2}$. Figure 20 illustrates the measured χ_L vs B for silver. A fit to the theoretical curve yields $B_{\rm loc}=44$ μT. However, the value $B_{\rm loc}=35$ μT, inferred from two different NMR measurements (Poitrenaud and Winter, 1964; Oja, Annila, and Takano, 1990), is somewhat lower. The latter result was adopted for the temperature measurements on silver (Hakonen and Yin, 1991).

There are several other possible ways to determine the local field. For example, measurement of loss in polarization caused by a rapid field reversal yields $B_{\rm loc}$ through Eq. (41).

Data on χ_L in different fields can also be used to determine the magnitude of the remanent field, as is shown in Fig. 20.

TABLE II. Curie constant $C=\frac{1}{3}I(I+1)\mu_0\hbar^2\gamma^2\rho/k_B$ and saturation magnetization $\mu_0 M_{\rm sat}$ for natural isotopic mixtures of copper, silver, and rhodium.

	C (nK)	$\mu_0 M_{\rm sat}$ (μT)
Copper	562	1200
Silver	2.0	45
Rhodium	1.3	41

D. Consistency checks using high-T expansions

Equations (25a)–(26b) are valid when the Zeeman energy is much larger than the interaction energy. In low fields one has to use other formulas. Exact thermodynamical relations can be derived within the high-T approximation. Although they are not valid in the most interesting range of high p, these approximations are useful for checking the consistency of thermometry in the low-p limit. Consult Van Vleck (1937) for additional terms in high-T expansions.

The two leading high-T terms for p can be written as[7]

$$p = (B/\mu_0 M_{\rm sat})\chi_0/[1-(R+L-D)\chi_0] , \tag{32}$$

where

$$\chi_0 = C/T \tag{33}$$

is the zero-field susceptibility of the noninteracting system and $C=\Lambda/V_m$ is the nuclear Curie constant [see Eq. (16)] per mole divided by the molar volume V_m. Here L and D are due to dipolar interactions: $L=\frac{1}{3}$ is the Lorentz constant, and D is the demagnetizing factor in the direction of the external field. R is the strength of the RK force, defined in Eq. (6). The values of C and $\mu_0 M_{\rm sat}$ have been collected into Table II for Cu, Ag, and Rh.

The longitudinal susceptibility $\chi_L=\mu_0(dM/dB)$ is obtained by calculating the derivative of Eq. (32):

$$\chi_L = \chi_0/[1-(R+L-D)\chi_0] . \tag{34}$$

The equation can also be inverted to give χ_0 in terms of the measured χ_L. This is a way to "reduce" the susceptibility of the interacting spin assembly to that of a virtual system with no interactions.

[7]The coefficient $[1-(R+L-D)\chi_0]^{-1}$ reduces to $1+(R+L-D)\chi_0$ in the high-T expansion. The two expressions are identical, however, to the order considered here.

The leading higher-order effects of the spin-spin interactions on the entropy S are given by

$$S = n\mathcal{R}\ln(2I+1) - n\Lambda(B^2+B_{\rm loc}^2)/2T^2 . \quad (35)$$

The spin temperature at $B=0$, for example, is determined by measuring the entropy or polarization in a high field, $B=B_{\rm calib}\gg B_{\rm loc}$. The relation between $T(B=0)$ and, say, $p(B=B_{\rm calib})$ can be obtained within the high-T approximation, Eqs. (32) and (35). One finds

$$T = CB/[\mu_0 p M_{\rm sat}(1+B^2/B_{\rm loc}^2)^{1/2}] , \quad (36)$$

showing the $T \propto p^{-1}$ dependence at small polarizations.

In temperature measurements on copper, silver, and rhodium, Eq. (36) was not employed to check the consistency of the data, but rather to fit the amplitude B_1 of the alternating field used to give a heat pulse ΔQ to the nuclear spins, as described by Eq. (23) (Huiku *et al.*, 1986; Hakonen and Yin, 1991; Vuorinen, Hakonen, Yao, and Lounasmaa, 1995). The value calculated from the coil geometry could not be used because the mu-metal tube (see Fig. 11) used to shield the sample against the remanent field was found to give a frequency-dependent change in the B vs electric-current relation of the heating coil. A direct measurement of B_1 was difficult to make as well. Therefore, in practice, B_1 was calibrated by forcing the data to follow the high-T expansion, i.e., Eq. (36).

A useful check to ascertain the consistency of nuclear thermometry would be to measure T in a high field, $B=B_{\rm calib}$, by using the heat-pulse method. The result could then be compared with the temperature obtained from Eq. (25a), valid for noninteracting spins. Alternatively, it would be possible to calibrate the excitation field B_1 in this same way. The physically more interesting behavior at low fields could then be measured without fixing the high-T behavior. The problem with this scheme might be, however, that applying ΔQ would require frequencies so high that the rf field would not penetrate the sample. Another possible source of problems could be the frequency dependence of the B vs current relation of the heating coil observed in some experimental setups.

E. Secondary thermometers

A direct measurement of the nuclear-spin temperature is a somewhat complicated and time-consuming procedure. If a secondary thermometer is available it often provides a more convenient method.

As an early example, in the study of the field-orientation dependence of the static susceptibility of copper (Huiku and Soini, 1983), the previously measured (Ehnholm *et al.*, 1980) transverse susceptibility was employed as a secondary thermometer to establish the T dependence of the longitudinal susceptibility.

During studies on silver, secondary thermometry was used extensively (Hakonen and Yin, 1991; Hakonen, Nummila, Vuorinen, and Lounasmaa, 1992). A drawback in the direct temperature measurement was that a rather large heat pulse ΔQ was needed to obtain sufficiently accurate values of ΔS. In terms of p, the change was typically 20% per one measurement of T, and therefore the direct procedure was not suitable for determining the ordering temperatures accurately.

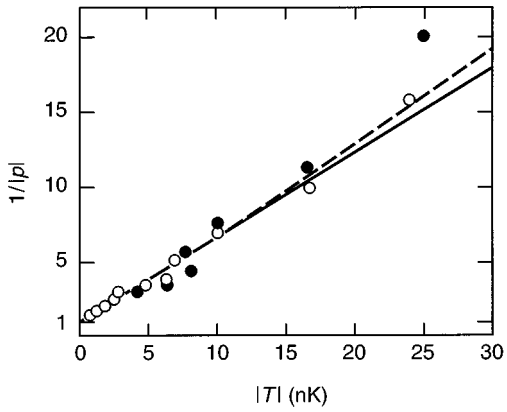

FIG. 21. Inverse nuclear polarization $1/|p|$ of silver at $B=0.19$ mT, plotted against the absolute value of temperature at $B=0$; ○, $T>0$; ● $T<0$. The dashed curve was obtained from the high-T expansion [see Eq. (36)], which has been joined smoothly to the linear low-T part passing through $p=1$. From Hakonen and Yin (1991).

Secondary thermometry in the silver experiments was based on the observation that the relationship between the zero-field temperature T and the inverse polarization determined at $B=B_{\rm calib}$ is linear over a wide range, as shown in Fig. 21. The linear relationship is guaranteed by Eq. (36) at high temperatures, but almost the same tendency continues to lower temperatures. In addition, the low-T limit is known approximately: neglecting quantum fluctuations, $p\to 1$ when $T\to 0$. Based on experimental data, a piecewise linear dependence was used: $1/p-1=0.55T$ below $T=10$ nK and $1/p=0.65T$ above 10 nK, where T is expressed in nK's. The same functional dependence was observed at negative temperatures as well, with T being replaced by $|T|$, although the scatter of the data was larger.

F. Nonadiabaticities

Nuclear-spin thermometry assumes that the state of the system develops adiabatically when, for example, the external field is reduced. There are, however, sources of nonadiabaticity, i.e., entropy increases, some of which can be avoided and some of which cannot.

Increased spin-lattice relaxation during a field ramp, due to eddy-current heating proportional to $(dB/dt)^2$, is an obvious candidate for raising T_e. The field change should be slow enough.

Other possible sources of nonadiabaticity include consequences from interactions with electronic magnetic impurities, spurious nuclear quadrupolar interactions caused by lattice defects, and surface phenomena possibly associated with quadrupolar effects in small particles (Komori *et al.*, 1986) or thin foils. These interactions may depend on the magnetic field and in some cases on

the rate at which B is being varied, for example, when cross relaxation takes place between the quadrupolar energy levels that cross each other as the field is being changed.

Even in an ideal sample there is some nonadiabaticity owing to thermal mixing, which was described in Secs. II.B and II.C. In a typical nuclear-ordering experiment, demagnetization of the specimen is fast in comparison to τ_1, and the cold Zeeman reservoir cools the hot interaction reservoir only in a field comparable to $B_{\rm loc}$.

To make our discussion quantitative, we employ the high-temperature expansion although it is not valid under the actual experimental conditions with the spins almost fully polarized. However, the high-T approximation should be sufficient to describe, for example, measurements during which the polarization scale is calibrated.

After the nuclei in the sample have been polarized in the 7-T field at submillikelvin temperatures, the system can be described by the density matrix

$$\sigma = 1 - \beta\mathcal{H} , \tag{37}$$

where $\beta = 1/k_{\rm B}T$ and $\mathcal{H} = \mathcal{H}_{\rm Z} + \mathcal{H}'_{\rm ss} + \mathcal{H}''_{\rm ss}$. Here $\mathcal{H}'_{\rm ss}$ is, as before, the secular part of the spin-spin interactions, i.e., the part that commutes with $\mathcal{H}_{\rm Z}$ ($[\mathcal{H}'_{\rm ss}, \mathcal{H}_{\rm Z}] = 0$), while $\mathcal{H}''_{\rm ss}$ is the remaining, nonsecular part for which $[\mathcal{H}''_{\rm ss}, \mathcal{H}_{\rm Z}] \neq 0$. After demagnetization has started, the changing field modifies the density matrix. Since dB/dt is fast in comparison to τ_1, which in turn is much faster than τ_m at $B = 7$ T, the heat reservoirs in Fig. 6 no longer are in thermal equilibrium. Furthermore, the order in the off-diagonal parts of σ, corresponding to the nonsecular interaction $\mathcal{H}''_{\rm ss}$, is destroyed, and σ acquires the form (Goldman, 1970)

$$\sigma = 1 - \alpha\mathcal{H}_{\rm Z} - \beta_i\mathcal{H}'_{\rm ss}, \tag{38}$$

where β_i is the inverse temperature at the beginning of demagnetization when $B = B_i$ and $\alpha = \beta_i B_i / B$ (*without* any $B_{\rm loc}$ corrections). Therefore only the Zeeman system is cooled during demagnetization in high fields, while the interaction reservoir remains at the precooling temperature.

When B becomes comparable to $B_{\rm loc}$, the Zeeman levels, broadened by the spin-spin interactions (see Fig. 5), start to overlap and thermal mixing takes place between $\mathcal{H}_{\rm Z}$ and $\mathcal{H}'_{\rm ss}$, which means that σ assumes again its equilibrium form given by Eq. (37). The equilibrium temperature β_f^{-1} will be somewhat higher than α^{-1} because the Zeeman system has to cool the interaction reservoir.

To calculate β_f, we assume that thermal mixing takes place at the constant field $B = B_m$. Although B decreases continuously during demagnetization, this assumption is reasonable since the field dependence of τ_m is very steep. During thermal mixing the energy remains constant, viz.,

$$\mathrm{Tr}\{\sigma\mathcal{H}\} = \mathrm{Tr}\{(1 - \alpha\mathcal{H}_{\rm Z} - \beta_i\mathcal{H}'_{\rm ss})\mathcal{H}\} = \mathrm{Tr}\{(1 - \beta_f\mathcal{H})\mathcal{H}\} . \tag{39}$$

Ignoring the small term $\beta_i\mathcal{H}'_{\rm ss}$, and recalling that $\alpha = \beta_i B_i / B$, we find

$$\begin{aligned}\beta_f &= \beta_i B_i B_m / (B_m^2 + B_{\rm loc}^2) \\ &= [\beta_i B_i / (B_m^2 + B_{\rm loc}^2)^{1/2}] \times [B_m / (B_m^2 + B_{\rm loc}^2)^{1/2}] .\end{aligned} \tag{40}$$

The last equation should be compared with Eq. (13), valid for adiabatic demagnetization. We see that in the present case there is a nonadiabaticity factor $B_m / (B_m^2 + B_{\rm loc}^2)^{1/2}$, which results from thermal mixing when $B = B_m$.

In a two-isotope system, such as a natural sample of copper or silver, the behavior is more complicated. During demagnetization it is then meaningful to describe the spin assembly in terms of three heat reservoirs. These will be discussed in Sec. XI.A.2 when describing the measurements of the thermal mixing time in silver. Although the behavior of the two-isotope system is more complicated than that with only one isotope, the former appears to be more adiabatic.

If the spin system is remagnetized after thermal mixing has occurred in a low field, the heat contact is again disconnected when $B > B_m$. During further field increases, the interaction reservoir remains at the low temperature it had when $B = B_m$, while $\mathcal{H}_{\rm Z}$ warms up in proportion to B. If a second demagnetization is then performed, the Zeeman system finds a cold interaction reservoir at $B = B_m$ and there is only a small irreversibility. There is some entropy increase, however, even in this case, as the off-diagonal order in σ, corresponding to the nonsecular $\mathcal{H}''_{\rm ss}$, is lost during field cycling. One also has to remember that the interaction reservoir warms towards the lattice temperature with the relaxation time $\tau_{1\rm ss}$, which is 2–3 times shorter than τ_1 in an ideal specimen (Goldman, 1970) and possibly even less in a real sample containing impurities.

Apart from direct measurements of τ_m in silver (Oja, Annila, and Takano, 1990), effects due to thermal mixing have been discussed (Ehnholm *et al.*, 1980; Soini, 1982) only briefly in the context of nuclear ordering experiments in metals. In insulators this process has been studied extensively (see the references in Abragam, 1961). Let us now calculate the entropy increase due to thermal mixing in silver. We make our estimates for a single-isotope system; the nonadiabaticity for a two-isotope assembly should be smaller. To define the thermal mixing field B_m, we choose a field at which $\tau_m(B) = 1$ s. Measurements (Oja, Annila, and Takano, 1990) yield $B_m \approx 0.25$ mT. The nonadiabaticity factor $B_m / (B_m^2 + B_{\rm loc}^2)^{1/2}$ then becomes 0.99. Thermal mixing thus leads to a nonadiabatic 1% decrease in polarization at $B = B_m$ [see Eq. (32)] and a 2% decrease in the entropy *reduction* [see Eq. (35)]. In addition, there is an *adiabatic* 1% decrease in p at $B = B_m = 0.25$ mT, caused by the conventional $(B_m^2 + B_{\rm loc}^2)^{1/2}$ term in Eq. (35). We conclude that, at least in the low-polarization limit, nonadiabaticity due to thermal mixing in silver leads to a rather small irreversibility, which, however, is significant for accurate measurements.

In the first set of experiments on nuclear-ordering in copper (Ehnholm *et al.*, 1980), a nonadiabatic 7% maximum loss in polarization was observed when a highly ordered spin system was demagnetized well below 1 mT, close to $B_{\rm loc}=0.36$ mT. The effect was attributed to thermal mixing. This large loss was found only for the first demagnetization. After remagnetization to 1 mT and demagnetization to zero field for the second time, the loss was much smaller (Soini, 1982). Nonadiabaticities were observed in later measurements on copper as well (Huiku *et al.*, 1986). This time, however, polarization losses were attributed to the ordering process rather than thermal mixing, and field sweeps between $B=1$ mT and zero field in the disordered state, at entropies above $0.61\mathcal{R}\ln 4$, were found to be adiabatic. Neutron-diffraction experiments (Annila *et al.*, 1992) have clearly shown that, indeed, during the transition from the (1 0 0) phase to the $(0\,\frac{2}{3}\,\frac{2}{3})$ phase in fields around $B=0.11$ mT, a large nonadiabaticity occurs. There should, however, be some polarization loss caused by thermal mixing, too, although it may occur in fields above $B=1$ mT.

G. Production of negative spin temperatures by a rapid field reversal

Although a rapid field reversal was used in the famous experiment by Purcell and Pound (1951, see Sec. II.D.1) in which negative temperatures were first produced, it was only rather recently that Oja, Annila, and Takano (1991) demonstrated that this method is feasible for studying nuclear magnetism in metals. Hakonen *et al.* (Hakonen, Yin, and Lounasmaa, 1990; Hakonen, Nummila, Vuorinen, and Lounasmaa, 1992; Hakonen and Vuorinen, 1992) did a lot of work to improve this technique for observing nuclear ordering in silver at $T<0$. For example, a special coil assembly and radiation shields were constructed to reduce eddy-current shielding.

The field-reversal procedure was somewhat complicated owing to the fact that the NMR spectra were measured in a transverse field $B_x=200$ μT, created by a small saddle-shaped coil, while the field inversion was performed using a solenoid producing a longitudinal field $B_z=400$ μT. First, before the field flip, the initial polarization was determined from the NMR spectrum measured in the transverse 200-μT field (see Fig. 22). Next, the longitudinal solenoid was remagnetized to $B_z=400$ μT in 40–60 s, and B_x was simultaneously reduced to zero. B_z was then changed to -400 μT quickly, in 1 ms. The field reversal increased the internal energy of the spin system considerably; the energy during this process is absorbed from the external magnetic field. Finally, B_z was slowly reduced to zero and B_x was simultaneously increased to its original value of 200 μT. The measured NMR emission spectrum (see Fig. 22) then showed that, indeed, the spin temperature and the nuclear polarization were negative. Final demagnetization was then performed by reducing B_x to zero.

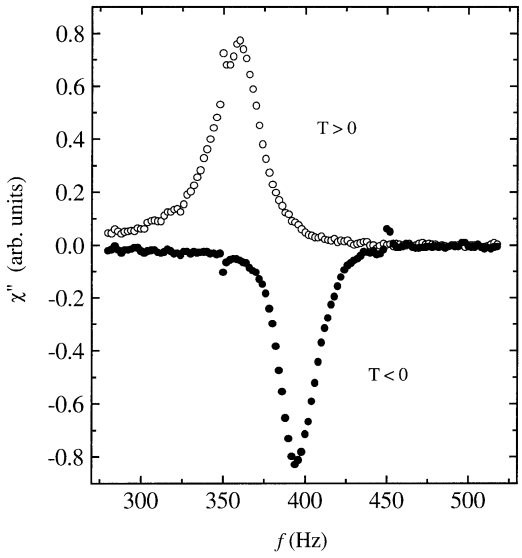

FIG. 22. NMR measurements of silver in a transverse field $B_x=200$ μT before and immediately after reversal of the longitudinal field $B_z=\pm 400$ μT: ○, absorption spectra; ●, emission spectra. The initial and final polarizations, calculated from these spectra, were 0.73 and -0.64, respectively. Note that the peak frequency is higher when $T<0$ because of the strong ferromagnetic susceptibility at negative temperatures. From Vuorinen (1992).

The rapid reversal of the 400-μT field always resulted in some loss of polarization in the nuclear-spin system. This is illustrated in Fig. 23. The inversion efficiency was about 95% at small polarizations around $p_i=0.4$ but decreased to 80% or lower at $p_i=0.8$. Therefore studies of silver at $T<0$ were limited to negative polarizations up to $p=-0.65$.

The observed polarization loss is explained, at least partly, by thermal-mixing effects, which were discussed

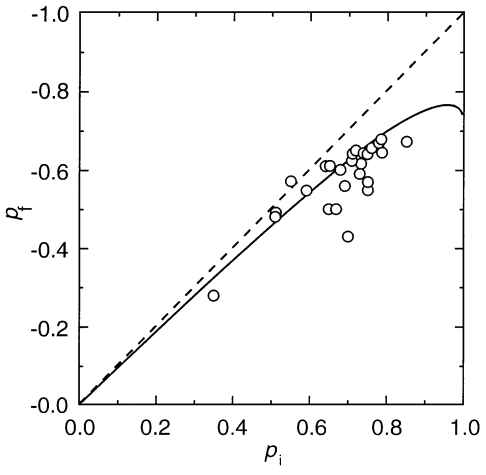

FIG. 23. Polarization p_f of nuclear spins in silver, after rapid field reversal, as a function of the initial polarization p_i. The solid line was calculated from a theoretical model described briefly in the original paper. The dashed line indicates the ideal case with no loss of polarization. From Hakonen and Vuorinen (1992).

in Secs. II.B, II.C, and IV.F. During the field flip, only the Zeeman temperature is reversed; the temperature of the interaction reservoir T_{ss} is not changed. An irreversible entropy increase results when $\mathcal{H}_Z$ warms the interaction reservoir $\mathcal{H}'_{ss}$ to negative temperatures. The calculation of this effect is similar to that described in Sec. IV.F. The equilibrium temperature T_f after a rapid field flip from $\mathbf{B}=+B\hat{\mathbf{z}}$ to $\mathbf{B}=-B\hat{\mathbf{z}}$ is (Slichter, 1990)

$$T_f=-T_i(B^2+B_{\rm loc}^2)/(B^2-B_{\rm loc}^2)\ , \tag{41}$$

where T_i is the initial temperature before the field flip.

According to the theoretical expression of Eq. (41), the polarization loss should be only 1.5% for the 400-μT flipping field used in the experiments. This is lower than the polarization losses found in actual experiments. In fact, it is not correct to use $B=400$ μT in Eq. (41) for silver, since thermal mixing is exceedingly slow in this high field (Oja, Annila, and Takano, 1990). According to the measured mixing times in silver, thermal contact between the Zeeman and interaction reservoirs takes place in fields $B<B_m\approx 250$ μT. Use of $B=250$ μT in Eq. (41) results in a 4% polarization loss, which is close to the observed low-p limit.

The decrease in the flipping efficiency with polarization can be understood in terms of a model that accounts for the fact that the high-T approximation overestimates the heat capacity of the Zeeman system for high p (Hakonen and Vuorinen, 1992). The large scatter of the data in Fig. 23 suggests, however, that something in the experimental conditions makes the efficiency of the field reversal somewhat irreproducible. It is therefore possible that saturation of the inversion efficiency at high polarizations is not fully an intrinsic property of silver.

In rhodium the decrease in flipping efficiency was more dramatic than in silver (Hakonen, Vuorinen, and Martikainen, 1993; Vuorinen, Hakonen, Yao, and Lounasmaa, 1995). As a result, polarizations at $T<0$ were limited to $p\approx -0.60$. Field flipping and negative temperatures in rhodium will be discussed in greater detail in Sec. X.

Negative spin temperatures in silver have also been produced by applying a 180° NMR tipping pulse (Hakonen and Yin, 1991). This technique was less successful than rapid field inversion. The problem with the pulse technique is that eddy currents shield the inner parts of the sample from the tipping field, making it impossible to apply a uniform 180° pulse.

V. SUSCEPTIBILITY AND NMR DATA ON COPPER

A. Susceptibility and entropy at $B=0$

The behavior of the static susceptibility $\chi'(0)$ and entropy of a polycrystalline copper sample were investigated as a function of temperature in four series of experiments in Helsinki (Ehnholm, Ekström, Jacquinot *et al.*, 1979; Huiku and Loponen, 1982; Huiku, Jyrkkiö, and Loponen, 1983; Huiku *et al.*, 1986). Here we describe the results of measurements made between 1982 and 1986, using the same specimen. The sample consisted of eight foils, 125 μm thick and 5 mm wide; the effective mass of the specimen was 0.035 mol, i.e., about 2.5 g. The foils were welded to the first nuclear stage. After internal oxidation of magnetic impurities, the ratio $r=\tau_1(15\ \text{mT})/\tau_1(0)=2.6$ was measured. The residual resistivity ratio increased from 260 to 8500 owing to the heat treatment; the effective RRR was about 5000. Only the transverse coil geometry [see Fig. 16(b)] was employed in the measurements; the highest sensitivity of the detection system was in the y direction, perpendicular to the external field and parallel to the 5-mm side of the foil bundle.

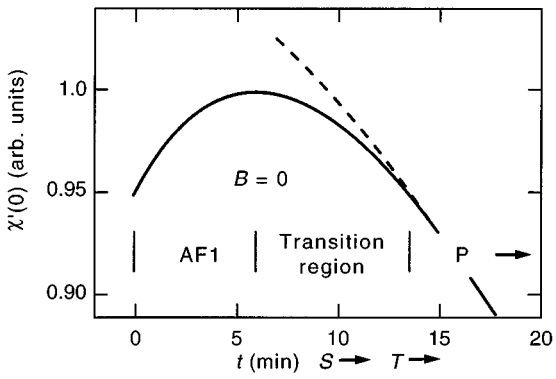

FIG. 24. Schematic behavior of the static susceptibility of copper nuclei after demagnetization to zero field. Entropy S and temperature T are increasing with time. The maximum in $\chi'(0)$ reveals a phase transition, in analogy with electronic antiferromagnets. AF1 is the ordered nuclear antiferromagnetic region, and P denotes the disordered paramagnetic phase. The metastable behavior of $\chi'(0)$, when demagnetization to zero field was started from a somewhat higher initial entropy, is shown by the dashed line. From Huiku *et al.* (1986).

The measured quantity was actually the dynamic susceptibility $\chi(f)=\chi'(f)-i\chi''(f)$ at $f=10$ Hz. At this low frequency, however, $\chi''(f)$ is so small that it can be neglected and the measurement yields the static susceptibility $\chi'(0)$ [see Sec. V.E for the frequency dependence of $\chi''(f)$]. The excitation field was typically on the order of 10 nT. An rf SQUID was used to measure the susceptibility signal as described in Sec. III.E.

The susceptibility vs time curve in zero field is schematically illustrated in Fig. 24. Following demagnetization, $\chi'(0)$ first increases and, after reaching a broad maximum, the relaxation settles roughly to an exponential decrease. The overall behavior is analogous to that observed in electronic antiferromagnets (Kittel, 1971). The experimental discovery (Huiku and Loponen, 1982) of antiferromagnetic ordering in copper was expected, because of the negative sign of the Ruderman-Kittel interaction parameter R [see discussion after Eq. (5)] and theoretical calculations based on the mean-field approximation (Kjäldman and Kurkijärvi, 1979).

A characteristic metastability accompanied the transition. When demagnetization from a 1-mT field was started with somewhat increased entropy, the suscepti-

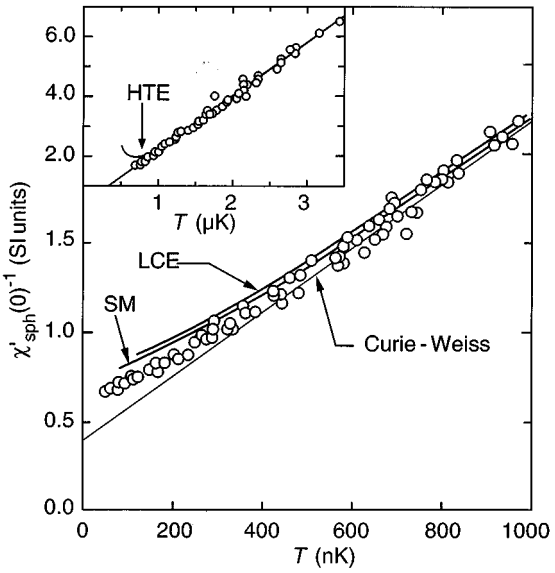

FIG. 25. Inverse of susceptibility $\chi'_{\rm sph}$ of copper, reduced for a spherical sample, as a function of temperature when $B=0$. The straight line shows the Curie-Weiss behavior. The theoretical curves refer to the high-temperature expansion (HTE, inset; Niskanen and Kurkijärvi, 1981), the spherical model (SM; Kumar *et al.*, 1980; Lindgård *et al.,* 1986), and the linked-cluster expansion (LCE; Niskanen and Kurkijärvi, 1983). Modified from Huiku *et al.* (1986).

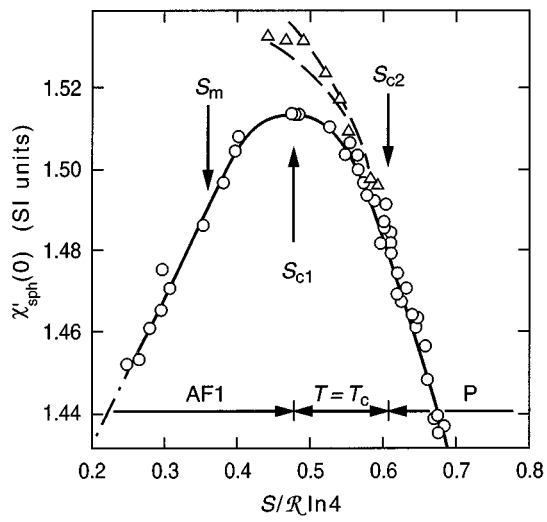

FIG. 26. Static nuclear susceptibility of copper in zero external field as a function of entropy. The data have been reduced to spherical sample geometry by using Eq. (42). The triangles were measured in a metastable state, and the circles in the antiferromagnetic phase AF1, in the paramagnetic phase P, or at $T=T_c$ in the transition region. S_{c1} and S_{c2} are the lower and upper critical entropies, respectively, for the first-order phase transition. Demagnetizations with initial entropies above S_m ended in the metastable state (dashed lines). From Huiku *et al.* (1986).

bility often did not follow the "curved" behavior but had a higher, exponentially decaying value, characteristic of the paramagnetic regime. The metastability was also accompanied by some nonadiabaticity. These effects will be discussed in Sec. V.C.

The static susceptibility of a polycrystalline copper sample as a function of temperature down to $T_{\rm N}$ was measured most extensively, and probably most accurately as well, in the work described by Huiku *et al.* (1986). Figure 25 shows the experimental $\chi'(0)^{-1}$ vs T dependency in zero field. The data have been reduced to spherical sample geometry by using the equation

$$\chi'_{\rm sph}(0)^{-1}=\chi'(0)^{-1}+1/3-D_y\,, \tag{42}$$

where $D_y=0.09$ is the demagnetization factor of the specimen. The inset shows the susceptibility at high T, together with a calculation using the high-temperature expansion (HTE; Niskanen and Kurkijärvi, 1981). The data obey the Curie-Weiss law $1/\chi'=T/C+\Delta$ down to 500 nK, with C=554 nK and $\Theta=-C\Delta=-215$ nK. The Ruderman-Kittel exchange parameter then has the value $R=-\Delta=-0.39$. This agrees well with $R=-0.42\pm0.05$, obtained from NMR measurements (Ekström *et al.*, 1979). Below about 500 nK, the experimental points depart from the high-temperature Curie-Weiss behavior. The deviation can be attributed to spin fluctuations (Kumar *et al.*, 1980). A more detailed comparison with the various theoretical calculations is deferred to Sec. XV.C.4.

The static nuclear susceptibility of copper as a function of entropy has been plotted in Fig. 26. The relation between $\chi'(0)$ and S was found simply by a series of demagnetizations to $B=0$. It was observed that a demagnetization ends in a metastable state when the initial entropy, before the final field sweep down, is in the range between $(0.36\pm0.02)\mathcal{R}\ln4$ and $(0.61\pm0.03)\mathcal{R}\ln4$. Above $S_i=0.61\mathcal{R}\ln4$, the relaxation of $\chi'(0)$ is exponential and the demagnetization adiabatic, which are characteristic features of the paramagnetic state. Therefore the higher critical entropy for the first-order transition in zero field is $S_{c2}=(0.61\pm0.03)\mathcal{R}\ln4$.

The lower critical entropy S_{c1} can be found by using the fact that the temperature is constant in the transition region and by assuming that the maximum of $\chi'(0)$ is obtained in the antiferromagnetic state immediately below T_c. The assumption is supported by the observation that electronic antiferromagnets, with an fcc lattice, usually have their transition points very close to the maximum of $\chi'(0)$ (Domb and Miedema, 1964). Therefore, since the paramagnetic $\chi'(0)$ immediately above T_c is smaller than the antiferromagnetic $\chi'(0)$ at T_c, the maximum of the $\chi'(0)$ vs S curve (see Fig. 26) corresponds to the low-entropy end of the coexistence region. This gives $S_{c1}=(0.48\pm0.03)\mathcal{R}\ln4$.

In Fig. 27 the entropy vs temperature curve is shown for copper in the paramagnetic region below 1 μK. The horizontal arrow pointing to the $S/\mathcal{R}\ln4$ axis indicates the experimentally determined critical entropy $S_{c2}=0.61\mathcal{R}\ln4$ for spontaneous nuclear ordering in zero field.

Comparisons with theory are also shown in Fig. 27. High-temperature expansions (HTE), with fifth-degree

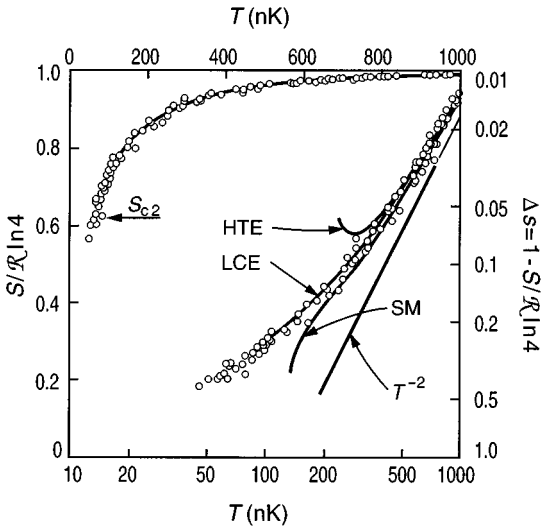

FIG. 27. Nuclear-spin entropy of copper. The horizontal axis at the bottom and the vertical axis on the right show T and $\Delta s = 1 - S/\mathcal{R}$ ln4, respectively, on a logarithmic scale for experimental points at the lowest temperatures. The curves show the results of theoretical calculations: HTE, high-temperature expansion; LCE, linked-cluster expansion; SM, spherical model (see text). The linear scales at top and at left refer to the uppermost curve. Modified from Huiku *et al.* (1986).

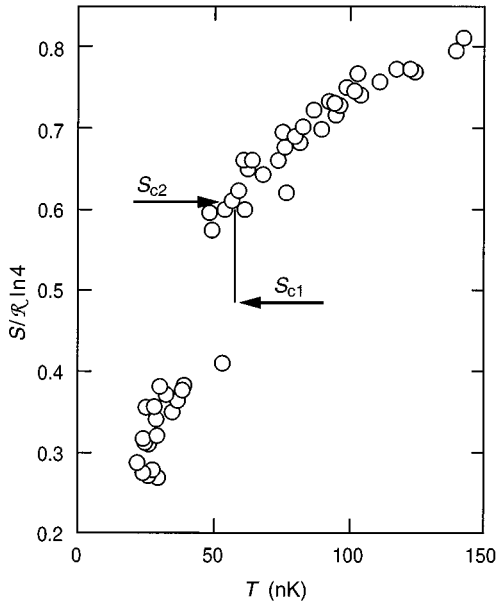

FIG. 28. Entropy of copper in zero external magnetic field as a function of temperature below 150 nK. At the time, $T_c = 58$ nK was the lowest transition temperature ever observed or measured. The vertical line was drawn to emphasize the first-order transition. The critical entropies are indicated by arrows. From Huiku *et al.* (1986).

terms in $1/T$ included, can describe the experimental data with reasonable accuracy down to 400 nK (Niskanen and Kurkijärvi, 1981). The agreement improves considerably when the spherical model (SM) is used (Kumar *et al.*, 1980; Kjäldman *et al.*, 1981). However, in view of the good agreement between the measured $\chi'(0)$ and the SM prediction, discrepancies for entropy at the lowest temperatures are puzzling. The experimental S vs T data agree best with calculations using the linked-cluster expansion (LCE) technique (Niskanen and Kurkijärvi, 1983).

In Fig. 28 the entropy curve for copper is illustrated below $T = 150$ nK. The vertical line emphasizes the phase change at $T_N = 58$ nK. The latent heat of the transition in zero field is $L = T_N(S_{c2} - S_{c1}) = 0.09$ μJ/mole. The experimental points show the rapid reduction of entropy below T_N.

B. Thermometry

Although the techniques for measuring the temperature T of copper nuclei were essentially the same as those described in Sec. IV, there were two important differences. As the sample had a very high electrical conductivity, it was necessary to give the heat pulse $\Delta Q = \pi f B_1^2 \chi''(f) \Delta t / \mu_0$ using an ac magnetic field of low frequency to ensure full penetration. Direct measurement of $\chi''(f)$ at $f = 50$ Hz was not feasible, however, owing to the small signal at low frequencies. Therefore $\chi''(f)$ was deduced from the measured $\chi'(0)$ using a relationship between $\chi''(f{=}50\text{ Hz})$ and $\chi'(0)$ that had been established from earlier NMR measurements by Ehnholm *et al.* (1980). It was estimated that the error caused by this approach did not exceed 10%. For the data in the ordered state, however, the error in T can be large since the shape of the NMR signal changes (see Fig. 32) and hence also the relationship between $\chi''(f = 50\text{ Hz})$ and $\chi'(0)$.

Another special problem of measuring T in copper was associated with the data in the ordered phase. It was observed that demagnetization to zero field resulted in an entropy increase, to be discussed in the following section. To overcome the difficulty, T was determined in the ordered state by using $\chi'(0)$ as the thermodynamic parameter and writing $T = (\delta Q/\delta\chi)(\delta S/\delta\chi)$ with $\chi = \chi'(0)$. The absolute temperature could then be measured in two steps. First, $\delta Q/\delta\chi$ was found by applying several heat pulses during the warmup at zero field. Second, S as a function of susceptibility was measured by sweeping the field at different stages of the warmup in zero field, i.e., at different values of $\chi'(0)$ up to 1 mT to monitor the polarization. The procedure was feasible as the entropy was found to increase only during a downward sweep. As a result, thermometry at $B = 0$ was possible although the downward sweep was nonadiabatic.

A drawback of using $\chi'(0)$ as a thermodynamic parameter is that the method loses sensitivity when $\chi'(0)$ changes only a little upon warming. This is the case near the transition when $\chi'(0)$ reaches its maximum value.

Thermometry was based on runs in which the demagnetization to zero field was performed for an initial entropy lower than $0.36\mathcal{R}$ ln4 to avoid problems associated with metastable states (see below).

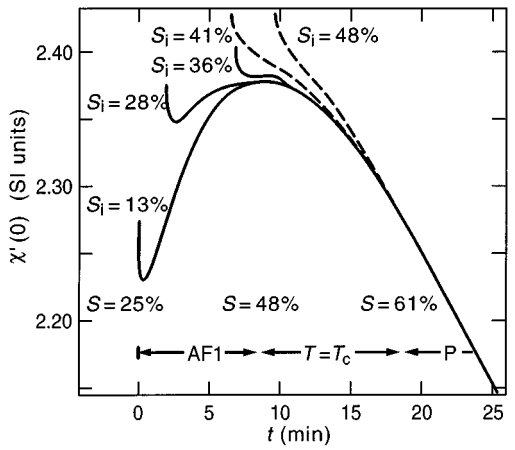

FIG. 29. Static susceptibility $\chi'(0)$ of nuclear spins in copper as a function of time after final demagnetization to zero field, performed from different initial entropies S_i. Here S is the final entropy in zero field, given as percentages of $\mathcal{R}$ ln4. Dashed lines indicate metastable behavior. The susceptibility data correspond to the demagnetization factor $D_y = 0.09$. From Huiku *et al.* (1986).

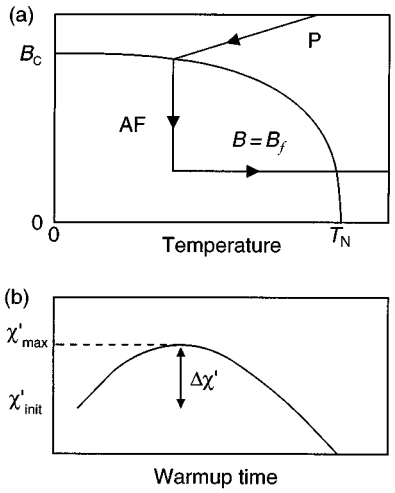

FIG. 30. Adiabatic demagnetization into an antiferromagnetic state: (a) Schematic illustration. The demagnetization is stopped at a final field $B = B_f$, and the static susceptibility χ' is recorded during warmup. (b) Definition of the three quantities important for characterizing the χ' data.

C. Metastability and nonadiabatic phenomena

In measurements on a polycrystalline copper sample (Huiku, Jyrkkiö, and Loponen, 1983), a characteristic metastability was observed after the magnetic-field sweep from $B = 1$ mT to zero. The behavior of $\chi'(0)$ after such a sweep is illustrated in Fig. 29 for several values of the initial entropy S_i at $B = 1$ mT. A metastability was evident when S_i was larger than $0.36\mathcal{R}$ ln4 but smaller than $0.61\mathcal{R}$ ln4. Then $\chi'(0)$ followed the behavior illustrated with the dashed lines. The static susceptibility was always larger than $\chi'(0)$ measured with initial entropies lower than $S_{c2} = 0.36\mathcal{R}$ ln4, which was believed to correspond to the equilibrium behavior.

A large irreversible entropy increase was observed, as well, after demagnetization from S_i lower than $0.36\mathcal{R}$ ln4. When B was swept to zero and then, after a few tens of seconds, back to 1 mT, an entropy increase of $\Delta S = 0.12\mathcal{R}$ ln4 was observed. The nonadiabaticity was constant within the experimental accuracy (0.5% of ΔS). The reverse sweep upward to 1 mT was adiabatic. Thus $\Delta S = 0.12\mathcal{R}$ ln4 was added to all S_i values below $0.36\mathcal{R}$ ln4 in order to obtain the actual spin entropy after demagnetization. In experiments during which metastable states were reached, ΔS was always smaller than 3%, and it vanished at $0.61\mathcal{R}$ ln4.

The time scale for the irreversibility to occur was on the order of seconds; with a stay of 2 s at $B = 0$, the measured nonadiabaticity was only $0.06\mathcal{R}$ ln4. It was suggested that the irreversibility is intimately associated with the ordering process. The minimum susceptibility after demagnetization was reached approximately 15 s after the external field had been reduced to zero (see Fig. 29). The behavior of $\chi'(0)$ and the development of the entropy loss both reflect a nucleation of the ordered phase from the supercooled nonequilibrium state.

Subsequent susceptibility and neutron-diffraction measurements on a single-crystal specimen have given more insight into the process by which irreversibility occurs. The entropy increase $\Delta S = 0.12\mathcal{R}$ ln4 was found to occur in a field around 0.1 mT (Huiku, Jyrkkiö *et al.*, 1984; Huiku *et al.*, 1986; Annila *et al.*, 1992), where a phase transition also takes place from the antiferromagnetic phase AF2 to AF1; see the phase diagram of Fig. 1. Neutron-diffraction experiments (Annila *et al.*, 1990) showed that in this region the high-field type-I order transforms into the $(0\,\frac{2}{3}\,\frac{2}{3})$ order. It was also directly seen that the ordering process is associated with kinetic phenomena within a time scale on the order of seconds. In the single-crystal experiments no metastable states were observed. Therefore it was concluded that grain boundaries in a polycrystalline sample slow down the nucleation of the ordered state, but that at entropies below $0.36\mathcal{R}$ ln4 a forced nucleation has to take place owing to the absence of metastability.

D. Field effects on a polycrystalline sample

The time dependence of the static susceptibility was also investigated by varying the external field at which the final demagnetization ended (Huiku and Loponen, 1982). The scheme for these measurements is schematically illustrated in Fig. 30(a). According to the mean-field theory for antiferromagnetic type-I order (see Sec. XV.B.5), adiabatic demagnetization in the ordered state follows a vertical path in the B-T plane and therefore does not produce any further cooling.

The susceptibility was recorded in the final field $B = B_f$ during warmup. Figure 30(b) illustrates the three quantities used to analyze the data: the susceptibility immediately after demagnetization to the final field, $\chi'_{\rm init}$, the maximum susceptibility $\chi'_{\rm max}$, and the difference

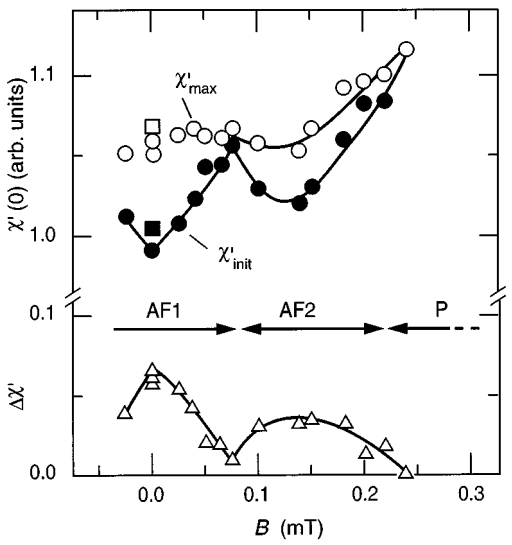

FIG. 31. Initial susceptibility $\chi'_{\rm init}=\chi'(0)$ at $t=0$, the maximum susceptibility $\chi'_{\rm max}$, and the difference $\Delta\chi'=\chi'_{\rm max}-\chi'_{\rm init}$ as functions of the external field B in copper (Huiku and Loponen, 1982). The ordered regions AF1 and AF2 and the paramagnetic phase P are indicated. From Huiku *et al.* (1986).

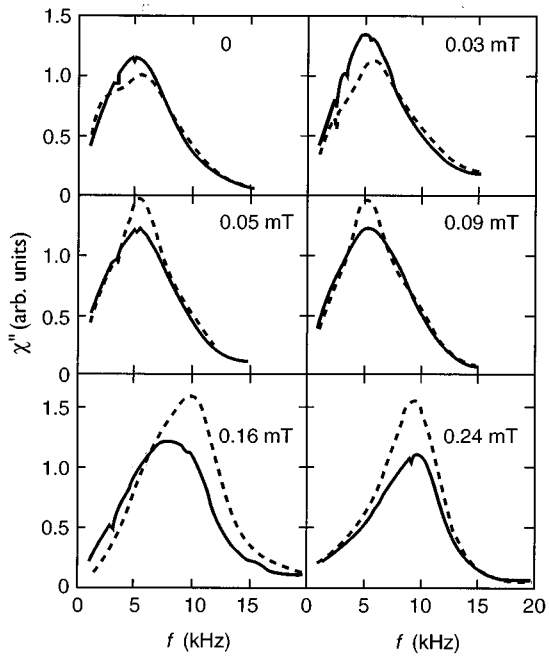

FIG. 32. NMR absorption line shapes of the dynamic susceptibility $\chi''(f)$ for copper in several external magnetic fields: Solid curves, paramagnetic regions; dashed curves, antiferromagnetic regions. From Huiku *et al.* (1986).

$\Delta\chi'=\chi'_{\rm max}-\chi'_{\rm init}$. In the beginning of the warmup, before reaching the state with maximum susceptibility, the nuclei were assumed to be in the antiferromagnetic state.

The measured data are shown in Fig. 31. In low fields the increase of $\chi'(0)$ is largest. As a function of the final field after demagnetization, $\Delta\chi'$ first decreases until, at about $B=0.08$ mT, a minimum is reached. Around $B=0.15$ mT, $\Delta\chi'$ has again grown to about half of the value observed when $B=0$. At still higher fields the initial increase decreases until, at $B=0.24$ mT, $\Delta\chi'$ finally disappears.

The anomaly at $B=0.08$ mT indicates a magnetic transition between two ordered states, which were named AFl and AF2 (Huiku and Loponen, 1982). Subsequent experiments (Huiku, Jyrkkiö *et al.*, 1984) on a single-crystal specimen, during which the longitudinal susceptibility was measured as well, revealed a third antiferromagnetic phase, AF3. Recent neutron-diffraction experiments (Annila *et al.*, 1992), also performed on a single-crystal specimen, have further shown that the antiferromagnetic ordering vectors, and hence also the spin structures, strongly depend on the alignment of the external magnetic field with respect to the crystalline axes. It is therefore remarkable that the data on a polycrystalline sample do not smear out the evidence for phase changes, especially at the AF1 ↔ AF2 transition.

E. NMR lineshapes of the ordered spin structures

The specimen employed in the NMR experiments (Huiku *et al.*, 1986) was made from the same 125-μm thick Marz-grade copper foil that was used in the measurements of static susceptibility. The foils were first selectively oxidized and then rolled to their final thickness, varying from 20 to 30 μm. The final sample consisted of 36 foil pieces. For this specimen the values $r=\tau_1(15\,{\rm mT})/\tau_1(0)=4$ and $\tau_1(0)=70$ min were measured, which are reasonably good for a sample made of thin foils. Again, only the transverse coil system [see Fig. 16(b)] was employed in the experiments. NMR spectra were measured using the technique described in Sec. III.E. During the warmup period, typically 8 to 10 curves were recorded before the sample entered the transition region.

The absorptive part of the dynamic susceptibility is plotted as a function of frequency in Fig. 32 at several final fields. The dashed curves show the lineshape just after demagnetization, i.e., the NMR signal in the antiferromagnetic region. The solid curves were measured 8–10 min after the end of demagnetization; they thus corrrespond to high polarization in the paramagnetic region.

It was found that the antiferromagnetic NMR line (AFL) differed at $B=0$ in two ways from the paramagnetic line (PL): At about $f=1.5$ kHz, the AFL was clearly enhanced, whereas from 3 to 7 kHz it was again smaller than the PL. The latter feature is responsible for the fact that the static susceptibility $\chi'(0)$, obtained from $\chi''(f)$ through the Kramers-Kronig relation [see Eq. (27)], increases with time (and temperature). This was taken as the signature of antiferromagnetic ordering in the measurements of static susceptibility. The increased $\chi''(f)$ around $f=1.5$ kHz further supports this conclusion, since antiferromagnetic ordering is expected to change the lineshape of the dynamic susceptibility. During warmup, the AFL smoothly approaches the PL.

Qualitatively similar lineshapes were obtained at $B=0.03$ mT.

At $B=0.05$ mT the appearance of the AFL changes. Now the absorption in the antiferromagnetic state is considerably stronger between 3 and 7 kHz than in the paramagnetic region. Furthermore, the AFL resembles the PL even immediately after demagnetization. In the beginning of the warmup, χ''(5 kHz) is almost 1.5 times larger than in zero field.

An examination of the dashed line at $B=0.09$ mT shows interesting features: χ''(10 kHz) is enhanced and, at lower frequencies, $\chi''(f)$ is small, which again indicates that the static susceptibility is rising as a function of time. At $B=0.16$ mT, the increase in χ''(10 kHz) exceeds that of the paramagnetic line. During warmup, the AFL shifts towards the PL. The absorption at low frequencies is again small. At $B=0.24$ mT, the lineshape does not change at low entropies. This shows that the spin system is paramagnetic immediately after demagnetization.

It is also worth noting that the paramagnetic "background" is large for all NMR lines measured in the antiferromagnetic phase and that the changes during warmup are relatively small. However, this is in agreement with the fact that the increase in the static susceptibility is small, too. A more thorough discussion of the NMR lineshapes at different fields is given in the original publication (Huiku *et al.*, 1986). It was concluded that the observed changes are strong evidence for magnetic ordering in copper nuclei.

Recent theoretical calculations by Heinilä and Oja (1995) have reproduced quite successfully the observed NMR lineshapes of copper in zero field (see Sec. XV.E and Fig. 121 below).

F. Susceptibility data of a single-crystal specimen

To obtain more information about the ordered nuclear-spin structures in copper, the Helsinki group conducted experiments on a single-crystal sample by again investigating the static susceptibility (Huiku, Jyrkkiö *et al.*, 1984; Huiku *et al.*, 1986). In contrast to all earlier work, $\chi'(0)$ was now separately measured in the three Cartesian directions x, y, and z. In addition to the excitation and pickup coils in the longitudinal z direction [see Fig. 16(a)], there were saddle-shaped excitation coils in both the x and y directions [see Fig. 16(b)]. The same saddle-shaped pickup coil was used to monitor the response in the latter two directions. The transverse (x,y) and longitudinal (z) signals could be measured during the same run.

The specimen was a natural copper single crystal of dimensions $0.5\times5\times20$ mm^3 along the x, y, and z axes, respectively. The sample material was of 99.99% purity, with the following magnetic contaminants: Mn<0.1 ppm, Cr=2 ppm, Ni<0.4 ppm, and Fe=3.0 ppm. After oxidation for 45 h, the residual resistance ratio (RRR) was 1500. The single crystal was again connected to the first nuclear stage by diffusion welding. For this specimen, $r=\tau_1(15\text{ mT})/\tau_1(0)=2.8$, which shows that all impurities were oxidized. Thermal contact was found to be excellent, and one could reach $T_e=50$ μK in the specimen. By x-ray-diffraction measurements it was found that the cubic (1 0 0) crystal axis was about 4° above the xy plane and 13° off of the x axis and that the (0 0 1) axis was about 8° off of the z axis. As the external field was aligned along the z direction, **B** was also aligned relatively accurately along the (0 0 1) crystalline axis.

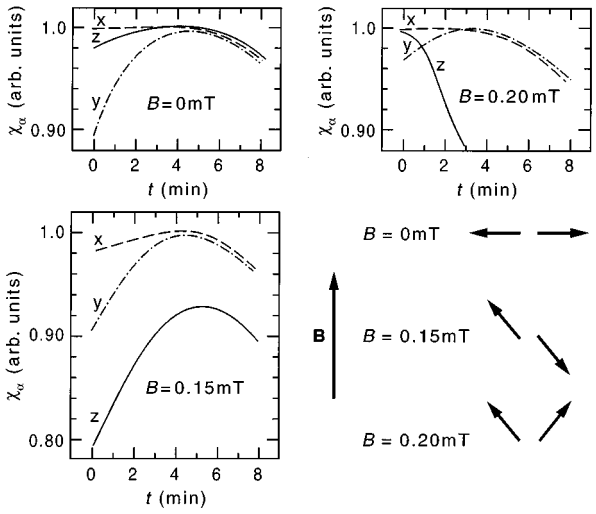

FIG. 33. The susceptibility χ_α of a copper single crystal along the three Cartesian directions ($\alpha=x,y,z$), as a function of time and in three external fields, $B=0$, 0.15, and 0.20 mT. These characteristically different behaviors indicate three antiferromagnetically ordered regions in the nuclear-spin system of copper. The suggested spin arrangements, based on an assumption of two sublattices, are also shown. From Huiku *et al.* (1986).

In order to compare the susceptibilities in the three mutually orthogonal directions, Huiku and co-authors had to apply a shape correction for the internal fields [see Eq. (34)] to the measured $\chi'_\alpha(0)$ ($\alpha=x,y,z$), using

$$\chi'_{\text{sph},\alpha}(0)^{-1}=\chi'_\alpha(0)^{-1}+(L-D_i+R)\,, \tag{43}$$

where $\chi'_{\text{sph},\alpha}(0)$ is the susceptibility related to a spherical sample. This correction reduces the measured $\chi'_\alpha(0)$ to the susceptibility of a virtual spin system with no molecular fields arising from spin-spin interactions. In the rest of this section, we use the shorter notation $\chi'_{\text{sph},\alpha}(0)=\chi_\alpha$. D_i was estimated from the dimensions of the specimen, assuming an ellipsoid of similar shape to that of the sample.

In Fig. 33 the time dependence of χ_α is shown for the x, y, and z directions at $B=0$, 0.15, and 0.20 mT, respectively; these characteristic plots correspond to different ordered regions. The existence of the third antiferromagnetic phase, AF3, is based on the behavior of the longitudinal susceptibility, which now was measured for the first time. This phase was found in fields above 0.18 mT.

In zero external field, a clear increase of χ_α was observed only in the y direction; this effect is about 10%. Surprisingly, the other transverse susceptibility, χ_x,

shows a long plateau, whereas a small increase in χ_z was seen. For $B=0.15$ mT, the initial value of the longitudinal susceptibility was roughly 20% smaller than in zero field, and χ_z increased at the beginning of the warmup by almost 15%. The increase in the y direction was not as great, but roughly the same as when $B=0$. Again, χ_x stayed almost constant for the first 5 min. In the last plot, with $B=0.20$ mT, a characteristic change can be seen for χ_z in comparison with the behavior observed at $B=0.15$ mT. Now χ_z decreases all the time, whereas an increase and a plateau for χ_y and χ_x, respectively, were found in the transverse directions.

Tentative suggestions for the spin arrangements in these phases were made by using a simple two-sublattice model and an analogy with electronic antiferromagnets (Huiku, Jyrkkiö *et al.*, 1984): When $\chi'(0)$ is measured perpendicular to the sublattice magnetization, the susceptibility stays roughly constant below T_c, whereas parallel to the sublattice magnetization, $\chi'(0)$ approaches zero as $T\rightarrow 0$ (de Klerk, 1956; Kittel, 1971). In the phase AF1 ($B=0$), the staggered magnetization is then mainly along the y axis. In the second antiferromagnetic state, AF2 ($B=0.15$ mT), the sublattice magnetization has its largest component in the z direction and a smaller component in the y direction. In AF3, the spins most probably are leaning toward $\mathbf{B}=B\mathbf{z}$. In contrast to the "paramagnetic" behavior of χ_z, a small increase in χ_y indicates a staggered magnetization parallel to y in this phase. These suggestions for the antiferromagnetic structures are schematically illustrated in Fig. 33.

More of the single-crystal data are illustrated in Fig. 34, where the net rise of susceptibility, $\Delta\chi_\alpha=\chi_\alpha^{\max}-\chi_\alpha^{\text{init}}$, has been plotted as a function of the external field at which the final demagnetization was stopped (Huiku *et al.*, 1986). In low magnetic fields, $\Delta\chi_y$ is roughly 10% of $\chi_y^{\max}$; the value of $\Delta\chi_y$ drops to about 2% for fields between 0.06 and 0.10 mT. From $B=0.13$ to 0.16 mT, $\Delta\chi_y$ is almost as large as in zero field. After $B=0.16$ mT, a small sudden drop can be seen. With increasing field, $\Delta\chi_y$ decreases to zero at about $B=0.25$ mT.

Data in the x direction are in sharp contrast: Over most of the region from $B=0$ to 0.25 mT, $\Delta\chi_x=0$. It is hard to know whether the increase around $B=0.14$ mT, supported essentially by one data point in Fig. 34, is real or not. The large susceptibility anisotropy between the x and y directions is puzzling. It was suggested (Huiku *et al.*, 1986) that the effect is caused by the slab shape of the specimen, which is sensed by the anisotropic dipolar interaction.

The data in the longitudinal geometry, illustrated in the lower part of Fig. 34, show that $\Delta\chi_z$ is small below 0.08 mT. In higher fields $\Delta\chi_z$ increases rapidly and is roughly 12% of $\chi_z^{\max}$ between $B=0.11$ and 0.16 mT. In still higher fields, $\Delta\chi_z$ decreases quickly and vanishes at $B=0.20$ mT, in contrast to $\Delta\chi_y$, which disappears only at $B=0.25$ mT.

From the results illustrated in Fig. 34 and from a careful analysis of the original data (Huiku *et al.*, 1986), the following picture emerges (see Fig. 1): The first antiferromagnetic phase, AF1, is stable below $B=0.06$ mT. Between 0.06 and 0.11 mT there is a transition region. The second phase, AF2, is stable from $B=0.11$ mT to $B=0.16$ mT. The transition from AF2 to AF3, between 0.16 and 0.18 mT, is marked by a large change in $\Delta\chi_z$ and by a small jump in $\Delta\chi_y$. The AF3 phase exists above $B=0.18$ mT and below $B=0.25$ mT. The transition to the paramagnetic state proceeds by tilting the spins more and more toward **B** until, at the critical field $B_c=0.25$ mT, AF3 and the paramagnetic phase P are the same.

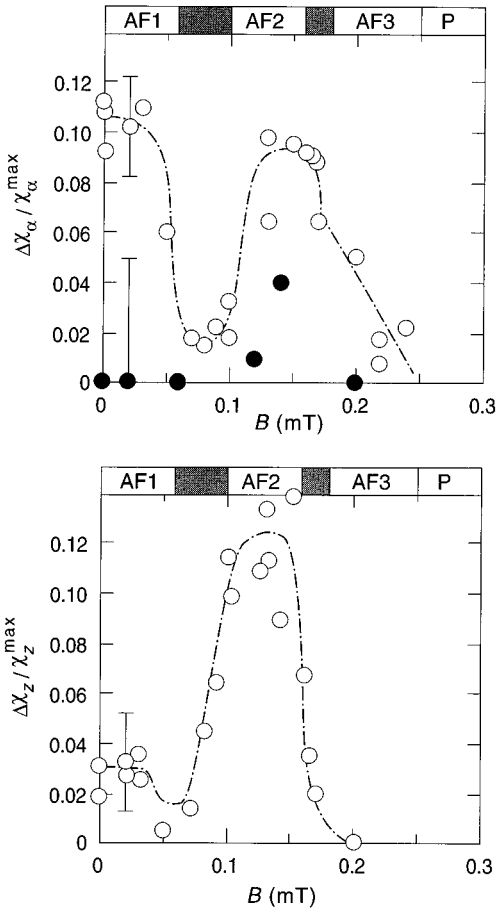

FIG. 34. Normalized net rise in the susceptibility of copper, $\Delta\chi_\alpha/\chi_\alpha^{\max}$, plotted as a function of the external field $\mathbf{B}=B\mathbf{z}$; $\chi_\alpha^{\max}$ is the maximum susceptibility. Data for the transverse directions are plotted in the upper frame [$\alpha=x$ (●); $\alpha=y$ (○)], and for the longitudinal z direction below. From Huiku *et al.* (1986).

The interpretation of the susceptibility data and the existence of the AF2 phase between AF1 and AF3 show that all the ordered spin structures have different symmetries, and therefore we are led to suggest that the transitions between them are of first order. Between AF1 and AF2 this conclusion is supported by the large nonadiabaticity, $\Delta S=0.12\mathcal{R}$ ln4, and by the metastabilities, discussed in the previous section. The first-order nature of the transition between AF2 and AF3 is based on the rapid change in $\Delta\chi_z$ and on an analogy with spin-

flop transitions in electronic systems (De Klerk, 1956). The transition from AF3 to P is of second order.

G. Magnetization

Magnetization has not been measured directly in the course of the Helsinki studies on copper. In principle, the magnetization **M** can be calculated by integrating the measured longitudinal susceptibility over the field B. Such a procedure was first performed by Annila *et al.* (1992) to analyze their neutron-diffraction data. It was necessary to know **M** to be able to correct for the demagnetization field, which is given by the shape-dependent demagnetization tensor $\underline{D}$ and **M**, viz.,

$$\mathbf{B}=\mathbf{B}_e+\mathbf{B}_d=\mathbf{B}_e-\mu_0\underline{D}\mathbf{M}. \tag{44}$$

Here **B** is the magnetic field in the sample, and $\mathbf{B}_e$ is the external field. In the earlier susceptibility measurements on copper, $\mathbf{B}_e$ was always applied along the long axis of the sample, i.e., the z axis. In this case, $\mathbf{B}_d$ vanishes because $\mathbf{M}\|\mathbf{z}$ and $D_{zz}\approx 0$. Therefore $\mathbf{B}=\mathbf{B}_e$. In the work of Annila *et al.* (1992), however, $\mathbf{B}_e$ was in some measurements applied almost along the hard direction of magnetization, which corresponds to a large demagnetizing factor (see Fig. 53 below for the geometry), so that B_d was even larger than B_e.

Magnetization for a certain field and entropy can be calculated by remembering that the measured χ_L is the adiabatic susceptibility $\mu_0(dM/dB)_S$ and by assuming that the demagnetization to zero field takes place at constant entropy. To obtain, for example, $M(B)$ immediately after demagnetization, one can integrate χ_L measured at $t=0$,

$$M(B)=\int_0^{B_c}\chi_L(B,t=0)dB/\mu_0\,. \tag{45}$$

The demagnetization to $B=0$ is not, however, adiabatic because of the entropy increase in fields around 0.1 mT. This makes the integration somewhat inaccurate.

Annila *et al.* (1992), nevertheless, used Eq. (45) to obtain an approximate M. A particularly interesting quantity is the magnetization at the critical field immediately after demagnetization. The χ_L data, calibrated at $B=0$ using the results of Huiku *et al.* (1986), yield $M=0.57M_{\rm sat}$ at $B=B_c=0.25$ mT. This value may seem small in view of the fact that the mean-field theory predicts $M=0.9M_{\rm sat}$ for the estimated entropy after demagnetization. The discrepancy can be explained by quantum effects and/or substantial antiferromagnetic short-range correlations.

The actual model used by Annila *et al.* (1992) to correct for $\mathbf{B}_d$ was, in fact, simpler than that obtained from Eq. (45). In the whole ordered region it was assumed that

$$\mathbf{M}=\chi\mathbf{B}/\mu_0\,, \tag{46}$$

with $\chi=3.1$. This approximation seems reasonable because the variation in $\chi_L(B)$, measured immediately after demagnetization, is only 14%. Furthermore, the mean-field theory for a type-I spin arrangement also predicts a temperature- and field-independent susceptibility in the ordered region (Kumar *et al.,* 1986). Equation (46) with $\chi=3.1$ gives $M=0.61M_{\rm sat}$ at B_c in good agreement with the above value obtained by integration. Further support for this model is given by neutron-diffraction measurements in which the intensity of the (1 0 0) Bragg reflection was measured in two symmetrically equivalent directions, namely, for **B** along the [011] and [01 1] axes. It was observed that the behavior of the (1 0 0) intensity as a function of B was similar in both directions, in spite of the different demagnetization corrections D=0.83 and 0, respectively [see Figs. 57(a) and (b)]. It was concluded that Eq. (46) gives **M** correctly within 15%.

H. Entropy diagram

By studying the susceptibilities χ_y and χ_z as functions of the entropy S_i just prior to the final demagnetization, it was possible to determine the magnetic field vs entropy diagram of the nuclear-spin system in copper (Huiku *et al.*, 1986). S_i was controlled by varying the demagnetization procedure: One simply had to wait for different lengths of time at $B=1$ mT before sweeping the magnetic field down to its final value; S_i could be calculated from τ_1 and the waiting time.

The B-S phase diagram for the nuclear-spin system in copper was already illustrated in Fig. 1; it was constructed by demagnetizing from different initial values of entropy, thus moving vertically down, and then by allowing the specimen to warm up, thus advancing horizontally to the right while the susceptibility was being measured. The shadowed areas indicate regions where one characteristic behavior of susceptibility changes to another because a first-order phase change is proceeding in this area. During transitions, neighboring phases coexist as macroscopic domains. The direction of the external field deviated 8° from the [001] crystalline axis. The critical field $B_c=0.27$ mT can be found by extrapolating the AF3 – P boundary to $S=0$; the value of B_c is slightly higher than that deduced in Sec. V.D.

The relation between entropy and temperature was not determined for the single-crystal specimen. According to data on the polycrystalline sample, however, the transition region in zero field corresponds to $T_c=58\pm 10$ nK (see Fig. 27).

VI. EXPERIMENTAL TECHNIQUES OF NEUTRON-DIFFRACTION MEASUREMENTS

A. Setup for neutron-diffraction experiments

The neutron-diffraction experiments on copper (Jyrkkiö *et al.*, 1989; Annila *et al.*, 1992) were carried out in the guide hall adjacent to the DR-3 reactor at the Risø National Laboratory in Denmark. From a cold source, a beam of long-wavelength neutrons was transmitted via a curved guide to the TAS-8 double-axis diffractometer,

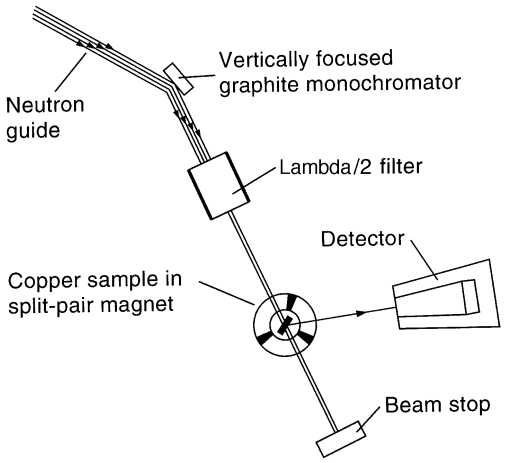

FIG. 35. Schematic top view of the neutron-diffraction setup at Risø. The cryostat can be rotated on the spectrometer turntable, and the detector can be positioned at the desired scattering angle. From Jyrkkiö *et al.* (1989).

constructed at the Hahn-Meitner Institute in Berlin. This arrangement reduced mechanical vibrations as well as electrical noise, and it provided a clean beam, free from γ rays and fast neutrons. The background radiation in the experimental hall was also very low. Further attenuation was obtained by decoupling the cryostat from the building and the pumping systems by effective vibration isolators and by employing extra electrical shields and filters for all current lines entering the refrigerator (see Sec. VI.B).

The diffractometer could be used in a polarized or an unpolarized mode. The setup for polarized neutrons (Jyrkkiö, Huiku, Clausen *et al.*, 1988) will be discussed in Sec. VI.D. Figure 35 shows schematically the experimental arrangement for unpolarized neutrons.

A graphite monochromator was used to select the desired wavelength from the neutron beam. Usually λ= 4.7 Å was chosen, but sometimes λ=2.4 Å was used. The flux at 2.4 Å was about 8×10^5 neutrons/cm^2 s, deduced from activation of a gold foil at the sample position.

In addition to the fundamental wavelength, the beam reflected from the monochromator contains neutrons with wavelengths $\lambda/2$, $\lambda/3$, etc. To obtain a fully monochromatic beam in an actual experiment, the higher-order contaminations were filtered out. A pyrolite graphite filter at λ=2.4 Å and a liquid-nitrogen-cooled BeO filter at λ=4.7 Å were employed. The higher-order reflections were useful, however, in obtaining the correct orientation of the sample and the detector before an actual experiment. For example, the lattice reflection (2 0 0) for the wavelength $\lambda/2$ is found at the same position as the antiferromagnetic Bragg reflection (1 0 0) for the wavelength λ. For this reason, an effective filtering of the $\lambda/2$ neutrons is needed during the ordering experiment.

In the first measurements, a single detector was used. During later experiments a horizontal, position-sensitive linear detector was employed as well. This was used to study the profile of the Bragg peak, since mechanical movements of the spectrometer during a lineshape scan might have heated the sample. Later it was found, however, that conventional scanning of reciprocal space can be used even when the nuclei are in the ordered state below T_N=58 nK (Annila *et al.*, 1990). Magnetic fields on the sample and on the first nuclear stage are then low and vibrational heating due to eddy currents is small. Scanning shortened the time spent in the ordered state by about 40% compared with experiments without mechanical movements. This reduction in the available measurement time was large but acceptable.

Both the incoming and scattered beams were effectively masked, using boron-containing plastic plates to minimize the background scattering seen by the detector. With a scattering angle close to 90°, the background count for the single detector was about 0.3 neutrons/s and for the linear detector about 0.7 neutrons/s.

B. Risø cryostat

The design of the Risø cryostat (Jyrkkiö *et al.*, 1989) is illustrated in Fig. 36. The apparatus consists again of a high-power dilution refrigerator and two copper nuclear stages, working in series. The operating principles are basically the same as for the Helsinki apparatus, described in Sec. III.B. To stop vibrations from entering the cryogenic system, the spectrometer was decoupled from the floor by spring-type vibration isolators.

The Risø cryostat was standing on a turnable spectrometer so that the sample could be oriented as desired. The surroundings of the specimen were designed to give maximum openings for the incoming and scattered neutron beams, with only minor attenuation. Therefore the solenoid used for demagnetizing the sample was a split-pair superconducting coil, producing 4.6 T at its center. The two halves of the magnet were separated by three aluminum wedges that covered about 45° of the scattering plane. The field of the split-pair magnet was asymmetric in such a way that there were no field-free volumes in the beam region. This is important for experiments with polarized neutrons, since a zero-field region would cause depolarization of the neutron beam.

The commercial Oxford 600 dilution unit (Oxford Instruments, Eynsham, OX8 1TL, England) was equipped with a continuously filling condenser. All pumping lines connected to the top of the cryostat were flexible to avoid transmission of vibrations to the apparatus. The first nuclear cooling stage was again made of a bulk piece of copper with vertical slits. Its weight was 2.5 kg but the effective mass in the 8-T field of the demagnetization magnet was only 1.0 kg, since large sections of the nuclear stage were located in the field-compensated regions. The heat switch, somewhat different from that in the Helsinki machine, was constructed of zinc foils having pressed contacts to copper "fingers."

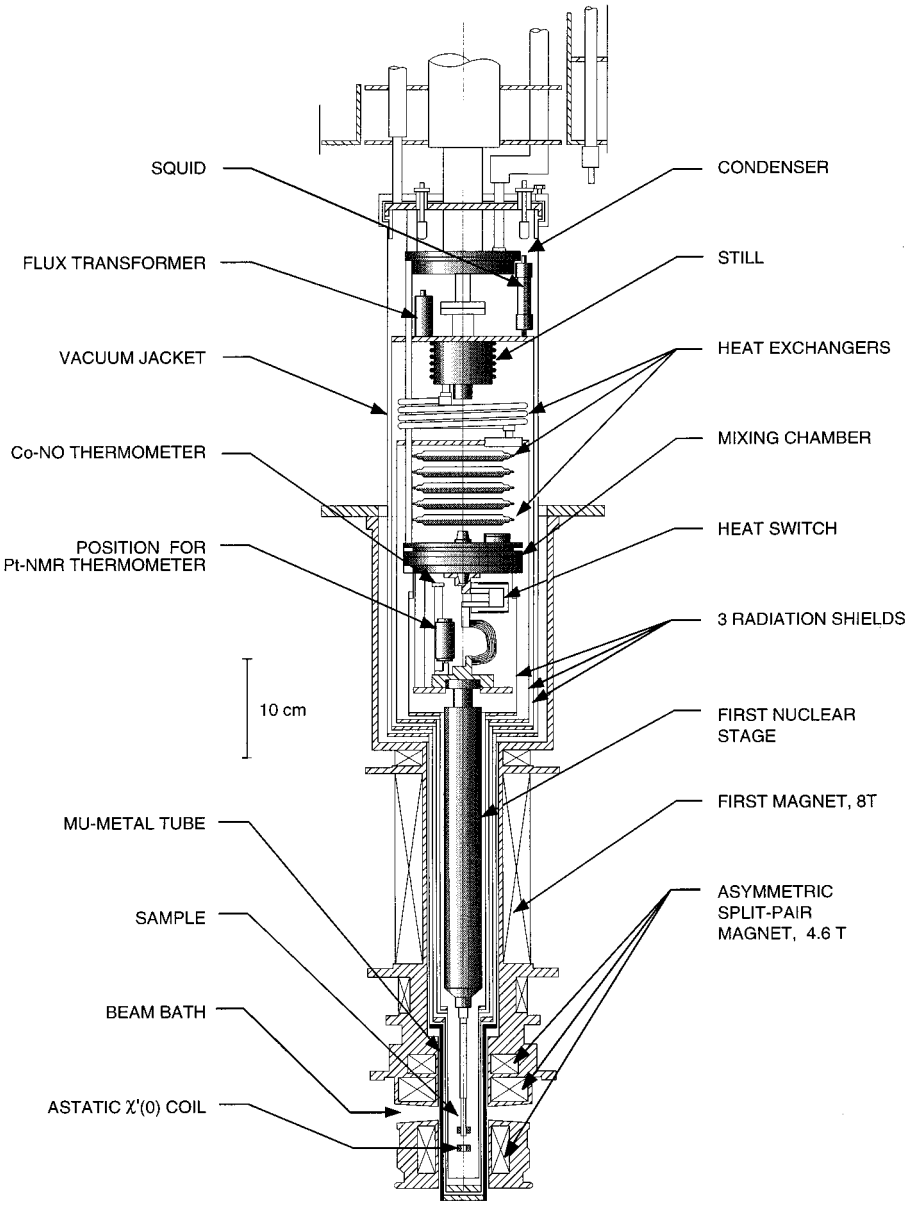

FIG. 36. Low-temperature parts of the two-stage nuclear-demagnetization cryostat at Risø. The whole assembly is immersed in a liquid-helium dewar. From Jyrkkiö *et al.* (1989).

The immediate surroundings of the sample are shown in more detail in Fig. 37. The specimen was connected to the first nuclear stage via a high-conductivity thermal link made of copper. There were two radiation shields around the sample: the inner one was anchored to the mixing chamber and the outer one to the still. A small symmetric split-coil magnet, wound on top of the outer radiation shield, produced the field on the sample after demagnetization of the main split-pair magnet. The excitation and pickup coils for measuring the susceptibility were placed below the split region of the magnet, since otherwise neutrons scattered from the coil system would have increased the background count during experiments.

Cooling of the sample was performed in the same way as in the earlier Helsinki experiments (see Sec. III.B). Small modifications were necessary, however, because of the larger heat capacity of the copper parts in the thermal link between the sample and the first nuclear stage. This was due to the field profile of the main split-pair magnet, with the field extending higher up than in the Helsinki apparatus.

The nuclear stages, the upper one typically magnetized to 7.6 T and the lower to 4.4 T, were first precooled by the dilution refrigerator to 10 mK in 36 h. This low starting temperature was necessary for obtaining almost perfect adiabaticity during nuclear cooling. The first stage was then demagnetized to 0.1 T in 8 h. During the field sweep, dB/dt was decreased several times to eliminate eddy-current heating towards the end of demagnetization. A conduction-electron temperature of about 150 μK was reached.

Next, the large split-pair sample magnet was demagnetized from 4.4 T to 2.0 T in 40 min. Immediately following, the fields in the upper and lower magnets were reduced, in 25 min, to 50 mT and to 1.0 T, respectively. The next step was a fast demagnetization of the split-pair magnet from 1 T to zero. At the same time, the first

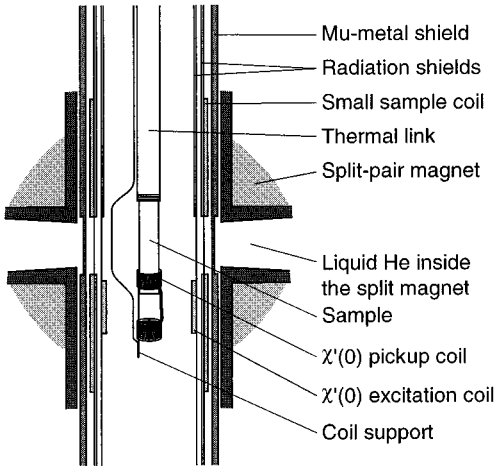

FIG. 37. Surroundings of the sample in the Risø cryostat, indicating the locations of the susceptibility coils, the small split-pair sample coil, and the mu-metal shield. From Jyrkkiö *et al.* (1989).

stage was further demagnetized to 30 mT.

The specimen was now in the 10-mT field produced by the small split-pair coil inside the mu-metal shield (see Fig. 37). One then had to wait 30 s to let the remanent field of the large split-pair magnet stabilize. The final step in the cooling procedure was demagnetization of the specimen from 10 mT to $B<0.3$ mT in about 20 s. The sample nuclei were thereby cooled below the antiferromagnetic ordering temperature $T_N=58$ nK, whereas the conduction electrons stayed at 50–100 μK.

Three different techniques were employed to determine the temperature during the various stages of the Risø experiments (Jyrkkiö *et al.*, 1989). A cobalt nuclear-orientation thermometer (Berglund *et al.*, 1972) was mounted on the first nuclear stage (see Fig. 36) to measure the precooling temperature. Since this thermometer could be used from 2 to 40 mK, it also indicated the temperature at the beginning of demagnetization. The cobalt thermometer was also employed indirectly for measuring the final nuclear temperature of the first stage, which was very close to the final T_e of the sample when the specimen was not heated by the neutron beam. For this purpose the upper nuclear stage was slowly magnetized from $B_f=30$ mT to a field between 1 and 2 T. Assuming an adiabatic process, the temperature in the low field was simply found from the reading of the cobalt thermometer and from the ratio of the fields [see Eq. (18)]. The lowest temperatures measured by this technique were about 70 μK.

The final conduction-electron and lattice temperature could also be found more directly by measuring τ_1 from the susceptibility signal and by using the Korringa relation, Eq. (9). The longest relaxation times observed corresponded to $T_e=50$ μK.

A polarized neutron-scattering technique was also developed for thermometry (Jyrkkiö, Huiku, Clausen *et al.*, 1988). The important advantage of this method is that neutrons probe the nuclei directly; the method thus avoids problems associated with insufficient thermal contact. The sensitive temperature range of this thermometer can be chosen at will by applying a suitable external magnetic field. The method was used to measure the nuclear-spin temperature from 20 mK down to 100 μK. We defer a thorough discussion of this versatile technique to Sec. VI.D.

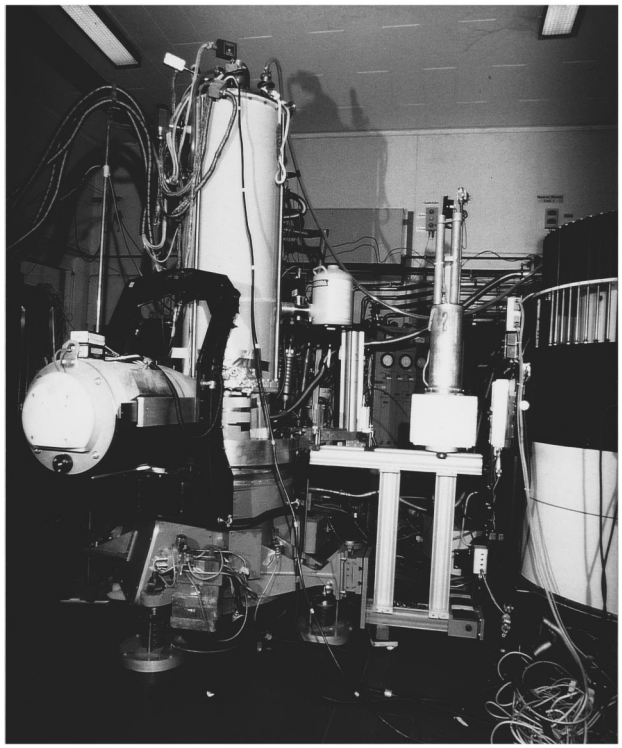

FIG. 38. Experimental setup employed in Risø for neutron-diffraction experiments on copper nuclei. The cryostat is mounted on the spectrometer turntable. The single-channel neutron counter is at left. Risø photograph.

Susceptibility measurements also played an important role in the Risø studies of nuclear ordering. A SQUID was used in the flux-locked mode (Lounasmaa, 1974), and a flux transformer was built to match the inductance of the pickup loop to the signal coil of the superconducting sensor. The positions of the SQUID, the flux transformer, and the astatic pickup coil are shown in Fig. 36.

Figure 38 is a photograph of the experimental arrangement in Risø.

C. Beam heating

An early series of measurements was made at Risø to determine beam heating of the copper sample (Jyrkkiö *et al.*, 1989). The reason for these experiments was twofold. First, for planning the work on copper, one had to know the expected amount of beam heating to make sure that neutrons would not prevent nuclear ordering altogether or destroy the ordered state too fast. Second, information about beam heating was important for all future neutron-diffraction experiments on nuclear magnetism, so that the reliability of calculated estimates

could be assessed. Beam heating manifests itself by raising the electronic temperature of the sample. This, in turn, speeds up the spin-lattice relaxation process [see Eq. (9)] and thereby warms the system faster across the order-disorder phase boundary.

The beam heats the target mainly by processes following thermal neutron absorption but also through possible contaminations of the beam by γ rays and/or by epithermal and fast neutrons (Steiner, 1985). In the Risø setup, all these effects, except the first, could be neglected because the curved neutron guide ensured a small background and reduced all contaminations to a very low level.

Neutron absorption is followed by prompt γ rays and, later, by β emission. The radioactive nucleus formed by neutron capture is in an excited state and decays within a few picoseconds to its ground level by emitting one or more prompt γ's. The energy of the ^{66}Cu excited state above the ground level is 7.1 MeV. Over 95% of it escapes because the mean paths of γ rays before they leave the sample are much shorter than the absorption length. The energy input from this source is about 0.1 nW, which should not cause serious difficulties.

Since the half-life of ^{64}Cu is 12.8 h, the heating caused by the β decay of this isotope has no practical significance in the experiments, which typically are finished in 15 min. However, the half-life of ^{66}Cu is 5.1 min, which means that its β decay must be assessed carefully. β heating is more complicated than that due to the γ's since the β-energy distribution is continuous and because the stopping-power formula in metals is relatively complicated (Knoll, 1968). It turns out that a large portion of the β energy is absorbed in the specimen and that the shape of the sample significantly affects the outcome. By making one dimension of the specimen clearly smaller than the others, one enables more of the β energy to escape. This was the reason why slablike, 0.5-mm-thick crystals were employed in all neutron-diffraction experiments on copper. Even with this construction, about 40% of the β energy was absorbed by the sample. Calculated values for the β heating are 0.1 nW for natural copper and 0.6 nW for ^{65}Cu. As expected, increasing the isotopic proportion of ^{65}Cu increased the β absorption significantly.

However, for reasons to be explained in Sec. VII.A, an isotopically enriched ^{65}Cu single crystal was employed in all neutron-diffraction measurements. Beam heating was accurately measured for the ^{65}Cu sample by studying its effect on the spin-lattice relaxation rate. This method is straightforward because it is based on the Korringa relation, Eq. (9); τ_1 was deduced from the $\chi'(0)$ signal, measured by a SQUID. It was only necessary to find the change in τ_1 due to the neutron beam. Since the beam heating increases T_e, τ_1 becomes shorter. The size of this effect is dependent on $\dot{Q}_{\rm beam}$ and on the thermal resistance between the sample and the first nuclear stage. The resulting temperature difference is given by

$$T_e^2 - T_{e1}^2 = 2R\dot{Q}_{\rm beam}\,, \tag{47}$$

where T_{e1} is the electronic temperature in the first nuclear stage and R is the heat resistance of the thermal link.

When the beam was off, the heat leak to the sample was very small and could be neglected. Therefore one only had to know R to apply Eq. (47). Experiments in zero or low field, without the beam, gave $\tau_1 = 40$ min; with a flux of 2×10^5 neutrons/cm^2 s the relaxation time was shortened to $\tau_1 = 20$ min. Using the measured values, $\kappa = 0.2$ sK in zero field and $R = 11$ K^2/W, in Eqs. (9) and (47), Jyrkkiö *et al.* (1989) obtained $\dot{Q}_{\rm beam} = 1.0$ nW. The agreement between the calculated value for β-ray heating and the experimental result is good.

D. Use of polarized neutrons

Measurements of spin polarization are an important part of nuclear thermometry. A conventional way to make these measurements is first to record the NMR signal of the sample nuclei as described in Sec. IV.A and then to calculate p. Another technique that has recently been employed to measure p makes use of polarized neutrons (Steiner *et al.*, 1981; Benoit *et al.*, 1982b; Steiner, 1990, 1993); the method is practical in materials for which the spin-dependent part of the scattering length b is comparable to, or larger than, the spin-independent part b_0. This, in fact, is the case for several nuclei (Koester and Rauch, 1981). Therefore the scattering cross section for thermal neutrons is strongly affected by the degree of nuclear polarization and by the relative orientation of the neutron and the nuclear spin. A measurement of Bragg intensities thus gives direct information on nuclear polarization of the sample.

Measurement of p with polarized neutrons has some advantages over the NMR method. The resonance condition often limits the NMR technique to certain magnetic fields, whereas this restriction does not apply to neutron thermometry. Difficulties due to skin depth and eddy-current heating in bulk metallic samples are also absent when using neutrons. Instead, one has to worry about the energy absorbed from the beam. This heat goes, however, primarily to the conduction-electron system, unlike the heat from an NMR tipping pulse applied to the sample nuclei. Beam heating affects the whole sample more uniformly than heating caused by a high-field NMR measurement; in the latter case the heat is absorbed in the skin layer. However, recording the NMR response, when feasible, is much faster than a polarized-neutron measurement.

The scattered intensities from Bragg reflections are proportional to the squares of the structure factors $|F_+(p)|^2$ and $|F_-(p)|^2$, which are different for interacting systems consisting of a nucleus and a neutron in total spin states $I+\frac{1}{2}$ and $I-\frac{1}{2}$, respectively. The structure factors are

$$|F_\pm(p)|^2 = 16(b_0^2 \pm b_0 b IPp + \tfrac{1}{4}I^2 b^2 p^2), \tag{48}$$

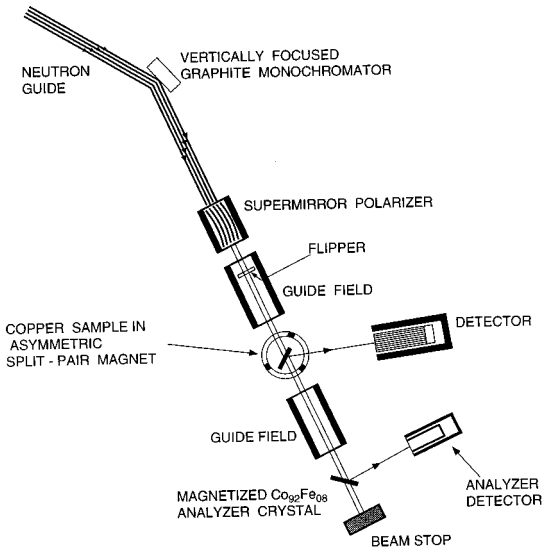

FIG. 39. Neutron-diffraction setup at Risø for studies on copper using a polarized beam. From Jyrkkiö, Huiku, Clausen *et al.* (1988).

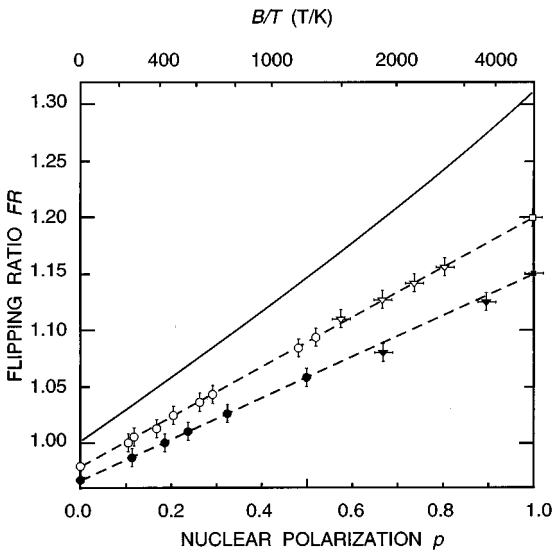

FIG. 40. Observed flipping ratio vs nuclear-spin polarization measured for a natural copper sample. Open symbols $\lambda = 2.4$ Å; filled symbols $\lambda = 3.0$ Å. The solid line is for an extinction-free sample. From Jyrkkiö, Huiku, Clausen *et al.* (1988).

where p is the nuclear polarization and P that of the neutron beam. The ratio between the scattered intensities for the two spin states is called the flipping ratio (FR),

$$FR = |F_+(p)|^2 / |F_-(p)|^2 . \tag{49}$$

This quantity is less sensitive to experimental errors than the absolute intensities. Furthermore, once the polarization of the beam is known, measurement of the flipping ratio directly gives p without any further calibrations. However, this is true only if the neutron beam is not significantly attenuated by scattering when it passes through the sample. In real crystals corrections due to extinction must be taken into account. The scattered intensity then increases more slowly than $|F_\pm(p)|^2$ and causes a decrease in the observed flipping ratios relative to those calculated by Eq. (49). The magnitude of extinction depends on the wavelength and on the quality of the crystal.

1. Experimental setup

The setup used at Risø to study scattering of polarized neutrons from copper nuclei is illustrated in Fig. 39 (Jyrkkiö, Huiku, Clausen *et al.*, 1988). A similar experimental arrangement was previously employed in the Hahn-Meitner Institute to investigate nuclear magnetism in $HoVO_4$ at much higher temperatures (Steiner, 1985; Steiner *et al.*, 1986). The use of polarized neutrons makes the whole setup somewhat more complicated than that needed for an unpolarized beam (see Fig. 35). For a general discussion of neutron instrumentation, we refer the reader to Windsor (1986). The neutrons were polarized after passing the graphite monochromator by a supermirror system. The polarization was approximately 95% and the transmission about 10%. Thus the flux was considerably smaller for polarized than for unpolarized neutrons. The polarizer and the neutron guide reduced the second-order contamination of the beam to less than 1% at the wavelength $\lambda = 2.4$ Å. Permanent magnets were used to produce the vertical guide fields before and after the cryostat.

The neutron-beam polarization could be reversed by a dc flipper, located in the guide field before the cryostat. The efficiency of the flipper was better than 99%. The beam polarization was monitored by an analyzer in the beam behind the cryostat. The analyzer measured the flipping ratio of the (2 0 0) reflection from a magnetically saturated $Co_{92}Fe_{08}$ crystal.

Measurements were made by first counting with the neutron polarization up (+) and then repeating the count with the polarization down (−); the change was produced by operating the flipper. The ratio of the peak counts from the (2 0 0) reflection of copper, corrected for the background, was then calculated. The simultaneously measured flipping ratio at the analyzer was employed to monitor the beam polarization.

2. Flipping ratio versus polarization in copper

The observed flipping ratio for a copper single crystal of natural isotopic mixture is plotted in Fig. 40 vs the nuclear-spin polarization (Jyrkkiö, Huiku, Clausen *et al.*, 1988). The measured flipping ratio is approximately 30% smaller than the theoretical prediction presented by the solid curve. The discrepancy was attributed to extinction and could be quantitatively explained in terms of a theoretical correction (Zachariassen, 1967). Another noteworthy feature of the data is the intercept at $p = 0$ where $FR = 0.98$ instead of 1. This effect is due to the different transmission coefficients for the two

neutron polarizations through the saturated mu-metal shield around the sample (see Fig. 37).

The measurement was later repeated for the ^{65}Cu specimen as well. Equation (49) then predicts that the slope of the FR vs p curve should be 2.5 times higher than that for natural copper. Surprisingly, however, it was found that flipping ratio is less sensitive to nuclear-spin polarization in the ^{65}Cu sample (Jyrkkiö *et al.*, 1989). The effect could be explained by larger extinction in the isotopically pure specimen.

Polarized-neutron measurements were used for several purposes in the course of the studies on copper. Since the experiments were always made in a high magnetic field, the nuclear-spin temperature could be obtained from the measured polarization using Eq. (25b). Spin-lattice relaxation was investigated under conditions in which the Zeeman splitting in temperature units is comparable to the electronic temperature of the sample. Theoretical calculations (Jauho and Pirilä, 1970; Bacon *et al.*, 1972; Shibata and Hamano, 1982) then predict deviations from the Korringa behavior $\tau_1 T_e = \kappa$ with increasing B/T_e. The measurements (Jyrkkiö, Huiku, Clausen *et al.*, 1988) supported the calculations, but the data did not extend to B/T_e values needed for a pronounced deviation from Korringa's equation.

Polarized neutrons were also employed to determine the thermal conductivity of the silver link between the sample and the first nuclear stage, as well as the heat leak to the copper specimen. It was also possible to monitor directly the sample polarization during demagnetization of the first nuclear stage. This provided a useful check for nuclear ordering experiments. While all these studies, in principle, could have been performed by measuring the NMR signal, assuming that difficulties associated with skin-depth effects would have been tolerable, polarized neutrons provided a versatile and useful tool that was not sensitive to the external magnetic field.

The insensitivity to B must be taken with some caution, however. It was observed (Jyrkkiö, Huiku, Clausen *et al.*, 1988) that changes in the stray fields of the two large superconducting magnets slightly affected the absolute intensities, although the flipping ratio (FR) was almost unchanged. More severe were the low-field restrictions. In the work on copper (Jyrkkiö *et al.*, 1989), the field on the sample had to be at least 0.2 T. Below this value the mu-metal shield (see Fig. 37) was not saturated, and therefore it would have strongly depolarized the neutron beam passing through the shield. Polarized-neutron measurements in lower fields would have been possible if, e.g., the mu-metal had been replaced by a superconducting shield made of aluminum.

It is not clear, however, whether measurements with polarized neutrons are feasible down to the fields needed for antiferromagnetic ordering in copper and silver, i.e., in fields on the order of 0.1 mT. A small guide field, typically on the order of 10 mT, or a strictly zero field is needed to preserve the polarization of the neutron beam. In any case, the order-of-magnitude lower neutron flux as compared with the unpolarized beam, and the ensuing long counting times, make it difficult to use polarized neutrons for investigations of the ordering itself, at least in copper and silver.

VII. NEUTRON-DIFFRACTION EXPERIMENTS ON COPPER

A. Neutron scattering from ordered copper nuclei

In the absence of an electronic magnetic moment, the squared structure factor F^2, to which the scattered-neutron intensities are proportional, can be written (Schermer and Blume, 1968; Moon *et al.*, 1969; Price and Sköld, 1986) as

$$|F(\mathbf{k})|^2 = \sum_{d,d'} [b_0^2 + \tfrac{1}{2} b_0 b \mathbf{P}\cdot(\langle \mathbf{I}_d\rangle + \langle \mathbf{I}_{d'}\rangle) + \tfrac{1}{4} b^2 \langle \mathbf{I}_d\rangle \cdot \langle \mathbf{I}_{d'}\rangle] \times \exp[-i\mathbf{k}\cdot(\mathbf{d}-\mathbf{d}')], \quad (50)$$

where b_0 is the coefficient of the spin-independent part and b that of the spin-dependent part of the neutron-nucleus scattering amplitude $b_0 + b\mathbf{I}\cdot\mathbf{s}$; here $\mathbf{I}$ is the spin of the nucleus, $\mathbf{s}$ is the neutron spin, $\mathbf{k}$ is the scattering vector, i.e., the difference between the initial and final wave vectors of the neutron, and $\mathbf{P}$ is the polarization of the neutron beam. $\langle \mathbf{I}_d\rangle$ denotes the thermal average of the spin at site $\mathbf{d}$. The sum is taken over the magnetic unit cell, its size depending on the ordered structure.

The first term b_0^2 in Eq. (50) is the normal structure factor of an fcc lattice, being nonzero and thus producing neutron peaks only for reciprocal-lattice vectors with all indices (hkl) even or all odd [(1 1 1), (2 0 0), (2 2 0), etc.]. The second term is the only one that depends on the beam polarization P; it plays an important role for experiments in the paramagnetic regime (see Sec. VI.D) and it is also crucial in studies of ferromagnetic ordering. However, for antiferromagnets in zero field, $\Sigma_d \langle \mathbf{I}_d\rangle = 0$ and the second term vanishes.

The third term in Eq. (50) is responsible for the appearance of additional Bragg peaks in the antiferromagnetically ordered state (Steiner, 1993). We call this term F_{AF} and rewrite it employing $\langle \mathbf{I}_d\rangle = p_d I \mathbf{n}_d$ where p_d is the nuclear polarization[8] or, in the ordered state, the antiferromagnetic sublattice polarization at site d, and $\mathbf{n}_d$ is a unit vector in the direction of the spin at the same site. By further assuming that $p_d = p$ for all d, one finds

$$|F_{\mathrm{AF}}(\mathbf{k})|^2 = \tfrac{1}{4} b^2 I^2 p^2 \left| \sum_d \mathbf{n}_d \exp(i\mathbf{k}\cdot\mathbf{d}) \right|^2 . \quad (51)$$

This term is zero for all fcc reflections, but nonzero for additional antiferromagnetic peaks, depending on sublattice spin directions $\mathbf{n}_d$. If the translational period of the antiferromagnetic unit cell is the same as the length of the fcc unit cell, reflections with $(h\ k\ l)$ mixed appear

[8] In conventional notation used in the literature on neutron scattering, the symbols P and p are exchanged. Here, however, we follow the notation that is consistent with the rest of our paper.

TABLE III. Neutron-scattering constants for natural copper and for ^{65}Cu.

Quantity	Natural Cu	^{65}Cu
b_0 (10^{-14} m)	0.77	1.00
b_0^2 (b)	0.593	1.00
b (10^{-14} m)	0.073	0.185
$\frac{1}{4}b^2I^2$ (b)	0.0030	0.0193

[(1 0 0), (1 1 0), (2 1 0), etc.]. For a larger magnetic unit cell or for an incommensurate structure, nonintegral indices become possible as well.

To offer an idea of the strength of the expected antiferromagnetic peaks, Table III lists constants b_0, b_0^2, b, and $\frac{1}{4}b^2I^2$ for natural copper and for ^{65}Cu (Koester and Rauch, 1981). The essential facts are that the intensity of all antiferromagnetic peaks are smaller than the fcc reflections by a factor of 100 or more, even in the case of full sublattice polarization, and that the use of ^{65}Cu leads to a sixfold gain in the scattered intensity compared to natural copper, since the spin-dependent scattering length of ^{65}Cu is larger than that of ^{63}Cu. This clearly favors the use of ^{65}Cu isotope for neutron-diffraction studies.

B. Observation of nuclear magnetic ordering

Mean-field calculations (Kjäldman and Kurkijärvi, 1979) for the ordered state in copper at $B=0$ predict an antiferromagnetic type-I structure in which the magnetic unit cell equals the primitive cell. The neutron-diffraction measurements were, therefore, started with a search for the antiferromagnetic Bragg peak at the (1 0 0) position, which is the fundamental reflection of a type-I structure. The first results of these experiments were reported by Jyrkkiö, Huiku, Lounasmaa, Siemensmeyer, Kakurai, Steiner, Clausen, and Kjems (1988). For a more detailed description, we refer the reader to Jyrkkiö *et al.* (1989).

In all experiments on nuclear ordering, a single-crystal ^{65}Cu specimen was used. It was prepared by starting from isotopically enriched ^{65}Cu powder, which contained several hundred ppm's of the magnetic contaminants Fe, Cr, Ni, and Mn. The material was first electrolytically purified, which reduced the impurity level by more than an order of magnitude. A single crystal was then grown in a graphite crucible, using a seed crystal to obtain the desired orientation. After the crystal was made, it was selectively oxidized; during this procedure the residual resistivity ratio increased from 50 to 350. For spin-lattice relaxation, the ratio $r=\tau_1(10\text{ mT})/\tau_1(0)\approx 6$ was measured, showing that impurities still significantly enhanced the relaxation.

The approximate dimensions of the sample were $35\times 7\times 0.6$ mm^3. The [01 1] axis pointed approximately along the longest edge of the specimen. After mounting, the [01 1] direction was along the applied external field within 4°, while the [100] and [011] axes were in the scattering plane, i.e., in the plane perpendicular to the axis of the sample magnet. The orientation of the specimen was made using the (2 0 0) fcc reflection and the $\lambda/2$ component of the neutron beam with $\lambda=4.7$ Å.

The single counter used in the early stages of these measurements was soon replaced by a linear, position-sensitive detector. Special precautions were needed to obtain fields below B_c because of insufficient shielding provided by the mu-metal tube around the sample. Consequently, during the short halt of demagnetization at the 10-mT field, generated by the small coil (see Fig. 37) inside the shield, a negative current was fed into the split-pair magnet to compensate for its remanent field. In later experiments, an additional mu-metal tube was employed, which improved the shielding considerably, and compensation was no longer necessary.

To minimize the heating caused by neutrons, the beam port was opened only during demagnetization from $B=10$ mT to the final experimental field $B<B_c$; this sweep took typically 20 s. After having reached the final field, the scattered intensity and the static susceptibility were monitored as functions of time. During the (1 0 0) experiments the magnetic field at the position of the susceptibility coil was about 10% less than in the upper part of the sample that was probed by neutrons. For later experiments the coil was remade so that the field homogeneity was ±5% over the entire specimen.

The most complete set of data (Jyrkkiö, Huiku, Lounasmaa et al., 1988; Jyrkkiö *et al.*, 1989) at $B=0$ is shown in Fig. 41. A clear Bragg reflection at the (1 0 0) position was observed after demagnetization to zero field. The neutron intensity increased slightly during the first minute. After this the count rate decreased, indicating a decay in the antiferromagnetic sublattice polarization [see Eq. (31)] as the nuclei warmed up because of the spin-lattice relaxation process. After 5 min the decrease became slower, and after 7–8 min no neutrons were observable above the background.

The inset in Fig. 41 illustrates the simultaneously measured static susceptibility: $\chi'(0)$ shows almost a plateau for the first 4–5 min and thus also indicates antiferromagnetic order. Later, $\chi'(0)$ bends towards the paramagnetic exponential relaxation, which is obvious 7–8 min after the final field was reached. The disappearance of the neutron signal thus coincides approximately with the onset of exponential relaxation of $\chi'(0)$. Therefore the neutron-diffraction data confirm the previous conclusions obtained from measurements of the static susceptibility (see Sec. V.A) (Huiku *et al.*, 1986).

To prove that the scattered intensity is, indeed, a Bragg peak, a position-sensitive detector was employed. The time evolution of the peak is shown in the lower part of Fig. 41, at four 75-s measuring periods. A line shape analysis indicated a small narrowing of the peak at the beginning of the experiment. This was probably due to the growth of antiferromagnetic domains when the ordered state was being formed.

C. Magnetic-field dependence of the (1 0 0) reflection for $\mathbf{B}\|[0\bar{1}1]$

To obtain more information about the phase diagram of nuclear-ordered copper, the magnetic-field depen-

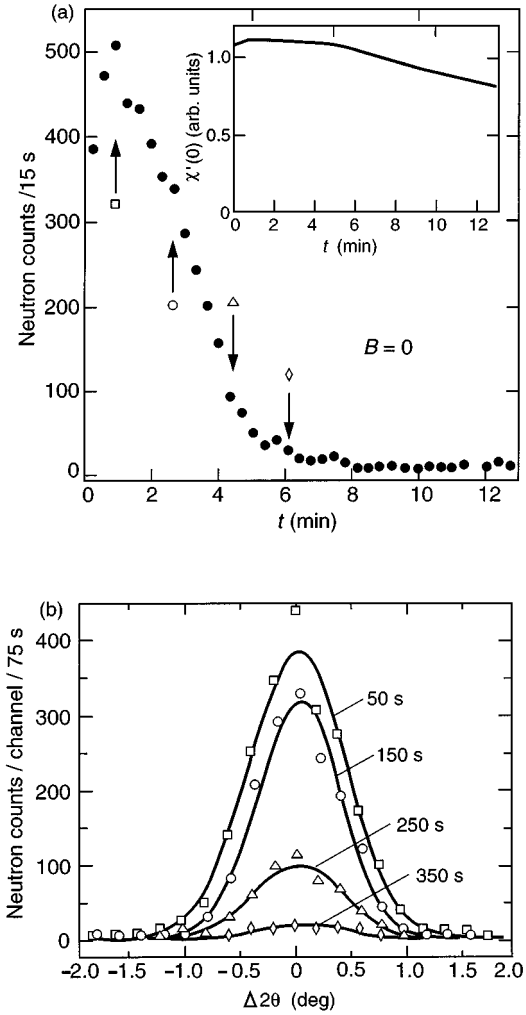

FIG. 41. Antiferromagnetic (100) Bragg reflection of copper. The main figure illustrates the integrated neutron count as a function of time after the zero field had been reached. The inset shows time dependence of the static susceptibility (in arbitrary units). The lower figure (b) depicts the time evolution of the (1 0 0) peak, as observed by a linear position-sensitive detector. The four 75-s measuring intervals are centered at times indicated for each solid curve by the corresponding symbol in the upper figure. These bell-shaped curves are the best Gaussian fits to the experimental data. From Jyrkkiö, Huiku, Lounasmaa, *et al.* (1988); Jyrkkiö *et al.* (1989).

dence of the antiferromagnetic (1 0 0) Bragg peak was investigated in a series of experiments during which the final demagnetization was terminated in different fields below B_c (Jyrkkiö, Huiku, Lounasmaa *et al.*, 1988; Jyrkkiö *et al.*, 1989). Special care was exercised to maintain similar starting conditions in each case before final demagnetization to the ordered phases. This was necessary since the coil system, shown in Fig. 37, could not be employed to measure the susceptibility perpendicular to the external field for determining the initial polarization using the procedures described in Secs. IV.A and IV.B. The precooling temperature of the nuclear stages was, in each case, the same within 10%, and the demagnetization was always carried out in an identical way. A further check on the experimental starting conditions was provided by measurements of the spin-lattice relaxation time in the paramagnetic regime, when the system had warmed above the ordering temperature; the observed τ_1 was 20±2 min in all experiments. On the basis of calculations of polarization losses during demagnetization and using previous susceptibility data (Huiku *et al.*, 1986), it was estimated that, just before entering the ordered phases, the initial polarization $p_i = 0.96 \pm 0.01$, corresponding to $S_i = 0.1\mathcal{R}$ ln4.

The experimental data are presented in Fig. 42. At $B = 0.04$ mT, the qualitative behavior of the neutron signal was the same as at $B = 0$, but the intensity was less. At $B = 0.08$ mT the neutron signal was further reduced. In all these fields, the static susceptibility $\chi'(0)$ parallel to the field was about the same, showing for the first 4–5 min almost a plateau.

At $B = 0.10$ mT, the neutron intensity was close to zero during the entire experiment while, in contrast to data at lower fields, the susceptibility showed a clear increase for the first 4 min. At $B = 0.12$ mT, the neutron count was drastically different from that at 0.10 mT. The intensity was very high, as when $B = 0$, immediately after the final field was reached, but showed, in contrast to the low-field behavior, a very rapid decrease at the beginning of the experiment. After about 2.5 min no neutrons were observable above the background. The susceptibility increased almost 20% during the first 4 min. The neutron intensity thus disappeared clearly before the susceptibility maximum was reached.

At $B = 0.16$ mT, the characteristics were again different. The neutron intensity was very high initially, as at 0.12 mT, but decreased more slowly. The signal disappeared at the maximum of $\chi'(0)$. The behavior of the susceptibility was qualitatively the same as at $B = 0.10$ mT and 0.12 mT, showing a clear increase in the beginning.

At $B = 0.20$ mT and 0.24 mT, the neutron signal was similar to that at $B = 0$, but the intensity was less, especially at 0.24 mT. The increase in susceptibility at $B = 0.16$ mT was reduced to a plateau at $B = 0.20$ mT, and at $B = 0.24$ mT only a short, nonexponential decay was observed initially. Finally, at $B = 0.30$ mT (not shown in Fig. 42), there were no signs of ordering.

The field dependence of the (1 0 0) Bragg reflection thus shows three distinct regions. In the low- and high-field (close to B_c) regimes, the peak was observed approximately until the susceptibility indicated transition to the paramagnetic phase. It was therefore concluded that in these field regions there exist antiferromagnetic phases characterized by type-I order.

In intermediate fields, the (1 0 0) signal showed a very low intensity or a transient behavior, disappearing clearly before the susceptibility indicated paramagnetism. It was suggested (Jyrkkiö *et al.*, 1989), in fact, that the rapidly decaying (1 0 0) signal at $B = 0.12$ mT was a metastable trace from the higher-field (1 0 0) phase formed during demagnetization. It was impossible, how-

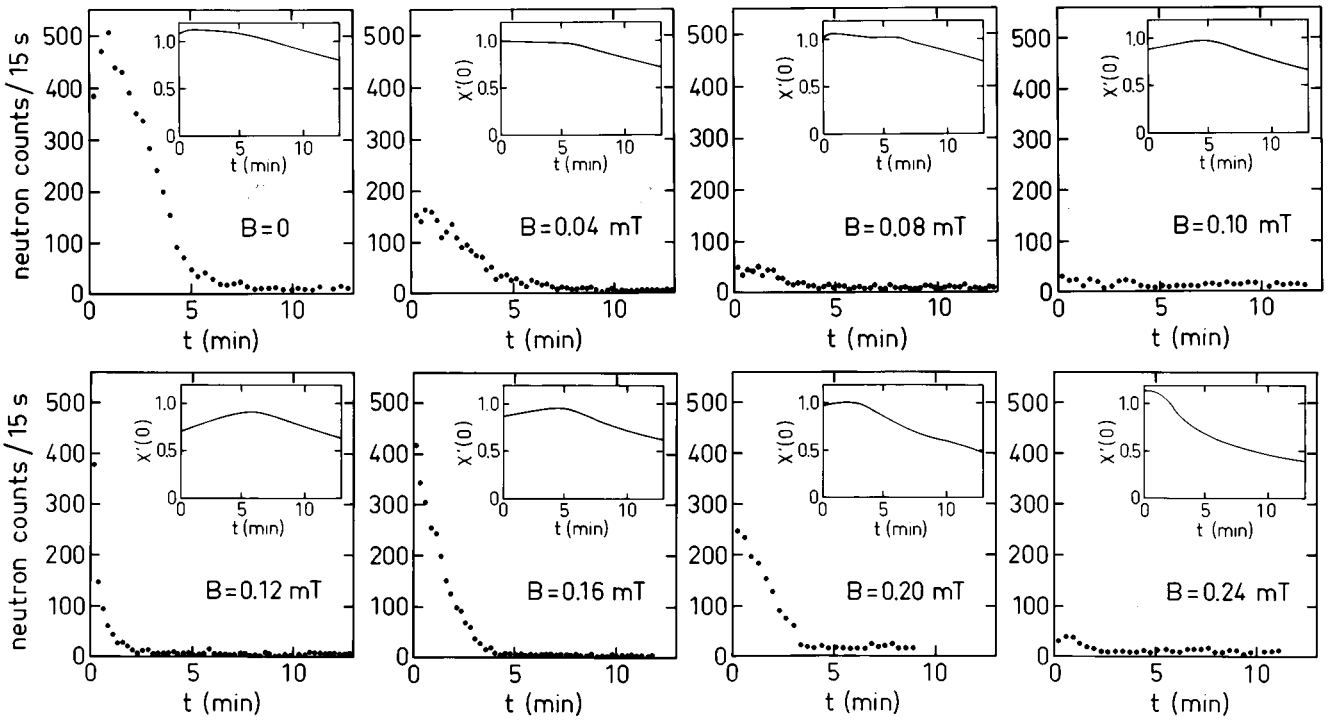

FIG. 42. Integrated neutron intensity measured for copper at the (1 0 0) Bragg position and the susceptibility $\chi'(0)$ (insets) as functions of time after final demagnetization to the field indicated on each frame; $\chi'(0)$ is given in arbitrary units. From Jyrkkiö, Huiku, Lounasmaa, *et al.* (1988).

ever, to determine accurately the phase-transition fields between the intermediate-field phase and the high- and low-field (1 0 0) phases.

The nature of the intermediate-field phase remained obscure during the course of the first set of neutron-diffraction experiments. The clear increase of $\chi'(0)$ pointed to the existence of a well-defined antiferromagnetic phase in this region. However, more exotic interpretations, such as the intermediate state's being an incommensurate phase or even a spin glass, could not be excluded.

In fields above $B=0.16$ mT, the neutron data could be understood in terms of the picture suggested on the basis of susceptibility measurements on the single-crystal specimen (see Sec. V.F and Fig. 1) (Huiku *et al.*, 1986). With increasing field, the nuclear spins tilted towards **B**, so that the antiferromagnetic Bragg peak became weaker. By extrapolating to the field at which the neutron intensity disappeared, one could obtain a critical field $B_c=0.25$ mT, in agreement with susceptibility measurements.

D. (0 $\frac{2}{3}$ $\frac{2}{3}$) reflection

An antiferromagnetic Bragg reflection from the intermediate-field phase was searched for during several experiments. In the first trials (Jyrkkiö *et al.*, 1989), a point-by-point inspection was made in the reciprocal lattice. In the second set of experiments by Annila, Clausen, Lindgård, *et al.* (1990), it was decided to attempt scans in the reciprocal lattice to make the search more effective. Initially, scanning did not appear feasible because of the inevitable eddy-current heating due to vibrations caused by movements of the diffractometer. It had been anticipated that this would destroy the order immediately. Fortunately, in fact, scanning shortened the time spent in the ordered state only by about 40% compared with experiments without scanning. This reduction was large but acceptable since it permitted about a ten times more efficient search than the stationary technique.

On the basis of theoretical studies (Lindgård, Wang, and Harmon, 1986; Lindgård, 1988a) an antiferromagnetic Bragg reflection of the form (0 ξ ξ) seemed a promising candidate for order in the intermediate-field phase. Owing to the symmetry of the fcc lattice, the (0 ξ ξ) point in reciprocal space is equivalent to (1 1-ξ 1-ξ). Since the neutron background was lower in the latter direction, it was chosen for the scans. Figure 43 shows the result of such a measurement (Annila *et al.*, 1990) in the field $B=0.07$ mT, which is in the region of the low (1 0 0) intensity. A very clear Bragg peak was found at (1 η η), with $\eta=\frac{1}{3}\pm0.01$. The small uncertainty in the commensuracy resulted from the statistical error of the counts according to the Poisson distribution and is also due to the continuous movement of the spectrometer during counting. The orientation of the sample was measured with good accuracy afterwards, using the lattice reflection (3 1 1) for the $\lambda/3$ contamination of the neutron beam.

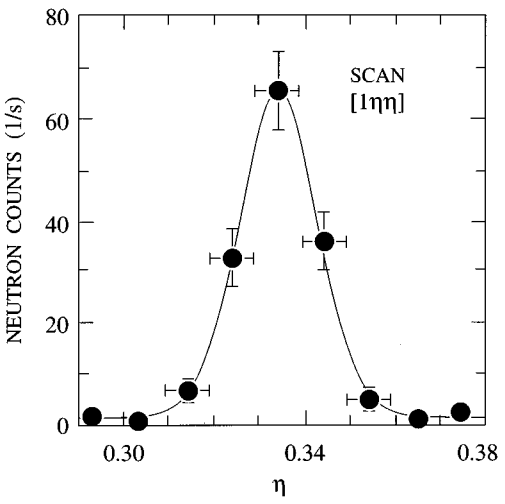

FIG. 43. $(1\ \frac{1}{3}\ \frac{1}{3})$ Bragg peak of copper nuclear spins at $B=0.07$ mT along the $[1\,\eta\,\eta]$ direction. From Annila *et al.* (1990).

Later, the symmetry-related $\pm(0\ \frac{2}{3}\ \frac{2}{3})$ and $(1-\frac{1}{3}-\frac{1}{3})$ reflections were observed as well. In consecutive experiments the neutron intensities of these three signals were measured as a function of time at $B=0.08$ mT while the spin system was warming owing to the spin-lattice relaxation (see Fig. 44). Because the shapes of the warmup curves were similar, it was concluded that the reflections, indeed, were equivalent.

Next, the neutron intensity of the $(1\frac{1}{3}\ \frac{1}{3})$ peak was measured at various constant magnetic fields as a function of time while the nuclear-spin system was warming up after demagnetization. Four examples of warmup curves are shown in Fig. 45. Neutron counts were recorded every 0.5 s during the first 150 s. Thereafter data were taken with a 15-s counting time. The final demagnetization and the subsequent stay at a constant field during warmup are schematically illustrated in the inset.

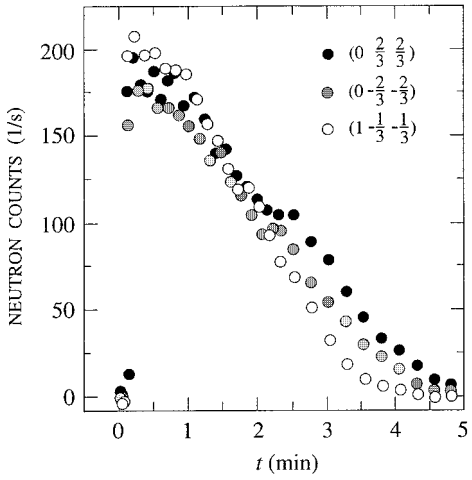

FIG. 44. Time dependence of the $\pm(0\ \frac{2}{3}\ \frac{2}{3})$ and $(1\ -\frac{1}{3}\ -\frac{1}{3})$ reflections in $B=0.08$ mT, measured for copper in consecutive experiments after similar cooling cycles. The spin temperature increases with time. From Annila *et al.* (1992).

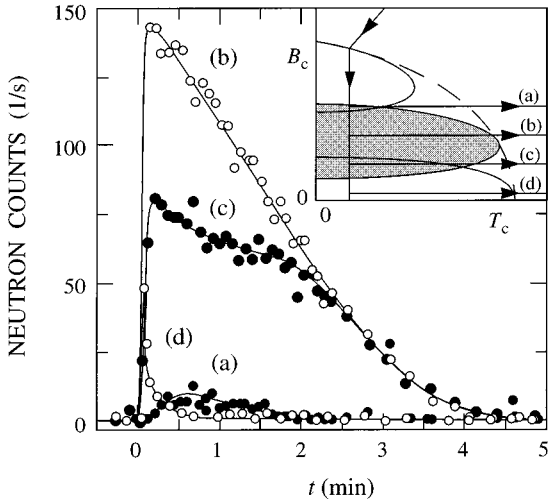

FIG. 45. Time dependence of the $(1\ \frac{1}{3}\ \frac{1}{3})$ reflection for copper at (a) $B=0.13$ mT, (b) 0.10 mT, (c) 0.05 mT, and (d) 0.01 mT. A schematic phase diagram in the B-T plane is shown by the inset, where arrows indicate demagnetization into the ordered phase along a vertical isentrope and subsequent measurements during horizontal warmup in the above-mentioned constant magnetic fields. From Annila *et al.*, (1992).

The data recorded at $B=0.10$ mT (see Fig. 45, curve b) showed a quick increase of the $(1\ \frac{1}{3}\ \frac{1}{3})$ intensity within 1 s after the termination of the field sweep. The signal then decreased approximately at a constant rate during the next four minutes as the antiferromagnetic sublattice polarization vanished owing to warmup. Along the tail of the curve, the rate of the intensity reduction became slower. The change in the shape of the signal may indicate a change in the time vs temperature relationship.

As the field strength was reduced, the maximum neutron intensity became smaller and its temporal behavior changed. At 0.05 mT (see Fig. 45, curve c), the signal decreased only slowly during the first 2 min. This tendency became more apparent when the field was lowered to about 0.03 mT. A mechanism that tends to counteract the decrease in intensity due to the warmup is needed to explain the observed behavior. Growth of the $(0\ \frac{2}{3}\ \frac{2}{3})$ domains was suggested as an interpretation (Annila *et al.*, 1990).

In very low fields, below 0.03 mT, the $(1\ \frac{1}{3}\ \frac{1}{3})$ intensity quickly disappeared. However, even at $B=0.01$ mT (see Fig. 45, curve d) some intensity was observed initially, probably caused by the remaining spin order that had been formed during demagnetization through the higher-field regions.

The maximum $(1\ \frac{1}{3}\ \frac{1}{3})$ intensity decreased rapidly in fields above 0.10 mT. At $B=0.13$ mT (see Fig. 45, curve a) a weak signal built up in 30 s and disappeared quite soon, in about 1.5 min. A maximum of about 10 counts/s was observed. Obviously, only a small portion of the crystal had developed long-range $(0\ \frac{2}{3}\ \frac{2}{3})$ order. This phase was not stable in high magnetic fields where the (1 0 0) reflection was strong.

E. Neutron-intensity contour diagram

A concise presentation of the data from 18 experiments was given in Fig. 3 in the form of a neutron-intensity contour diagram. In this graph, new data on the (1 0 0) peak, measured in the same way as the $(1\ \frac{1}{3}\ \frac{1}{3})$ reflection, were supplemented with the earlier results of Jyrkkiö and co-workers (Jyrkkiö, Huiku, Lounasmaa *et al.*, 1988; Jyrkkiö *et al.*, 1989). The most important difference between the two sets of experiments is that the final demagnetization had been made at the sweep rate of 10 μT/s in the earlier measurements, whereas $dB/dt = 60$ μT/s was used in the later experiments by Annila *et al.* (1990, 1992). Previously it had been observed that the faster the field sweep was in the high-field region, the more (1 0 0) intensity was detected during the sweep (Siemensmeyer *et al.*, 1990). This effect could result if the (1 0 0) domains were preferred over the (0 1 0) and (0 0 1) domains. No such sweep-rate dependence was found for the $(1\ \frac{1}{3}\ \frac{1}{3})$ intensity.

Three maxima occur in the contour diagram: at $B = 0.09$ mT for the $(1\ \frac{1}{3}\ \frac{1}{3})$ peak, and at $B = 0$ and $B = 0.15$ mT for the (1 0 0) reflection. The $(1\ \frac{1}{3}\ \frac{1}{3})$ signal is strongest when the (1 0 0) signal is weakest and vice versa, suggesting the presence of three distinct phases. The upper boundary is sharp, with the contours closely spaced, whereas in low-intermediate fields, $0.02 \leqslant B \leqslant 0.06$ mT, both reflections coexist over a wide region.

F. Kinetics of phase transitions when $\mathbf{B} \| [0\bar{1}1]$

Several features of the neutron-diffraction data can be associated with the decay and growth of nuclear magnetic order. The time scale of the kinetics is long compared with that of electronic magnets because of the weak interactions between nuclear spins. In this respect nuclear magnets are very suitable systems for direct studies of the ordering processes. On the other hand, conditions for true thermal equilibrium cannot be produced readily because of the long time constants.

1. Initial temporal development of neutron intensity

The temporal behaviors of the neutron signals in the two transition regions were different (see Fig. 46). At $B = 0.12$ mT, the (1 0 0) intensity disappeared while the $(1\ \frac{1}{3}\ \frac{1}{3})$ signal appeared about 30 s after the demagnetization had ended. The background level was reached in a few minutes. The transients show how the (1 0 0) structure, formed during the field sweep through the upper phase, transforms into the $(0\ \frac{2}{3}\ \frac{2}{3})$ spin configuration. The transition is sharp, since the width of the phase boundary appears to be on the order of the field inhomogeneity $\Delta B = 0.01$ mT.

In the lower 0.04-mT transition region, the signals did not show the initial kinetics and decreased only gradually during the first 1.2 min, whereafter the typical tail of a warmup curve was observed. Since no transients were seen and both signals persisted for a long time, with similar temporal behaviors, it must be concluded that in this region, $0.02 \leqslant B \leqslant 0.05$ mT, the (1 0 0) and the

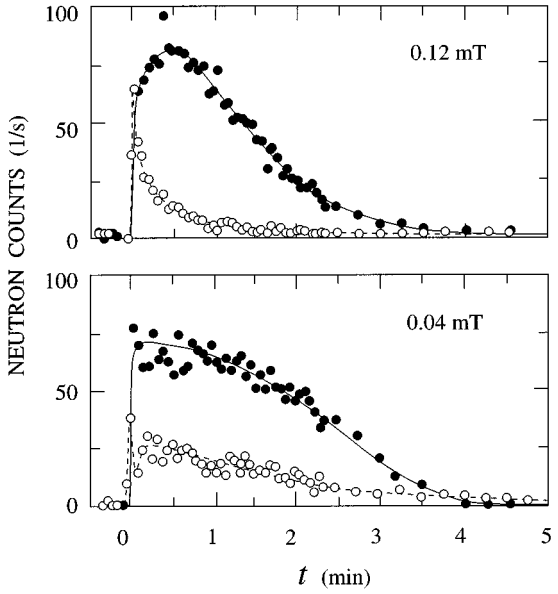

FIG. 46. Neutron counts from copper nuclear spins vs time near the upper phase boundary at $B = 0.12$ mT and in the lower transition region at $B = 0.04$ mT: ○, (1 0 0) peak; ●, $(1\ \frac{1}{3}\ \frac{1}{3})$ reflection. From Annila *et al.* (1992).

$(0\ \frac{2}{3}\ \frac{2}{3})$ orders coexist, either in the form of domains of two different spin configurations or as a combined (1 0 0) and $(0\ \frac{2}{3}\ \frac{2}{3})$ multiple-**k** structure. In the former case, the (1 0 0) and $(0\ \frac{2}{3}\ \frac{2}{3})$ configurations must be nearly degenerate in energy. In the latter, a combination structure continuously transforms from the pure $(0\ \frac{2}{3}\ \frac{2}{3})$ order to the (1 0 0) order when the magnetic field is decreased, and the lower transition is not a phase transition at all.

2. Hysteresis at phase boundaries

The phase boundaries were probed by successively sweeping the magnetic field down and up across the transition regions [see Fig. 47(a), inset]. At the upper boundary around $B = 0.12$ mT [see Fig. 47(b)], when the field was lowered, the (1 0 0) signal disappeared at fields smaller than those at which it reappeared when the field was raised again. Accordingly, the $(1\ \frac{1}{3}\ \frac{1}{3})$ counts began to increase at smaller fields when B was swept downward as compared with the field where counts started to decrease when the field was being swept upward. In this way a pair of hysteresis loops were created.

In the low-field region, loops were observed as well, but the changes in the intensities were opposite to those at the upper boundary [see Fig. 47(c)]. Hysteresis was seen over the same field interval where the (1 0 0) and $(1\ \frac{1}{3}\ \frac{1}{3})$ counts had similar time evolutions. The two transition regions appeared similar during the field-sweep experiments, in contrast to the constant-field measurements (see Fig. 46).

The boundary across $B_c(T)$ to the paramagnetic phase was examined in a similar manner for comparison [see Fig. 47(a)]. No hysteresis was found in this case, consistent with a second-order phase transition.

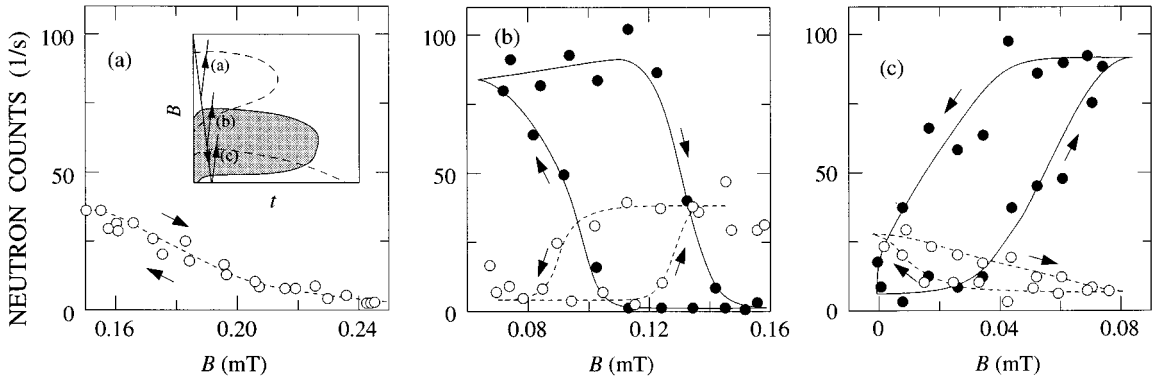

FIG. 47. Neutron counts for copper vs magnetic field (a) near B_c and at (b) the upper, and (c) the lower transition regions when the magnetic field was swept across the phase boundaries at the rate 8 μT/s [see inset in (a)]. ○, (1 0 0) peak; ●, (1 $\frac{1}{3}$ $\frac{1}{3}$) reflection. From Annila *et al.* (1992).

3. Temporal changes in the width of the Bragg peak

Figure 48 shows the peak width of the (1 0 0) Bragg reflection during warmup in three different external fields. The error bars are those given by the fitting routine, and they provide an estimate on the relative quality of the fit. The data show that for all applied fields a small narrowing is observed at first. This can be explained by the growth of the antiferromagnetic domains. The peak width is smallest in fields close to $B=0$ and broader in higher fields; the broadest peak was observed at $B=0.12$ mT.

Separate measurements on samples of different materials, such as a germanium crystal and Al_2O_3 powder, showed that the instrumental resolution varied from 0.8° to 1.1°. For example, the first data points at $B=0.20$ mT and all the $B=0.12$ mT data are clearly broader than the instrumental peak width. Since $B=0.12$ mT is in the region of the upper phase boundary, the larger peak width is not surprising. The system is probably in a metastable state and does not find its way to a well-defined state during the short lifetime of the neutron count. A rough calculation on the broadening of the peak in the beginning of the $B=0.12$ mT experiment indicates domain sizes on the order of 500 Å.

4. Decay of metastable states

Relaxation times associated with magnetic ordering in the low-field region were also investigated in the course of the two experiments illustrated in Fig. 49. The time evolution of the neutron intensity was measured in fields $B=+0.04$ mT and $B=-0.04$ mT, where the negative sign indicates that, during the final demagnetization, the field was swept through and beyond zero. The characteristic difference was the very fast decay of the 0.04 mT signal during the first 1.5 min. It was believed that this

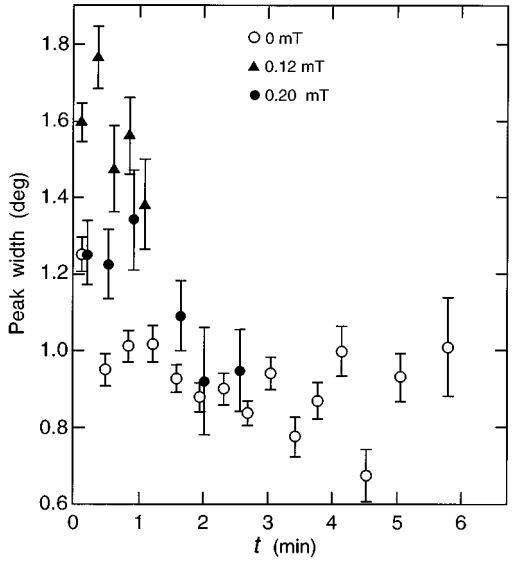

FIG. 48. Widths of the (1 0 0) Bragg peaks in copper as functions of time, deduced from Gaussian fits to the linear-detector data in three selected fields. From Jyrkkiö *et al.* (1989).

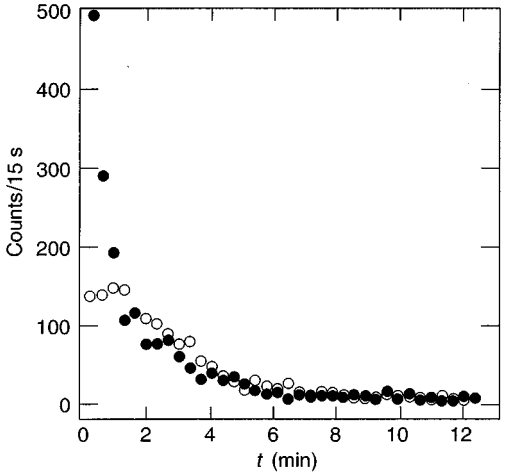

FIG. 49. Time evolution of the (1 0 0) neutron intensity for copper in two successive experiments: ○, demagnetization stopped at $B=0.04$ mT; ●, demagnetization continued through zero to the same field in the opposite direction. From Jyrkkiö *et al.* (1989).

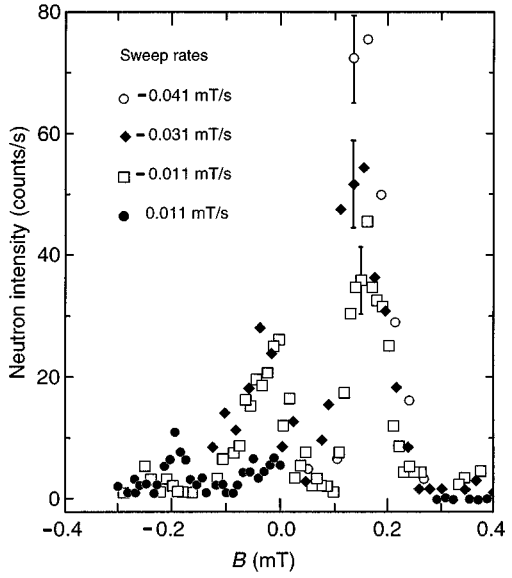

FIG. 50. Neutron intensity at the (1 0 0) Bragg position during field changes at three different rates. The measurements with negative sweep rates proceeded from a positive to a negative field. From Siemensmeyer *et al.* (1990).

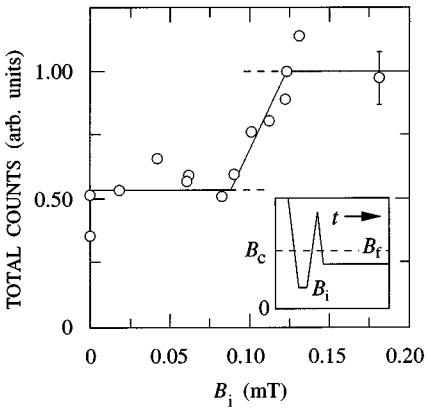

FIG. 51. Total (1 0 0) neutron counts from copper nuclear spins measured at $B_f = 0.18$ mT vs the magnetic field B_i. The sample was brought to B_f from the paramagnetic phase after a short stay in B_i (see inset). From Annila *et al.* (1992).

was again due to metastability, i.e., a remanent, quickly disappearing trace of the spin arrangement created close to $B = 0$. After 1.5 min, the two signals were behaving in the same way, which indicates symmetry in the phase diagram around $B = 0$.

Relaxation times in higher fields showed interesting features as well. The neutron count rate at the (1 0 0) reflection in fields from 0.1 to 0.17 mT, immediately after the end of demagnetization, was found to depend on how quickly the field had been decreased to this region. Intensities measured for three different sweep rates are presented in Fig. 50 (Siemensmeyer *et al.*, 1990). During the fastest scans the intensity reached a value almost three times higher than what was observed in the experiments under a constant field with a counting time of 15 s. There must be a fast relaxation process that causes the quick decay of the (1 0 0) intensity. From the sweep rates the relaxation time of this process was estimated to be in the range between 2 and 5 s.

Intriguing behavior was observed when the field sweep with rate -11 μT/s was continued through zero to negative fields. First, only a weak (1 0 0) reflection was observed in the high-field phase, when $B = -0.12 - -0.25$ mT, as is shown by the data points indicated by rectangles in Fig. 50. The field was changed until $B = -0.3$ mT was reached, at which point the direction of the sweep was reversed. The spins were then in the paramagnetic phase since $B_c = 0.25$ mT. The antiferromagnetic phase was reentered at the sweep rate of 11 μT/s, as shown by the neutron data illustrated by solid circles. The (1 0 0) reflection in the high-field phase, $B = -0.12 - -0.25$ mT, was approximately twice as high as the intensity observed during the first field sweep. This was surprising since antiferromagnetic order should decay with time due to the spin-lattice relaxation process. A possible explanation is that during the first field sweep, when the (1 0 0) intensity was low, spins partly remained in the metastable state with $(0\ \frac{2}{3}\ \frac{2}{3})$ order.

5. Entropy losses

Nonadiabatic behavior at the phase boundaries was further investigated by Annila *et al.* (1992) in a series of experiments. The magnetic field was first reduced to a selected value B_i above, in, or below the $(0\ \frac{2}{3}\ \frac{2}{3})$ state, then raised well above B_c, and finally lowered to $B_f = 0.18$ mT, where the (1 0 0) neutron counts were recorded (see Fig. 51, inset). This elaborate sequence of field sweeps assured that the measuring field B_f was always reached at the same time and in the same way, independently of B_i. Therefore the spin structure created at B_i could not possibly affect the distribution of the total intensity among the (1 0 0), (0 1 0), and (0 0 1) domains and thus the measured (1 0 0) neutron intensity. Counts collected at B_f were summed in order to acquire better statistics, and all the data were scaled by a reference measurement at $B_i = 0.12$ mT (see Fig. 51).

It was found that the total neutron count at B_f clearly dropped when B_i was reduced from 0.12 mT to 0.08 mT. The midpoint and the width of the decrease coincided with the center and the width, respectively, of the hysteresis loops along the upper phase boundary [see Fig. 47(b)]. The loss of intensity was related to a gain of entropy during a first-order phase transition. This also explains, at least partly, why the (1 0 0) intensity at zero field was lower than at $B = 0.16$ mT (see Sec. VII.C); part of the signal was simply lost, owing to nonadiabaticity, when the upper phase boundary was crossed. The nature of the lower transition could not be resolved within the experimental error.

G. Comparison with simultaneous susceptibility measurements

The longitudinal, low-frequency susceptibility χ_L was measured simultaneously with the neutron signal from

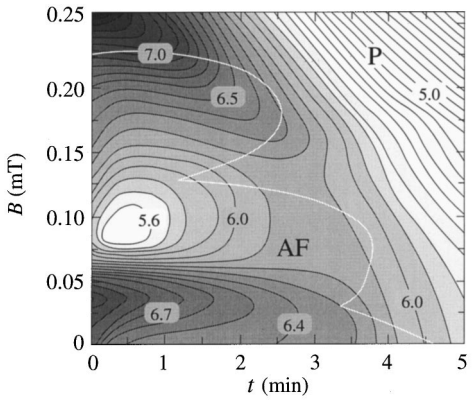

FIG. 52. Longitudinal susceptibility of copper shown by contours in arbitrary units as a function of time and magnetic field along the [01 1] direction. The antiferromagnetic region (AF) is bounded by the paramagnetic phase (P) where the contours eventually become diagonal and uniformly spaced. The white curve follows the outermost neutron-count-rate contours of Fig. 3. The antiferromagnetic region extends slightly beyond this curve; the difference can be especially large in fields around 0.13 mT owing to the presence of the $(\pm\frac{2}{3}\ \pm\frac{2}{3}\ 0)$ and $(\pm\frac{2}{3}\ 0\ \pm\frac{2}{3})$ signals shown in Fig. 57(c). These reflections have a different field dependence than the $(0\ \frac{2}{3}\ \frac{2}{3})$ order illustrated in Fig. 3. Modified from Annila *et al.* (1992).

the lower section of the sample (see Fig. 37). A contour map (see Fig. 52), similar to the neutron-intensity diagram (see Fig. 3), was composed from measurements at constant fields (Annila *et al.*, 1992). A comparison of the two graphs helps to determine whether the antiferromagnetic behavior of the susceptibility signal can be attributed to the (1 0 0) and $(0\ \frac{2}{3}\ \frac{2}{3})$ reflections only, or whether other Bragg peaks should be present as well.

The critical field is about 0.26 ± 0.01 mT according to the χ_L data, compared to $B_c=0.25$ mT obtained by neutrons. The phase boundary of the ordered state, determined from χ_L, closely engulfs the outermost neutron-intensity lines of Fig. 3. The clearest discrepancy occurs around $B=0.13$ mT. The outer contours of the (1 0 0) and $(1\ \frac{1}{3}\ \frac{1}{3})$ signals bend strongly inwards before crossing, which might indicate a transition into the disordered state only 1.5 min after demagnetization and hence may point to a re-entrant $B_c(T)$ curve around this field. However, the spins seem to be antiferromagnetically ordered for $t>1.5$ min as well, because the maximum of χ_L is observed at $t=2.5$ min. This suggests another phase, with neither (1 0 0) nor $(0\ \frac{2}{3}\ \frac{2}{3})$ modulation in the time interval $t=1.5-2.5$ min.

The clear minimum in χ_L at intermediate fields (see Fig. 52) coincides in field and time with the maximum of the $(1\ \frac{1}{3}\ \frac{1}{3})$ intensity. The neutron maxima of the (1 0 0) reflections (see Fig. 3) do not correspond to distinctive features in the susceptibility diagram. The phase transitions also look different in the two graphs. The sharp upper boundary in the neutron diagram is contrasted with a smooth decrease of susceptibility. In low fields, in the coexistence region of the slowly changing $(1\ \frac{1}{3}\ \frac{1}{3})$ and (1 0 0) intensities, there is a local maximum of χ_L at $B=0.04$ mT. The differences between the susceptibility and the neutron-diffraction data in the appearances of the transition regions might be better understood if the two other Cartesian components of susceptibility had been measured, as was done earlier for $\mathbf{B}\|[001]$ (Huiku *et al.*, 1986).

Following this reasoning, discussed in Sec. V.F in the context of Fig. 33, Annila *et al.* (1992) concluded, on the basis of their χ_L data, that in high fields the antiferromagnetic sublattice magnetization of the (1 0 0) structure is perpendicular to **B**. When the magnetic field is lowered, the sublattice magnetization becomes more and more parallel to the field and reaches its extremal orientation at $B=0.09$ mT, corresponding to the $(1\ \frac{1}{3}\ \frac{1}{3})$ reflection. Further reductions of the field causes the sublattice magnetization to become more perpendicular to the field. The extremum is at about $B=0.04$ mT. In still lower fields, part of the sublattice magnetization appears to be parallel to the field as well.

H. Other field directions

An obvious extension to the neutron-diffraction experiments on copper described so far was to examine the phase diagram with the magnetic field aligned along crystallographic axes other than the [01 1] direction. This is important because not only the spin configurations but also the number of phases, as predicted by theoretical studies, might differ for various field directions. The results of these experiments have been described by Annila *et al.* (1992).

The external field **B** could be applied along an arbitrary direction by using an orthogonal pair of saddle coils and a split-pair solenoid, perpendicular to the saddle coils (see Fig. 53). The magnetic structures could then be studied by measuring the (1 0 0) and $(0\ \frac{2}{3}\ \frac{2}{3})$ reflections in various orientations of the field. Figure 54 illustrates how the high-symmetry directions of the first Brillouin zone are related to the scattering plane.

Because it would have been impractical to investigate the phase diagram in the same detail as was done for the [01 1] field direction by means of a series of warmup measurements in a constant field, a new scheme was employed to establish first an overall picture. Furthermore, it was technically difficult to fix the field accurately along all desired axes for a long time, since the demagnetization field (see Sec. V.G) kept decreasing owing to spin-lattice relaxation. Therefore the field was repeatedly swept from $B=0.3$ mT$>B_c$ down to zero and up again, with $dB/dt=10$ μT/s. At this rate, one cycle took 60 s and a reduction of polarization during that period did not affect the field in the specimen substantially, even in the worst cases.

Annila *et al.* (1992) took great care to maintain identical initial conditions for the field-sweep experiments. Reproducibility of the data was not usually investigated to save beam time.

1. [100] directions

The three directions [100], [010], and [001] are equivalent under cubic symmetry. The latter two are symmetric

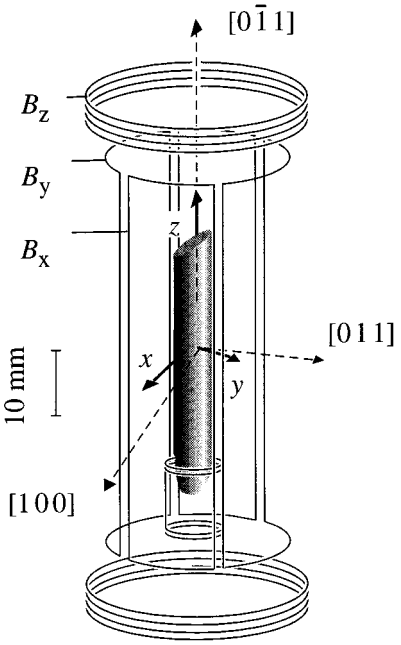

FIG. 53. Schematic view of the coil system surrounding the sample inside the 4.6-T split-pair superconducting solenoid. The crystallographic [100], [011], and [01 1] directions are shown with respect to the x, y, and z axes of the specimen. Components of the external magnetic field along the Cartesian axes are generated by three field coils, B_x, B_y, and B_z. The upper part of an astatically wound small detection coil for measuring the susceptibility surrounds the lower end of the sample. From Annila *et al.* (1992).

with respect to the accessible (1 0 0) and $\pm(0\,\frac{2}{3}\,\frac{2}{3})$ positions in the scattering plane (see Fig. 54). Therefore it sufficed to make measurements at **B**‖[100] and [001]. Data for the first down-and-up sweeps are shown in Fig. 55.

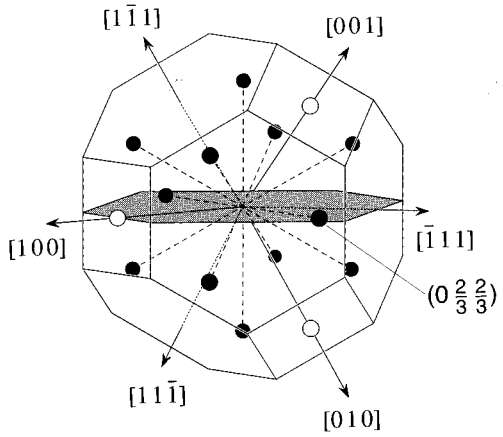

FIG. 54. The star of **k**: the first Brillouin zone of an fcc lattice with some of the crystallographic directions shown. Under cubic symmetry, there are three equivalent (1 0 0) positions (○) and 12 equivalent $(0\,\frac{2}{3}\,\frac{2}{3})$ positions (●). In the first Brillouin zone, only the (1 0 0) and the $\pm(0\,\frac{2}{3}\,\frac{2}{3})$ points were in the scattering plane (shaded) and accessible to the experiments. From Annila *et al.* (1992).

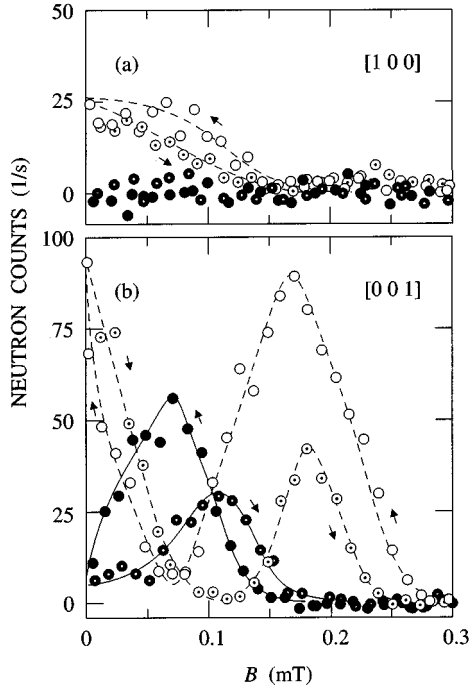

FIG. 55. Neutron intensity of the (1 0 0) (○) and $(0\,\frac{2}{3}\,\frac{2}{3})$ (●) peaks for copper vs the magnetic field for downward sweeps along (a) the [100] and (b) the [001] field directions at the rate 10 μT/s. The counts collected when the magnetic field was raised are marked by ⊙ for the (1 0 0) peak and by ❍ for the $(0\,\frac{2}{3}\,\frac{2}{3})$ peak. The directions of the field sweeps are indicated by arrows as well. From Annila *et al.* (1992).

The signals were clearly different in the two directions. In high fields, the (1 0 0) intensity was very low for **B**‖[100] whereas it was high in the [001] field direction. In low fields, the (1 0 0) reflection was observed for both directions, but its intensity in the [001] direction was higher by a factor of 3. The $(0\,\frac{2}{3}\,\frac{2}{3})$ reflection was not present at all for **B**‖[100], but with **B**‖[001] the $(0\,\frac{2}{3}\,\frac{2}{3})$ signal was observed at intermediate and low fields.

From Fig. 55(b) one obtains a critical field of about 0.27 mT and a phase transition to the intermediate-field structure at $B \approx 0.13$ mT. These fields at which a phase change occurs are the same as for **B**‖[01 1] (Fig. 47) within the uncertainty in B.

When $B=0$, one would expect equal intensities, as the field no longer breaks the symmetry. Because the observed signals clearly differed (see Fig. 55), this matter was further investigated by two experiments in which B was rapidly swept to zero along the [100] and [001] directions, respectively, whereafter neutrons were counted as a function of time (see Fig. 56).

The signals were quite different for the two directions of the demagnetization field. The data demonstrate that the magnetic structures were created during demagnetization and determine how the order was divided among the (1 0 0) magnetic domains when $B=0$. The time scale required for thermal equilibrium between domains is long compared to the measuring time available.

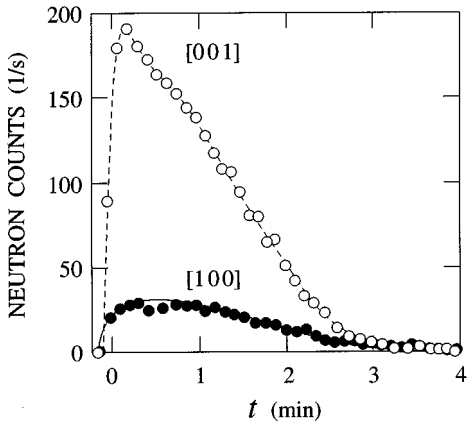

FIG. 56. (1 0 0) neutron intensity for copper as a function of time after demagnetization to $B=0$ along the [001] and the [100] field directions at the rate 50 μT/s. From Annila *et al.* (1992).

2. [110] directions

For the [110] field alignments, there are two nonequivalent directions with respect to the (1 0 0) reflection and three directions for the $(0\ \frac{2}{3}\ \frac{2}{3})$ peak (see Fig. 54). The results from field sweeps along the [011], [01 1], and [1 01] directions are shown in Fig. 57. Even though the [01 1] alignment had been investigated in a large number of experiments, as described in the previous sections, field sweeps in this direction were included as well to facilitate direct comparison with the data in the other directions.

In high and low fields, the (1 0 0) signal was observed in all three directions. For the (1 0 0) peak, the [011] and [01 1] directions are equivalent under fcc symmetry; equal neutron signals thus ought to be recorded [see Figs. 57(a) and (b)]. Experimentally, this was true only to the extent that the (1 0 0) reflection was seen over the same field region for both directions, but the intensities were unequal. A small misalignment of the external field or slightly different cooling conditions, affecting the initial polarizations and warmup rates during the two experiments, could be responsible for this effect. Disproportionate signals between the high- and low-field regions for the [011] and [01 1] directions may have resulted from unbalanced populations of the various domains.

When sweeping up again from $B=0$, the high-field (1 0 0) signal was much smaller than expected. Even if the intensity loss due to entropy gain during the first-order transition (see Fig. 51) and the subsequent warmup were taken into account, according to the data in Fig. 3, it was expected that at least one-fourth of the initial counts should have been recovered. Moreover, the susceptibility signal clearly showed that the system was not in the immediate vicinity of a transition to the paramagnetic phase. This finding is in accordance with earlier observations (Siemensmeyer *et al.*, 1990) described in Sec. VII.F.4 (see also the data in Fig. 50).

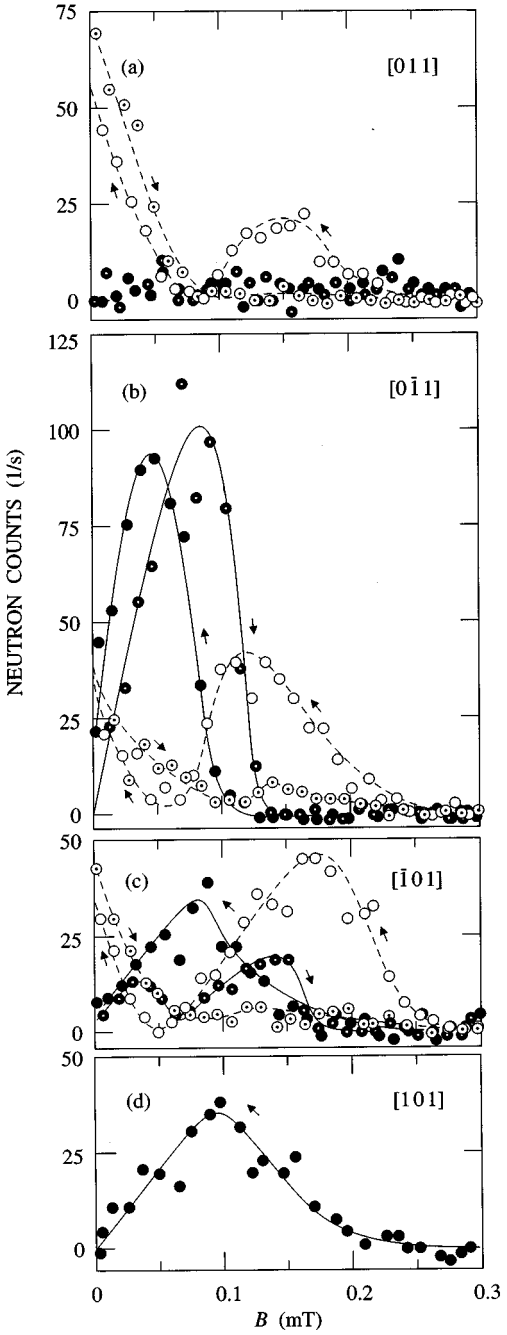

FIG. 57. Neutron intensity of the (1 0 0) (○) and $(0\ \frac{2}{3}\ \frac{2}{3})$ (●) peaks for copper vs the magnetic field for downward sweeps at the rate 10 μT/s with **B** along the (a) [011], (b) [01 1], (c) [1 01], and (d) [101] directions. The counts measured during upward field sweeps are marked by ⊙ for the (1 0 0) peak and by ❍ for the $(0\ \frac{2}{3}\ \frac{2}{3})$ peak. From Annila *et al.* (1992).

In intermediate fields, the three $(0\ \frac{2}{3}\ \frac{2}{3})$ signals of Fig. 57 are different. When $\mathbf{B}\|[011]$ the reflection was absent [see Fig. 57(a)], whereas for $\mathbf{B}\|[01\ 1]$ [see Fig. 57(b)] and $\mathbf{B}\|[1\ 01]$ [Fig. 57(c)] the $(0\ \frac{2}{3}\ \frac{2}{3})$ reflection was there, but the signals were different both in intensity and in their magnetic-field dependence. The $(0\ \frac{2}{3}\ \frac{2}{3})$ order was found in higher fields for $\mathbf{B}\|[1\ 01]$ than for $\mathbf{B}\|[01\ 1]$. Annila *et al.* (1992) took this as evidence for two different spin structures with $(0\ \frac{2}{3}\ \frac{2}{3})$ order.

The new $(0\ \frac{2}{3}\ \frac{2}{3})$ phase observed for $\mathbf{B}\|[\bar{1}\,01]$ provides a possible explanation, as well, for the sweep-rate-dependent (1 0 0) intensity, discussed in Sec. VII.F.4. As is shown by Fig. 57(c), the $(0\ \frac{2}{3}\ \frac{2}{3})$ intensity starts to increase already around $B=0.17$ mT for $dB/dt=10\ \mu$T/s, which is approximately the field below which the sweep-rate-dependent (1 0 0) intensity was observed. Taking into account that there are altogether eight equivalent $(0\ \frac{2}{3}\ \frac{2}{3})$ reflections with respect to the [1 01] field direction, one can estimate that at $B=0.12$ mT, for example, the total intensity of these reflections is 2–3 times higher than the intensity of the (1 0 0) peak. Therefore a characteristic time scale, on the order of a few seconds, for the growth of the $(0\ \frac{2}{3}\ \frac{2}{3})$ order would explain the sweep-rate effect.

Annila *et al.* (1992) suggested, on the basis of the hysteresis loops in Fig. 57(c), that the low- and high-field boundaries of the $(0\ \frac{2}{3}\ \frac{2}{3})$ phase for $\mathbf{B}\|[1\ 01]$ are of first order.

Fig. 57(d) shows the neutron intensity of the $(0\ \frac{2}{3}\ \frac{2}{3})$ reflection when the magnetic field was swept to zero along the [101] direction. The shape of the signal is similar to that of the $(0\ \frac{2}{3}\ \frac{2}{3})$ reflection in Fig. 57(c), as it should be because these two crystalline directions are equivalent with respect to the $(0\ \frac{2}{3}\ \frac{2}{3})$ position.

3. [111] directions

For a field aligned along any of the [111] axes, the three (1 0 0) peaks are equivalent. For the $(0\ \frac{2}{3}\ \frac{2}{3})$ reflection, there are two nonequivalent directions (see Fig. 54), for example, [111] and [11 1], which were chosen for measurements.

The most striking feature of the data in Fig. 58 is the missing high-field (1 0 0) phase. This perplexing question is discussed separately in Secs. VII.J. and XV.G. From the susceptibility measurements the critical field $B_c=0.26$ mT was deduced.

The $(0\ \frac{2}{3}\ \frac{2}{3})$ peak was absent when **B** was parallel to [111], but it was observed at intermediate fields for the [11 1] alignment. The transition from the high-field phase to the $(0\ \frac{2}{3}\ \frac{2}{3})$ structure took place at $B=0.13$ mT. The form of the $(0\ \frac{2}{3}\ \frac{2}{3})$ signal during the field sweeps was rather similar to that with $\mathbf{B}\|[01\ 1]$. At low fields the (1 0 0) peak appeared but with somewhat different intensities for the two field directions. The region with overlapping (1 0 0) and $(0\ \frac{2}{3}\ \frac{2}{3})$ reflections resembled the low-field region when $\mathbf{B}\|[01\ 1]$.

4. Selection of stable domains by external-field alignment

The field-sweep experiments illustrated in Figs. 55, 57, and 58 contain a great deal of information on both the static and the dynamic properties of the nuclear-spin system in copper. As for the equilibrium spin structure, it is important to know how the total order is divided among the different domains which, without the symmetry-breaking external field, would be equivalent in a cubic crystal. To this end, it is useful to show the essentials of the field-sweep data in a different form. In Fig. 59, the neutron intensities of the three (1 0 0) and

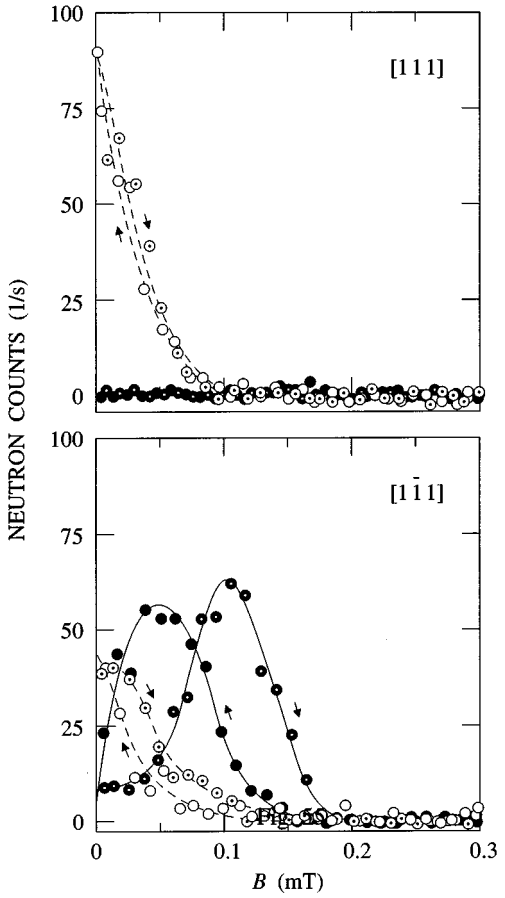

FIG. 58. Neutron intensity of the (1 0 0) (○) and $(0\ \frac{2}{3}\ \frac{2}{3})$ (●) peaks for copper vs the magnetic field for downward sweeps at the rate 10 μT/s with **B** along the [111] (upper frame) and [11 1] (lower frame) directions. The counts for upward sweeps are marked by ⊙ for the (1 0 0) peak and by ❍ for the $(0\ \frac{2}{3}\ \frac{2}{3})$ peak. From Annila *et al.* (1992).

the twelve $(0\ \frac{2}{3}\ \frac{2}{3})$ reflections have been presented using a gray scale. Rather than illustrating the results for the two fixed reflections with different alignments of **B**, the data are displayed by fixing the direction of **B** with the crystalline axes and rotating the reflections accordingly. The field-sweep data towards $B=0$, in Figs. 55, 57, and 58, have been employed in constructing the diagram. The measured signal of a symmetry-related reflection was assigned to those (1 0 0) and $(0\ \frac{2}{3}\ \frac{2}{3})$ reflections which were not directly observed. When results from equivalent field directions were available, data from the experiment for which the demagnetization correction was smallest (see Sec. V.G) were used.

The data emphasize the fact that an application of the field completely destroys the cubic symmetry in the sense that definite selection rules are observed. For example, in the high-field phase when **B** was parallel to [100], no neutron signal was seen for the (1 0 0) Bragg reflection although there was intensity at the (0 1 0) and (0 0 1) positions. In the intermediate-field region, some of the twelve $(0\ \frac{2}{3}\ \frac{2}{3})$ reflections had strictly zero intensity, while other positions showed a high intensity. These selection rules provide important tests for theoretically

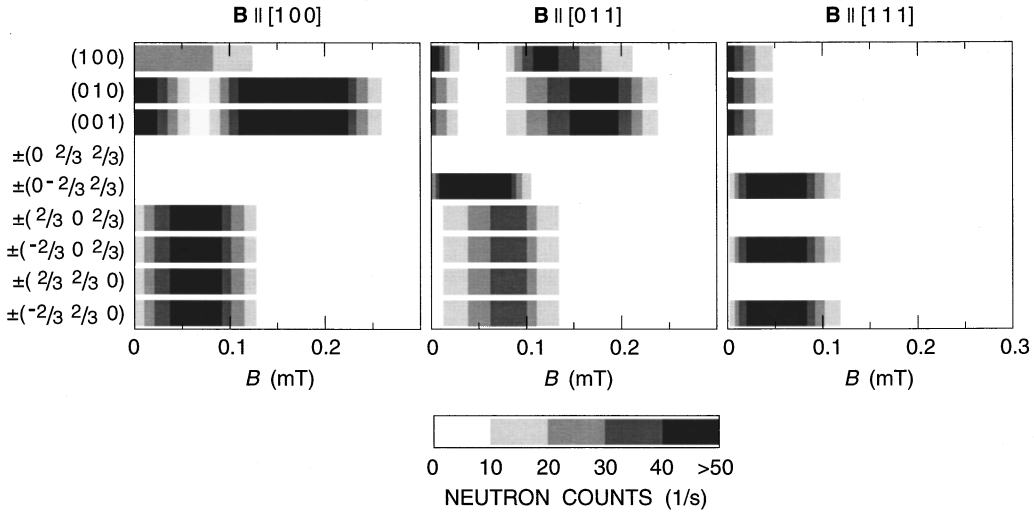

FIG. 59. Neutron intensity, according to the gray-scale shown below, for the three (1 0 0) and the twelve $(0\ \frac{2}{3}\ \frac{2}{3})$ Bragg reflections from copper nuclear spins as a function of the magnetic field parallel to the three high-symmetry crystallographic directions. From Annila *et al.* (1992).

calculated spin structures (see Sec. XV.F.2). The experimental data are in agreement with the spin configurations predicted earlier by Viertiö and Oja (1987, 1990b).

The selection rules observed especially for the $(0\ \frac{2}{3}\ \frac{2}{3})$ reflections in copper differ in important respects from typical domain selections by the field, as observed in electronic magnets. Usually, application of **B** stabilizes those zero-field domains which display sublattice magnetization perpendicular to the field, while domains with sublattice magnetization along the field become unstable. In copper, however, $(0\ \frac{2}{3}\ \frac{2}{3})$ is not stable at $B=0$ to begin with. Instead, the field induces order for certain Bragg peaks among the twelve cubic-symmetry-related $(0\ \frac{2}{3}\ \frac{2}{3})$ reflections.

Annila *et al.* (1992) were able to draw some conclusions on the spin configurations based on the data presented in Fig. 59. They reasoned as follows.

For $\mathbf{B}\|[100]$ in high fields, $0.10<B<0.25$ mT, the copper sample contained either two types of domains, in which the antiferromagnetic order propagates along $\mathbf{k}=(\pi/a)(0,1,0)$ or $\mathbf{k}=(\pi/a)(0,0,1)$, respectively, or there was a simultaneous modulation along both vectors. In the former case the structure would be single-**k** and in the latter double-**k**, but a distinction could not be made on the basis of the experimental data. In intermediate fields, $B<0.12$ mT, the $(0\ \frac{2}{3}\ \frac{2}{3})$ modulations were not observed for $\mathbf{k}\perp\mathbf{B}$, but they were clearly seen for **k** making a 45° angle with **B**. Again it was not possible to distinguish between multidomain and multiple-**k** phases.

For $\mathbf{B}\|[011]$ in high fields, the (1 0 0) order was observed in addition to the two symmetrically equivalent (010) and (001) propagations. The field dependencies were somewhat different. One can conclude that the spin configuration was not a single-**k** structure, since then only the (1 0 0) reflection or, alternatively, only the (0 1 0) and (0 0 1) Bragg peaks would have been observed. The structure could be a triple-**k** state or a double-**k** spin configuration composed of (1 0 0) and (0 1 0) propagations or, equivalently, of (1 0 0) and (0 0 1) propagations.

In intermediate fields, those $(0\ \frac{2}{3}\ \frac{2}{3})$-type reflections for which $\mathbf{k}\|\mathbf{B}$ were absent, those with $\mathbf{k}\perp\mathbf{B}$ were most intense, and those with **k** making a 60° angle with **B** were strong, too. There are most certainly two different $(0\ \frac{2}{3}\ \frac{2}{3})$-type structures, because the magnetic-field dependence for $\mathbf{k}\perp\mathbf{B}$ was clearly different from that for the other eight propagations.[9]

For $\mathbf{B}\|[111]$ in high fields, the ordered phase was not identified. In intermediate fields, the six $(0\ \frac{2}{3}\ \frac{2}{3})$ modulations perpendicular to **B** were observed.

At least in zero field, the domain population is affected by the route along which the spins are demagnetized to $B=0$, as was clearly shown by the data in Fig. 56. This raises the question of to what extent the same applies in higher fields. The experimental, clear-cut selection rules for the $(0\ \frac{2}{3}\ \frac{2}{3})$ and the (1 0 0) reflections suggest, however, that equilibrium domain populations were observed in intermediate and high fields. Besides, when the system enters the ordered region at $B=B_c=0.26$ mT, there is no antiferromagnetic order to start with, and the developing domain population should therefore correspond to the equilibrium spin distribution.

I. Intensity diagram for different field alignments

The ambitious goal of the work by Annila *et al.* (1992) was to construct the phase diagram for different directions of the external magnetic field in the plane containing the high-symmetry crystalline alignments [100], [011], and [111]. In order to span the directions between

[9]In their first paper, Annila *et al.* (1990) indirectly but erroneously concluded that only $\mathbf{k}\perp\mathbf{B}$ reflections were present.

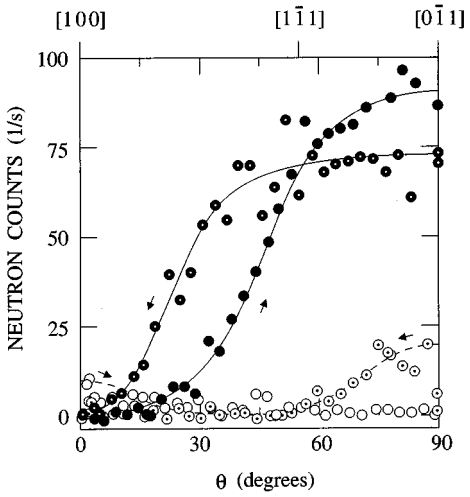

FIG. 60. Neutron intensity for the (1 0 0) peak (○) at $B=0.16$ mT and for the $(0\ \frac{2}{3}\ \frac{2}{3})$ reflection (●) at 0.09 mT when the magnetic field on the copper specimen was rotated from the [100] axis, $\theta=0°$, to the [01 1] direction, $\theta=90°$, at a rate of 3°/s. The counts collected during reverse turns are marked by ⊙ for the (1 0 0) peak and by ❍ for the $(0\ \frac{2}{3}\ \frac{2}{3})$ peak. Directions of the field rotations are indicated by arrows as well. From Annila *et al.* (1992).

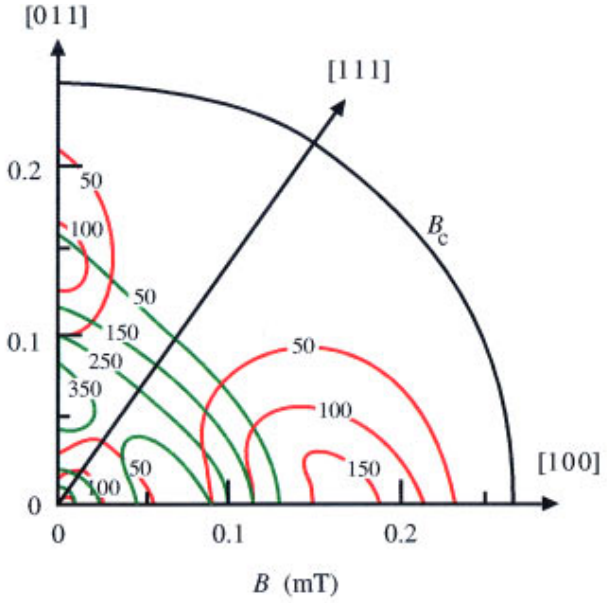

FIG. 61. Neutron intensity of nuclear spins in copper as a function of the magnetic field in the plane of the three high-symmetry directions. Counts for field alignments equivalent under the fcc symmetry are summed together. Contours (neutrons/s) for the (1 0 0) intensity are red and for the $(0\ \frac{2}{3}\ \frac{2}{3})$ intensity they are green. The antiferromagnetic phase is bordered by the second-order B_c curve. Modified from Annila *et al.* (1992).

these axes, Annila *et al.* supplemented the results of the field sweep measurements (see Sec. VII.H) with data from experiments during which the magnetic field was rotated at a constant strength. These field-rotation measurements were done at $B=0.09$ mT and at $B=0.16$ mT, for the $(0\ \frac{2}{3}\ \frac{2}{3})$ and (1 0 0) reflections, respectively. The two neutron peaks are most intense in these fields.

The results of one rotation experiment are illustrated in Fig. 60. The external field was turned first from the [100] axis, via the [11 1] field alignment, parallel to the [01 1] direction. A reverse rotation was then performed. Both field rotations took 30 s. At $B=0.09$ mT, the $(0\ \frac{2}{3}\ \frac{2}{3})$ intensity smoothly increased as the field was turned. Apart from some hysteresis, the reverse rotation displayed rather similar behavior. The absence of any large-intensity loss suggests that, during rotation, there is only one complicated multiple-**k** structure in the sample or several different structures separated by continuous transitions.

At $B=0.16$ mT, the (1 0 0) signal was initially slightly above the background but soon disappeared as the rotation continued. At the [01 1] field alignment, no neutrons above the background were observed, in disagreement with a large number of measurements that had been performed earlier in this field direction (see Sec. VII.C). The spins were then momentarily brought into the paramagnetic phase by increasing the field above B_c and by immediately lowering it back to 0.16 mT. A clear (1 0 0) reflection was then observed. When the field was rotated back towards the [100] alignment, the signal vanished before the [11 1] direction was reached, consistent with the field-sweep measurements of Fig. 58.

Supplemented with the field-rotation data, a neutron-intensity diagram was constructed on the basis of the field sweeps to $B=0$. In Fig. 61, the neutron counts obtained from reflections with the same symmetry with respect to the field direction were added together. The intensities measured for the symmetric positions were assigned to those Bragg peaks which were not directly observed. Ideally this would be equivalent to observing all three (1 0 0) and all twelve $(0\ \frac{2}{3}\ \frac{2}{3})$ reflections. Since the experiments were affected by time-dependent phenomena, hysteresis, and entropy gains, the neutron-count contours are approximate but, nevertheless, give an overall picture of the ordered phases.

The antiferromagnetic state in Fig. 61 is bounded by the critical-field line B_c, which is presumably of second order for all directions. B_c was determined from the neutron data and susceptibility measurements. In high fields, there are two (1 0 0) phases. One resides over a wide span of directions around **B**∥[100] and the other is over a smaller region about **B**∥[011].

The ordering vector for the high-field phase for **B**∥[111], is a puzzle. The region with no neutron intensity covers a large area of the phase diagram (see Fig. 61). The unknown structure seems to be metastable in the [011] directions as well, because, after the field below B_c was rotated via the [11 1] alignment parallel to the [01 1] axis, the (1 0 0) signal remained absent but could be recovered after a sweep to a field above B_c and back (see Fig. 60).

The transitions from the high-field phases to the $(0\ \frac{2}{3}\ \frac{2}{3})$ structures are all presumably of first order. A pure $(0\ \frac{2}{3}\ \frac{2}{3})$ phase is present only over a narrow interval in all directions, before the low-field (1 0 0) phase begins

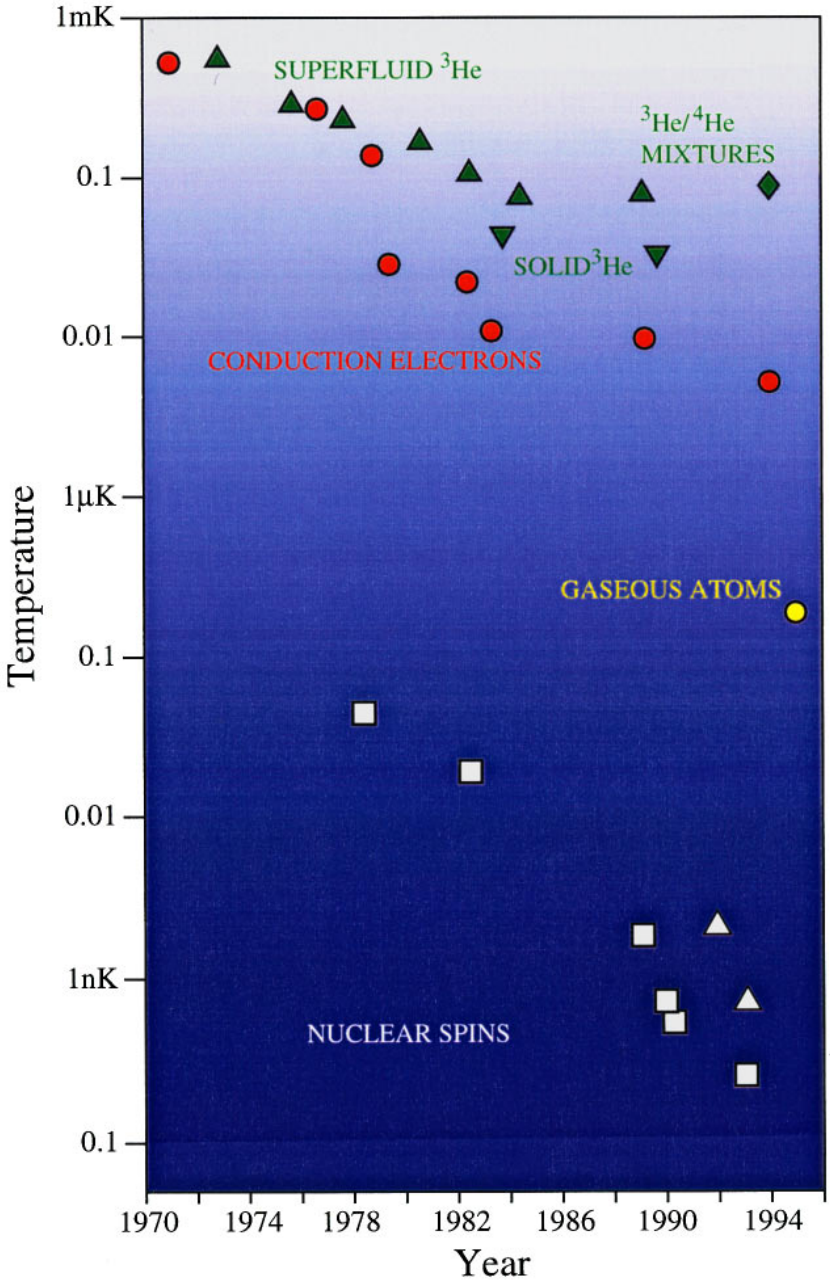

FIG. 132. Low-temperature records: green triangles, superfluid ^{3}He; green inverted triangles, solid ^{3}He; green diamond, ^{3}He/^{4}He mixture; red spheres, conduction electrons in copper; yellow sphere, Bose-Einstein condensation in gaseous Rb; white squares, nuclear spins in Cu, Ag, or Rh; white triangles, negative nuclear-spin temperatures in Ag or Rh. For references, see Sec. XVI.C.

to emerge. Therefore the same pattern as was already observed for $\mathbf{B}\|[01\,1]$, namely, a $(0\ \frac{2}{3}\ \frac{2}{3})$ order coexisting with a $(1\,0\,0)$ structure over a relatively wide interval in low fields, seems to be valid for all directions. The zero-field ground state apparently is of pure $(1\,0\,0)$ type.

J. Search for other antiferromagnetic Bragg peaks

Since the $(1\,0\,0)$ reflection was not observed in the high-field region with **B** along a [111] crystalline axis, several experiments were performed to look for other antiferromagnetic Bragg peaks (Annila *et al.*, 1992). Also, during some earlier stages of the Risø measurements, the reciprocal lattice was searched for new reflections (Jyrkkiö *et al.*, 1989; Annila *et al.*, 1990). No neutrons above the background were observed in any of these experiments.

Figure 62 summarizes the positions in the reciprocal lattice that have been investigated when the external field was applied along the $[01\,1]$ direction. The search scans, which are marked by thick lines, were performed at $B=0.07$ mT and also at $B=0$ because the $(1\,0\,0)$ signal in zero field appeared to be too small in comparison with its intensity at fields around $B=0.16$ mT. Several commensurate positions, marked by solid squares, were also investigated. The possibility of a reflection at $(0\ \frac{1}{3}\ \frac{1}{3})$, which could be a harmonic component of the $(0\ \frac{2}{3}\ \frac{2}{3})$ peak, was inspected over the whole field range below B_c, but no neutrons above the background were found. Several other commensurate points were

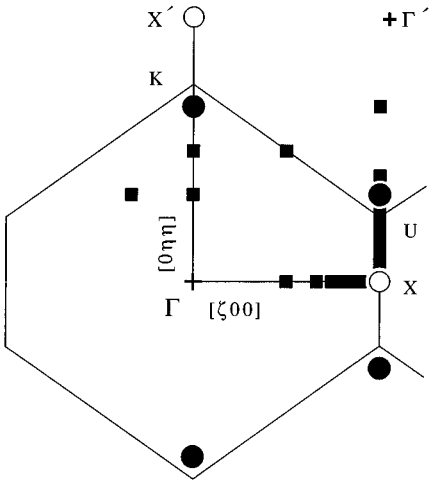

FIG. 62. First Brillouin zone of the fcc lattice in the $[0\bar{1}1]$ scattering plane. The search scans are marked with heavy lines: ●, the observed $\pm(0\ \frac{2}{3}\ \frac{2}{3})$, $(1\ \frac{1}{3}\ \frac{1}{3})$, and $(1{-}\frac{1}{3}{-}\frac{1}{3})$ reflections; ○, the observed (1 0 0) reflections; ■, commensurate positions, where neutron intensity was not found. From Annila *et al.* (1990).

investigated as well, but with the same negative result.

For a field applied in the [111] direction, the $(0\ \frac{1}{2}\ \frac{1}{2})$ and $(\frac{1}{2}\ \frac{1}{2}\ \frac{1}{2})$ positions, which correspond to conventional type-II and type-IV antiferromagnetic structures (Smart, 1966; see also Fig. 110), were investigated in all fields below B_c but again with negative results (Annila *et al.*, 1992). Type-III reflections were not in the scattering plane and thus could not be examined. The scans at $B=0.17$ mT for $\mathbf{B}\|[11\ 1]$ covered the $(0\ \eta\ \eta)$ line in the reciprocal lattice from $\eta=\frac{1}{3}$ to $\eta=\frac{3}{4}$ (the K point) and the $(\eta\ 0\ 0)$ line from $\eta=\frac{1}{3}$ to $\eta=1$ (see Fig. 62). Disappointingly, no neutrons above the background were detected. A similar scan along the $(0\ \eta\ \eta)$ line should have been performed also, using the $\mathbf{B}\|[111]$ field alignment, as this would have tested one of the subsequent theoretical suggestions for the ordering vector (Oja and Viertiö, 1992).

Theoretical calculations of the spin structure in the high-field phase for $\mathbf{B}\|[111]$ will be discussed in Sec. XV.G.

VIII. SUSCEPTIBILITY AND NMR DATA ON SILVER

An introduction and overview of investigations on nuclear magnetism in silver was given in Sec. I.E. The spin Hamiltonian can be written in the form $\mathcal{H}=\mathcal{H}_D+\mathcal{H}_{RK}+\mathcal{H}_Z$. The dominating spin-spin energy is the nearest-neighbor antiferromagnetic exchange interaction $\mathcal{H}_{RK}$, proposed by Ruderman and Kittel (1954). The dipolar force $\mathcal{H}_D$ between nearest neighbors is smaller by a factor of 3 in silver. This is the most important difference between silver and copper; $\mathcal{H}_D$ for neighboring copper nuclei is larger than $\mathcal{H}_{RK}$ by a factor of 2. Owing to the strong exchange interaction, the spin system in silver bears a close resemblance to an fcc Heisenberg antiferromagnet and has been the object of much theoretical interest; the ground-state properties are affected by frustration (Binder and Young, 1986). Because the nuclear spin $I=\frac{1}{2}$, quantum effects are expected to be prominent.

Technically, the essential difference between nuclear-ordering studies of silver and copper is the smaller magnetic moment of silver nuclei, which results, e.g., in weaker spin-spin interactions, a lower ordering temperature, and weaker coupling to the conduction electrons. These features made it possible for the Helsinki group to extend earlier studies of nuclear magnetism in metals into a new regime, namely, to negative spin temperatures. The general features of nuclear magnetism at $T<0$ were discussed in Sec. II.D.

A. Introduction to experiments at negative spin temperatures

Purcell and Pound (1951) first produced negative temperatures by means of population inversion, using LiF as the working substance. The implications of these early NMR experiments, in which $\tau_1\approx 5$ min and $T\approx -1$ K were reached, have been discussed by Ramsey (1956) and by Van Vleck (1957). Interestingly, negative temperatures are hotter than positive ones. Later, nuclear cooperative phenomena at $T>0$ and at $T<0$ were investigated extensively by Abragam and Goldman and co-workers (Abragam and Goldman, 1982) in dielectric materials like CaF_2 and LiH and by Wenckebach and co-workers (Van der Zon, Van Velzen, and Wenckebach, 1990) in $Ca(OH)_2$. These studies, however, were limited to ordering by the truncated dipolar force because adiabatic demagnetization took place in a rotating coordinate frame. The main weakness of the method (see Sec. XIV) is, however, the inevitable presence of electronic paramagnetic impurities, introduced purposely for dynamic nuclear polarization by the "solid effect." The local fields produced by the impurities probably blur, to a certain extent, some of the features of the nuclear long-range order (Abragam, 1987).

Copper, silver, and rhodium, cooled in the laboratory frame by the more general "brute force" method (Lounasmaa, 1974), without recourse to electronic impurities, have provided the most general and interesting systems, so far, for studies of nuclear magnetism near the absolute zero, at $T>0$ and $T<0$ (Hakonen, Lounasmaa, and Oja, 1991). The Helsinki group has produced negative spin temperatures in silver and in rhodium.

Negative temperatures are more difficult to achieve in metals than in insulators for two reasons: first, substantial effort is needed to reach the high initial spin polarizations and, second, eddy currents make the production of inverted spin populations difficult. First evidence for spontaneous nuclear magnetic ordering and for a negative spin temperature was found by Oja, Annila, and Takano (1991) in silver. Better data were subsequently obtained by Hakonen and Yin (1991). Later, population inversion from $T>0$ to $T<0$ was achieved very successfully in silver and rhodium (Hakonen, Nummila, Vuo-

rinen, and Lounasmaa, 1992; Hakonen, Vuorinen, and Martikainen, 1993). These feats were accomplished at ultralow temperatures by reversing the magnetic field B quickly, in a time $t \ll \tau_2 = 10$ ms, so that the nuclei had no chance to rearrange themselves adiabatically among the energy levels. In a certain sense, the transition from positive to negative temperatures occurs via $T = +\infty \rightarrow -\infty$, without crossing the absolute zero. Therefore the third law of thermodynamics is not violated.

Rhodium nuclei have been refrigerated to 280 pK and to -750 pK; these are, respectively, the current low- and "high"-temperature world records on positive and negative sides of the absolute zero (see Sec. XVI.C). Production of negative temperatures has not succeeded in copper owing to the short spin-spin relaxation time, $\tau_2 = 150$ μs, of this metal.

At negative temperatures, nuclear spins provide new models for studies of magnetism. For example, in a ferromagnet at $T<0$, the presence of long-range dipolar forces gives rise to the formation of magnetic domains of a kind not found at $T>0$ (Abragam and Goldman, 1982). The situation is more diverse in metals than in insulators (Viertiö and Oja, 1992). Since an external magnetic field does not provide a symmetry axis in brute-force-cooled Cu, Ag, or Rh, in contrast to CaF_2 and LiH cooled in the rotating frame, the spin structures in these metals have a large degeneracy. A broad spectrum of domain configurations are expected to occur.

It has sometimes been argued, that negative temperatures are fictitious quantities because they do not represent true thermal equilibrium in a sample consisting of nuclei, conduction electrons, and the lattice. However, the experiments on silver, in particular, show conclusively that this is not the case: the same interactions produce ferro- or antiferromagnetic nuclear order in silver, depending on whether $T<0$ or $T>0$ (see Sec. VIII.C.3). Besides, true equilibrium, in the strictest sense of the word, hardly ever exists in nature. Furthermore, the large difference between the temperatures of conduction electrons and of nuclei has no effect on the nuclear-spin structures.

B. Nuclear magnetic susceptibility of silver

The first measurements of the magnetic susceptibility of silver down to the ordering temperature at $T>0$ were made by Oja, Annila, and Takano (1991). The susceptibility was measured only as a function of spin entropy; the spin temperature was not determined. For this reason, and also because the susceptibility scale was not calibrated, the data did not give much information about the thermodynamics of the spin system.

These workers first realized and experimentally demonstrated that negative spin temperatures in silver can be reached by a rapid field reversal (see Fig. 63). NMR emission, instead of absorption, showed that $T<0$. The field flip caused, however, a large loss of polarization.

The work on silver was continued subsequently by Hakonen and Yin (1991). They performed extensive

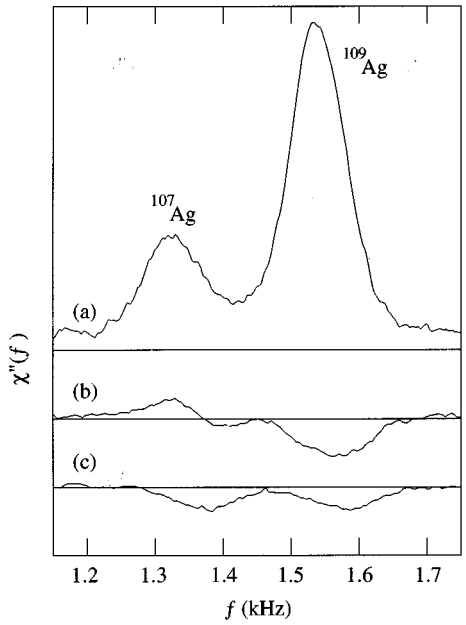

FIG. 63. Production of a negative spin temperature in silver. (a) Initial NMR spectrum at 0.77 mT. (b) Spectrum at –0.77 mT after a quick reversal of the field. The negative absorption, i.e., emission of the ^{109}Ag spins indicates that $T_{109}<0$. However, T_{107} still appears to be positive, perhaps owing to a very low temperature T_{ss} of the interaction reservoir (see Fig. 6). (c) Spectrum after lowering the field to zero and bringing it back to –0.77 mT. Now $T_{107} = T_{ss} = T_{109} < 0$. From Oja, Annila, and Takano (1991).

measurements of the magnetic susceptibility and entropy of silver nuclei down to the extremely low spin temperature of 0.8 nK and, at $T<0$, up to -4.3 nK. These temperatures are much lower than those reached in copper (see Sec. V.A) because the interactions are weaker in silver. The highest initial polarizations in the experiments were $p = 0.72$ at $T>0$ and $p = -0.40$ at $T<0$. The work has been described in considerable detail by Hakonen and Yin (1991).

All magnetic-susceptibility measurements were made on a bundle of polycrystalline silver foils. A typical specimen weighed 2 g and consisted of 78 foils, 25 μm $\times$4.5 mm $\times$40 mm along the x, y, and z directions, respectively. The material, of 99.99% nominal purity, was selectively oxidized at 750 °C for 20 h in 0.1 mbar pressure of dry air to neutralize the magnetic impurities, which otherwise might have shortened the spin-lattice relaxation time τ_1 in small magnetic fields. The heat treatment and oxidization increased the residual resistivity ratio (RRR) of the silver sample from 100 to 900. Details of sample preparation were discussed in Sec. III.D.

The dynamic susceptibility $\chi'(f) - i\chi''(f)$ of the silver specimens was measured by using low-frequency SQUID-NMR techniques, which were described in Sec. III.E. Two coaxial mu-metal cylinders were used as magnetic shields around the silver foils to exclude the ± 3-mT remanent field of the main demagnetization solenoid. Inside the shields, three small coils were as-

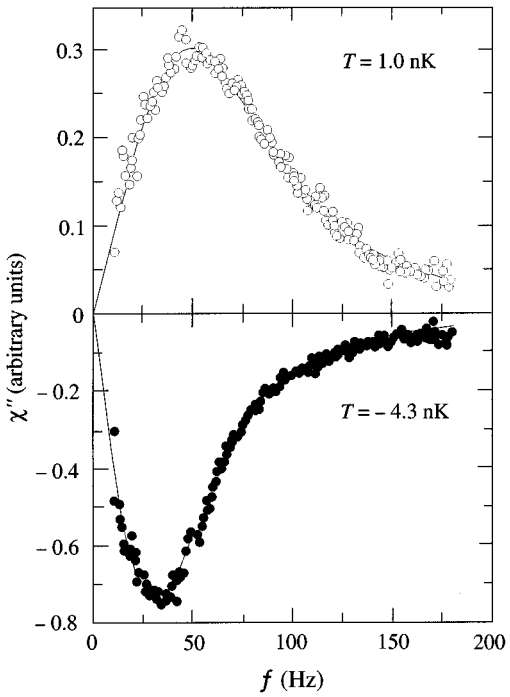

FIG. 64. NMR absorption and emission spectra for silver measured in zero magnetic field: ○, at $T=1.0$ nK; ●, at $T=-4.3$ nK. Solid curves are fits of Lorentzian line shapes $\chi_L''(f)-\chi_L''(-f)=A/[1+(f-f_0)^2/\Gamma^2]-A/[1+(f+f_0)^2/\Gamma^2]$ to the experimental data, with $A=0.457$, $f_0=39.6$ Hz, and $\Gamma=59.6$ Hz at $T=1$ nK and with $A=-0.911$, $f_0=19.8$ Hz, and $\Gamma=43.8$ Hz at $T=-4.3$ nK, respectively. Note the different vertical scales for $T>0$ and $T<0$. Γ is the half-width of the NMR peak. From Hakonen, Yin, and Lounasmaa (1990).

sembled for NMR experiments, as illustrated in Fig. 16. Most NMR measurements were performed in a steady field $\mathbf{B}=B_y\mathbf{y}$ along the y direction, i.e., parallel to the 4.5-mm-long edge of the sample foils. This field was produced by a saddle-shaped coil while the rf excitation field $B_z^{\rm rf}$ was generated by a solenoid. An astatic pair of coils was used for pickup (see Fig. 16).

The spin temperature was measured as described in Sec. IV. Polarization was determined from the NMR absorption χ'', recorded in a field $B \gg B_{\rm loc}=35$ μT, by using the equation $p=A\int\chi''(f)df$, where f is the NMR excitation frequency. A small field, $B_y=191$ μT, was chosen for the polarization measurements because the separate isotopic identity of the spins is then largely lost, which results in a single exchange-narrowed NMR line, integrable with good precision. The accuracy of the polarization calibration was estimated as 5%, at both positive and negative spin temperatures.

NMR data on silver at $T=1$ nK and -4.3 nK (Hakonen, Yin, and Lounasmaa, 1990) are displayed in Fig. 64; χ'' was measured by increasing the frequency at the rate $df/dt=1$ Hz/s. At $T<0$, χ'' was negative, indicating that, instead of absorbing, the spin system was emitting energy. The magnitude of χ'' was almost three times higher at negative temperatures because of the large ferromagnetic susceptibility. The peak frequency of the

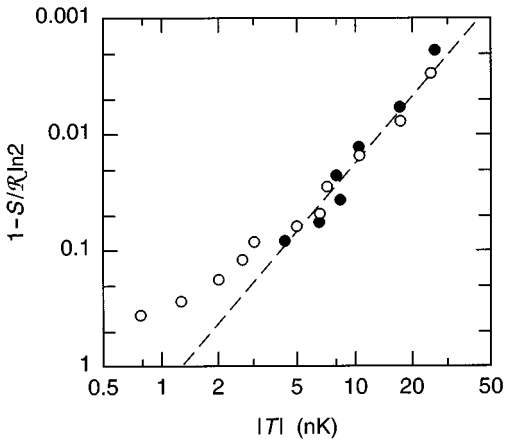

FIG. 65. Reduced entropy $1-S/\mathcal{R}$ ln2 vs the absolute value of the spin temperature in silver: ○, $T>0$; ●, $T<0$. The dashed line displays the leading $1/T^2$ term of the high-T expansion. From Hakonen, Yin, and Lounasmaa (1990).

NMR spectra is clearly lower at $T<0$ than at $T>0$. The experimental points fit nicely to Lorentzian lineshapes.

The nuclear entropy, calculated from polarization [see Eq. (26a)], is shown in Fig. 65 as a function of $|T|$. The high-temperature expansion fits the data above 5 nK, but clear deviations from the $1/T^2$ law are observed below. Within the experimental accuracy, the results at $T>0$ and at $T<0$ coincide.

In Fig. 66, the absolute value of the inverse static susceptibility $|1/\chi'(0)|$ of silver, calculated from the Kramers-Kronig relation [see Eq. (27)] $\chi'(0)=(2/\pi)\int(\chi''/f)df$ by integrating from 30 to 180 Hz, is plotted as a function of $|T|$ in nanokelvins. Clearly, the susceptibility at $T<0$ is much larger than at $T>0$. This results from the fact that the spin system tries to maximize its energy at constant entropy when $T<0$, as discussed in Sec. II.D.3. Since the exchange interaction is antiferromagnetic in silver, the maximum-energy state

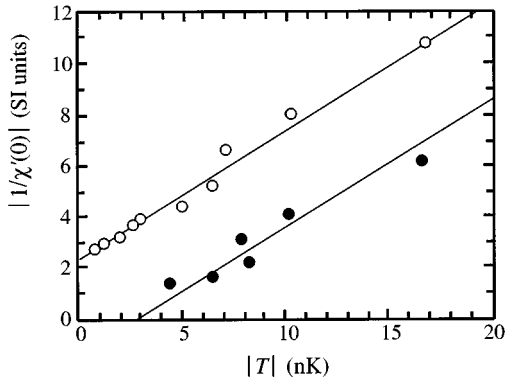

FIG. 66. Absolute value of the inverse static susceptibility $|1/\chi'(0)|$ vs the absolute value of temperature for silver: ○, measured at $T>0$; ●, measured at $T<0$. Straight lines correspond, respectively, to the antiferromagnetic and ferromagnetic Curie-Weiss laws. The external magnetic field $B=0$. From Hakonen, Yin, and Lounasmaa (1990).

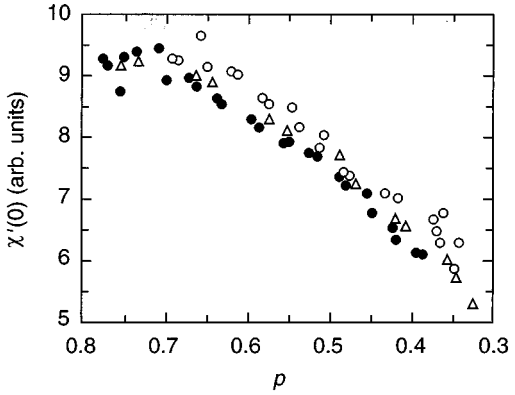

FIG. 67. Static susceptibility $\chi'(0)$ of silver as a function of polarization p, which decreases with time after demagnetization. The different symbols refer to three separate cooldowns. From Oja, Annila, and Takano (1991).

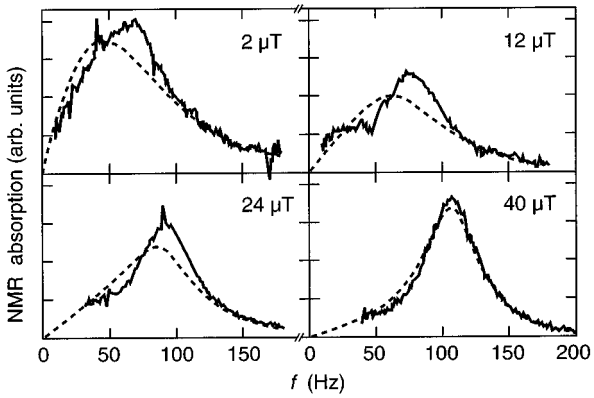

FIG. 68. NMR spectra of silver nuclei measured 5 min after demagnetization had been completed to the final field denoted in each frame. Dashed lines depict data recorded in the paramagnetic phase about 1 h later. For further explanations, see text. From Hakonen and Yin (1991).

has a ferromagnetic alignment of spins, and the susceptibility is large.

The data in Fig. 66 display an antiferromagnetic Curie-Weiss law, $\chi = C_{\mathrm{Ag}}/(T-\theta_A)$ at positive temperatures, with $\theta_A = -4.8$ nK; $C_{\mathrm{Ag}} = 2$ nK is the Curie constant. At $T<0$, a ferromagnetic law, $|\chi| = C_{\mathrm{Ag}}/(|T|-\theta_F)$ with $\theta_F = 2.8$ nK, was obtained. According to the mean-field theory, $|\theta_A| = |\theta_F|$ (see pp. 715 – 718 in Ashcroft and Mermin, 1976). By averaging the two measured values and taking into account the Lorentz and demagnetizing factors [see Eq. (34)], one finds $\theta/C_{\mathrm{Ag}} = -2.5$ in accordance with data obtained using spin dynamics (Oja, Annila, and Takano, 1990).

It is worth noting that both sets of results in Fig. 66 follow the Curie-Weiss law to the lowest temperatures. The susceptibility displays no saturation as would be expected close to an antiferromagnetic transition temperature when $T>0$ (Huiku *et al.*, 1986). Furthermore, in the measurements by Hakonen, Yin, and Lounasmaa (1990), no changes were observed in the NMR lineshapes that could be assigned to actual antiferromagnetic or ferromagnetic ordering at $T>0$ or at $T<0$, respectively. Clearly, the transition temperatures were not reached in these early experiments.

C. Nuclear ordering of silver at $T>0$

1. Search for the transition

The first signs of spontaneous nuclear ordering in silver were seen in the experiments of Oja, Annila, and Takano (1991). Spin entropies down to $0.50\mathcal{R}\ln 2$, corresponding to polarizations up to $p = 0.78$, were obtained. Indications of antiferromagnetic ordering were detected in the static magnetic susceptibility, which showed clear saturation at the beginning of the warmup after cooling to $T<1$ nK (see Fig. 67). The amount of useful data gathered in these experiments was, however, somewhat marginal.

More extensive and successful measurements then followed (Hakonen and Yin, 1991; Hakonen, Yin, and Nummila, 1991). The experimental procedure and the preparation of the specimens were the same as already described, except for a simple but important improvement: folding of the sample foils (see insert in Fig. 15) to increase rigidity, which resulted in a decrease of vibrational heat produced in the specimen. The highest polarization reached by the silver nuclei was $p = 0.94$, which corresponds to a 190 μK nuclear-spin temperature in the 7.3-T field.

The clearest indication of antiferromagnetism in silver came from changes in the NMR spectra upon ordering. The results depended on the way in which the demagnetization was performed. Usually the magnetic field was reduced directly to its final value. Figure 68 depicts four examples of the recorded line shapes; the dashed curve corresponds to the paramagnetic state. The spectra display an upward frequency shift after demagnetization, especially in low fields.

The most important observable in these experiments was, however, again the static susceptibility, $\chi'(0) = (2/\pi)\int(\chi''/f)df$, obtained by integrating over the measured NMR lines. Figure 69 illustrates the evolution of $\chi'(0)$ with time. The data, which correspond to a steady increase of temperature and entropy, display several features that may be associated with a magnetic transition. The fast initial decrease of susceptibility at 2 μT was probably caused by the rapid disappearance of the supercooled paramagnetic phase. Next, in small fields, a slight increase of $\chi'(0)$ was observed before a maximum, marked by an arrow, was reached; a monotonic decrease of susceptibility then started. In higher fields, there was only a kink in the $\chi'(0)$ vs t curve, and sometimes no transition at all could be identified.

In analogy with electronic magnets, the maximum of susceptibility in small fields was regarded as an indication of antiferromagnetic order in the nuclear-spin system of silver. The kink was identified approximately with the Néel temperature T_{N}. The values $p_{\mathrm{N}} = 0.765 \pm 0.02$ and $T_{\mathrm{N}} = (560 \pm 60)$ pK were deduced from these experiments. Since demagnetization of the

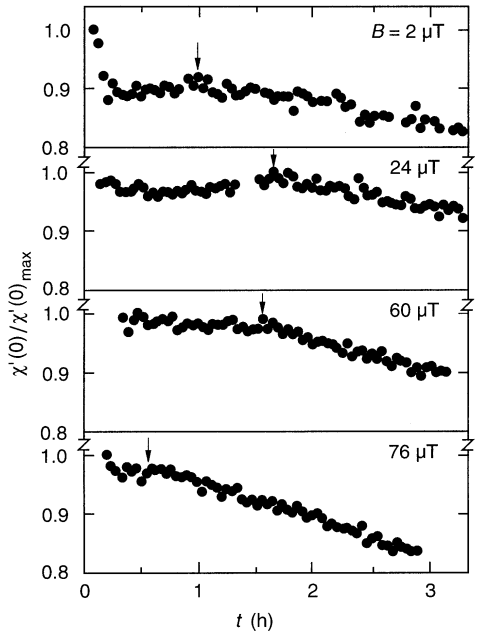

FIG. 69. Static susceptibility of silver nuclei as a function of time after demagnetization to four different external magnetic fields. Each set of data is scaled by the maximum susceptibility $\chi'_{\max}(0)$ for that run. Small arrows indicate the transition point from the ordered to the paramagnetic phase. From Hakonen and Yin (1991).

sample was adiabatic, critical polarization could be converted to critical entropy using the equations of the paramagnetic state [see Eq. (26a)]; the resulting phase diagram will be discussed in Sec. VIII.C.3.

2. Magnetic preparation of the sample by the demagnetization scheme

Hakonen and Yin (1991) also conducted experiments in which the sample was "prepared" by first demagnetizing it to a small reversed field, –5 μT, before the sweep to the final field. These measurements were initially motivated by the strange shape of the phase diagram, to be discussed in Sec. VIII.C.3, which suggested that the "real" ground state was hidden by a large hysteresis with respect to the external field. Some of the results are illustrated in Fig. 70. In small final fields, the absorption at low frequencies was enhanced as shown by the first curve. When the final field was 24 μT, the NMR absorption split into two resonances, one below and the other slightly above the peak in the paramagnetic state. There was a transfer of intensity from the low-frequency peak to the high-frequency mode as the spins warmed up. The line shapes were fairly reproducible, although the actual spectral weights of the peaks varied from run to run.

The frequency of the low-f mode, f_d, obtained from measurements in which the sample was prepared in a reversed field, is independent of B, as is illustrated by Fig. 71. The position of the upper absorption peak, f_u, is also shown, as well as the location of the paramagnetic

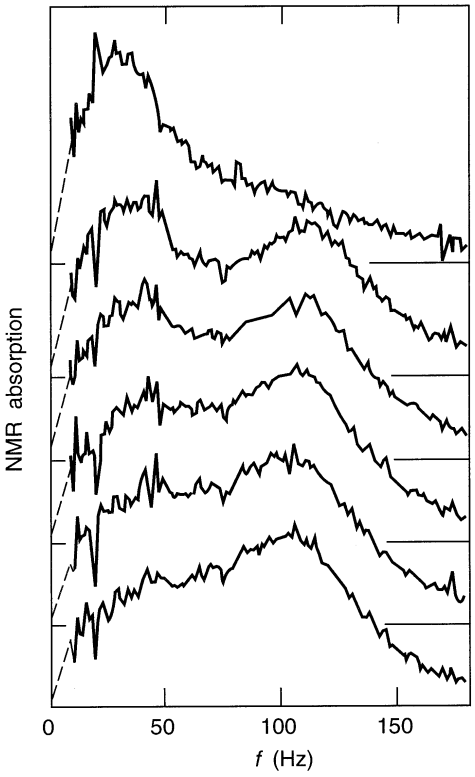

FIG. 70. NMR absorption spectra of silver, after the sample-preparation sequence $B = 190\ \mu\text{T} \rightarrow -5\ \mu\text{T} \rightarrow 24\ \mu\text{T}$, measured every 15 min. The topmost curve, however, was recorded at $B = -5\ \mu$T, just before the spectrum below. The lowest curve corresponds to the paramagnetic state. The successive spectra are shifted downwards along the vertical axis as shown. From Hakonen and Yin (1991).

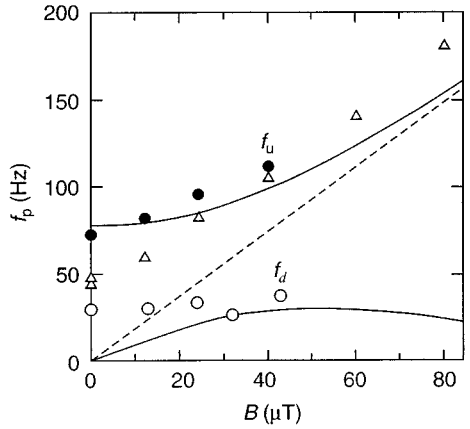

FIG. 71. Frequencies of the NMR peak amplitudes f_p vs the external magnetic field for silver. The antiferromagnetic branches are ●, f_u and ○, f_d. The peak position in the paramagnetic region (△) was determined slightly above T_N. Dashed line, Larmor frequency $f = \gamma B/2\pi$, averaged over the two silver isotopes. The experimental data were taken from Hakonen, Yin, and Nummila (1991). Solid lines, calculated positions of antiferromagnetic resonances in a single-**k** structure as given by Eq. (153) (Heinilä and Oja, 1996).

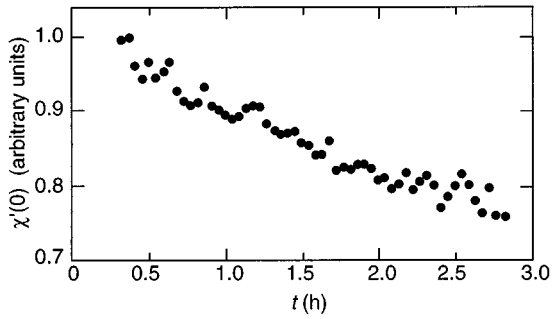

FIG. 72. Static susceptibility of silver vs time obtained from the NMR spectra shown in Fig. 70. From Hakonen and Yin (1991).

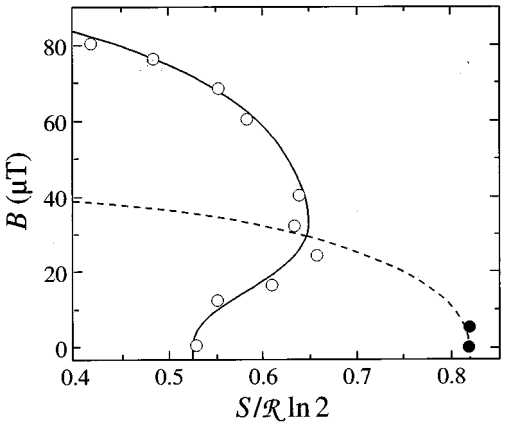

FIG. 73. Phase diagram of nuclear spins in silver at $T>0$ (full curve) and at $T<0$ (dashed curve) in a magnetic field (B) vs reduced entropy ($S/\mathcal{R}$ ln2) plane. Inside the solid curve, the spin system is antiferromagnetically ordered. The experimental points at $T>0$ (○) are from the paper by Hakonen, Yin, and Nummila (1991). The dashed curve for $T<0$ displays the phase boundary between the ferromagnetic domain state (inside) and the paramagnetic region. The curve was determined by the two data points and its intercept with the $S=0$ axis. The shape of the dashed curve is based on the mean-field theory [see Eq. (93)] by assuming a linear relationship between S and T. Modified from Hakonen, Nummila, Vuorinen, and Lounasmaa (1992).

peak. The upper absorption peak f_u was determined from spectra recorded when demagnetization proceeded directly to the final field. The position of the upper peak in experiments with magnetic sample preparation was slightly higher in frequency.

When the line shapes illustrated in Fig. 70 are integrated using the Kramers-Kronig relation [see Eq. (27)], one obtains the susceptibility vs time dependency shown in Fig. 72. It can be seen that $\chi'(0)$ decays continuously with time; the behavior is very different from the case when the final field $B=24$ μT was reached directly (see Fig. 69). Furthermore, the initial susceptibility is about 20% higher than in measurements during which demagnetization proceeded directly to the final field. Signs of a plateau in the $\chi'(0)$ vs t curves could be seen, however, in experiments with magnetic preparation to final fields lower than 10 μT or higher than 50 μT.

Another feature that is difficult to understand is that, based on measurements illustrated in Fig. 69, the lowest NMR absorption curve in Fig. 70 corresponds to the paramagnetic state, although the enhanced absorption at low frequencies suggests that antiferromagnetism is still present.

Hakonen and Yin (1991) discussed various possibilities to explain these findings. The most natural reason for the decay of $\chi'(0)$ with time would be the coexistence of a supercooled paramagnetic phase together with an ordered state, since the susceptibility of the paramagnetic phase well below T_N is higher than the susceptibility of the ordered state. Another possibility would be that the spin structure obtained after sample preparation in a reversed field is a nonequilibrium ordered state, or a nonequilibrium combination of different domains, with a slow relaxation towards equilibrium. The enhanced low-f part of the NMR spectrum above T_N is a problem, however. It is difficult to understand why the spectrum should deviate from the paramagnetic shape.

3. Antiferromagnetic phase boundary

Figure 73 (see also Fig. 4) summarizes the NMR results on magnetic ordering in silver and displays the phase diagrams for the ferro- and antiferromagnetic states in the B-S plane (Hakonen, Nummila, Vuorinen, and Lounasmaa, 1992). At $T>0$, the phase boundary between the paramagnetic and antiferromagnetic phases is of second order in high fields. In small fields, below approximately 30 μT, the transition is presumably of first order, as is suggested by the fact that the positions of the antiferromagnetic features in the NMR lineshapes do not change when the spins warm towards T_N.

The shape of the phase diagram at $T>0$ in Fig. 73 is interesting: silver seems to order magnetically more easily in a small field than in $B=0$. The matter has been discussed at some length by Hakonen and Yin (1991). If the phase diagram in the B-T plane is similar in form to that in the B-S plane, as in Fig. 4, the Clausius-Clapeyron equation of magnetic systems, $dB/dT=-(S_p-S_o)/(M_p-M_o)$, would imply that M_o, the magnetization in the ordered state, is larger than M_p in the paramagnetic phase, since thermodynamic stability requires that $S_p>S_o$. This would suggest ferromagnetism. All susceptibility data, however, point towards antiferromagnetism at $T>0$. Therefore the phase diagram in the B-T plane must have the conventional shape with $dB/dT<0$. This means that the isentropes must be nonmonotonic, which agrees with the crossing of the measured entropies in the paramagnetic phase as illustrated in Fig. 74.

Hakonen and Yin (1991) directly measured T_N in $B=32$ μT. They found $p_N=0.67\pm0.02$ and $T_N=(700\pm60)$ pK. Since $T_N=(560\pm60)$ pK in $B=0$, the shape of the phase boundary in the B-T plane should be similar to that in the B-S plane. However, the measured Néel temperatures in $B=0$ and 32 μT were not considered convincing proof of a positive dB/dT in low fields

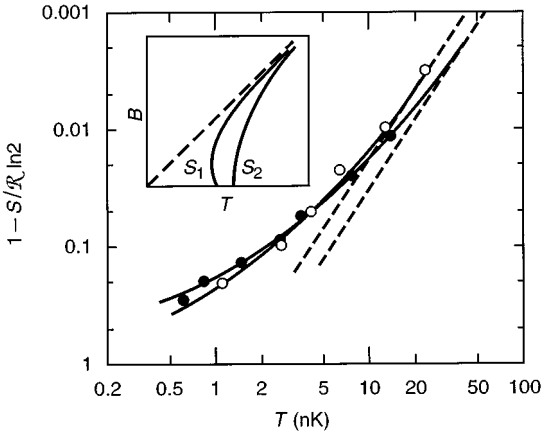

FIG. 74. Reduced entropy $1-S/\mathcal{R}$ ln2 of silver vs temperature: ○, $B=0$; ●, $B=32$ μT. Note the crossing of the two curves; the inset illustrates the shape of the isentropes S_1 and S_2 ($>S_1$). The dashed lines display the leading $1/T^2$ terms of the high-temperature expansions. From Hakonen and Yin (1991).

since, in addition to the error margins of T_N quoted above, there was the possibility of an additional 10% systematic error owing to the relative calibrations of p between 0 and 32 μT.

In their discussion, Hakonen and Yin (1991) mention the additional possibility that silver nuclei could display some exotic non-Néel-type short-range order, similar to that discussed by Anderson (1973). If this were the case, this suggestion would provide a new interpretation for several observations, like the shape of the phase diagram, the decay of $\chi'(0)$ with time (see Fig. 72), and the NMR line shapes of Fig. 70.

4. Number of antiferromagnetic phases

It is difficult to decide, on the basis of experimental data, how many antiferromagnetic structures there are in the magnetically ordered region of silver spins. The explanation preferred by Hakonen, Yin, and Nummila (1991) is that there is only one antiferromagnetic phase in the whole ordered region, a single-**k** structure. The two antiferromagnetic peaks, centered at frequencies f_u and f_d (see Fig. 71), would then correspond to the two antiferromagnetic resonance modes of a single-**k** structure with type-I order (Kumar *et al.*, 1986; Heinilä and Oja, 1996). The enhancement of the f_d mode after an excursion to a small reversed field could result from a reorientation of spins in the various ordered crystallites.

In principle, the f_u and f_d modes may also result from two different ordered phases, for example, single-**k** structures, and the intensity of the f_u and f_d modes could reflect the relative proportions of the two coexisting phases.

Hakonen, Yin, and Nummila (1991) also point out that the behavior of the antiferromagnetic absorption peaks can be used to argue for a phase transition in fields on the order of $B=50$ μT. As is shown by Fig. 71, the shift of the upper antiferromagnetic mode at $f=f_u$ from the paramagnetic line vanishes around this field, and the intensity of the lower mode becomes very small. This transition would have to be of second order.

The NMR behavior of silver is distinctly different from that of copper. In polycrystalline Cu, Huiku *et al.* (1986) found two phases that displayed different resonance frequencies (see Fig. 68): a low-field peak below the paramagnetic resonance and a high-field peak above the paramagnetic line. In silver, similar frequency shifts were observed but in small fields only. In addition, the frequency of the f_u mode in silver depends on B, in contrast to the behavior observed in copper.

5. Comparison with theory

At $T>0$, the general features of ordering seem to agree with theoretical predictions. The measured transition temperature, 560 pK in zero field, agrees well with the value, 500 pK, obtained from Monte Carlo simulations by Viertiö (1990). The first-order nature of the transition in small fields is reproduced by these calculations as well, but the critical entropy was not computed. The theoretically calculated critical field, $B_c=140$ μT, is somewhat higher than the extrapolated experimental value of 100 μT. The prediction for T_N depends sensitively, however, on the spin I. The Monte Carlo results were obtained for classical spins. An estimate for the quantum correction due to the spin $I=\frac{1}{2}$ of silver nuclei, to be discussed in Sec. XV.C.3.c, yields a factor-of-3 too high ordering temperature, $T_N=1.5$ nK. The same T_N is also predicted by the spherical model calculation of Harmon *et al.* (1992).

The spin-spin interactions of silver have been computed from the first-principles electronic band structure (Harmon *et al.*, 1992). These calculations will be discussed in Sec. XV.A. The overall strength of the theoretically calculated spin-spin interaction is in good agreement with the values obtained from susceptibility data (Hakonen, Yin, and Lounasmaa, 1990) and from NMR measurements (Poitrenaud and Winter, 1964; Oja, Annila, and Takano, 1990; Hakonen, Nummila, and Vuorinen, 1992).

Comparison of the measured susceptibility against spherical-model calculations gives the best fit if the strength of the RK interaction is decreased in absolute value from $R=-2.3$ to $R=-1.7$ (Harmon *et al.*, 1992). A weaker coupling would also decrease the discrepancy between the experimental and theoretical ordering temperatures.

The magnetic phase diagram of silver has been investigated in several calculations. One might naively expect that there is only a single ordered state because the forces between silver atoms are rather isotropic since the Ruderman-Kittel interaction dominates. It turns out, however, that for a type-I fcc antiferromagnet with only isotropic, nearest-neighbor interactions, there is a transition between a low-field single-**k** structure and a high-field triple-**k** state (Heinilä and Oja, 1993a, 1994b; see Sec. XV.D.6). For isotropic interactions, the spin structures do not depend on the direction of the field with

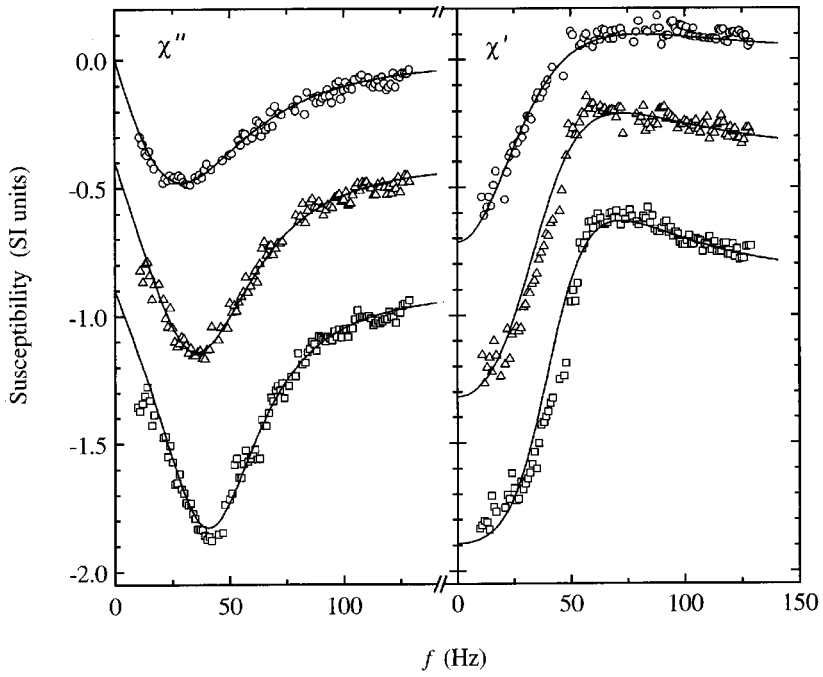

FIG. 75. NMR emission χ'' and dispersion χ' curves vs frequency for the nuclear-spin system of silver at $T<0$, measured in $B=0$ for reduced entropies: ○, $S/\mathcal{R}$ ln2=0.87; △, $S/\mathcal{R}$ ln2=0.80; □, $S/\mathcal{R}$ ln2=0.73. These entropies correspond in the paramagnetic state to polarizations $p=-0.42$, -0.51, and -0.59, respectively. In both frames, the zeros for the two lower curves have been shifted downwards by 0.4 and 0.9 units, respectively. From Hakonen, Nummila, Vuorinen, and Lounasmaa (1992).

respect to crystalline axes, which is the case when the dipolar interaction between silver nuclei, albeit relatively small, is taken into account. The ground-state calculations including dipolar interactions are discussed in detail in Sec. XV.D.7. The overall conclusion from various theoretical models is that there should be a single-**k** → triple-**k** transition in the field interval $B/B_c=0.3-0.6$ when **B** is aligned along the [001] or [110] crystalline axis, but that when **B** is parallel to [111] a triple-**k** structure exists only in a small region at intermediate fields (Viertiö, and Oja, 1987; Viertiö, 1992; Heinilä and Oja, 1993a). In addition, a transition between two different single-**k** structures is possible in low fields. However, neutron-diffraction measurements of Tuoriniemi, Nummila *et al.* (1995) on silver (see Sec. IX) revealed only one single-**k** structure in fields below B_c when $\mathbf{B}\|[001]$.

The NMR frequencies of type-I fcc antiferromagnets have been calculated by Kumar *et al.* (1986) by solving the mean-field equations of motion. By comparing the peak positions f_u and f_d of the observed antiferromagnetic resonances with theoretical predictions for a single-**k** structure, Hakonen, Yin, and Nummila (1991) concluded that such a configuration can describe the data in the whole ordered region. The matter has been studied theoretically in more detail by Heinilä and Oja (1996), who also conclude that the observed antiferromagnetic resonances can be accounted for by a single-**k** structure. For more details, see Sec. XV.E.2.

D. Nuclear ordering in silver at $T<0$

1. Observation of the ferromagnetic transition

The final success, nuclear ordering in silver at $T<0$, came in 1991 (Hakonen, Nummila, Vuorinen, and Lounasmaa, 1992). In order to facilitate the production of negative temperatures by rapid field reversal, a new coil arrangement and improved radiation shields were carefully prepared to prevent eddy currents, which must have been the main problem during previous, less successful experiments. Two saddle-shaped static field coils B_x and B_y and a solenoid B_z were assembled on a coil former inside the brass radiation shield, which had four cuts along its length (see Fig. 53). An astatically wound pickup coil was oriented parallel to the z axis.

The final phase of the demagnetization sequence (see Sec. III.C) was modified, as well. Degaussing of the second-stage magnet was employed: +7.4 T → –0.1 T → +0.02 T → 0. This guaranteed proper operation of the SQUID measurement system, which was susceptible to vibrational noise in the presence of even a small remanent field between 0 and 5 μT. Fortunately, the field-cycling procedure did not substantially decrease the largest initial polarization, $p=0.85$, achieved in these experiments. The external demagnetization field was in the vertical direction, $\mathbf{B}=B\mathbf{z}$.

The solenoidal magnetic field B_z, employed in the rapid field reversal, was typically 400 μT. The best inversion efficiency, 90%, was reached for small initial polarizations on the order of $p=0.3$. At higher polarizations, the results varied irregularly. Despite many efforts by changing the speed, symmetry, and magnitude of the field reversal, the optimum inversion efficiency was only 60–75% at $p=0.85$. Polarizations at $T<0$ were thus limited to $p\approx-0.65$.

Figure 75 illustrates NMR line shapes measured in zero field at $T<0$. Instead of absorption, the spin system is again emitting energy (see Fig. 64). The emission maximum shifts towards higher frequencies with increasing $|p|$. The solid curves are simultaneous fits of the emission and dispersion curves to Lorentzian line shapes.

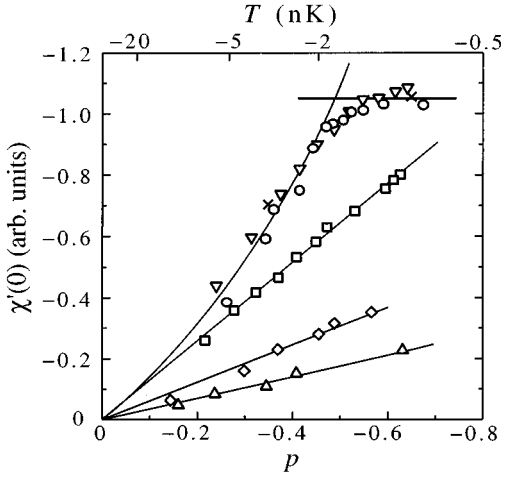

FIG. 76. Static susceptibility $\chi'(0)$ vs polarization p of silver nuclear spins at $T<0$: ○, measured in a magnetic field $B_y=0$, ▽, $B_y=5$; □, $B_y=20$; ◇, $B_y=50$; △, $B_y=100$ μT; ×, $B_z=5$ μT. The scale on top gives the estimated temperature based on the formula $1/|p|-1=0.55$ $|T/\mathrm{nK}|$, which applies at $B=0$; values to the right of -2 nK are only suggestive. From Hakonen, Nummila, Vuorinen, and Lounasmaa (1992).

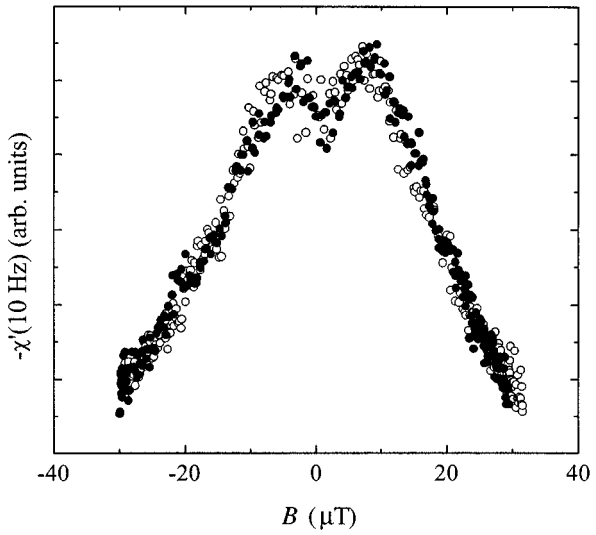

FIG. 78. Transverse ac susceptibility $-\chi'(10\ \mathrm{Hz})$ of silver, measured at $p=-0.65$ while sweeping the magnetic field back and forth: ○, sweeps to the left; ●, sweeps to the right. **B** was oriented perpendicular to the sample foils. From Hakonen and Vuorinen (1992).

Figure 76 displays the perpendicular static susceptibility $\chi_\perp=\chi'(0)$, integrated from the Kramers-Kronig relation [see Eq. (27)], as a function of polarization in zero field and at four different values of B_y. In addition, data obtained in the parallel field $B_z=5$ μT are also shown. In zero field and at 5 μT, there is first a monotonic increase of $\chi'(0)$ with p, which then saturates in the region $p=-0.4$ – -0.5. This behavior is caused by ferromagnetic ordering; the susceptibility is governed by dipolar interactions through the formation of ferromagnetic domains, which, in the ideal case, would lead to $\chi_\perp=-1$ in the silver sample. Two possible configurations are shown in Fig. 77.

In zero field and at small polarizations the susceptibility of silver is of the form $\chi'(0)=\chi_0/[1-(R+L-D_z)\chi_0]$, [see Eq. (34)] where $\chi_0=1.30p$ is the Curie-law value for a noninteracting spin system and the Lorentz factor $L=\frac{1}{3}$. The uppermost curve in Fig. 76 is the best fit of points in the region $|p|<0.45$ by this equation, using $R=-1.1$, which differs significantly from the value $R=-2.5\pm0.5$ obtained from other NMR experiments (see Sec. XI.B.2). This indicates that substantial deviations from the mean-field behavior are already taking place at intermediate polarizations. Within the scatter of the measured data, the same curve fits the experimental results at $B=0$ and at $B=5$ μT. As is typical for dipolar ferromagnetism (Abragam and Goldman, 1982), the data do not saturate completely even when the polarization is high but, nevertheless, it was possible to describe the results for $|p|>0.55$ approximately by a constant value, $\chi=\chi_{\mathrm{sat}}=-1.05$.

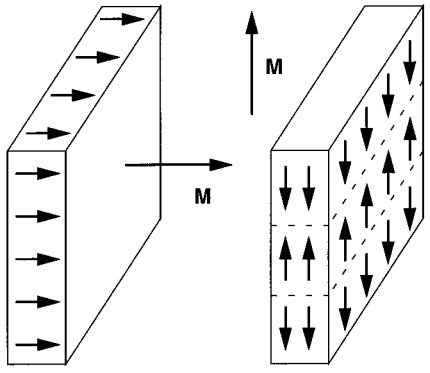

FIG. 77. Two examples of proposed (Viertiö and Oja, 1992) domain configurations in flat silver specimens. The single-domain structure at left is possible only when **M** is perpendicular to the surface of the foils. In the multidomain structure at right, **M** is parallel to the foils.

Hysteresis is often a characteristic feature of ferromagnetic ordering, best seen in a χ' vs B plot. Figure 78 depicts transverse ac susceptibility at $f=10$ Hz (Hakonen and Vuorinen, 1992) when the field was swept back and forth between ±30 μT at $p=-0.65$. The dip in the middle is due to the fact that the ratio $\chi'(10\ \mathrm{Hz})/\chi'(0)$ increases with the field. On the basis of Fig. 78 and similar plots, no hysteresis was found in the ferromagnetic phase of silver. This is consistent with the theoretical structure discussed earlier: Because of the large degeneracy in the spin directions, the magnetic domains can adjust smoothly to variations in the external field (Viertiö and Oja, 1992).

2. Phase boundary of the domain state

Figure 73 (see also Fig. 4) summarizes the results on magnetic ordering in silver and displays the phase diagrams for the ferro- and antiferromagnetic states in

the B-S plane (Hakonen, Nummila, Vuorinen, and Lounasmaa, 1992). At $T<0$, there are experimental points only at zero and 5-μT fields; at 10 μT the transition could not be identified reliably from the susceptibility experiments (see Fig. 76) on which Fig. 73 is based. The dashed line sketches the stability region for the domain states when $T<0$. The curve was obtained by applying the mean-field theory, together with the estimate $B_c(T=0)=-\mu_0 M_{\rm sat}/\chi_{\rm sat}\approx 40$ μT, calculated by using the observed saturation value of the susceptibility $\chi_{\rm sat}=-1.05$.

The crossing of the two uppermost lines in Fig. 76 was identified as the transition point to the ferromagnetic state. Owing to the rounding of the $\chi'(0)$ vs p curve, a conservative estimate for the critical polarization, in zero field and at $B=5$ μT is $p_c=-0.49\pm0.05$, which corresponds to $S_c/\mathcal{R}\ \ln 2=0.82\pm0.035$. By employing the linear relationship between the temperature and inverse polarization (see Fig. 21), $1/|p|-1=0.55|T/\text{nK}|$, one obtains for the Curie point $T_C=(-1.9\pm0.4)$ nK.

3. Comparison with theory

At negative spin temperatures, according to the mean-field theory, $T_C=\theta=(R+L-D)C=-5.7$ nK in silver, which is clearly different from the observed value; here we have used $R=-2.2$, $L=\frac{1}{3}$, and $D=1$.[10] Calculations on the spin-$\frac{1}{2}$ Heisenberg model (De Jongh and Miedema, 1974) in an fcc lattice yield $T_C=0.67\theta=0.67\frac{1}{3}I(I+1)12J$. Use of the theoretical (see Table V) nearest-neighbor interaction $J/k_B=-1.3$ nK gives $T_C=-2.6$ nK, while $\theta=-5.7$ nK yields -3.8 nK. Since the latter result takes into account the dipolar interaction as well, it is clear that the experimental T_C is significantly lower than theoretical estimates. In addition, the critical entropy in the Heisenberg model, $S_c=0.66\mathcal{R}\ \ln 2$, is clearly lower than the experimental value $0.82\mathcal{R}\ \ln 2$. This is reasonable since the long-range dipolar force, which was not included in the calculation, acts ferromagnetically at negative temperatures and should increase S_c.

Monte Carlo calculations by Viertiö and Oja (1992) predict $T_C=-1.7$ nK, which is close to the measured result. These computations were made, however, assuming classical spins. An estimate for the correction due to the spin $I=\frac{1}{2}$ of silver nuclei multiplies the predicted ordering temperature by a factor of 3, thus yielding $T_C=-5.1$ nK (see Sec. XV.C.3.c). This theoretical value is in approximate agreement with the result obtained by correcting the Curie temperature of De Jongh and Miedema (1974) with the dipolar interaction. Monte Carlo simulations yielded $S_c=0.93\mathcal{R}\ \ln 2$, which deviates substantially from the experimental value. This is not surprising, since a too high S_c is likely to ensue when a quantum-spin assembly is modeled using a classical system. It seems, therefore, that there remains a serious discrepancy between the measured and predicted ordering temperatures in silver, although there is at least a rough agreement for critical entropies.

The saturation of susceptibility to $\chi_{\rm sat}\approx -1$ in the ordered state at $T<0$ can be explained only by the formation of domains, since otherwise the susceptibility would diverge at T_C. The domain configurations are such that they maximize the magnetic enthalpy $H=U-BM$. Instead of needles, as at $T>0$, platelike domains are expected when $T<0$ (Abragam and Goldman, 1982). There is a rich variety of different energetically degenerate domain configurations (Viertiö and Oja, 1992). These will be described in detail in Sec. XV.H. A common feature of the different domain structures is that the susceptibility along the external field is $\chi_{\rm sat}=\mu_0 M/B=-1/(1-D_M)$, where D_M is the demagnetization factor along **B**. This is in agreement with the experimental data at $B=0$ and 5 μT. The observed behavior is clearly different from ferromagnetic ordering at positive temperatures; in this case the susceptibility saturates at $\chi_{\rm sat}=1/D$. The difference is caused by the shape of ferromagnetic domains in silver. At $T<0$, the tangential component of the magnetization is always continuous and the normal component changes sign at a domain boundary; this is illustrated in Fig. 4. The opposite is true at positive temperatures.

IX. NEUTRON-DIFFRACTION EXPERIMENTS ON SILVER

A. Experimental arrangements

By means of NMR measurements it is not possible to verify the details of the spin structure in silver. Experiments employing scattering of neutrons are necessary for this purpose. Tuoriniemi, Nummila *et al.* (1995) have recently observed long-range nuclear antiferromagnetic order by neutron diffraction in a single crystal of silver. Further details of this research have been described by Tuoriniemi, Lefmann (1995), Lefmann *et al.* (1995), Tuoriniemi (1995), Tuoriniemi *et al.* (1996), Lefmann *et al.* (1996), and Nummila *et al.* (1997). For this work the sample had to be isotopically pure, since ^{107}Ag (51.8%) and ^{109}Ag (48.2%) in natural silver have opposite signs of the spin-dependent scattering lengths, strongly depressing the coherent neutron signal that indicates the alignment of nuclear spins. The experiment used a 99.7% enriched material of ^{109}Ag to grow the $0.7\times12\times25$ mm^3 single crystal. The [11 0] axis was parallel to the longest edge of the crystal, which was mounted upright in the cryostat. The cubic direction [001] pointed 24° away from the flat surface of the sample, see Fig. 79(a).

The experiments were performed at the BER II reactor of the Hahn-Meitner-Institut in Berlin, in the group of Prof. M. Steiner. The diffracted neutrons were recorded at a fixed scattering angle by a single counter or by an area-sensitive detector. Another neutron counter monitored the transmitted beam. The $\lambda/2$ contamination was removed from the monochromatic beam by a beryllium filter.

[10] T_C should be computed for $D=0$ at $T>0$ and for $D=1$ at $T<0$.

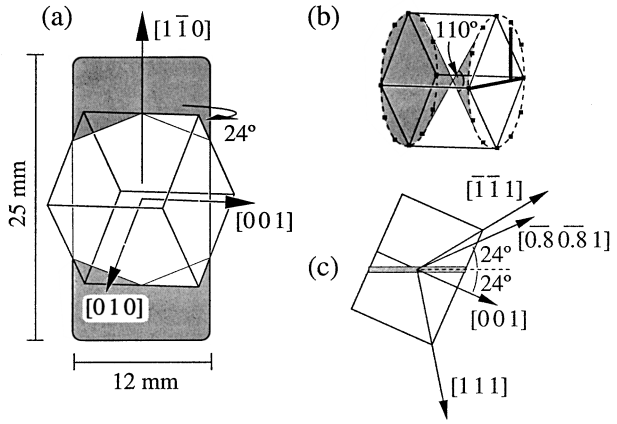

FIG. 79. Field-rotation observations of silver. (a) Orientation of the crystallographic axes within the slab-shaped silver sample (shaded rectangle) is illustrated by a cube in the appropriate alignment. (b) Field directions in which the (0 0 1) reflection was observed during the field-rotation experiments are shown by heavy lines (the center of the cube is at the origin). The end points and their symmetry equivalents are marked by black squares. A structure with $\mathbf{k} = (\pi/a)(0,0,1)$ was thus confined so that **B** had to be around [001] within a cone of 110° full opening; its outer surface is shaded in the figure. (c) Field directions, [001] and [$\overline{0.8}$ $\overline{0.8}$1], in which the phase diagram was studied in greater detail; the crystal is viewed from above. From Tuoriniemi, Nummila *et al.*, 1995.

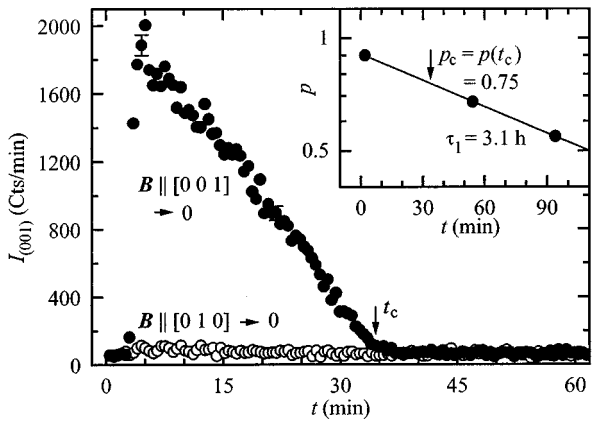

FIG. 80. Time dependence of neutron intensity, measured by a single counter (30 s per point) at the (0 0 1) position. The initial polarization $p = 0.91 \pm 0.02$ was recorded in a 500-μT field in the paramagnetic phase, after which **B**, in the [001] or [010] direction (● and ○, respectively), was reduced to zero (± 5 μT) at $t = 3$ min. The (0 0 1) neutron signal appeared immediately below B_c, but only when **B**∥[001]. The inset shows the exponential relaxation of the nuclear polarization, with $\tau_1 = 3.1$ h. The critical value $p_c = 0.75 \pm 0.02$ was found by interpolation. From Tuoriniemi, Nummila *et al.*, 1995.

The sample was cooled in a cascade nuclear-demagnetization cryostat (see Sec. VI.B), which had a 9-T magnet surrounding the massive copper cooling stage and a 7-T magnet for the sample. The copper refrigerant, demagnetized to 60 mT, kept the lattice temperature at 100 μK while the ^{109}Ag nuclei were polarized to about 95%. The silver nuclei were cooled further into the picokelvin range by reducing the 7-T external field to zero. Before the end of demagnetization, an additional 500-μT field was applied to the sample by a set of small coils, so that the ordered state could be entered from any field direction. During all stages of the experiment, the lattice and the conduction electrons of the ^{109}Ag sample remained in thermal contact with the copper nuclear stage. During measurements the neutron beam was the main source of heat, reducing τ_1 from 12 h to 3 h. Prior to demagnetizations, the diffractometer was aligned to the (0 0 1) Bragg position of a type-I antiferromagnet in an fcc lattice.

B. Results

In Fig. 80 two sets of neutron-diffraction data in $B = 0$ are shown. The nuclei were demagnetized into the ordered state with the external field **B** along the [001] or [010] directions, and neutron counts were monitored while the spin system warmed up. A clear (0 0 1) reflection appeared when demagnetization was made with **B** parallel to the corresponding ordering vector. The presence of this signal provided unambiguous proof of antiferromagnetic order in silver. It is important to note that the neutron signal remained essentially absent when the ordered state was entered from the perpendicular direction [010], although in zero field the three ordering vectors, producing the (100), (010), and (001) reflections, are equivalent owing to the cubic symmetry. It was concluded that the observed antiferromagnetic state had a simple single-**k** structure and that the stable spin configuration was created during demagnetization.

To demonstrate that the observed intensity indeed was a Bragg peak, Tuoriniemi, Nummila, *et al.* (1995) used an area-sensitive detector. Time development of the diffraction pattern, integrated over the vertical dimension, is shown in Fig. 81. The line shape of the antiferromagnetic peak was Gaussian, and its width was comparable to that of the (0 0 2) second-order lattice reflection.

The critical entropy of ordering was found using the neutron-transmission data. The nuclear polarization p could be deduced from the count rate when the nuclei were aligned by a field in the paramagnetic state because the neutron absorption as well is spin dependent. For this purpose the 500-μT field was applied at the beginning of each experiment. The orientation of this field also determined the direction along which the ordered state was entered. Polarization was measured again a few times after the disappearance of the antiferromagnetic signal, and the critical value p_c was found by interpolation. The nuclear entropy S could then be calculated from the paramagnetic polarization in 500 μT. The field changes were nearly adiabatic ($\Delta S \sim 0.01 \mathcal{R}$ ln2 for each sweep between $B = 0$ and 500 μT), whereby the entropy was known in any field. In the zero-field experiment of Fig. 80, $p_c = 0.75 \pm 0.02$ was obtained, corresponding to $S_c = (0.54 \pm 0.03)\mathcal{R}$ ln2.

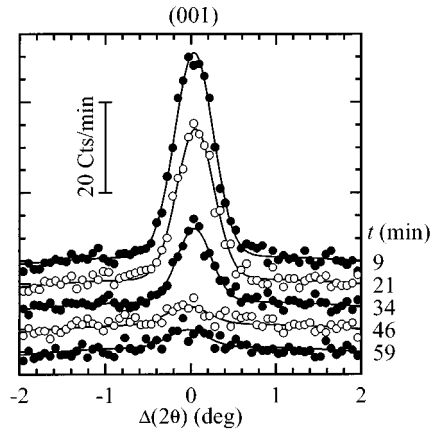

FIG. 81. Time evolution of the antiferromagnetic Bragg peak in a 30-μT field. The 2θ dependence of scattered neutrons is plotted as a function of deviation from the (0 0 1) position. The bell-shaped curves are Gaussian fits to counts collected during six-minute intervals. Only every second spectrum is shown. For clarity, the successive spectra are offset vertically by 5 cts/min. The residual peak, visible in the lower curves, is the (0 0 2) lattice reflection of second-order neutrons leaking through the Be filter (transmittance 0.3% at $\lambda/2$). The initial and critical polarizations in this experiment were 0.89 ± 0.02 and 0.69 ± 0.02, respectively. From Tuoriniemi, Nummila *et al.*, 1995.

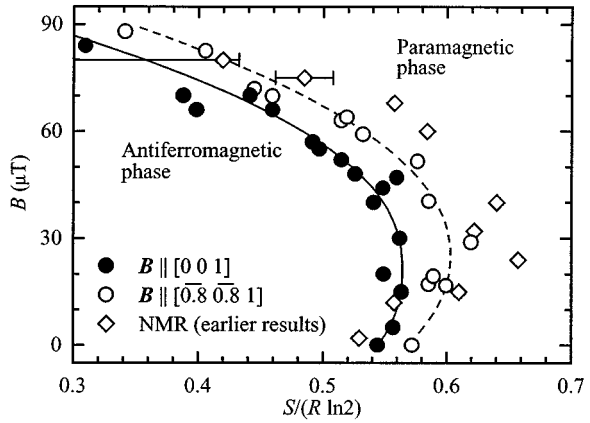

FIG. 82. Magnetic field vs entropy phase diagram of silver; ●, **B** was along the [001] direction; ○, **B** was along the [$\overline{0.8}$ $\overline{0.8}$ 1] direction; ◇, earlier NMR results (Hakonen, Yin, and Nummila, 1991; Hakonen and Yin, 1991) on a polycrystalline sample, shown for comparison. The curves are just guides for the eye. From Tuoriniemi, Nummila *et al.*, 1995.

To estimate the Néel temperature of nuclear ordering in ^{109}Ag, Tuoriniemi, Nummila *et al.* (1995) used the semiempirical relation between T in zero field and p in the paramagnetic state, $1/p-1 \propto T$, established in earlier NMR measurements on natural silver (see Sec. IV.E): $T_N=(700\pm80)$ pK. This is larger than 560 pK for natural silver because the strength of the mutual interactions is scaled by the magnetic moment squared, i.e., by a factor of 1.15.

The antiferromagnetic sublattice polarization p_{AF} was estimated by comparing the Bragg intensity $I_{(001)}$ with the strength of the (0 0 2) second-order lattice peak. The maximum signal in Fig. 80, at $p=0.90$, corresponds to $p_{AF}=0.48\pm0.10$. Extrapolation of the almost linear dependence of $I_{(001)}$ on $(1/p_c-1/p)$ suggests that p_{AF} at $p=1$ ($T=0$) is still clearly below complete polarization $p_{AF}=1$. This may reflect quantum fluctuations or frustration in the fcc lattice.

It was interesting to examine the response of the spin system to an applied magnetic field and to its alignment. With **B**‖[001], the antiferromagnetic intensity decreased smoothly when approaching the critical field B_c. The spins thus lined up continuously towards the increasing field, as in the spin-flop phase of a weakly anisotropic antiferromagnet. No field-induced phase transitions within the ordered state could be identified, which is in contrast to the single-**k** to triple-**k** transition theoretically predicted by Viertiö (1992) and by Heinilä and Oja (1993a). Repetitive field cyclings across the phase boundary to the paramagnetic state did not produce any appreciable hysteresis nor excess nonadiabaticity; therefore the ordering transition was presumably of second order.

The effect of the field direction was studied by rotating **B** with respect to the crystal axes. In a turn extending from [1 1 0] to [110], the (0 0 1) reflection was visible when the magnetic field ($B=50$ μT) was aligned between the axes [1 1 1] and [111]. Within this arc (~110°), the neutron intensity did not vary substantially. Another field rotation was made in a perpendicular plane, starting from [$\frac{1}{2}$ $\frac{1}{2}$1] and passing over [01 1] towards [11 0]. The neutron signal disappeared about 10° beyond the [01 1] axis, confining the observed antiferromagnetic phase roughly within a cone of 110° full opening. This is illustrated in Fig. 79(b).

Further experiments were made in two different field directions within this cone: **B**‖[001] and **B**‖[$\overline{0.8}$ $\overline{0.8}$1]. The latter is close to the edge, about 7° from the [1 1 1] axis. These directions were symmetric with respect to the shape of the crystal, about 24° away from the flat surface [see Fig. 79(c)], so that the same correction for the demagnetization effect could be applied. The results were compiled into an entropy-versus-field phase diagram, shown in Fig. 82. The observed neutron intensities during the respective experiments in the two directions were comparable. On the other hand, the critical entropy was systematically higher near the edge of the cone than along the central [001] axis.

C. Comparisons with theory

The neutron-diffraction data of Tuoriniemi, Nummila *et al.* (1995) can be compared with theoretical work. First of all, the observed type-I ordering vector had been predicted for silver on the basis of measured and calculated interaction parameters (Oja and Kumar, 1987; Harmon, Wang, and Lindgård, 1992). The ground-state spin structure in Ag had been studied by perturbation analysis (Heinilä and Oja, 1993a) and by Monte Carlo simulations (Viertiö, 1992). Both methods indicated that

in $\mathbf{B}\|[001]$ a single-$\mathbf{k}$ configuration is stable in low magnetic fields below $B\sim 0.5B_c$. A structure with $\mathbf{k}=(\pi/a)(0,0,1)$ was expected, in perfect agreement with the experimental observations. In higher fields, however, a triple-$\mathbf{k}$ configuration was predicted. According to the simulations this structure is stable only if $\mathbf{B}$ is within a narrow cone ($<5°$) around the [100]-type axes. The measurements did not provide any evidence for the triple-$\mathbf{k}$ state, although it was searched for in field-sweep and rotation experiments.

The simulations suggested further that only one $\mathbf{k}$-vector, $\mathbf{k}=(\pi/a)(0,0,1)$, appears if $\mathbf{B}$ lies between the [001] and [111] axes, apart from the triple-$\mathbf{k}$ region close to [001]. This is in agreement with the experimental data, except for the proposed triple-$\mathbf{k}$ phase. When $\mathbf{B}$ is turned beyond the [111] axis, the structure should transform first into another single-$\mathbf{k}$ configuration, giving rise to a (1 0 0) or a (0 1 0) reflection. Closer to [110], another triple-$\mathbf{k}$ state should exist when $B>0.5B_c$. These predictions have not been tested experimentally, and their verification requires measurements in other field orientations.

X. STUDIES ON RHODIUM

A. Nuclear magnetic susceptibility

The natural choice for the Helsinki group to investigate, after copper and silver, would have been gold. There is some prospect of this metal's becoming a superconductor around $T_e=100$ μK (Buchal *et al.*, 1982). The anticipated difficulties in obtaining a sufficiently pure gold specimen, however, made rhodium the actual choice. One reason for selecting Rh metal was the possibility of investigating the effect of superconductivity on the nuclear-spin system. In rhodium the critical parameters are B_c=4.9 μT and T_c=325 μK (Buchal *et al.*, 1983). Strong supercooling, even after active compensation of the remanent field down to 0.2 μT, may have been the reason why the Helsinki group did not observe superconductivity, but, as a result of their study, rhodium now provides another nuclear-spin system in which negative temperatures have been produced (Hakonen, Vuorinen, and Martikainen, 1993). The spin-spin relaxation time in Rh, τ_2=10.5 ms, is almost the same as in silver.

For a Heisenberg model in an fcc lattice, with an appreciable next-nearest neighbor interaction, it is possible that both the minimum ($T>0$) and the maximum ($T<0$) energy states are antiferromagnetic. Rhodium appears to be the first such metal known. In addition to the dipolar and Zeeman energies, the Hamiltonian contains contributions from the isotropic Ruderman-Kittel interaction and from the anisotropic, so-called pseudodipolar interactions (Bloembergen and Rowland, 1955). The theory of indirect exchange interactions is discussed in Sec. XV.A. There is only one stable isotope, ^{103}Rh, with spin $I=\frac{1}{2}$. Quadrupolar contributions to the Hamiltonian are thus absent. In rhodium, the strength of the exchange interactions, as compared to dipolar forces, is intermediate between those in copper and silver. It can be concluded, on the basis of NMR linewidth measurements, that the exchange interaction is nearly isotropic (Narath, Fromhold, and Jones, 1966). Pseudodipolar interactions are either small in comparison with the dipolar forces or, alternatively, they effectively change the sign of the dipolar interaction. For detailed discussions we refer the reader to Vuorinen, Hakonen, Yao, and Lounasmaa (1995).

The first measurements on rhodium were made by Hakonen, Vuorinen, and Martikainen (1993) using two specimens. Both samples were assembled from thin foils. The first specimen contained about 100 ppm of iron impurities, which were responsible for a decrease of the Korringa constant κ (see Sec. II.B) from 10 sK to 0.06 sK in small magnetic fields. In the second specimen, with less than 15 ppm of electronic magnetic impurities, $\kappa=0.2$ sK in zero field. After heat treatment at 1330 °C in an oxygen atmosphere of 0.4 mbar for 16 h, the residual resistivity ratios (RRR) of the two specimens were 250 and 530, respectively, and their effective iron contents 14 and 6 ppm. Most of the results reported were obtained using the purer Rh sample.

The experimental arrangement and the cooling procedure were basically the same as employed in earlier nuclear-refrigeration experiments in Helsinki (see Sec. III.B.). The Rh sample again formed the second stage of the cascade nuclear refrigerator. The specimen was assembled in the same manner as the silver sample (see Fig. 15). To increase rigidity, rhodium foils were shaped in the form of the letter "U." Owing to the poor thermal conductivity of Rh, the sample was connected to the cross-shaped thermal link via intermediate silver strips.

The initial polarization achieved in the rhodium spin assembly before demagnetization was limited, as in silver, by the long spin-lattice relaxation time of Rh, $\tau_1=14$ h at 200 μK. Two mu-metal tubes, with a shielding factor of 400, were installed to reduce the remanent field of the demagnetization solenoid at the site of the sample. To reach negative temperatures, adiabatic demagnetization of the specimen was stopped at 400 μT and a population inversion was made before continuing the field sweep. As for silver (see Sec. IV.G), the inversion efficiency, 85–60%, depended on the initial polarization before the field flip. The effect was more dramatic in rhodium. As is shown by Fig. 83, the polarization after the field flip, as a function of the initial polarization, reaches a maximum around $p_i\approx 0.6$. This behavior remains a puzzle; it cannot be explained, for example, by considering thermal mixing between the Zeeman and the interaction reservoirs. For $T<0$, therefore, the experimentally achievable polarizations were limited to $|p|\leq 0.60$. Inversion fields between 100 μT and 2 mT were tried, but the efficiency did not change much.

Examples of the measured dynamic susceptibility $\chi(f)=\chi'(f)-i\chi''(f)$, recorded by sweeping the frequency f of the excitation field, are displayed in Fig. 84, both when $T>0$ and when $T<0$. At negative temperatures $\chi''<0$, which again is a sign of energy emission. The static susceptibility $\chi'(0)=(2/\pi)\int(\chi''/f)df$

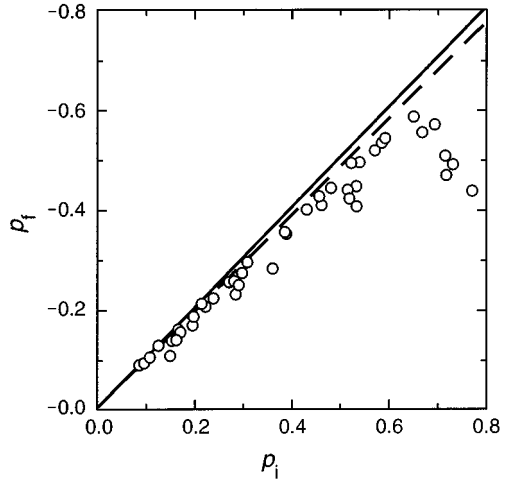

FIG. 83. Loss of polarization in rhodium during a field reversal: p_f and p_i are the final and initial polarizations, respectively. The ideal case is depicted by the solid line, while the dashed line shows the calculated result (see text). From Vuorinen, Hakonen, Yao, and Lounasmaa (1994).

and polarization $p=A\int\chi''(f)df$ could then be calculated. The integration was performed between 0 and 150 Hz, and the proportionality constant A was determined from experiments around 1 mK where the initial high-temperature polarization could be calculated from $p=\tanh(\mu B/k_{\rm B}T_e)$, using the pulsed Pt-NMR thermometer to determine $T=T_e$. The platinum scale, in turn, was calibrated against the superconducting transition point, 22.6 mK, of beryllium. In the ultralow-temperature region the temperature of the Rh nuclei was again found by using the second law of thermodynamics, $T=\Delta Q/\Delta S$. For more details, see Sec. IV.

The local field $B_{\rm loc}$, caused by spin-spin interactions, was carefully determined in these experiments. $B_{\rm loc}$ was obtained by fitting the measured field dependence of the longitudinal susceptibility χ_L to the theoretical expression $\chi_L\propto(1+B^2/B_{\rm loc}^2)^{-3/2}$ (see Sec. IV.C). This equation had worked reliably for calculating local fields in copper and silver (Ehnholm *et al.*, 1980; Hakonen, Yin, and Nummila, 1991). When applied to the data on rhodium, the equation yields $B_{\rm loc}=(34\pm3)$ μT, which is very close to the result 35 μT found for silver, but much smaller than $B_{\rm loc}=0.36$ mT observed for copper.

Figure 85 displays the measured susceptibility of Rh as a function of polarization. For small $|p|$, $\chi'(0)$ follows the high-T approximation $\chi'(0)=\chi_0/[1-(R+L-D_z)\chi_0]$, where $\chi_0=Ap=C/T$ is equivalent to the Curie-law susceptibility of noninteracting spins (see Sec. IV.D). The data points were fitted to the theoretical expression in the range $-0.1<p<0.2$; this yielded $R=-1.3\pm0.2$ and the dash-dotted curve illustrated in Fig. 85. Since R is on the order of one, the dipolar interactions may influence the ordered spin structures substantially in rhodium.

One of the interesting features of the data in Fig. 85 is that, at $T<0$, the susceptibility is a nearly linear function of polarization all the way down to $p=-0.6$. No saturation of $\chi'(0)$ was observed as in silver at $p_c=-0.49$.

The absolute value of the inverse static susceptibility of Rh nuclei as a function of $|T|$ is shown in Fig. 86. The solid line represents the antiferromagnetic Curie-Weiss law, $\chi=C/(T-\theta_A)$, with $C=1.3$ nK and $\theta_A=C(R+L-D_z)=-1.4$ nK, obtained at positive temperatures from the low-polarization data. At $T<0$, the ferromagnetic dependence is displayed by the dashed line. At low temperatures the Curie-Weiss approximation is known to deviate, especially when $I=\frac{1}{2}$, from the more accurate results based on high-T series expansions (De Jongh and Miedema, 1974). For negative temperatures (filled circles), the measured data show a crossover

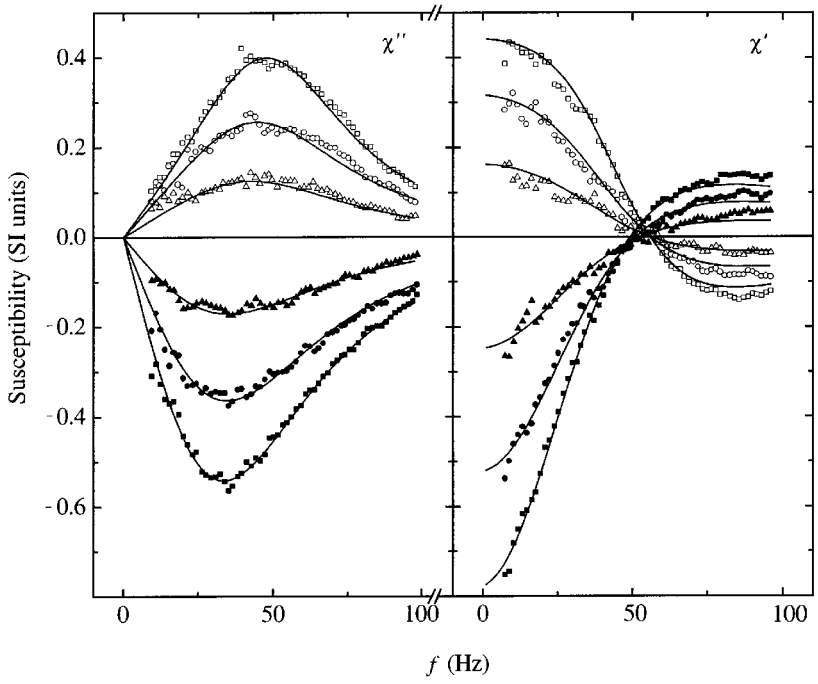

FIG. 84. NMR absorption χ'' and dispersion χ' curves of rhodium nuclei measured in zero magnetic field. Initial polarizations for $T>0$: □, $p=0.51$; ○, $p=0.32$; △, $p=0.15$. Initial polarization for $T<0$: ■, $p=-0.51$; ●, $p=-0.35$; ▲, $p=-0.17$. The solid curves are least-squares fits to Lorentzian line shapes (see legend of Fig. 64), applied simultaneously to the absorption and dispersion curves. From Hakonen, Vuorinen, and Martikainen (1993).

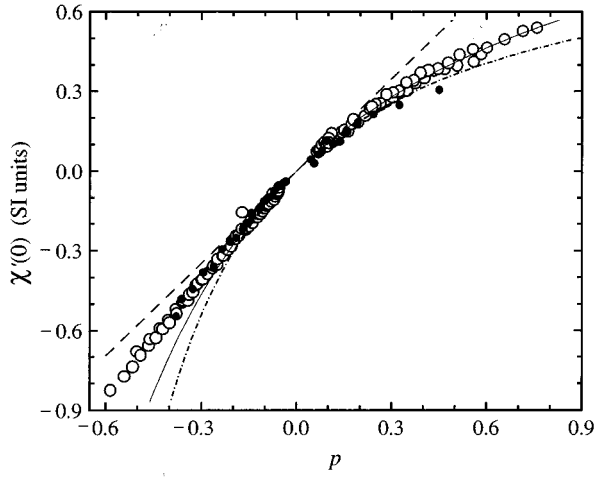

FIG. 85. Static susceptibility $\chi'(0)$ vs polarization p of rhodium nuclear spins in zero field for two specimens with 14 and 6 ppm of effective iron impurities (open and filled circles, respectively). The dashed line is the Curie susceptibility $\chi_0=1.16\ p$. The mean-field prediction $\chi'(0)=\chi_0/[1-(R+L-D_z)\chi_0]$ [see Eq. (34)] is illustrated by the dash-dotted curve for $R=-1.35$ and by the solid curve for $R=-1.0$, using $D_z=0.05$. Modified from Hakonen, Vuorinen, and Martikainen (1993).

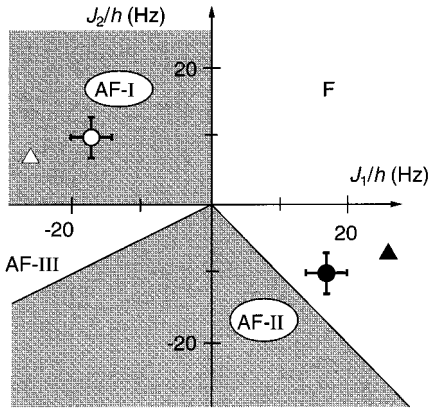

FIG. 87. Phase diagram for magnetic ordering in rhodium metal in the J_1 vs J_2 plane as predicted by the mean-field theory (Smart, 1966). Regions of type-I, type-II, and type-III antiferromagnetic order (see Fig. 110) are depicted by AF-I, AF-II, and AF-III, respectively, while F refers to the ferromagnetic phase. Locations for Rh (circles) and Ag (triangles) are given; the open and filled symbols refer to positive and negative spin temperatures, respectively. The ratio J_1/J_2 is approximately the same in Cu and in Ag, but the exchange constants in Cu are larger by an order of magnitude (see Table IV).

from ferro- to antiferromagnetic behavior around –5 nK. This indicates that the energy of the nuclear-spin assembly in rhodium is both minimized and maximized by antiferromagnetic order.

The data at $T>0$ extend to 280 pK and at $T<0$ to –750 pK. Both temperature records are roughly a factor of 2 closer to the absolute zero than the corresponding temperatures reached during the measurements on silver (see Sec. VIII). Phase transitions, however, were not seen in rhodium, even though the experimentally produced polarizations of Rh nuclei, $p=0.83$ and $p=-0.60$ at $T>0$ and at $T<0$, respectively, were higher than those required for ordering in silver. At positive temperatures, in particular, a careful search for ordering was made. Disappointingly, no plateaus in the $\chi(t)$ scans, characteristic of antiferromagnetic order (see Sec. VIII.C), were observed in experiments at 0, 19, and 36 μT. The initial polarizations were 6, 14, and 15 percentage units larger than those required for antiferromagnetic ordering in silver. The mean frequency of the absorption spectrum did not show any kinks either.

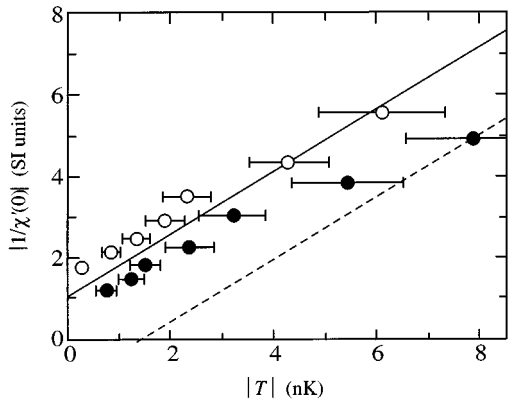

FIG. 86. Absolute value of the inverse static susceptibility $|1/\chi'(0)|$ vs absolute value of temperature for rhodium nuclei: ○, measured at $T>0$; ●, measured at $T<0$. The straight lines were calculated, using the Curie-Weiss law, from experimental data at small polarizations. The error bars denote the 20% uncertainty in the measurements of temperature. From Hakonen, Vuorinen, and Martikainen (1993).

B. Exchange constants and ordered spin structures

The susceptibility data can be used to extract the nearest- and next-nearest-neighbor exchange coefficients J_1 and J_2 since the measured R yields $\Sigma_j J_{ij}$ and $B_{\rm loc}$ gives $\Sigma_j J_{ij}^2$ in Rh [see Eqs. (66) and (30a)]. This is, of course, possible only if interactions beyond second-nearest neighbors are neglected. The values obtained from experimental results are $J_1/h=-17\pm3$ Hz and $J_2/h=10\pm3$ Hz (Hakonen, Vuorinen, and Martikainen, 1993). There is also another mathematical solution for the exchange constants that is, however, unlikely because it would require $|J_2|\gg|J_1|$.

It is interesting to know the ordered spin structures that correspond to these exchange constants. Mean-field calculations, to be discussed in Sec. XV.B.7, have been employed to predict regions of different types of magnetic ordering in the J_1 vs J_2 plane (Smart, 1966). The results are illustrated in Fig. 87. In an fcc lattice, the possible ordered structures include the ferromagnetic phase and three different antiferromagnetic states, known as structures of type I, II, and III. The magnetic unit cells of these antiferromagnetic states are illustrated

in Fig. 110. Rhodium lies well inside the type-I region at $T>0$. At $T<0$, the signs of the J's are effectively reversed. The corresponding point in Fig. 87 is located in the ferromagnetic sector but rather close to the type-II antiferromagnetic border. Neglecting the dipolar interaction, the mean-field estimates of the Néel temperatures for the type-I and type-II orders are 1.5 nK and –0.7 nK, respectively (Vuorinen, Hakonen, Yao, and Lounasmaa, 1995).

At $T<0$, description of rhodium using the J_1,J_2 model fails since the experiments of Hakonen, Vuorinen, and Martikainen (1993) indicate antiferromagnetism rather than ferromagnetism. Inclusion of the dipolar interaction cannot explain the discrepancy, since this would just further stabilize the ferromagnetic state. It also seems unlikely that the discrepancy is caused by the crudeness of the mean-field approximation. In fact, when thermal fluctuations are included, the phase boundary between the ferromagnetic and type-II states moves further away from the position corresponding to the observed exchange constants of rhodium (Heinilä and Oja, 1993b). A quite possible explanation is that interactions between third-nearest neighbors play a significant role, since J_2 is only slightly smaller than J_1. Pseudodipolar interactions could also be important in deciding between ferromagnetism and type-II antiferromagnetism.

As another, at least partial explanation of the behavior of Rh at negative temperatures, one can argue that the polarization range $-0.1<p<0.2$, which Hakonen, Vuorinen, and Martikainen (1993) used to fit $\chi'(0)$ against the high-T approximation to obtain R, was too narrow (see Fig. 85). At small $|p|$, only the simple Curie behavior was observed and the fit was not sensitive to R. On the other hand, the high-T approximation is strictly valid only at small $|p|$. It is clear, however, that if the fit had been made in a larger polarization interval, the overall result would look much better since the bending of the best-fitting theoretical curve would decrease at large $|p|$. The mean-field curve with $R=-1.0$ agrees with the data quite well, as is shown by the solid curve in Fig. 85. Adopting this R and the measured $B_{\rm loc}$ we obtain $J_1/h=-16$ Hz and $J_{\rm nnn}/h=13$ Hz. The corresponding point still falls within the ferromagnetic region in the J_1J_2 plane, but now the boundary to the type-II state is within the error bar. Yet another indication that the originally quoted $R=-1.3$ is too large in absolute value comes from the susceptibility comparison (see Table VI in Sec. XV.B.5). The absolute values of the susceptibilities in type-I and type-II structures, as calculated for the above J_1 and J_2, are about 30% smaller than the largest measured susceptibilities at $T>0$ and $T<0$, respectively. These discrepancies would also decrease if $|R|$ were reduced.

In any case, rhodium lies close to the border between the ferromagnetic and the type-II antiferromagnetic regions at $T<0$. This should result in strong fluctuations that lower the ordering temperature from the mean-field estimate. It is therefore not surprising that ordering was not seen at negative temperatures. It remains puzzling, however, why the ordered state was not observed at $T>0$ either. When the mean-field prediction for the ordering temperature, $T_{\rm N}^{\rm MF}=1.5$ nK, is corrected for fluctuations according to the high-temperature expansions (Pirnie *et al.*, 1966), one obtains a theoretical $T_{\rm N}$ around 1.0 nK, much higher than the lowest temperature of 0.28 nK reached in the experiments. Perhaps rhodium exhibits behavior similar to that of silver (so far unexplained): The measured ordering temperatures of silver nuclei were smaller than the theoretical predictions by a factor of 3 both at $T>0$ and at $T<0$ (see Sec. VIII.C.5).

C. Spin-lattice relaxation in rhodium

The acceleration in the spin-lattice relaxation, caused by electronic magnetic impurities, has not been investigated much in the microkelvin range and below, in spite of the significance of τ_1 for reaching the lowest nuclear temperatures. However, the Helsinki group recently made measurements on two rhodium specimens (Hakonen, Vuorinen, and Martikainen, 1994). Surprisingly, the data show that in weak magnetic fields there is a clear difference in τ_1 at $T>0$ and $T<0$. The observed behavior is consistent with electrons scattering from iron impurities, provided that the scattering rate has a contribution proportional to the inverse of the nuclear-spin temperature.

The spin-lattice relaxation time is defined (see Sec. II.B) by the relationship

$$d(1/T)/dt=-(1/\tau_1)(1/T-1/T_e). \tag{52}$$

Since $T_e \gg T$ and $p \propto 1/T$ [see Eq. (32)], one obtains $d\ \ln p/dt=-(1/\tau_1)$. The cooling procedure and the samples in the relaxation experiments were the same as used in earlier studies on rhodium (see Sec. X.A). Two methods were employed in the experiments. Between 40 and 400 μT, a fixed-field technique was applied by monitoring, at successive times, the area under the NMR absorption or, at $T<0$, emission signal χ''; this again yielded the polarization according to the relation $p=A\int\chi''(f)df$. The spin-lattice relaxation time was found by plotting the measured points on a log p vs t graph (see Fig. 88). The straight line, least-squares fitted to the data obtained during the second half of the experiment, illustrates a constant relaxation rate, while the steeper slope at the beginning of the run indicates a much shorter τ_1.

In order to compare the relaxation rates at $T>0$ and $T<0$ directly, population inversions were made at regular time intervals while recording p. Data at the beginning of such an experiment, performed at 40 μT, are illustrated in Fig. 89. The results show clearly that τ_1 is longer at $T<0$ than at $T>0$, even though the spin-lattice relaxation slows down notably with time when $T>0$. This unexpected effect is much smaller in high fields but, when $B=0$, the measured τ_1 is almost a factor of 2 longer at negative temperatures.

The second method for measuring τ_1, a field-cycling sequence, was used in small fields, $B\leqslant 100$ μT, and also at 1 mT $<B<1$ T. First, 5–7 NMR spectra were re-

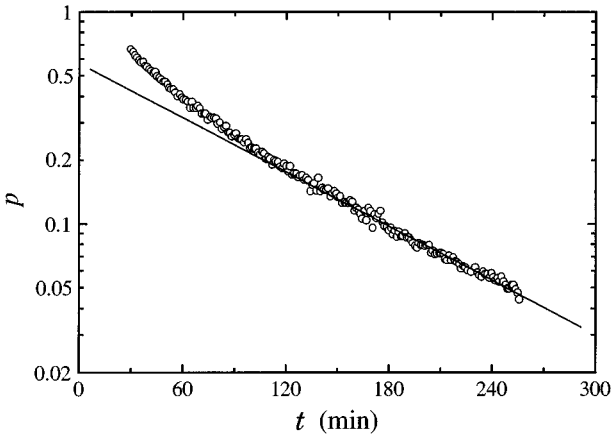

FIG. 88. Polarization p of rhodium nuclei as a function of time at $T>0$ and $B=100$ μT. A constant spin-lattice relaxation time is characterized in this semilogarithmic plot by the straight line, which is a least-squares fit to the latter half of the data points. The polarization dependence of τ_1 is quite obvious at the beginning of the experiment. From Vuorinen, Hakonen, Yao, and Lounasmaa (1995).

corded at 400 μT to obtain the initial polarization. Next, B was swept, in 5–15 s, to the desired low field and then kept constant for a time $\Delta t=1-90$ min, after which the field was returned back to 400 μT and 5–7 NMR spectra were again recorded. The decay of polarization during Δt, from which the relaxation at $B=400$ μT was removed, was then employed to calculate τ_1. Before the next experimental cycle was started, a population inversion was made so that data at $T>0$ and $T<0$ were again measured consecutively.

The experimental results on the sample with 6 ppm of iron impurities are summarized in Fig. 90, which displays

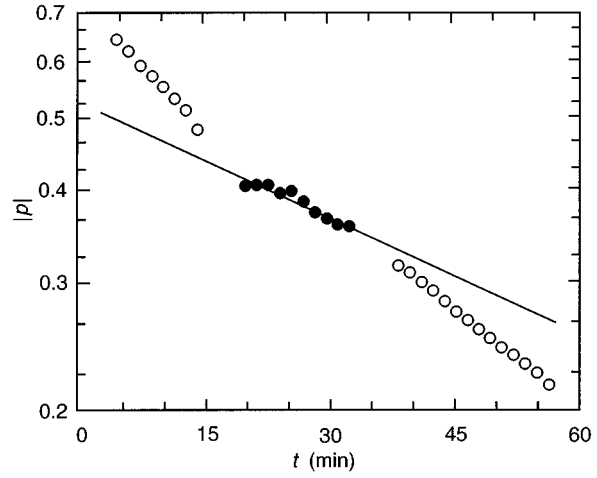

FIG. 89. Polarization $|p|$ of rhodium spins as a function of time measured in a magnetic field of 40 μT: ○, at $T>0$; ●, at $T<0$. The straight line is a least-squares fit to the data at $T<0$. During the blank sections the polarization was checked at 400 μT, and the spin populations were inverted by rapid field reversals. From Hakonen, Vuorinen, and Martikainen (1994).

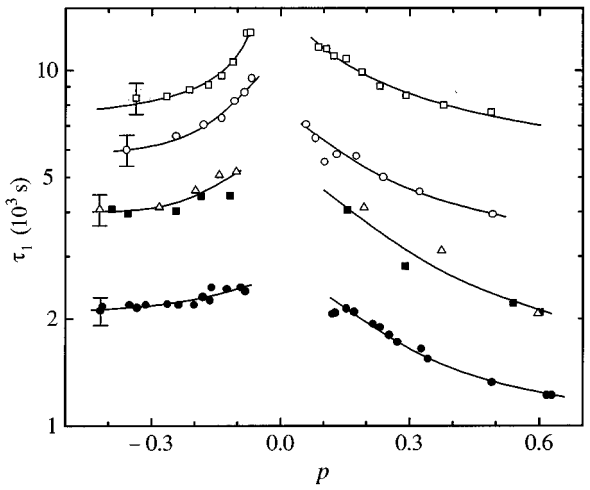

FIG. 90. Spin-lattice relaxation time τ_1 of a rhodium sample with 6 ppm of iron impurities as a function of the high-field polarization p of the Rh nuclei; ●, measured at $B=0$; ■, △, $B=50$ μT; ○, $B=100$ μT; □, $B=400$ μT. The open and filled symbols refer to measurements performed with the fixed-field and the field-cycling techniques, respectively. From Hakonen, Vuorinen, and Martikainen (1994).

the spin-lattice relaxation times measured in magnetic fields $B=0$, 50, 100, and 400 μT at the electronic temperature $T_e=120$ μK. The salient features of the data are that τ_1 clearly decreases with increasing $|p|$ and decreasing B. In addition, there is a clear asymmetry in τ_1 between $T>0$ and $T<0$, especially in low fields.

If the usual Korringa's law is valid for the specimen under study, the spin-lattice relaxation time should have been $\tau_1=\kappa_0/T_e$=23 h=8.3·10^4 s for the data in Fig. 90 in fields larger than $B_{\rm loc}=34$ μT. In fields lower than $B_{\rm loc}$, τ_1 should always be shorter (see Sec. II.B), but only by a factor between 2 and 3. Instead, the zero-field data show reductions by a factor of about 50 from the value predicted by high-field Korringa constant $\kappa_0=10$ sK. It seems, therefore, difficult to explain the observed differences in τ_1 at $T>0$ and at $T<0$ by intrinsic properties of rhodium.

The magnetic-field dependence of κ has been plotted at a constant T_e for the two Rh specimens in Fig. 91. The Korringa constant begins to decrease in fields smaller than 10 mT for both samples. The relaxation is faster, by a factor of 5, in the sample with 14 ppm of Fe impurities than in the sample with 6 ppm of Fe. The reduction of κ in Rh was therefore attributed to iron impurities. Similar results had been observed previously in copper (Huiku, Loponen, *et al.*, 1984). The data on Rh also show that the effect is enhanced when the electronic temperature is lowered.

The scattering rate $\tau_1^{\rm imp}(B)$, caused by impurities, can be related to the observed τ_1 by the equation $\tau_1^{-1}=T_e/\kappa_0+[\tau_1^{\rm imp}(B,T)]^{-1}$. According to phenomenological arguments, the impurity scattering rate, affected by the susceptibility-dependent field distribution around a magnetic center (Hakonen, Vuorinen, and Martikainen, 1994), is of the form $[\tau_1^{\rm imp}(B,T)]^{-1}$

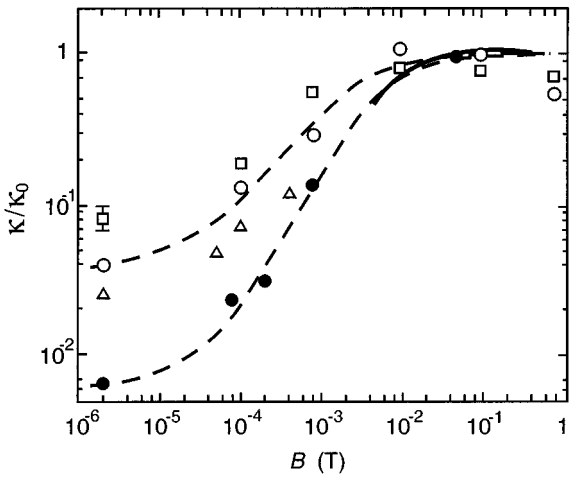

FIG. 91. Field dependence of Korringa's constant for a Rh sample with 6 ppm of iron impurities: △, at $T_e=0.12$ mK; ○, at $T_e=0.2$ mK; □, at $T_e=1.2$ mK; ●, a 14 ppm sample at $T_e=0.2$ mK. The nuclear-spin temperature is positive in all cases. The dashed curves are only guides for the eye. The solid line in the high-field region depicts the behavior of platinum (Roshen and Saam, 1980, 1982). From Vuorinen, Hakonen, Yao, and Lounasmaa (1995).

$=[\tau_{p=0}(B)]^{-1}[1+\xi\chi(B)]$, where $\tau_{p=0}(B)$ is the relaxation time in a magnetic field B at zero spin polarization and ξ is a constant close to unity. In Fig. 92, data points have been compared with these arguments for $\xi=0.5$ using the measured χ. Within experimental uncertainties, the calculated curves agree with the measured results. It can then be concluded that the origin of the anomalous behavior of τ_1 is scattering from isolated Fe impurities, modified by the large susceptibility of Rh nuclei. The change in $\tau_1^{\rm imp}(B,T)$ is proportional to $1/T$.

One property that distinguishes Rh from Cu and Ag is the temperature dependence of electrical resistivity

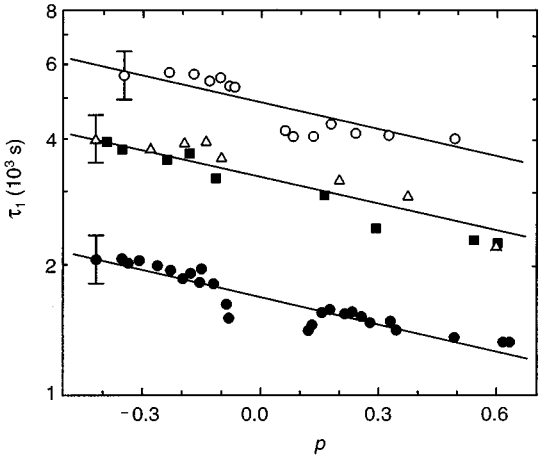

FIG. 92. Spin-lattice relaxation times of Fig. 90, scaled by the polarization dependence of τ_1 at $B=400$ μT. The fitted straight lines have been drawn with equal slope. For further explanation, see text. From Hakonen, Vuorinen, and Martikainen (1994).

caused by magnetic impurities. *Rh*Fe belongs to the so-called Coles alloys (Rivier and Zlatic, 1972), which display a positive temperature coefficient in their low-temperature resistivity. In these materials (*Ir*Fe, *Pt*Fe, *Pd*Fe, ...), both the host and the impurity are transition metals, whereas in Kondo alloys (*Au*Mn, *Al*Mn, ...), which exhibit a resistance minimum, the host and the impurity have different electronic structures. However, according to theory, both classes of alloys should display very similar universal behavior that can be understood in terms of electrons scattered from localized spin fluctuations around the impurity (Roshen and Saam, 1980, 1982). Such a description is not successful for *Rh*Fe; the decrease in κ predicted by theory is four orders of magnitude too large.

Spin-lattice relaxation measurements on copper have been made by Smeibidl, Schröder-Smeibidl, and Pobell (1994) between 60 μK and 10 mK on three specimens having RRR values of 260, 960, and 1300, respectively. No deviations from the Korringa law were observed.

XI. NMR STUDIES IN THE PARAMAGNETIC PHASE

In this section we describe some NMR measurements on highly polarized nuclear spins. Although these experiments were performed in the paramagnetic state they also reveal features important for nuclear ordering. There are several "high-temperature" NMR techniques that yield information on the absolute magnitude of spin-spin interactions but not on the sign; for a discussion of these methods we refer the reader to Oja (1987).

We first review measurements of cross relaxation between the Zeeman temperatures of ^{107}Ag and ^{109}Ag (Oja, Annila, and Takano, 1990). This work elucidates the important thermal mixing process in which the cold Zeeman reservoir cools the interaction reservoir after demagnetization to a low field (see Sec. II.B). Next, we discuss the so-called "suppression-enhancement" of isotopic NMR lines. This effect has been observed in two-isotope systems such as those in copper (Ekström *et al.*, 1979) and in silver (Oja, Annila, and Takano, 1990; Hakonen, Nummila, and Vuorinen, 1992). An analysis of the data yields the overall strength of the exchange interaction, i.e., the parameter R defined by Eq. (6). The result can be directly compared with that obtained from the Curie-Weiss fit to the static susceptibility vs temperature curve or with electronic band-structure calculations. Finally, we discuss the observation and analysis of the second-harmonic NMR absorption peak in low fields for highly polarized copper spins. The position of the peak also yields R. This technique can be used in single-isotope spin systems as well.

A. Cross relaxation between ^{107}Ag and ^{109}Ag

Cross relaxation in spin systems has been investigated extensively since the NMR experiment of Abragam and Proctor (1958) and the studies by Bloembergen and Pershan and co-workers (Bloembergen, Shapiro, Pershan, and Artman, 1959; Pershan, 1960). The majority of later

investigations have been on rotating-frame Zeeman systems using the spin-locked NMR technique (Schmid, 1973). The studies on silver by Oja, Annila, and Takano (1990) involved a conceptually simpler case, cross relaxation between two laboratory-frame Zeeman systems. As their data extended to many orders of magnitude lower temperatures than before, it was possible, for the first time, to investigate the polarization dependence of the cross-relaxation time.

Natural silver is a mixture: 51.8% of ^{107}Ag and 48.2% of ^{109}Ag. The two isotopes have a 13% difference in their gyromagnetic ratios: $\gamma_{107}/2\pi$=1.73 MHz/T and $\gamma_{109}/2\pi$=1.98 MHz/T. This suggests that thermodynamically the system can be described using four heat reservoirs, each of them having its own temperature: T_{107} and T_{109} for the two Zeeman reservoirs, T_{ss} for the common spin-spin interaction reservoir through which T_{107} and T_{109} communicate, and T_e for the lattice and the conduction electrons.

The reason why one must assign separate Zeeman temperatures for the different spin populations is rather simple. Consider two nearby silver spins, one of the 107 isotope and the other of the 109 isotope. Energy is transferred between the two spin populations when one of the spins is flipped ($\downarrow\rightarrow\uparrow$) and the other is flopped ($\uparrow\rightarrow\downarrow$). The overall Zeeman energy is not conserved in the flip-flop process because the gyromagnetic ratios of the two spin species are different. The law of energy conservation requires then that an equal but opposite change in energy occur in the interaction reservoir. As the spread of the spin-spin interaction energies is reflected in the NMR linewidth, one might expect that the rate at which T_{107} and T_{109} approach each other is proportional to the degree of overlap of the two NMR lines (Bloembergen, Shapiro, Pershan, and Artman, 1959). The higher the magnetic field, the smaller is the overlap, and the longer is the cross-relaxation time τ_x.

The data of Oja, Annila, and Takano (1990) showed the expected increase of τ_x with B. It was remarkable, however, that the observed cross-relaxation times were orders of magnitude longer than what one would have expected from the overlap of the NMR lines. The reason underlying the failure of the naive argument highlights a fundamental aspect of spin-temperature theory: There is a hierarchy of relaxation processes and times in the system, associated with mutual flips of unlike spins, single-spin flips, and finally the τ_1 process, all with their own, well-defined (quasi-)equilibrium states.

1. Measurement of the cross-relaxation time τ_x

The specimen of Oja, Annila, and Takano (1990), consisting of 28 polycrystalline silver foils, was mounted as the second nuclear stage in the Helsinki refrigerator (see Sec. III.B). An rf SQUID, connected to an astatic pickup coil, detected the NMR signal. A linear excitation field of 40-nT amplitude was used. The measuring frequencies were below 2 kHz, which guaranteed full penetration of the excitation field into the sample. Since the nuclei were practically isolated from the lattice in these measurements (the spin-lattice relaxation times were about 14 h), very slow cross-relaxation processes could be investigated. For other details of the experimental procedure, see Secs. III.B and III.E.

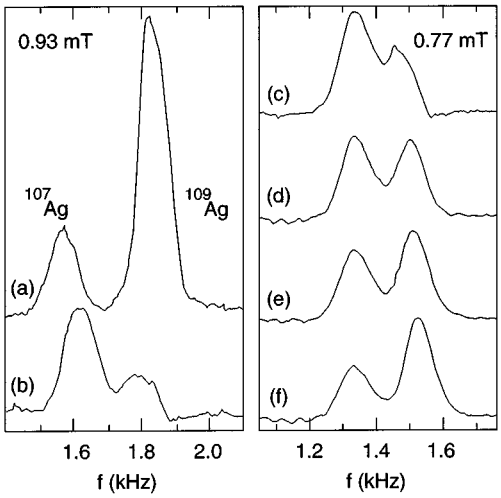

FIG. 93. NMR spectra demonstrating cross relaxation in silver. For explanations, see text. From Oja, Annila, and Takano (1990).

The final step of cooling consisted of lowering the field on the silver specimen from 7.3 T to 0.93 mT. The continuous-wave NMR signal, illustrated by curve (a) in Fig. 93, was then measured in order to determine the initial polarization. Next, the ^{109}Ag NMR signal was almost saturated by applying a strong audio-frequency field near the 109 resonance. The Zeeman temperature T_{109} of the ^{109}Ag spins (curve b in Fig. 93) thereby became much higher than T_{107}. The magnetic field was then lowered to a holding value of 0.77 mT for experimental convenience (curve c in Fig. 93). In this field, τ_x is practically infinite.

However, when the field was reduced to 0.22 mT, for only a short time Δt=0.20 s, and then increased back to 0.77 mT, a different spectrum was obtained: the two peaks were now approximately equal (curve d). This means that the 109 spins had cooled down and the 107 spins had warmed up. Two more cycles and the spectrum (curves e and f) began to look as it had in the original equilibrium situation (curve a). Thus, by means of the field-sweep sequence 0.77 mT $\rightarrow$ 0.20 mT $\rightarrow$ 0.77 mT, "snapshots" of thermal equalization between the two spin species were obtained.

The cross-relaxation time was calculated from the change in the NMR signals as a function of the cumulative period spent in the low field, at 0.20 mT. A single exponential time constant described the changes in the integrated areas under the ^{107}Ag and the ^{109}Ag peaks. For data in the highest fields, the intensities of the NMR signals had to be corrected for decay caused by the spin-lattice relaxation described by τ_1. In the low-field measurements, B was changed quickly in order to ensure negligible cross relaxation during the field sweep. To determine the dependency of τ_x on the spin temperature, a second cross-relaxation measurement was usually made immediately afterwards by starting from the final state

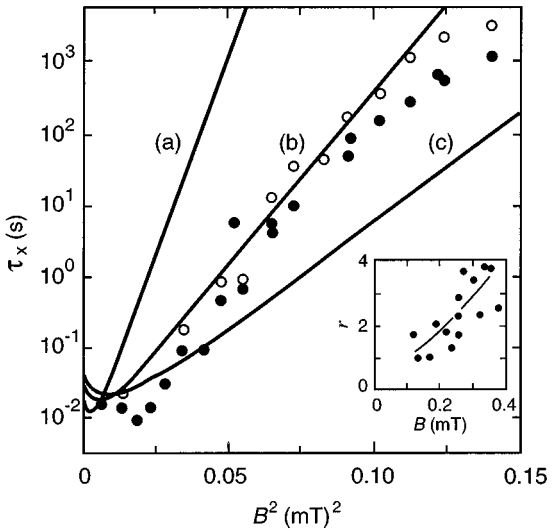

FIG. 94. Time constant τ_x for cross relaxation in silver as a function of the external magnetic field squared: ●, high polarization; ○, low polarization. The solid lines are theoretical curves for τ_x at low p, using various values for the antiferromagnetic nearest-neighbor RK interaction. (a) $J/h=20$ Hz, (b) $J/h=31$ Hz, (c) $J/h=40$ Hz. Inset: The ratio $r=\tau_x(\text{low } p)/\tau_x(\text{high } p)$ vs B; the curve is only to guide the eye. From Oja, Annila, and Takano (1990).

of the first run (curve f in Fig. 93): the ^{109}Ag spins were again heated and the snapshot procedure was repeated.

The data of Oja, Annila, and Takano (1990) can therefore be divided into two sets. The high-polarization results, obtained in the first cross-relaxation experiments during run (a), correspond to the following initial conditions after the ^{109}Ag signal was almost saturated: p_{107}=0.41–0.61 and $p_{109}=0.16-0.31$; $T_{107}=45-73$ nK and $T_{109}=110$–230 nK. The low-polarization data, collected during the second series of experiments, relate to initial conditions $p_{107}=0.11$–0.20 and $p_{109}=0.04$–0.11. The measured values of τ_x, as a function of B^2, are presented in Fig. 94; the data cover five decades. In the lowest fields $\tau_x\approx\tau_2=10$ ms. When $B>0.15$ mT, $\log\tau_x$ is approximately linear in B^2, although the increase in τ_x becomes less steep at $B\approx 0.35$ mT. Comparison of the high-p and low-p data shows that the cross-relaxation time decreases with polarization. However, the ratio $\tau_x(\text{low } p)/\tau_x(\text{high } p)$ clearly increases with B, as is illustrated in the inset of Fig. 94.

2. Theoretical description

The quantum-statistical theory of cross relaxation was developed by Provotorov (1962). To describe cross relaxation in a two-isotope system, such as the natural mixtures of silver and copper, it is useful to present the system in terms of the four nuclear-spin heat reservoirs illustrated in Fig. 95 (Goldman, 1970): the average Zeeman energy $\mathcal{H}_Z^{\text{av}}$, the differential Zeeman energy $\mathcal{H}_Z^{\text{diff}}$, the interaction reservoir $\mathcal{H}'_{\text{ss}}$, and the conduction-electron reservoir. The average and the differential Zeeman energies are defined by

$$\mathcal{H}_Z^{\text{av}}=-\hbar\gamma_{\text{av}}B\sum_i I_i^z, \tag{53}$$

$$\mathcal{H}_Z^{\text{diff}}=-\hbar(\gamma_a-\gamma_b)B\sum_i (x_b I_{a,i}^z-x_a I_{b,i}^z), \tag{54}$$

where $\gamma_{\text{av}}=x_a\gamma_a+x_b\gamma_b$ and the concentrations of the two spin species a and b are x_a and x_b, respectively. The direction of the external field is denoted by z. The total Zeeman energy $\mathcal{H}_Z$ for the two spin species equals the sum $\mathcal{H}_Z^{\text{av}}+\mathcal{H}_Z^{\text{diff}}$. The usefulness of this decomposition becomes evident when we consider cross relaxation caused by mutual spin flips.

The interaction reservoir $\mathcal{H}'_{\text{ss}}$ consists of those terms in the Hamiltonian that commute with $\mathcal{H}_Z$. The conserving and nonconserving terms can be distinguished by introducing the conventional notation using raising and lowering operators, defined as $I_i^+=I_i^x+iI_i^y$ and $I_i^-=I_i^x-iI_i^y$ respectively (see, for example, Van Vleck, 1948). The full spin-spin interaction $\mathcal{H}_{\text{ss}}=\mathcal{H}_{\text{D}}+\mathcal{H}_{\text{RK}}$ [see Eqs. (2) and (3)] can then be written as

$$\mathcal{H}_{\text{ss}}=\mathcal{A}+\mathcal{B}+\mathcal{C}+\mathcal{D}+\mathcal{E}+\mathcal{F}, \tag{55}$$

where

$$\mathcal{A}=\sum_{i<j} a_{ij}I_i^zI_j^z, \tag{56a}$$

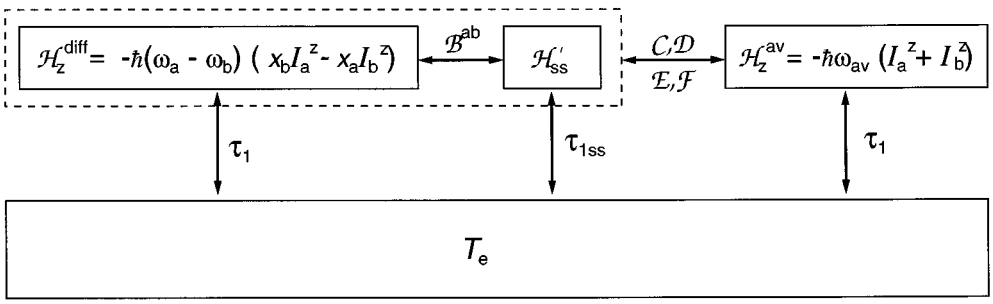

FIG. 95. Heat reservoirs in a two-isotope system: ^{107}Ag and ^{109}Ag nuclei and conduction electrons at low temperatures. The reservoirs are for the average Zeeman energy $\mathcal{H}_Z^{\text{av}}$, the differential Zeeman energy $\mathcal{H}_Z^{\text{diff}}$, the interaction reservoir $\mathcal{H}'_{\text{ss}}$, and the conduction-electron reservoir at T_e. See text for details.

$$\mathcal{B}=\sum_{i<j} b_{ij}(I_i^+ I_j^- + I_i^- I_j^+), \tag{56b}$$

$$\mathcal{C}=\sum_{i<j} c_{ij}(I_i^+ I_j^z + I_i^z I_j^+), \tag{56c}$$

$$\mathcal{D}=\mathcal{C}^\dagger, \tag{56d}$$

$$\mathcal{E}=\sum_{i<j} e_{ij} I_i^+ I_j^+, \tag{56e}$$

$$\mathcal{F}=\mathcal{E}^\dagger. \tag{56f}$$

Here $\mathcal{O}^\dagger$ denotes the Hermitian operator of $\mathcal{O}$. The notation $\Sigma_{i<j}$ implies that pairs (i,j) are to be counted only once. The various coefficients appearing above are

$$a_{ij}=-J_{ij}+\hbar^2\gamma_i\gamma_j r_{ij}^{-3}[1-3(\cos\theta_{ij})^2], \tag{57a}$$

$$b_{ij}=-\tfrac{1}{2}J_{ij}+\tfrac{1}{4}\hbar^2\gamma_i\gamma_j r_{ij}^{-3}[3(\cos\theta_{ij})^2-1], \tag{57b}$$

$$c_{ij}=-\tfrac{3}{2}\hbar^2\gamma_i\gamma_j r_{ij}^{-3}\sin\theta_{ij}\cos\theta_{ij}\exp(-i\phi_{ij}), \tag{57c}$$

$$e_{ij}=-\tfrac{3}{4}\hbar^2\gamma_i\gamma_j r_{ij}^{-3}(\sin\theta_{ij})^2\exp(-2i\phi_{ij}), \tag{57d}$$

where θ_{ij} and ϕ_{ij} are the azimuthal and polar angles of $\mathbf{r}_{ij}$ with respect to the z axis.

The expression for the truncated spin-spin interaction $\mathcal{H}'_{\rm ss}$ is

$$\mathcal{H}'_{\rm ss}=\mathcal{A}+\mathcal{B}^{aa}+\mathcal{B}^{bb}, \tag{58}$$

where the superscripts aa and bb denote the species of the interacting spins i and j. Therefore mutual flips of like spins are included in $\mathcal{H}'_{\rm ss}$, but those for unlike spins are not since the latter do not conserve the Zeeman energy, i.e., $[\mathcal{B}^{ab}+\mathcal{B}^{ba},\mathcal{H}_{\rm Z}]\neq 0$. Neither do single flips $(\mathcal{C}+\mathcal{D})$ or double flips $(\mathcal{E}+\mathcal{F})$ conserve $\mathcal{H}_{\rm Z}$.

The operators $\mathcal{H}_{\rm Z}^{\rm av}$, $\mathcal{H}_{\rm Z}^{\rm diff}$, and $\mathcal{H}'_{\rm ss}$ are mutually orthogonal, i.e., they commute with each other. Thus each of them can be viewed as a heat reservoir having its own temperature. When spin-lattice relaxation can be neglected, these reservoirs approach a common temperature only through spin-spin interactions not contained in $\mathcal{H}'_{\rm ss}$. In an external field, the most frequent of these processes are mutual flips of unlike spins, since one such process changes the Zeeman energy only by $(\gamma_a-\gamma_b)B$. These processes bring $\mathcal{H}_{\rm Z}^{\rm diff}$ and $\mathcal{H}'_{\rm ss}$ into thermal equilibrium with each other. The temperature of the *average* Zeeman reservoir is not affected, however, since $[\mathcal{B}^{ab}+\mathcal{B}^{ba},\mathcal{H}_{\rm Z}^{\rm av}]=0$. This explains the failure of the overlap argument of isotopic NMR lines in accounting for the cross-relaxation time constant: mutual flips of unlike spins do not bring about thermal equilibrium (Goldman, 1970; Rodak, 1971).

Therefore thermal equilibrium is obtained via slower processes involving single spin flips, described by $\mathcal{C}+\mathcal{D}$ in Eq. (55). These terms are caused by the dipolar interaction alone, whereas mutual spin flips depend also on the exchange interaction. During a single spin-flip process, the reservoir $\mathcal{H}_{\rm Z}^{\rm diff}+\mathcal{H}'_{\rm ss}+\mathcal{B}^{ab}+\mathcal{B}^{ba}$ can be treated as a single system in internal thermal equilibrium. The fact that there are two different spin species plays then only a minor role, since the process is essentially the same as thermal mixing, which equalizes the temperatures of the interaction and Zeeman reservoirs in systems with only one kind of spin (see Sec. II.B and Fig. 6). The presence of two spin species is important, however, for the detection of cross relaxation, since the process shows up as opposite changes in the isotopic Zeeman temperatures, which can be measured by continuous-wave NMR techniques, and because the initial nonequilibrium state can be realized by simply saturating one of the resonances.

3. Extraction of the exchange constant

Cross relaxation offers, in principle, a very sensitive probe for determining the strength of the exchange interaction. Using Provotorov's (1962) theory, τ_x can be computed for given spin-spin interactions, although the calculation is somewhat complicated. Oja, Annila, and Takano (1990) computed τ_x numerically by taking into account dipolar interactions up to the sixth shell of neighbors and by assuming different strengths for the nearest-neighbor RK interaction $-J\mathbf{I}_i\cdot\mathbf{I}_j$. More distant J's were neglected, since their values are small. The relevant spin-correlation function was assumed to have the Gaussian form (Goldman, 1970; Demco, Tegenfeldt, and Waugh, 1975). It then follow, approximately, that $\tau_x=\tau_0\exp(B^2/b^2)$, where the constant b is on the order of $B_{\rm loc}$ and τ_0 is on the order of the spin-spin relaxation time τ_2 (Goldman, 1970). The rather linear behavior of the measured τ_x in a $\log\tau_x$ vs B^2 plot supports this assumption (see Fig. 94), although in high fields the increase in τ_x with B was not so steep. For $|J|/h>20$ Hz, it was found that $b^2\approx 11J^2/(\hbar^2\gamma_{\rm av}^2)+x_a x_b(\gamma_a-\gamma_b)^2B^2/\gamma_{\rm av}^2$. The best fit to the experimental data on silver was obtained with an antiferromagnetic $J/h=-(31\pm2)$ Hz; the agreement between theoretical and experimental values of τ_x is rather good.

Poitrenaud and Winter (1964) deduced from a linewidth analysis of their NMR data at high temperatures $|J|/h=(26.5\pm1.5)$ Hz, but they were unable to extract the sign of J. As long as $|J|$ is much larger than the nearest-neighbor dipolar interaction, τ_x is also rather insensitive to the sign of J. The relative changes in the equilibrium intensities of the ^{107}Ag and ^{109}Ag signals as a function of polarization show clearly, however, that J is antiferromagnetic. This so-called "suppression enhancement" will be discussed in detail in Sec. XI.B. This effect, too, yields J consistent with the τ_x analysis. In addition, $J/h=-(31\pm2)$ Hz is in good agreement with band-structure calculations (Harmon *et al.*, 1992) and susceptibility measurements (Hakonen, Yin, and Lounasmaa, 1990).

Buishvili and Fokina (1994) have recently investigated the dependence of the cross relaxation on polarization. Their theoretical calculations show that, in sufficiently low fields, τ_x decreases with increasing p and that the ratio $\tau_x(\text{low}\,p)/\tau_x(\text{high}\,p)$ increases with B, as was observed in the measurements (see Fig. 94).

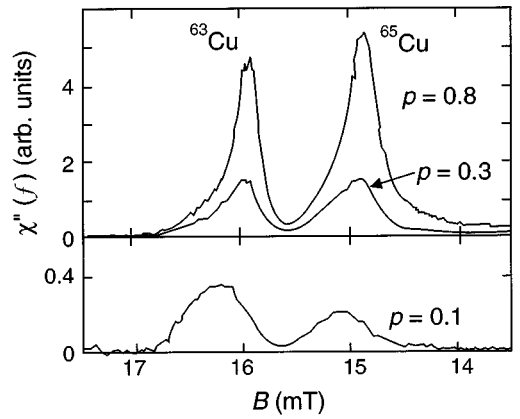

FIG. 96. NMR absorption $\chi''(f)$ of copper at the frequency $f=183$ kHz, measured by sweeping the external magnetic field. Nuclear-spin polarizations p have been indicated for each curve. From Ekström *et al.* (1979).

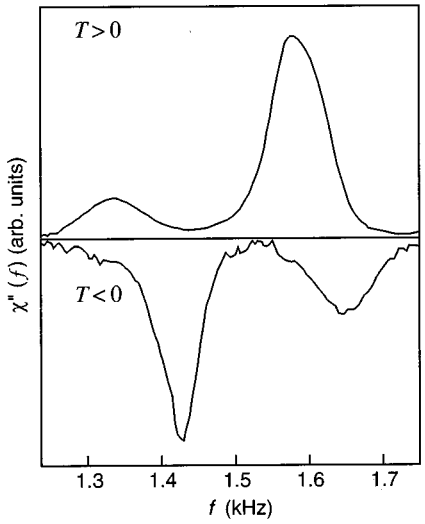

FIG. 97. NMR absorption $\chi''(f)$ of silver, scaled to the external field $B=0.8$ mT, at positive and negative polarizations $|p|\approx 0.7$. The curve at $T>0$ was obtained from the data of Oja, Annila, and Takano (unpublished) at $B=0.774$ mT and $p=0.70$, after scaling their frequency axis by 1.034. The spectrum for $T<0$ is from measurements of Hakonen, Nummila, and Vuorinen (1992) at $B=0.822$ mT and $p=-0.68$, scaled down in frequency by the multiplier 0.973.

Knowledge of τ_x is crucial in the interpretation of time-dependent phenomena associated with spontaneous nuclear ordering. In fields below 0.1 mT, where nuclear ordering has been observed (see Fig. 73), $\tau_x \approx \tau_2$ and cross relaxation is fast in comparison with typical demagnetization and remagnetization rates used in the nuclear-ordering experiments. Assuming that the same holds for copper, slowness of cross relaxation cannot be the source of nonadiabaticity (see Secs. V.C and VII.F.5), contrary to a proposal by Lindgård (1988a). This is important to know, since thermometry in these experiments (see Sec. IV) relies on adiabatic field changes.

B. Polarization-induced suppression and enhancement of isotopic NMR lines

1. Copper

The suppression-enhancement effect was discovered by Ekström *et al.* (1979) when they made NMR measurements of highly polarized copper spins. The effect is illustrated in Fig. 96. It shows the NMR absorption $\chi''(f)$, measured using the field-sweep technique at the frequency $f=183$ kHz. Peaks for the two isotopes ^{63}Cu and ^{65}Cu are clearly separate at all polarizations. The positions of the peaks correspond approximately to the gyromagnetic ratios $\gamma_{63}/2\pi=11.3$ MHz/T and $\gamma_{65}/2\pi=12.1$ MHz/T. The intensities of the two resonances are proportional to the abundancies of the isotopes, $x_{63}=0.69$ and $x_{65}=0.31$, only at small polarizations. At high p, there is a clear discrepancy between the expected and observed intensity ratios. When $p=0.9$, the signal from the less abundant isotope ^{65}Cu is much larger than the signal from ^{63}Cu. The intensity ratio, determined from the areas of the peaks, is 1.7 and decreases towards 0.5 in the low-polarization limit.

Ekström *et al.* (1979) explained this effect by the use of an internal-field model. The local ac field on ^{63}Cu spins consists of the external excitation field B_1 and the internal fields due to exchange and dipolar interaction with ^{65}Cu, and vice versa. The latter is proportional to the magnetization. The effect of the exchange interaction is to replace the magnetic field $\mathbf{B}_0=B_{\rm ext}\mathbf{z}+B_1\mathbf{x}$ by $\mathbf{B}_i^*=\mathbf{B}_0+\mu_0 R\mathbf{M}_j$, acting on the isotope i. The ac field is modified, in turn, by the factor $[1-R\chi_j(\omega)]^{-1}$, and far from the resonance frequency $\omega_j^*=\gamma_j B_{jz}^*$ one may approximate by noting that $\chi_j \propto (\omega_j^*-\omega)^{-1}$. Thus for $R<0$, the excitation at the higher resonance frequency is enhanced by the other isotope, as is shown by the data in Fig. 96.

This model was employed to determine the exchange constant R. The observed line shapes could be reproduced by assuming $R=-0.43\pm 0.04$. This value is somewhat different from $R=-0.39$, obtained from susceptibility measurements (see Sec. V.A). The theoretically calculated exchange interactions yield a lower R as well (see Table IV in Sec. XV.A). It seems also that the value $|R|=0.43$ is 10–20 % too large to be consistent with the NMR linewidth measurements of Andrew *et al.* (1971).

2. Silver

Silver is another two-isotope system, consisting of ^{107}Ag and ^{109}Ag, in which the suppression-enhancement effect has been investigated. Measurements at $T>0$ were performed by Oja, Annila, and Takano (1990) and at $T<0$ by Hakonen, Nummila, and Vuorinen (1992). Figure 97 shows absorption spectra at both positive and negative polarizations $|p|\approx 70\%$. There is an interesting qualitative difference between the spectra. At $T>0$, the peak at the higher frequency was enhanced with increasing polarization. This was caused by the antiferromagnetic exchange interaction, as in copper. At $T<0$, how-

ever, the opposite behavior was observed, as if the interactions were ferromagnetic. This can be understood in terms of internal fields that depend on the exchange interaction through the product pR. Therefore, by reversing the sign of either polarization or the exchange interaction, one obtains the same behavior.

The other characteristics of the spectra in Fig. 97 include an overall down shift of the two resonances at $T>0$, while an up shift is observed at $T<0$. Finally, in a fashion similar to the repulsion of any coupled energy levels in second-order perturbation theory, increasing polarization makes the two NMR peaks repel each other at positive and negative temperatures.

Hakonen, Nummila, and Vuorinen (1992) presented data on the intensity ratio of the two absorption lines in silver for polarizations in the range $0--0.70$. In addition, the separation of the peak frequencies was measured. At positive temperatures, the ratio of the intensities for the ^{107}Ag and ^{109}Ag lines had been measured by Oja, Annila, and Takano (1991). These authors used the suppression-enhancement effect for matching the spin-polarization scales of their two experimental setups.

The internal-field model of Ekström *et al.* (1979) was applied, quite successfully, to describe the data both at $T>0$ and $T<0$. The best fit to the experimental results was obtained with the exchange parameter $R=-2.3--2.5$, in good agreement with the values obtained from susceptibility measurements (Hakonen, Yin, and Lounasmaa, 1990), from cross-relaxation data (Oja, Annila, and Takano, 1990), from an analysis of the NMR linewidth (Poitrenaud and Winter, 1964), and from electronic-structure computations (Harmon *et al.*, 1992).

3. Theoretical calculations

The internal-field model of Ekström *et al.* (1979) has recently been elaborated by Heinilä and Oja (1994d). These authors give analytical expressions for the intensities and positions of the resonance peaks for spins interacting via exchange forces only. More importantly, they introduce a new method for accurately calculating NMR line shapes for a system consisting of classical spins. The technique is based on a combination of Monte Carlo simulations and numerical solutions of the microscopic equations of motion. The calculations were used to establish the accuracy of the approach used by Ekström *et al.* (1979). It was found that the model works well, especially at intermediate polarizations when the lines are clearly separated. In certain cases, however, Heinilä and Oja observed that the internal-field model fails. These authors also investigated how the NMR response is affected by the random distribution of spins over the lattice sites.

Eska (1989) has studied, by the use of numerical simulations, the response of a system with two isotopes to large NMR tipping pulses. His results show, for example, that the roles of suppressed and enhanced resonances are exchanged when the tipping angle approaches $\pi/2$. It would be interesting to test this prediction by extending NMR studies of highly polarized spins to large tipping angles; the experiments on copper and silver were performed using continuous-wave NMR in the limit corresponding to small tipping angles.

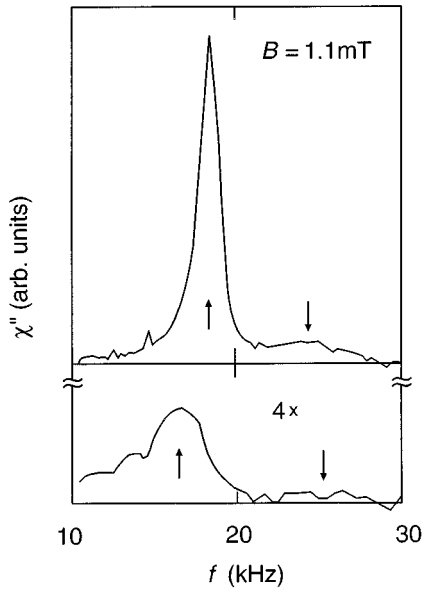

FIG. 98. NMR absorption χ'' of copper in the external magnetic field $B=1.1$ mT. Nuclear-spin polarization is 0.9 in the upper frame and 0.15 in the lower. The vertical scale has been expanded by 4 in the lower frame. From Ekström *et al.* (1979).

The suppression-enhancement effect has also been investigated theoretically by employing the perturbation approach of Kubo and Tomita (1954; Oja, Annila, and Takano, 1988) and by the Green's-function technique (Buishvili, Kostarov, and Fokina, 1994). These calculations, as well as the simulations of Heinilä and Oja (1994d), can also account for the fact that exchange interactions cause merging of the isotopic absorption lines when their Larmor frequencies are sufficiently close to each other and the polarization is small.

C. Second-harmonic Larmor line

In their measurements of highly polarized copper spins, Ekström *et al.* (1979) observed an interesting NMR phenomenon related to the second-harmonic Larmor line, i.e., absorption near $\omega_{2L}=2\gamma B$. The line is very difficult to see in high external fields since, according to Anderson (1962), the intensity of the ω_{2L} resonance is approximately proportional to $(1+B^2/b^2)^{-1}$ times the intensity of the ω_L peak, where b is on the order of the local field. As $B_{\rm loc}=0.34$ mT in copper, the ω_{2L} resonance can be observed in fields around 1 mT. This is illustrated by Fig. 98. The second harmonic is seen clearly in the data for the polarization $p=0.9$ above the main peak. The position of the resonance is shifted below the high-temperature value $\omega_{2L}/2\pi=2\gamma B$. At $p=0.15$, the intensity of the second harmonic is low but sufficient to show that the resonance is located at a higher frequency than when $p=0.9$.

Ekström *et al.* were able to explain the origin of the shift by analyzing the equations of motion for spins rotating at frequencies near the Larmor value and its second harmonic. It was found that coupling between these modes of rotation yielded the estimate $R=-0.41\pm0.04$ for the strength of the exchange interaction, in good agreement with $R=-0.43\pm0.04$ obtained from an analysis of the suppression-enhancement effect. The fact that the shift in the ω_{2L} line is definitely negative sets an upper limit of -0.33 for R.

Moyland *et al.* (1993) have extended the work of Ekström *et al.* (1979) by calculating the intensities and resonance frequencies for the ω_L and ω_{2L} lines in silver and gold, as well. They found that the intensities of the ω_{2L} lines decay quickly away from the field in which ω_L and ω_{2L} resonance frequencies anticross. This is caused by the large exchange interactions in these metals. Detection of the second harmonics would therefore be difficult. The authors conclude, however, that determination of R through coupling of the ω_L and ω_{2L} modes may still be possible by observing a break in the Larmor mode at the anticrossing field.

XII. EXPERIMENTS ON THALIUM, SCANDIUM, AND $AuIn_2$

In these metals, with $\kappa=4.4$ msK for Tl, 90 msK for Sc, and 110 msK for $AuIn_2$, the spin-lattice relaxation time τ_1 is so short that the conduction-electron and nuclear-spin temperatures are essentially equal. This means that the exchange interaction is strong, probably producing nuclear order at a relatively high temperature, and that thermal isolation of the nuclei from external sources of heat leaks is not possible relying on a long spin-lattice relaxation. Consequently, experiments on Tl, Sc, and $AuIn_2$ have been carried out in quite different regimes than those on Cu, Ag, and Rh. Instead of nano- and picokelvin nuclear temperatures, one works in the microkelvin range and with $T=T_e$ (Pobell, 1994).

In this section we shall first discuss briefly the experiments on thallium, in which NMR measurements have shown interesting behavior at low temperatures (Eska and Schuberth, 1987; Leib *et al.*, 1995). We then present, in more detail, the data on scandium (Suzuki *et al.*, 1994; Koike *et al.*, 1995) and on $AuIn_2$ (Herrmannsdörfer and Pobell, 1995; Herrmannsdörfer, Smeibidl *et al.*, 1995). Magnetic susceptibility measurements on Sc show that this metal probably orders ferromagnetically at about 100 μK. In the intermetallic compound $AuIn_2$ a ferromagnetic transition has been discovered at 35 μK. This is the first unambiguous observation of spontaneous nuclear magnetic ordering in a non-hyperfine-enhanced metal (see Sec. XIII) with thermal equilibrium between the nuclei and the conduction electrons. We would like to remind the reader, however, that nuclear-spin order in Cu, Ag, and Rh is not influenced by the temperature of conduction electrons. Besides, the spin temperature of the gold nuclei may differ from T_e owing to the much larger Korringa constant of Au in $AuIn_2$.

A. Thallium

The NMR behavior (Eska and Schuberth, 1987) and nuclear specific heat (Schröder-Smeibidl *et al.*, 1991) of thallium have been investigated using two-stage nuclear-demagnetization refrigerators in Garching and in Bayreuth. Among metallic elements, thallium has the strongest known nucleus-electron coupling, which results in the Korringa constant $\kappa=\tau_1 T_e=4.4$ msK (Eska *et al.*, 1986). The absolute strength of exchange interactions has been determined by studying merging of the NMR absorption lines of ^{203}Tl and ^{205}Tl (Karimov and Shchegolev, 1961). Assuming only nearest-neighbor exchange interactions, $|J|/h=37.5$ kHz. If the interaction is ferromagnetic, one obtains the mean-field estimate $T_C=\frac{1}{3}I(I+1)zJ/k_B=5$ μK using $z=12$ and $I=\frac{1}{2}$. Unfortunately, thallium is toxic and readily oxidizes when it is exposed to air. This will severely limit the use of this metal as a nuclear refrigerant.

Eska and Schuberth (1987) refrigerated their 4N-pure thallium samples to temperatures as low as 70 μK. A change in the NMR signal was observed for spin polarizations exceeding 40%: the single line split into two peaks with a nearly temperature- and field-independent separation. This was, at the time, attributed to the onset of nuclear-spin ordering. The intensity of the NMR line, above the assumed transition, was enhanced over the value expected from a Curie-law susceptibility.

Schröder-Smeibidl *et al.* (1991) later measured the nuclear heat capacity of a 0.79 mol thallium sample, 5N-pure, at 70 μK $\leqslant T \leqslant$ 20 mK and 20 mT $\leqslant B \leqslant$ 230 mT. The specific-heat data indicated simple nuclear paramagnetic behavior in the investigated temperature and field regions. Therefore the NMR anomalies observed earlier by Eska and Schuberth (1987) cannot have resulted from phase transitions. Spontaneous nuclear ordering in thallium metal must thus occur well below 70 μK, as was originally expected.

NMR behavior of thallium has also been investigated in several theoretical studies. Calculations based on the linear-response theory have not been able to reproduce the observed NMR anomalies (Oja, Annila, and Takano, 1988; Eska, 1989; Heinilä and Oja, 1994d; Buishvili, Kostarov, Fokina, unpublished). According to recent theoretical and experimental work by Eska and coworkers, the line splitting results from the combination of two effects: nonlinear spin dynamics due to a large NMR tipping angle and interference effects of the magnetization gradients in the rf penetration depth (Bäuml *et al.*, 1994; Leib *et al.*, 1995).

B. Scandium

Nuclear-spin order in scandium metal has been studied in Tokyo and Kanazawa by Suzuki and co-workers (Suzuki *et al.*, 1994; Koike *et al.*, 1995). Behavior that might have been due to nuclear ferromagnetism was observed from magnetic-susceptibility measurements car-

ried out during the warmup after demagnetization from 2.5 T and 0.28 mK to zero field. Spin-glass-like phenomena were also detected.

Owing to its small Korringa constant, $\kappa = 90$ msK, exchange interactions are expected to be strong in scandium. Since the crystal structure is hcp and $I = \frac{7}{2}$ for the only stable isotope ^{45}Sc, there is a quadrupole interaction between the crystalline electric-field gradient eq and the nuclear quadrupole moment Q. One then must add to the Hamiltonian of Eq. (1) the term

$$\mathcal{H}_Q = \sum_i [3e^2qQ/4I_i(2I_i-1)][I_{iz}^2 - \tfrac{1}{3}I_i(I_i+1)]. \tag{59}$$

Pollack *et al.* (1992) have found that in zero magnetic field the ground state of Sc is $\pm\frac{7}{2}$, with the first excited state $\pm\frac{5}{2}$ located at 18 μK. Spontaneous nuclear ordering of scandium can be described using an Ising system if the critical temperature is clearly below 18 μK.

Starting from the value of the nuclear magnetic moment, $\mu = 4.76\mu_N$, the dipole-dipole interaction $\mathcal{H}_D$ can be calculated; the result (Koike *et al.*, 1995) predicts an antiferromagnetic transition at 130 nK. Estimates show, however, that the Ruderman-Kittel interaction $\mathcal{H}_{RK}$ will produce nuclear ordering at a higher temperature, in the low microkelvin range.

A two-stage copper/scandium nuclear-demagnetization cryostat in Tokyo was used for these experiments. The sample was a $25\times3\times3$ mm^3 single crystal, with the long edge parallel to the direction of the hexagonal c axis. The second-stage demagnetizing field was in the same direction. To produce zero magnetic field, a mu-metal shield surrounded the sample. The magnetic impurities of the specimen were 3 ppm of Fe, 0.23 ppm of Cr, and 3.2 ppm of Mn. Although this impurity level is not high, the residual resistivity ratio was only $\rho(300\text{ K})/\rho(4.2\text{ K}) = 37$, while the best value reported so far for scandium is 400. This reflects the large exchange enhancement of Pauli paramagnetism and the strong tendency towards ferromagnetism in this metal.

The lowest temperature reached in the first nuclear stage was about 100 μK, attained by demagnetizing from 7 T. The ac magnetic susceptibility χ was recorded using a SQUID-based inductance bridge. The temperature of the copper nuclear stage was measured by a Pt-NMR thermometer. A serious weakness of these experiments is that the temperature of the Sc nuclei was inferred from indirect evidence only and never measured.

Suzuki *et al.* (1994) first determined the temperature dependence of χ in zero magnetic field between 0.1 and 10 mK. Below a dip at about 0.3 mK, the nuclear susceptibility showed approximately Curie-like behavior. Later, the scandium single crystal specimen was cooled in a field of 2.4 T, keeping the first nuclear stage at 0.28 mK for over 10 days, which should have been long enough to refrigerate the Sc spins to the same temperature. Under these conditions, 90% of the entropy $\mathcal{R}$ ln2 of the ground-state doublet $\pm\frac{7}{2}$ was probably removed. Demagnetization from 2.4 T to zero field was

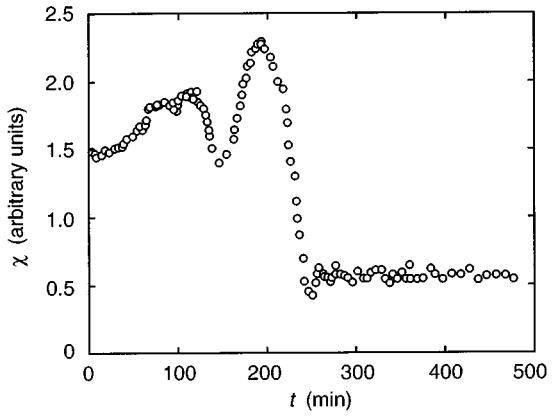

FIG. 99. Time dependence of the magnetic susceptibility χ of scandium metal during warmup, after demagnetization to $B = 0$ from a 2.4 T external field parallel to the c axis of the hcp single crystal. The starting temperature before demagnetization was 0.59 mK. From Suzuki, Koike, Karaki, Kubota, and Ishimoto (unpublished).

then carried out in 30 min. The time variation of the magnetic susceptibility parallel to the c axis of the Sc crystal during subsequent warmup was measured next. Two maxima in the χ vs time curve were observed with a sharp dip at a higher temperature. Several demagnetization experiments from different starting temperatures were performed with almost identical results; data for another run, starting at 0.59 mK, are plotted in Fig. 99. The temperature, although not measured, is a monotonically increasing function of time.

From the Curie-law behavior of χ at higher temperatures, it was estimated that the upper peak in Fig. 99 occurred around 70 μK. Using a polycrystalline sample of 50 ppm Fe impurity, observed a shift of the maximum to 0.8 mK. They suggest that the dependence of the peak position on impurity concentration shows that the higher-temperature maximum of χ is due to freezing of the electronic spin glass made of Fe impurities. It might also be possible that the lower-temperature peak is due to spin-glass phenomena as well, either directly or indirectly. If this were the case, however, the peak should increase proportionally to the Fe impurity concentration, which was not observed. According to the authors, the most likely explanation is that the lower maximum in the magnetic susceptibility of scandium corresponds to nuclear ordering and to the formation of ferromagnetic domains.

Unfortunately, there are at least two serious difficulties in the interpretation of the data by Suzuki *et al.* (1994) and Koike *et al.* (1995): The temperature of the specimen was not measured directly and the effect of magnetic impurities remains somewhat unknown. Therefore several uncertain conclusions had to be made. Further work on scandium is clearly warranted. To increase the reliability of the data interpretation, we feel that it is also important to study how a quadrupolar system, with no cooperative ordering due to spin-spin interactions, behaves during demagnetization and the subsequent warmup in a low field. Nevertheless, it is possible

that a ferromagnetic transition was reached in scandium.

C. Nuclear ordering in $AuIn_2$

The ultralow-temperature group at Bayreuth has measured the nuclear specific heat C, the nuclear magnetic susceptibility χ, and nuclear-magnetic-resonance spectra of $AuIn_2$ down to 30 μK. The large nuclear magnetic moment ($\mu = 5.5\mu_N$) and the high nuclear spin ($I = \frac{9}{2}$), as well as the small Korringa constant ($\kappa = 90$ msK), would make indium metal, in principle, a favorable candidate for studies of nuclear magnetic ordering phenomena. The low value of κ ensures that there is thermal equilibrium in the sample at all times, i.e., $T = T_e$. However, the strong nuclear electric quadrupole interaction in tetragonal indium, producing a relatively large splitting (0.3 mK) of the nuclear hyperfine levels even in zero external magnetic field (Symko, 1969; Karaki *et al.*, 1994), and the rather high superconducting critical field of 28 mT, preventing demagnetization to lower fields because thermal contact to electrons is lost in a superconductor, are severe drawbacks for studies of nuclear ordering in indium metal itself.

To avoid these problems, the Bayreuth group has investigated ordering of ^{115}In nuclei in the cubic intermetallic compound $AuIn_2$ (Herrmannsdörfer and Pobell, 1995; Herrmannsdörfer, Smeibidl, Schröder-Smeibidl, and Pobell, 1995), which has a superconducting critical field of only 1.45 mT. Because of the small nuclear magnetic moment of ^{197}Au ($\mu = 0.14\mu_N$), the contribution of gold to the nuclear magnetic interactions in $AuIn_2$ is negligible. In addition, the Korringa constant $\kappa = 110$ msK of $AuIn_2$ is almost as small as for indium metal. Measurements of the heat capacity, magnetic susceptibility, and NMR spectra were made at 30 μK $\leqslant T \leqslant$ 10 mK and at 2 mT $\leqslant B \leqslant$ 115 mT. Earlier NMR results have been reported by Gloos *et al.* (1990).

The $AuIn_2$ samples were prepared by melting 5N-pure gold and 6N-pure indium in a graphite crucible. The specimens were annealed for 40 h at 420°C; this heat treatment resulted in a residual resistivity ratio RRR=500. From measurements of the static magnetic susceptibility an upper limit of 0.5 ppm was deduced for the concentration of electronic magnetic impurities. X-ray diffraction data showed that the investigated $AuIn_2$ samples were single crystals.

The experiments were performed in a copper nuclear refrigerator (Gloos *et al.*, 1988, 1991; Pobell, 1992b) into which sample holders made of silver were installed for the NMR specimen, a calorimeter, a susceptometer, as well as for a pulsed Pt-wire NMR thermometer. For measurements of the NMR spectra, a $4\times12\times0.7$ mm^3 piece of $AuIn_2$ was used, soldered with In to the specimen holder. The calorimeter for the nuclear heat-capacity measurements was thermally isolated from its surroundings by a superconducting heat switch made of aluminum; the $AuIn_2$ sample was a cylinder, 17 mm long and 5 mm in diameter. A set of three coils and niobium shields for the Pt-NMR thermometer, the $AuIn_2$ sample, and the superconducting heat switch surrounded the calorimeter. The setup also contained a pair of coils for mutual-inductance measurements of the nuclear susceptibilities χ' and χ'' of the $AuIn_2$ specimen.

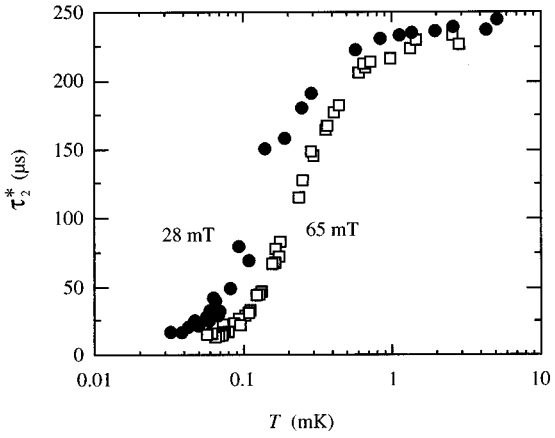

FIG. 100. Temperature dependence of the effective nuclear spin-spin relaxation time τ_2^* of ^{115}In in $AuIn_2$ at $B = 28$ and 65 mT. The rather low saturation value of 230 μs for $T > 1$ mK is due to field inhomogeneities in the experimental setup. With improved arrangements relaxation times up to 600 μs were observed. From Herrmannsdörfer, Smeibidl *et al.* (1995).

The copper nuclear refrigerator cooled the calorimeter and the $AuIn_2$ sample to the starting conditions $B = 115$ mT and $T = 85$ μK, which correspond to an entropy reduction $\Delta S/S_{\max} = 0.35$ and polarization $p = M/M_{\text{sat}} = 0.74$. The heat switch was then put into its off position and the $AuIn_2$ sample was demagnetized to the low measuring field. The tiny heat leak, between 2 and 10 pW, to the coldest parts of the apparatus and the small Korringa constant of $AuIn_2$ allowed good thermal equilibrium between the nuclei and the conduction electrons; the maximum difference ΔT between the sample and the thermometer was 12% at the lowest temperatures and decreased rapidly as T was increased.

In the millikelvin temperature region, the NMR spectra of ^{115}In showed a resonance peak at the nuclear Larmor frequency. The effective spin-spin relaxation time τ_2^*, deduced from the NMR linewidths and measured between 7 and 115 mT, was constant down to about 2 mK, with values up to 600 μs, but then decreased substantially to a minimum of 15 μs at 50 μK (see Fig. 100); this strong temperature dependence of τ_2^* was rather surprising and the first hint of a magnetic transition nearby. For the Korringa constant, a field- (28 mT $\leqslant B \leqslant$ 115 mT) and temperature- (75 μK $\leqslant T \leqslant$ 10 mK) independent value $\kappa = 112 \pm 15$ msK was deduced.

The nuclear magnetization of ^{115}In was found from the free induction decay of the NMR signal, extrapolated to the middle of the excitation pulse. The results obtained in an external field of 28 mT are shown in Fig. 101. The magnetization increased with decreasing temperature according to the Curie-Weiss law, reached a maximum at about 55 μK, and then decreased by about a factor of 2 while the temperature was lowered to 30 μK. The Weiss temperature $\theta \approx 30$ μK. A similar T dependence was seen in 65- and 94-mT fields.

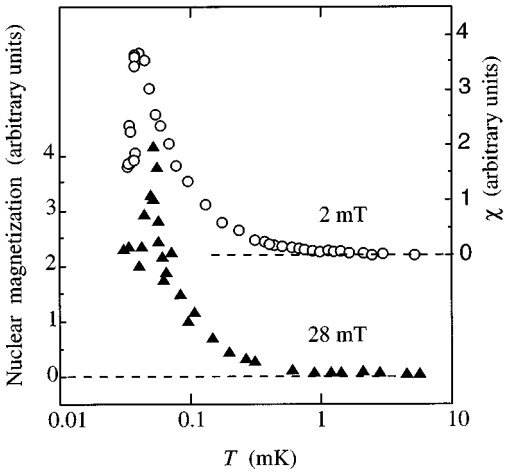

FIG. 101. Nuclear magnetization and susceptibility of ^{115}In in $AuIn_2$. Open circles are results from ac mutual-inductance measurements at 16 Hz in a 2 mT field. Filled triangles are data points deduced from NMR spectra at 260 kHz and 28 mT. From Herrmannsdörfer, Smeibidl *et al.* (1995).

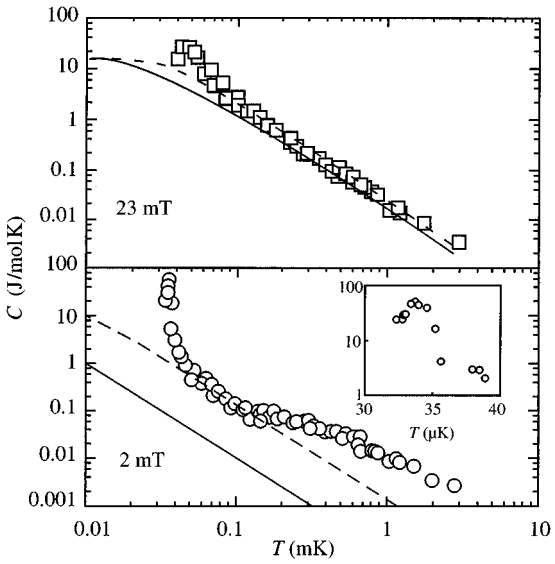

FIG. 102. Nuclear specific heat C of ^{115}In in $AuIn_2$, measured in 23 mT and 2 mT external magnetic fields. The solid lines are calculated for noninteracting In nuclei. The dashed curves in the upper and lower figures are for $B_{\rm eff}=(B^2+b^2)^{1/2}=27$ mT, $b=14$ mT and for $B_{\rm eff}=7.3$ mT, $b=7$ mT, respectively. The inset shows the behavior of C near $T_C=34$ μK. Modified from Herrmannsdörfer, Smeibidl *et al.* (1995).

The mutual-inductance measurements of the nuclear susceptibility, performed in 2-, 5-, and 13-mT fields, showed the same behavior. Data at 2 mT are plotted in Fig. 101. The susceptibility changes again followed the Curie-Weiss law, but with $\theta\approx 43$ μK; the maximum of χ was reached at 40 μK, indicating a phase transition nearby. According to both types of magnetic measurements, the Weiss temperature is thus positive, which shows that the magnetic interactions between the nuclear spins of In in $AuIn_2$ are predominantly ferromagnetic.

The Bayreuth data on the nuclear specific heat of $AuIn_2$, in an external magnetic field of 115 mT and between 0.08 and 8 mK, lie nicely on the curve calculated for a nuclear paramagnet with the properties of noninteracting In moments. There was a small enhancement at 0.11 mK, which was more pronounced and occurred at lower temperatures in fields of 70 and 47 mT. However, in an external field of 23 mT (see Fig. 102) one could see, at all temperatures, an enhancement of the experimental data over the curve for noninteracting nuclear spins; the heat-capacity maximum was at 45 μK. This behavior was more pronounced in a 13-mT field and most convincingly demonstrated by the data measured in the smallest external field of 2 mT. The heat-capacity maximum was 58 J/Kmol, which is almost three orders of magnitude higher than the noninteracting value. The enhancement of C in the paramagnetic range corresponds to an internal field $b=7.0$ mT acting on the In nuclei in $AuIn_2$. The temperature of the maximum, $T_C=35\pm 3$ μK, is in excellent agreement with the susceptibility data.

The ratio $T_C/\theta\approx 0.82$ is in good accord with the value 0.72 calculated for a Heisenberg ferromagnet with large spins in cubic surroundings (Herrmannsdörfer and Pobell, 1995). Similarly, the specific-heat enhancement, $\Delta C\approx 55$ J/K(mol of $AuIn_2$)=27 J/K(mol of In), agrees well with the prediction of the Heisenberg model giving $\Delta C=20$ J/Kmol. The relative reduction of entropy $\Delta S/S_{\rm max}=0.09$ at T_C and in $B=2$ mT is smaller than the value of about 0.14 for a simple cubic Heisenberg ferromagnet with $I=\frac{9}{2}$.

The steep maximum in the nuclear specific heat (see Fig. 102) near T_C and shifts on the order of several kHz in the position of the NMR resonance both suggest that the phase transition may be of first order. Dipolar forces between the In nuclei in $AuIn_2$ are on the order of 1 μK. Hence the interactions must be dominated by exchange coupling, which is presumably of the Ruderman-Kittel type. Using the measured Weiss temperature $\theta\approx 43$ μK, which equals $\frac{1}{3}I(I+1)\Sigma_j J_{ij}/k_B$ in the mean-field theory, Herrmannsdörfer, Smeibidl, *et al.* (1995) find the parameter $R=52$ for ^{115}In in $AuIn_2$. The large value of R indicates a much stronger exchange dominance in $AuIn_2$ than, for example, in silver.

The Bayreuth measurements of the nuclear specific heat, nuclear magnetic susceptibility, and NMR spectra of ^{115}In in $AuIn_2$, in the range of 30 μK$\leqslant T\leqslant$10 mK and 2 mT $\leqslant B\leqslant$115 mT, show that a ferromagnetic first-order phase transition occurs at the surprisingly high Curie point T_C=35 μK. The Weiss temperature $\theta=43$ μK, and the internal field in the paramagnetic state $b=10$ mT. Many features of the data can be understood within the nearest-neighbor, ferromagnetic Heisenberg model for a simple cubic ferromagnet with a large spin (Herrmannsdörfer and Pobell, 1995).

XIII. HYPERFINE-ENHANCED NUCLEAR MAGNETISM IN PRASEODYMIUM COMPOUNDS

In singlet ground-state ions like Pr^{3+}, with high Van Vleck susceptibilities, large hyperfine fields can be in-

duced at the nucleus by moderate external fields. When $B_{ext}=0$, these ions have a nonmagnetic electronic singlet ground state of their $4f$ shell, but an applied field changes the wave function and induces an electronic magnetic moment on the ground state. This moment, in turn, produces a much stronger hyperfine field at the nucleus, which adds to the applied field. Enhancement factors $\alpha=1+K$, where K is the Knight shift, around 20–100 are not uncommon. The apparent magnetic moment of the nucleus is then one to two orders of magnitude smaller than the Bohr magneton but two to one orders of magnitude larger than the nuclear magneton.

The prerequisites for a high value of α are a small separation between the singlet ground state and the first excited levels, which leads to a high Van Vleck susceptibility, and a large hyperfine coupling constant. Rare-earth ions with integral values of the angular momentum J suit these requirements best. Among them Pr^{3+} and Tm^{3+} are particularly good because they have the lowest spin angular momentum $S=1$. A small value of S is favorable, since this reduces exchange interactions between ions and thus makes spontaneous electronic polarization less likely.

Use of hyperfine-enhanced materials for nuclear cooling has been reviewed by Andres and Lounasmaa (1982). This paper is still generally current as far as nuclear refrigeration is concerned; recent work has mostly concentrated on matters important to nuclear ordering.

A. Nuclear refrigeration

The possibility of hyperfine-enhanced nuclear refrigeration was theoretically suggested by Al'tshuler (1966) and first put into practice by Andres and Bucher (1968). Reviews have been written by Lounasmaa (1974), by Andres and Lounasmaa (1982), and by Pobell (1992b). Andres and Bucher (1972 and references therein) have investigated many intermetallic compounds in search of singlet ground-state behavior.

More often than not, however, they observed magnetic order at liquid-helium temperatures, indicating that exchange interactions between the electronic magnetic moments of the ions are strong enough to polarize the singlet ground states. Van Vleck paramagnetism was found in intermetallic compounds of the type RX, where $R=$ Pr or Tm and $X=$ Cu, Sb, Bi, Se, or Te. Indications of nuclear refrigeration were seen in all these materials, but irreversible generation of heat, when the external magnetic field was swept downwards, often overshadowed the nuclear cooling effect and thus made the outcome disappointing. Promising results were obtained with $PrPt_5$, $PrCu_6$, $PrTl_3$, and especially $PrNi_5$. In these materials the spin-lattice relaxation time τ_1 is short, but bulk thermal equilibrium is reached only slowly owing to the poor heat conductivity of the samples. Buchal, Fischer *et al.* (1978) have also obtained good results for PrS. They were able to reach 0.72 mK by demagnetizing a sample made of this compound.

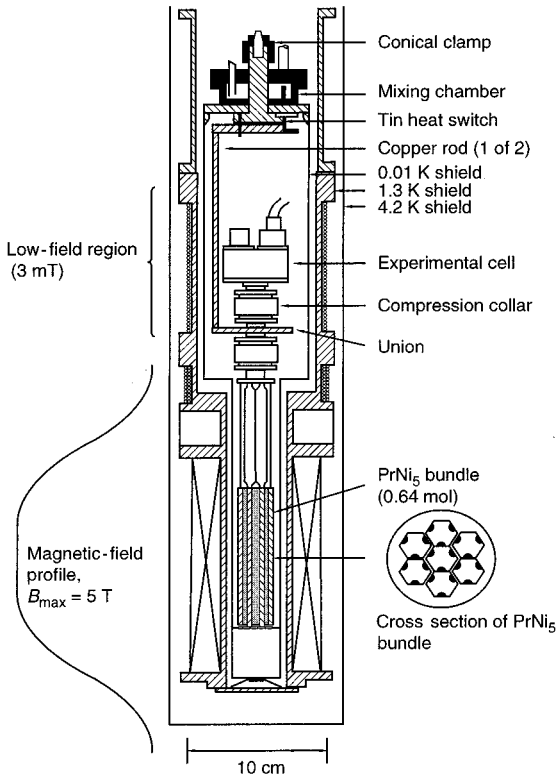

FIG. 103. Low-temperature parts of the $PrNi_5$ nuclear refrigerator of Greywall (1985). The $PrNi_5$ bundle consists of seven 8-mm diameter hexagonal rods, 95 mm long.

An obvious advantage of hyperfine-enhanced nuclear refrigeration is the strong polarizing field acting on the nuclei, which is usually at least ten times higher than the applied field. In polycrystalline $PrNi_5$, which is a hexagonal compound, the average hyperfine-enhancement factor is 12. Although the Pr nuclear-spin density in $PrNi_5$ is smaller than Cu spins in copper, the cooling entropy per unit volume is about ten times larger in the praseodymium compound. The local field $B_{loc}=18$ mT entering Eq. (13) is quite high.[11] These properties make it possible to build rather small refrigerators for reaching temperatures of 0.4 mK. Disadvantages when using $PrNi_5$, on the other hand, are the not-so-ready availability of the material, its poor thermal conductivity, and the rather high limiting low temperature.

Many cryostats based on hyperfine-enhanced nuclear cooling have been built, especially during the early eighties. Successful machines have been described by Mueller *et al.* (1980), by Andres, Hagn *et al.* (1975), and by Greywall (1985). As an example of a modern cryostat, we show in Fig. 103 the apparatus of Greywall.

Recently nuclear refrigeration using copper has, once again, become more popular. An important advantage of brute force nuclear cooling with copper is the ready availability of this metal in high-purity ingots, which re-

[11]Kubota *et al.* (1980) have found that B_{loc} is not constant but increases with field from the value quoted at $B=0$.

sults in excellent thermal conductivity at low temperatures. The easily variable cooling capacity, proportional to B^2, and the wide temperature range available give considerable flexibility to nuclear refrigerators based on copper.

B. Nuclear ordering

Different types of Van Vleck paramagnets can be classified using the parameter $\eta=2\alpha^2 J(\mathbf{Q})/\Delta$, where Δ is the energy separation between the ground state and the first excited state and $J(\mathbf{Q})$ is the Fourier transform, at wave vector $\mathbf{Q}$, of exchange interactions between the ions. If $\eta<1$ and if there are no hyperfine interactions, no magnetic ordering takes place in singlet ground-state systems at any temperature, i.e., there is no induced moment (Jensen and Mackintosh, 1991).

With hyperfine coupling $\mathcal{H}_{\rm hf}=\underline{A}\mathbf{I}\cdot\mathbf{J}$ between the nuclear spins and the $4f$ electrons, two important effects occur. First, external fields felt by the nuclei are enhanced as discussed above. Second, there is a magnetic transition even if $\eta<1$. The nature of the transition is very different if η is near the critical value, i.e., close to one, in comparison with the situation in which $\eta\ll 1$.

For nearly critical η, the phase change can be described as a nuclear-induced electronic transition. The theory of this process has been developed by Murao (1972, 1981). The nuclei remain disordered just below T_c and align only at lower temperatures. Ordering to such a mixed electron-nuclear state has been observed in $PrCu_2$ below 50 mK (Andres, Bucher, Maita, and Cooper, 1972) and in $PrCu_5$ below 40 mK (Andres, Bucher *et al.*, 1975; Genicon, Tholence, and Tournier, 1978). These compounds have also been investigated in neutron-diffraction experiments by Benoit *et al.* (1981) and Nicklow *et al.* (1985). Pure praseodymium metal appears to be a mixed electron-nuclear system. Early studies of the magnetic behavior of praseodymium produced controversial results, presumably due to magnetic impurities in the specimens. Cooperative magnetic ordering at $T_c=25-30$ mK was established in the heat-capacity measurements by Lindelof, Miller, and Pickett (1975). A sinusoidal modulation of the nuclear magnetic moment in Pr has been observed in neutron-diffraction measurements below 60 mK (Kawarazaki *et al.*, 1988; McEwen and Stirling, 1989).

For $\eta\ll 1$, the hyperfine-enhanced system can best be described as a nuclear magnet in which the moments, enhanced by the factor $1+K$, are coupled by an indirect exchange interaction. Magnetism in such a spin assembly is similar to that found, for example, in copper at nanokelvin temperatures. The exchange interaction in enhanced nuclear magnets can be thought of as follows: The magnetic nucleus in a Pr ion i induces a $4f$ electronic moment in that ion. This moment then couples to the $4f$ electrons in a neighboring ion j by the Ruderman-Kittel-Kasuya-Yosida interaction and, in turn, to nucleus j through the hyperfine interaction (Ruderman and Kittel, 1954; Kasuya, 1956; Yosida, 1957).

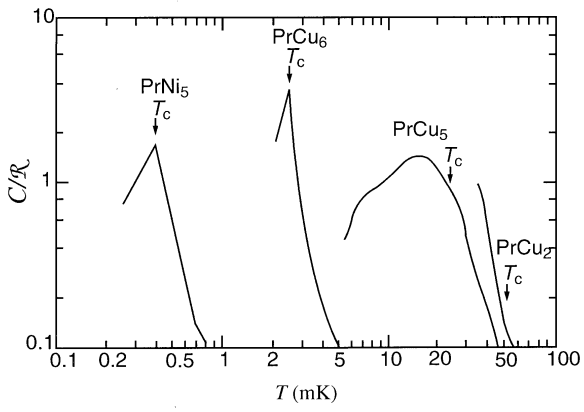

FIG. 104. Reduced specific heats $C/\mathcal{R}$ of $PrNi_5$, $PrCu_6$, $PrCu_5$, and $PrCu_2$ vs temperature. The arrows indicate the positions of the maxima in the susceptibility vs temperature curves for the corresponding compounds. The figure has been modified from that of Babcock *et al.* (1979) by including the data for $PrNi_5$ from Kubota *et al.* (1980).

In summary, the energy scales for Pr^{3+} ions are such that the ordering is purely of nuclear origin only if the transition temperature is below 10 mK. For T_c's in the range between 10 mK and 1 K, the ordering is to a mixed electron-nuclear state. Finally, if T_c is above 1 K, the transition is probably purely electronic.

Among praseodymium compounds for which $\eta\ll 1$, ferromagnetic ordering has been observed at $T_C=2.5$ mK for $PrCu_6$ (Babcock *et al.*, 1979) and at $T_C=0.40$ mK for $PrNi_5$ (Kubota *et al.*, 1980). Nonferromagnetic, presumably antiferromagnetic nuclear ordering has been seen at $T_N=0.5$ mK in PrSe (Kubota *et al.*, 1987). These three compounds are the only metals, besides diluted $PrNi_5$, for which hyperfine-enhanced spontaneous nuclear magnetic ordering has been reported.

The other compounds in the series, PrS, PrSe, and PrTe, are also interesting systems for studies of nuclear magnetism. Kubota *et al.* (1984) measured the ac susceptibility of PrS down to 80 μK, but they observed no evidence for magnetic ordering. PrS, PrSe, and PrTe have the simple NaCl structure in which Pr nuclei occupy fcc sites. It would be interesting to study the spin-spin interactions and ordered magnetic structures of these metals in more detail, as well as to compare them with the properties of Cu, Ag, and Rh.

The specific-heat data for $PrCu_6$ and $PrNi_5$ are illustrated in Fig. 104. A sharp anomaly is observed at T_C, which coincides with a peak in the magnetic susceptibility vs temperature curve. Figure 104 also shows results for $PrCu_2$ and $PrCu_5$, in which the transition takes place in a mixed nuclear-electronic state. The different character of the ordering is evident: The specific-heat peak in $PrCu_2$ and $PrCu_5$ is broad and the magnetic susceptibility reaches its maximum value at a higher temperature than does the specific heat.

Other investigations of $PrNi_5$ by the Jülich group include the finding that the ratio of the Curie constant to the saturation magnetization is larger than what one would expect for localized hyperfine-enhanced moments

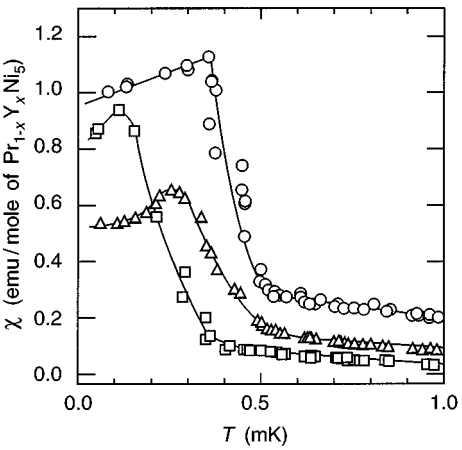

FIG. 105. Nuclear magnetic susceptibility of $Pr_{1-x}Y_xNi_5$ below 1.0 mK as a function of temperature: ○, $x=0$; △, $x=0.05$; □, $x=0.20$. The maxima of the curves occur approximately at the nuclear Curie temperature T_C. From Herrmannsdörfer, Uniewski, and Pobell (1994a, 1994b).

on the basis of the known enhancement factor $1+K=12$ (Kubota *et al.*, 1983). This was taken as evidence for extra fluctuating magnetic moments that have a long wavelength and do not give large contributions to the specific heat at low temperatures.

The group at Osaka has measured the electrical resistivity ρ of $PrCu_6$ across the magnetic phase transition (Miki *et al.*, 1992). A decrease in ρ started at T_C=2.6 mK, which was attributed to ferromagnetic ordering. Resistivity also displayed critical phenomena just above T_C.

The influence of magnetic dilution on the electronic and nuclear magnetic properties of $Pr_{1-x}Y_xNi_5$ was investigated recently by Herrmannsdörfer, Uniewski, and Pobell (1994a, 1994b) for yttrium concentrations $x=0$, 0.02, 0.05, 0.10, 0.20, and 1.00. Replacement of Pr^{3+} by Y^{3+} was expected to have a substantial effect on the electronic and nuclear magnetic properties of these compounds because yttrium lacks the $4f$ electron. The mutual-inductance measurements of the 16-Hz nuclear susceptibilities were made in the temperature range 50 $\mu K \leqslant T \leqslant 8$ mK and in fields $B_{ext} \leqslant 0.1$ mT. Each of the six specimens had a mass of about 0.1 g.

The nuclear susceptibility χ of $Pr_{1-x}Y_xNi_5$ is plotted as a function of temperature in Fig. 105 between 50 μK and 1.0 mK for three yttrium concentrations. In the paramagnetic region at high temperatures, the $1/\chi$ vs T plots display a typical ferromagnetic behavior. At $T<0.6$ mK, a substantial increase of χ is observed for each compound, indicating a spontaneous nuclear magnetic ordering transition. The maximum of each curve was assumed to define the Curie temperature T_C. All samples containing praseodymium showed a nuclear phase transition, with T_C reduced from 370 μK at $x=0$ to 100 μK at $x=0.20$. The substantial depression of the ordering temperature might make the diluted $PrNi_5$ compounds useful for nuclear refrigeration into the microkelvin region.

The ratio of the observed nuclear Curie and Weiss temperatures depends strongly on the yttrium concentration: T_C/θ increases from 1.7 for $x=0$ to 7.7 for $x=0.20$. The measured values of $T_C(x)$ are in reasonable agreement with those calculated from the mean-field theory.

Moyland *et al.* (1995) have recently measured the zero-field nuclear ac susceptibility of $PrBe_{13}$ from 3 mK to 20 mK. Their data indicate antiferromagnetic Curie-Weiss behavior with the Weiss temperature $\theta=-2.2$ mK.

Various theoretical aspects of hyperfine-enhanced nuclear magnets have been investigated extensively by Ishii and co-workers (see, for example, Ishii and Aoyama, 1991; Akai and Ishii, 1994).

XIV. SPONTANEOUS NUCLEAR ORDER IN INSULATORS AT $T>0$ AND $T<0$

Owing to the poor thermal conductivity of insulators and their long intrinsic spin-lattice relaxation times, studies of nuclear ordering in dielectric materials are quite different from corresponding investigations on metals. Abragam and Goldman and their co-workers at Saclay (Chapellier, Goldman, Chau, and Abragam, 1970; Abragam and Goldman, 1982; Abragam, 1987) have conducted experiments that clearly demonstrate nuclear antiferromagnetism in CaF_2 and nuclear domain ferromagnetism in LiH, both materials being insulators of cubic crystal structure with spin $I=\frac{1}{2}$ of the ^{19}F or ^{1}H nuclei. Wenckebach and co-workers (Marks, Wenckebach, and Poulis, 1979; Van der Zon, Van Velzen, and Wenckebach, 1990) have investigated $Ca(OH)_2$ at $T<0$. Several aspects of these studies are worthy of a short digression from our main topic. We also refer the reader to a recent review by Bouffard *et al.* (1994).

A. Dynamic nuclear polarization

First, it should be noted that for studies of nuclear cooperative phenomena in insulators it is neither necessary nor is it possible to refrigerate the lattice to a temperature of 1 mK or below. It is sufficient just to cool the nuclei; the very long spin-lattice relaxation time τ_1, especially in insulators, again ensures that after demagnetization the nuclei are effectively decoupled from the rest of the specimen and thus remain cold long enough for experiments to be carried out.

The magnet used by Chapellier *et al.* (1970) generated a field $B=2.7$ T. With the internal field $b\approx 0.2$ mT at the site of the ^{19}F nuclei in CaF_2, it was found that $T_f/T_i=7\times10^{-5}$ if demagnetization were carried out from $B_i=2.7$ T all the way to $B_f=0$. A starting temperature $T_i<10$ mK would thus be necessary for reaching the microkelvin range. Although this temperature can easily be produced today by means of a suitable precooling stage, it is doubtful whether the fluorine nuclei could ever be cooled in equilibrium with the lattice, even with the help of electronic paramagnetic impurities, to the

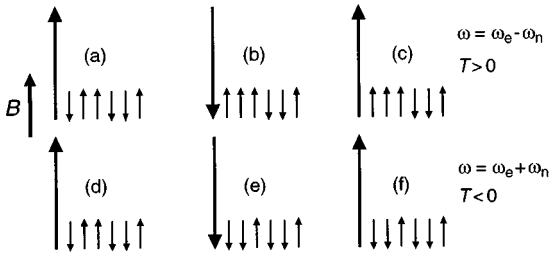

FIG. 106. Positive (upper sequence) and negative (lower sequence) nuclear-spin temperatures produced by the "solid effect." Long arrows depict electronic and short arrows nuclear magnetic moments. For further details, see text.

vicinity of 10 mK because of the extremely long relaxation time. The problem had to be solved in a different way.

The CaF_2 specimen, a sphere of about 1.5 mm in diameter, was first cooled at the tip of a copper cold finger to 0.7 K by means of a ^{3}He refrigerator. The ^{19}F nuclei were then dynamically polarized by a method known as the "solid effect," which now will be explained with the help of Fig. 106.

Let us consider a specimen in which a few electronic moments are mixed with the magnetic nuclei; this was achieved in the experiments of Chapellier *et al.* (1970) by introducing U^{3+} (or Tm^{2+}) ions, at a concentration of 10^{-4}, as paramagnetic impurities into the CaF_2 lattice. At $T=0.7$ K and $B_i=2.7$ T, the polarization of the nuclei was almost zero, whereas the three orders of magnitude larger electronic magnetic moments were nearly fully polarized ($p\approx 1$). Next, the system was pumped by a microwave field of angular frequency $\omega_e-\omega_n$, equal to the difference between the Larmor frequencies of the electronic and nuclear spins. Such a field can induce "flip-flop" transitions, the required energy being absorbed from the field of microwave power. Starting from the situation depicted in Fig. 106(a), the first time the electronic spin flips, one of the nuclear spins that originally pointed down will reverse its direction as in Fig. 106(b); an energy quantum $\hbar(\omega_e-\omega_n)$ is thereby absorbed by the spin system.

Owing to its short relaxation time with the lattice, the electronic spin quickly returns to its original direction, by simultaneously transferring an energy quantum $\hbar\omega_e$ to the lattice, while the nuclear spin, because of its very long relaxation time, will remain in its new direction as in Fig. 106(c). The process is then repeated, and, one by one, the nuclei in the vicinity of the U^{3+} impurity become polarized in the direction of the external magnetic field. By spin diffusion the polarizing effect of each electronic impurity gradually spreads out.

An interesting feature of the solid effect is that it can be used just as well for producing negative absolute temperatures in the nuclear-spin system. If the microwave frequency employed for pumping equals $\omega_e+\omega_n$, a pair of electronic and nuclear moments pointing originally in the same direction will reverse together in a flip-flip transition. The end result [see Figs. 106(d)–106(f)] is that the nuclei become polarized in the direction opposite to the external magnetic field $\mathbf{B}_i$. There are thus more nuclei in the higher energy level than in the lower one, i.e., the spin temperature T is negative (see Fig. 8).

In practice, the Saclay group produced up to 90% nuclear polarization in CaF_2 after three hours of microwave pumping at 0.7 K. The power was then turned off, which allowed the system to cool to 0.3 K, the temperature of the ^{3}He precooling stage. At 0.3 K the nuclear polarization p decayed sufficiently slowly for experiments. It should be noted that $p=0.5$ in a 2.7-T magnetic field corresponds to a spin temperature $T=\pm 4$ mK [see Eq. (25a)], the sign depending on the direction of polarization.

B. Adiabatic demagnetization in the rotating frame

Having thus reached the desired starting conditions for nuclear cooling, $T_i=\pm 4$ mK and $B_i=2.7$ T, the next step in the experiment of Chapellier *et al.* (1970) was to demagnetize. One could, of course, reduce the external field to zero in the hope of reaching very low positive or negative temperatures in the nuclear-spin system, depending on whether $T_i>0$ or <0, respectively. This simple procedure, however, is unsatisfactory because in insulators with paramagnetic ions the spin-lattice relaxation proceeds through impurities. In a low external field, the energy difference $\hbar(\omega_e-\omega_n)$ becomes small in absolute value and direct energy exchange between the nuclear- and electronic-spin systems can occur easily. The cold nuclei would thus reach equilibrium rather rapidly with the far hotter electronic impurities and lose their order quickly. To avoid these difficulties, demagnetization was performed in a rotating frame of reference, which we now describe.

It was already mentioned that after the microwave pumping was stopped the sample cooled to 0.3 K in a constant external field $B_i=2.7$ T. One assumes that the field is pointing in the z direction. In this field the ^{19}F nuclei have a Larmor frequency $\omega_n/2\pi=107$ MHz. One then applies to the specimen a small external magnetic field, $\mathbf{b}_0\approx 5$ μT, rotating in the xy plane, i.e., at right angles to $\mathbf{B}_i$, with an angular frequency ω_0 that is of the same order of magnitude as ω_n. In the frame rotating with $\mathbf{b}_0$, the Larmor frequency of the nuclear spins appears to be $(\omega_n-\omega_0)/2\pi$, i.e., the magnetic field that the nuclei see in the z direction is $(\omega_n-\omega_0)\mathbf{B}_i/\omega_n$. The sign of the initial temperature T_i is then positive or negative depending on whether the initial magnetization is parallel or antiparallel to $\mathbf{B}_i$.

In the rotating coordinate frame, $\mathbf{b}_0$ appears to be constant in its direction and magnitude and at right angles to $\mathbf{B}_i$. The nuclear spins thus experience an effective field whose magnitude is $B_{\rm eff}=\{[(\omega_n-\omega_0)/\gamma_n]^2+b_0^2\}^{1/2}$. Adiabatic demagnetization can now be performed by sweeping the field (or the frequency) from $B_i=\omega_n/\gamma_n$ to $B_f=\omega_0/\gamma_n$; here γ_n is the gyromagnetic ratio. The minimum value of the effective magnetic field, $B_{\rm eff}=b_0$, is reached at resonance $\omega_n=\omega_0$. If dipole-dipole and exchange interactions are ignored the

nuclear-spin system should now reach a temperature $T_f=(b_0/B_i)T_i\approx\pm 10$ nK, the sign of T_f being the same as the sign of $T_i=\pm 4$ mK. The actual final temperature is, however, between 0.1 and 1 μK (or between –0.1 and –1 μK) owing to dipolar interactions between nuclear spins. The final demagnetization of b_0 is then performed, followed by remagnetization in the sequence 5 μT$\rightarrow$0$\rightarrow$5 μT; this is the well-known adiabatic fast-passage technique.

Similarly to the situation in the laboratory frame, the final field after demagnetization in the rotating coordinate system can be nonzero. This is the case if ω_n is not swept all the way to $\omega_n=\omega_0$. Nuclear spins will then experience an effective external field that competes with the dipolar forces.

For the U^{3+} electronic moments at $B_i=2.7$ T, the Larmor frequency $\omega_e/2\pi=70$ GHz$\gg\omega_n/2\pi$. In the frame rotating at the nuclear Larmor frequency $\omega_0/2\pi$, the effective field on electronic moments hardly changes at all. Demagnetization in the rotating frame is thus "selective:" electronic moments stay hot while nuclear spins are cooled. Nuclei maintain their high degree of order for a long time, since direct energy exchange between the nuclei and the electrons does not occur because $\hbar(\omega_e-\omega_n)$ is large.

C. Truncated dipolar Hamiltonian

In the rotating coordinate frame, spins feel only the truncated part of the dipolar interaction, viz.,

$$\mathcal{H}_{\text{trunc}}=\sum_{i<j} a_{ij}^{*}(2I_i^zI_j^z-I_i^xI_j^x-I_i^yI_j^y), \tag{60}$$

$$a_{ij}^{*}=\tfrac{1}{2}\hbar^2\gamma_i\gamma_j r_{ij}^{-3}[1-3(\cos\theta_{ij})^2], \tag{61}$$

where θ_{ij} is the angle between $\mathbf{r}_{ij}$ and $\mathbf{B}_i$; here $\mathbf{r}_{ij}$ is the lattice vector from site i to site j. Thus the orientation of the external field determines the spin-spin coupling as well as the ordered ground state.

This can be predicted using the method described in Sec. XV.B. One important characteristic of the problem is the distinction between longitudinal and transverse spin configurations with respect to the external field. Both types of structures have been observed, as will be discussed below. Many features of longitudinal structures could be described in terms of an Ising system with long-range interactions. In the transverse configurations only the components normal to $\mathbf{B}_i$ are ordered. Therefore, although the underlying crystal structure is cubic, magnetic ordering in the rotating frame never display features associated with cubic symmetry, which are important for spin structures in copper and silver.

D. Experimental results on CaF_2, LiH, and $Ca(OH)_2$

The first and most extensively studied dielectric compound for nuclear ordering was CaF_2 (Chapellier, Goldman, Chau, and Abragam, 1970). The nuclear magnetic moment of ^{19}F is almost as large as that of ^{1}H, whereas most calcium nuclei are of the spinless isotope ^{40}Ca. The

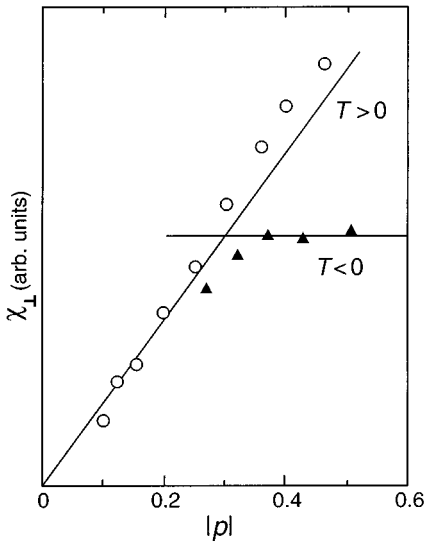

FIG. 107. Transverse susceptibility of the ^{19}F spin system in CaF_2, measured in the rotating frame, as a function of polarization: ○, at positive nuclear temperatures; ▲, at negative nuclear temperatures. From Chapellier *et al.* (1970).

behavior of the ^{19}F nuclei after demagnetization was investigated using the adiabatic fast-passage technique, i.e., by recording the NMR dispersion curve while sweeping the field $\mathbf{b}_0=5$ μT at the rate $d\mathbf{b}_0/dt=10$ mT/s. At $b_0=0$ the height of the dispersion signal is proportional to the transverse susceptibility $\chi_\perp$. The NMR absorption signal χ'' was employed for determining the nuclear polarization before and after each fast passage.

Figure 107 shows experimental results by the Saclay group on the transverse susceptibility with $\mathbf{B}_i$ parallel to a [100] direction of the CaF_2 single crystal. At $T<0$ and at initial polarizations $|p|>0.3$, $\chi_\perp$ becomes constant, indicating that the nuclei order antiferromagnetically. It was not possible to determine the transition temperature. At $T>0$, the susceptibility behaves, up to $p=0.45$, in a way that is characteristic of paramagnetism. An antiferromagnetic structure is expected in this case as well, but with a higher critical polarization.

A variety of other kinds of spin structures were observed in CaF_2 depending on the sign of T and the direction of the external magnetic field. A great deal of information was obtained by using the magnetic isotope ^{43}Ca, with the concentration of 0.13% in natural calcium, as a probe. For the [111] alignment of the external magnetic field, a domain ferromagnet was observed at $T<0$. At $T>0$, the spin arrangement was found to be a helix in which spins precess in the plane perpendicular to $\mathbf{B}_i$ at the Larmor frequency while preserving their relative orientations (Urbina *et al.*, 1982, 1986).

The Saclay group also investigated nuclear magnetic ordering in single crystals of LiH by means of neutron-diffraction techniques (Roinel *et al.*, 1978, 1980, 1987). This compound is a suitable choice because of its simple cubic structure and because the spin-dependent scattering cross section is large for protons. Figure 108 illus-

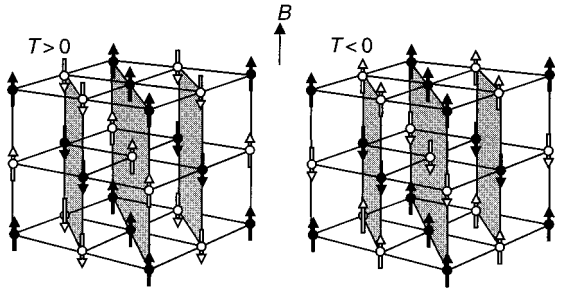

FIG. 108. Nuclear antiferromagnetic structures in LiH when the external field is aligned along a [100] axis: black arrows ^{7}Li; white arrows ^{1}H. From Roinel *et al.* (1978).

trates the antiferromagnetic spin configurations at $T>0$ and at $T<0$, with $\mathbf{B}_i$ parallel to the [001] crystalline axis, deduced from the neutron data. Both structures are longitudinal since spins are either parallel or antiparallel to $\mathbf{B}_i$. For $T<0$ and with $\mathbf{B}_i \| [110]$, the structure is a domain ferromagnet.

The Leiden group of Wenckebach has investigated nuclear magnetic ordering of protons in $Ca(OH)_2$. The experimental method was the same as that employed at Saclay. Data were obtained at negative spin temperatures with the external magnetic field parallel to the crystalline c axis (Marks *et al.*, 1979; Van der Zon *et al.*, 1990). The results, illustrated in Fig. 109, show that, for $|p_i|<0.3$, the nuclear-spin structure is paramagnetic, while at larger polarizations $\chi_\perp$ is nearly independent of p_i, agreeing approximately with the curve calculated for the longitudinal domain structure with ferromagnetic order. $T_C=-0.9\pm0.2$ μK was deduced for the Curie temperature.

The Leiden group (Van Kesteren *et al.*, 1985) also investigated the possibility of removing two of the greatest drawbacks of the dynamic nuclear polarization method:

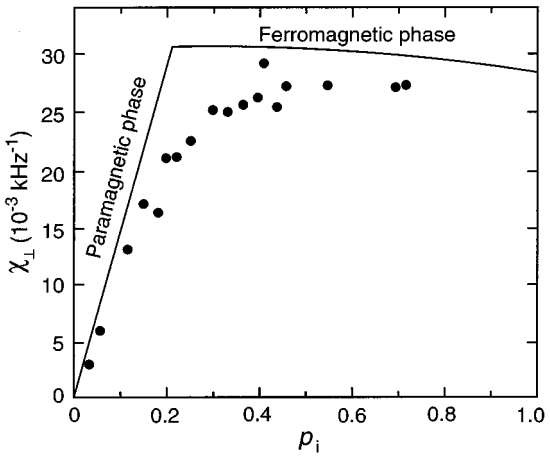

FIG. 109. Transverse susceptibility $\chi_\perp$ vs the initial polarization p_i before adiabatic demagnetization in the rotating frame. The curves were calculated using the restricted-trace approximation. Modified from Van der Zon, Van Velzen, and Wenckebach (1990).

(i) the relatively rapid destruction of the nuclear order, through spin-lattice relaxation, by the large local fields produced by the needed electronic impurities, U^{3+} or Tm^{2+} ions; and (ii) the influence of these local fields on the long-range nuclear-spin configurations. It was hoped that the use of microwave-induced optical nuclear polarization (MIONP) (Deimling *et al.*, 1980) would remove both problems. A suitable substance for trying the MIONP method is fluorene, $C_{13}H_{10}$, doped with phenantharene $C_{14}D_{10}$. UV light photo-excites the phenantharene molecules to their lowest triplet state, creating electronic spins $S=1$. After the ^{1}H nuclei are polarized by the solid effect, the light is turned off and the phenantharene molecules decay to their "harmless" diamagnetic ground state. With this method, Van Kesteren *et al.* (1985) achieved proton polarizations $p=0.42$. Unfortunately, it turned out that this was not enough to produce nuclear ordering, and further development of the MIONP technique has been abandoned.

XV. THEORY

In this long section we first describe (Sec. XV.A) the theory of spin-spin interactions mediated by conduction electrons. In Sec. XV.B we present the mean-field description of magnetic ordering which provides the basic framework for the entire chapter. Section XV.C compares measured magnetic properties, such as the critical temperature and the behavior of susceptibility and entropy with temperature, of Cu, Ag, and Rh nuclei with theoretical calculations.

An exhaustive discussion of ordered spin structures then follows. We first deal with type-I antiferromagnetism in Sec. XV.D. Since the mean-field theory does not yield a unique ground state, one has to consider effects due to thermal and quantum fluctuations. The ground-state spin configuration depends sensitively on the direction of the external magnetic field because of the anisotropic dipolar interaction. The spin structures are first calculated for fields along the crystalline high-symmetry directions. The results are then compared with neutron-diffraction measurements on copper, where type-I order has been found in the high-field region.

In Sec. XV.F we thoroughly discuss the $(0\ \frac{2}{3}\ \frac{2}{3})$ spin structures observed for copper in intermediate external fields. A relatively simple mean-field description reproduces the neutron-diffraction results. The problem of the so-far-unknown ordering of copper nuclei in high fields aligned close to the [111] crystalline direction is discussed in Sec. XV.G. Finally, in Sec. XV.H, we review the theory of the ferromagnetic domain structure observed in silver at negative temperatures.

A. Exchange interactions

Indirect exhange interactions mediated by conduction electrons are crucial in determining the structure of ordered spin configurations in metals. The force between

the nuclear spins arises from the hyperfine interaction between an electron and a nuclear spin, as was first shown by Ruderman and Kittel (1954) and soon afterwards by Bloembergen and Rowland (1955). The interaction can be understood in terms of two processes: One nuclear spin scatters a conduction electron into an excited energy level, and another spin then scatters the electron back to its initial state. This virtual process leads to an effective coupling between the two nuclear spins.

The theory of indirect exchange was quickly applied to magnetic coupling between ion cores by Kasuya (1956) and by Yosida (1957). Such an interaction is considered particularly important in the rare-earth metals. We refer the reader to the review by Kittel (1968) for the vast number of publications written on this topic.

1. Ruderman-Kittel interaction

Let us first recall the original result of Ruderman and Kittel (1954), which was derived using the free-electron approximation. By applying second-order perturbation theory, they showed that the contact interaction

$$\mathcal{H}_{\text{el-n}}^{\text{cont}}=\frac{8\pi}{3}\hbar^2\gamma_n\gamma_e\mathbf{I}\cdot\mathbf{S}\delta(\mathbf{r}) \tag{62}$$

between the nuclear spin $\mathbf{I}$ and the electron spin $\mathbf{S}$, with the respective gyromagnetic ratios γ_n and γ_e, leads to the isotropic spin-spin interaction

$$\mathcal{H}_{\text{RK}}=-\tfrac{1}{2}\sum_{i,j} J_{ij}\mathbf{I}_i\cdot\mathbf{I}_j, \tag{63}$$

where

$$J_{ij}=\eta\frac{\mu_0}{4\pi}\frac{\hbar^2\gamma_n^2}{r_{ij}^3}\left[\cos(2k_F r_{ij})-\frac{\sin(2k_F r_{ij})}{2k_F r_{ij}}\right]. \tag{64}$$

The coupling constant J_{ij} oscillates with distance and has a long range. The coefficient[12] η is negative and depends on the density of conduction electrons at the site of the nucleus as $|\psi(0)|^4$. The free-electron model is able to yield only slightly better than an order-of-magnitude estimate for η. Much more accurate predictions can be obtained from first-principles electronic band-structure calculations, at least in simple elemental metals such as copper and silver.

The first state-of-the-art band-structure calculation of the Ruderman-Kittel (RK) interaction in copper was made by Lindgård, Wang, and Harmon (1986). Rather than calculating J_{ij} in real space, these authors first computed the Fourier transform

$$J(\mathbf{q})=\frac{64\pi^2}{9}\hbar^4\gamma_n^2\gamma_e^2\frac{1}{N}\sum_{\nu,\nu',\mathbf{k}}\frac{f_\nu(\mathbf{k})[1-f_{\nu'}(\mathbf{k}+\mathbf{q})]}{E_{\nu'}(\mathbf{k}+\mathbf{q})-E_\nu(\mathbf{k})}\times|\psi_{\nu,\mathbf{k}}(0)|^2|\psi_{\nu',\mathbf{k}+\mathbf{q}}(0)|^2+\text{constant}, \tag{65}$$

where $f_\nu(\mathbf{k})$ is the Fermi function corresponding to the band energy $E_\nu(\mathbf{k})$ for a wave vector $\mathbf{k}$ in the first Brillouin zone with a band index ν, and $|\psi_{\nu,\mathbf{k}}(0)|^2$ is the electron density at the nucleus. Only s electrons with a spherical charge distribution have a nonvanishing $|\psi_{\nu,\mathbf{k}}(0)|^2$. The constant is the "self-energy" term, which ensures that $J_{ij}=0$ for $\mathbf{r}_{ij}=0$ when $J(\mathbf{q})$ is Fourier transformed back to real space, i.e., $\Sigma_{\mathbf{q}}J(\mathbf{q})=0$.

Lindgård *et al.* (1986) found that the most significant contributions to $J(\mathbf{q})$ arise from the pairs of bands $(\nu,\nu')=(1,6)$ and (1,7), which have strong s-like character, while the contribution from $(\nu,\nu')=(6,6)$ near the Fermi level was less significant. The authors noted that this is contrary to the free-electron calculation of Ruderman and Kittel (1954) in which the charge densities in Eq. (65) were assumed constant and equal to an average value at the Fermi level.

Lindgård *et al.* calculated $J(\mathbf{q})$ for 14 different values of $\mathbf{q}$. The results were then fitted to an eight-nearest-neighbor model to obtain the interaction in real space. The calculated J_{ij}'s are given in Table IV. A comparison with the free-electron model shows that the nearest-neighbor coupling clearly dominates the J_{ij} values calculated by the band theory. The J_{ij}'s also show an oscillation with r_{ij} but with a much reduced amplitude.

The RK interaction in copper has also been computed from the electronic band structure by Frisken and Miller (1986, 1988b). Their method of calculation yielded the interaction directly in real space and emphasized precise integration of the energy denominator in Eq. (65). The accuracy of the matrix elements, $|\psi_{n,\mathbf{k}}(0)|^2$, in their first paper (1986) was, however, criticized by Harmon and Wang (1987). Frisken and Miller later improved the treatment of the matrix elements (Miller and Frisken, 1988). Results of their nonrelativistic orthogonalized plane-wave calculations are included in Table IV. The data agree reasonably well with those of Lindgård, Wang, and Harmon (1986), while the discrepancy with the traditional RK result is large.

It is perhaps surprising that relativistic effects are significant for the RK interaction even in an element as light as copper. Corrections to the band structure are small but they have a significant influence on the radial functions of s electrons near the nucleus. A self-consistent, scalar relativistic calculation for atomic copper, using the proper relativistic hyperfine operator, shows that atomic hyperfine splitting is increased by 14% in comparison with the corresponding nonrelativistic value (Oja, Wang, and Harmon, 1989). The RK interaction in bulk copper is enhanced by approximately the same amount by relativistic corrections, as is shown in Table IV.

The RK interaction in silver has been calculated using the same techniques as in copper (Miller and Frisken, 1988; Harmon *et al.,* 1992). The results are presented in Table V. The general features are the same as in the case of copper. The interaction is more clearly dominated by the nearest-neighbor coupling than the free-electron result, although the sign of J_{ij} oscillates simi-

[12]The relationship between η and R of Eq. (6) is $R=0.587\eta$.

TABLE IV. Ruderman-Kittel coupling strength J_{ij} for copper according to various calculations. The values are listed in nK.

$\mathbf{r}_{ij}$	LWH[a]	FM[b]	OWH[c]	Free el.[d]
(1,1,0)	−11.67	−8.99	−12.74	−11.60
(2,0,0)	1.41	1.56	1.63	5.18
(2,1,1)	−1.31	−0.76	−1.88	−2.88
(2,2,0)	0.11	−0.67	−0.17	−0.36
(3,1,0)	0.25	0.61	0.56	1.47
(2,2,2)	0.61	0.34	0.94	0.25
(3,2,1)	−0.06	−0.13	0.08	−0.83
(4,0,0)	−0.18	−0.17	−0.35	−0.49
(4,1,1)			−0.03	−0.27
R	−0.34	−0.25	−0.37	
$R_{\text{exp}}=-0.42\pm0.05$[e]				
Q	0.091	0.070	0.101	
$Q_{\text{exp}}=0.095\pm0.003$[f]				

[a]Nonrelativistic calculation of Lindgård, Wang, and Harmon (1986).
[b]Nonrelativistic calculation of Frisken and Miller (1988b).
[c]Relativistic calculation of Oja, Wang, and Harmon (1989).
[d]Free-electron approximation with overall scaling to yield $R=-0.42$.
[e]From NMR measurements on highly polarized spins by Ekström *et al.* (1979).
[f]NMR linewidth measurement of Andrew *et al.* (1971).

larly in both cases. The relativistic corrections enhance the RK coupling in silver by 40%.

The theoretical values for J_{ij} can be directly compared with two experimentally determined parameters. The strength of the RK interaction is often described by the dimensionless quantity

TABLE V. Ruderman-Kittel coupling strength J_{ij} for silver according to various calculations. The values are listed in nK.

$\mathbf{r}_{ij}$	MF[a]	HWL[b]
(1,1,0)	−0.895	−1.335
(2,0,0)	0.065	0.193
(2,1,1)	−0.145	−0.193
(2,2,0)	−0.051	−0.031
(3,1,0)	0.086	0.077
(2,2,2)	0.127	0.118
(3,2,1)	−0.013	−0.009
(4,0,0)	−0.041	−0.055
(4,1,1)		−0.008
R	−1.53	−2.26
$R_{\text{exp}}=-2.5\pm0.5$[c]		
Q	0.406	0.598
$Q_{\text{exp}}=0.553\pm0.031$[d]		

[a]Nonrelativistic calculation of Miller and Frisken (1988).
[b]Relativistic calculation of Harmon, Wang, and Lindgård (1992).
[c]From NMR measurements on highly polarized spins (Oja, Annila, and Takano, 1990; Hakonen, Yin, and Lounasmaa, 1990; Hakonen, Nummila, and Vuorinen, 1992).
[d]NMR linewidth measurement of Poitrenaud and Winter (1964).

$$R=\sum_j J_{ij}/(\mu_0\hbar^2\gamma^2\rho), \tag{66}$$

which can be deduced from various NMR and susceptibility measurements on highly polarized spins (see Sec. XI). A positive R is characteristic of ferromagnetic interactions, whereas a negative R indicates antiferromagnetism.

Experiments in the limit of a small nuclear-spin polarization yield the parameter

$$Q=\left(\sum_j J_{ij}^2\right)^{1/2}\Big/(\mu_0\hbar^2\gamma^2\rho), \tag{67}$$

which describes the average strength of the local fluctuating field. In a system with two or more spin species, measurements of the second moment of the NMR absorption line (Van Vleck, 1948) yield Q. Such an experiment is straightforward in silver (Ruderman and Kittel, 1954; Poitrenaud and Winter, 1964) but difficult in copper because the second moment is mainly determined by the dipolar interaction. Using the magic-angle spinning technique it is, however, possible to remove the dipolar contribution from $\langle\Delta\nu^2\rangle$ and to obtain Q accurately (Andrew *et al.*, 1971; Andrew, 1973; Andrew and Hinshaw, 1973).

2. Anisotropic exchange interactions

In addition to the contact interaction, there are two other contributions to the hyperfine forces (Lindgren and Rosen, 1974a, 1974b), viz., the dipolar interaction between the nuclear and electronic moments

$$\mathcal{H}_{\text{el-n}}^{\text{dip}}=-\hbar^2\gamma_n\gamma_e r^{-3}[\mathbf{I}\cdot\mathbf{S}-3r^{-2}(\mathbf{I}\cdot\mathbf{r})(\mathbf{S}\cdot\mathbf{r})], \tag{68}$$

and the orbital interaction

$$\mathcal{H}_{\text{el-n}}^{\text{orb}}=\hbar^2\gamma_n\gamma_e r^{-3}\mathbf{I}\cdot\vec{\ell}. \tag{69}$$

Here $\mathbf{r}$ is the vector separating the nucleus and the electron and $\vec{\ell}$ is the electronic angular momentum. Both $\mathcal{H}_{\text{el-n}}^{\text{dip}}$ and $\mathcal{H}_{\text{el-n}}^{\text{orb}}$ contribute to the indirect nuclear-spin coupling, as was first shown by Bloembergen and Rowland (1955). The resulting force is, in general, anisotropic in spin space. In the so-called Bardeen's (1937) spherical approximation for the electronic band structures, which was employed by Bloembergen and Rowland, the resulting interaction can be divided into an isotropic term like the RK coupling and an anisotropic term with the symmetry of the dipolar interaction. The anisotropic term is therefore often known as the pseudodipolar interaction. The terminology is, however, misleading since the dipolarlike symmetry results only from the use of the spherical approximation for the band structure. It would be more appropriate to call the forces arising from $\mathcal{H}_{\text{el-n}}^{\text{dip}}$ and $\mathcal{H}_{\text{el-n}}^{\text{orb}}$ non-s-electron-mediated interactions, since s electrons do not contribute to them.

The relative importance of the traditional RK term mediated by the contact interaction, and hence only by s electrons, obviously depends on the partial-wave character of conduction electrons. In some transition metals, such as platinum and lead, anisotropic interactions not mediated by s electrons are comparable to isotropic forces (Froidevaux and Weger, 1964; Alloul and Froidevaux, 1967). In copper and silver, which have one unpaired s electron and filled d shells in their atoms, one would expect a dominating RK interaction.

Interestingly, however, the d-electron terms in copper contribute as much as 20% to the measured spin-lattice relaxation rate through the orbital hyperfine interaction (Asada *et al.*, 1981; Ebert *et al.*, 1984). This led Oja and Kumar (1987) to investigate the role of forces not mediated by s electrons. They concluded that orbital interactions are important in the nuclear-spin coupling to the extent of possibly changing the ground-state ordering vector from what it would be without these terms. However, since the band structure was modeled only in terms of the crude spherical approximation (Bardeen, 1937), a more sophisticated study was needed to settle the question.

First-principles band-structure calculations for all interactions not mediated by s electrons were performed by Oja, Wang, and Harmon (1989). Using scalar relativistic wave functions obtained from a linear, augmented-plane-wave calculation, they found that orbital interactions do make a significant contribution to exchange forces between copper nuclei, as was suggested by Oja and Kumar (1987). The theoretical nearest-neighbor interaction matrix was found to be

$$\underline{A}^{\text{ex}}[\mathbf{r}_{ij}=(a,a,0)]/k_{\text{B}}=\begin{pmatrix}-12.6 & -2.0 & 0\\ -2.0 & -12.6 & 0\\ 0 & 0 & -9.4\end{pmatrix}, \tag{70}$$

where the units are nK. Interactions not mediated by s electrons are such that they decrease the theoretical values for R and Q by 10%. Deviations from the fully isotropic interaction are on the order of 20% (see Table IV). The symmetry of calculated anisotropic interactions is not dipolar in form but is determined, in general, only by the symmetry of the lattice (Griffiths *et al.*, 1959; Oja *et al.*, 1989).

The anisotropy of exchange interactions in copper is, however, small in comparison with the anisotropy of the dipolar interaction. For nearest neighbors

$$\underline{A}^{\text{dip}}[\mathbf{r}_{ij}=(a,a,0)]/k_{\text{B}}=\begin{pmatrix}12.7 & 38.1 & 0\\ 38.1 & 12.7 & 0\\ 0 & 0 & -25.4\end{pmatrix}. \tag{71}$$

The full nearest-neighbor interaction, $\underline{A}_{ij}=\underline{A}_{ij}^{\text{ex}}+\underline{A}_{ij}^{\text{dip}}$, is

$$\underline{A}[\mathbf{r}_{ij}=(a,a,0)]/k_{\text{B}}\approx\begin{pmatrix}0 & 36 & 0\\ 36 & 0 & 0\\ 0 & 0 & -35\end{pmatrix}, \tag{72}$$

emphasizing the fact that the mutual spin forces in copper are, indeed, very anisotropic.

Interactions not mediated by s electrons have not been computed for silver. The calculated (Asada *et al.*, 1981; Ebert *et al.*, 1984) relative effects of p- and d-electron contributions to the spin-lattice relaxation rate in this metal are smaller than in copper by a factor of 3. A similar reduction can be expected to hold for forces not mediated by s electrons.

3. Other interactions

In an interesting paper, Siemensmeyer and Steiner (1992) investigate the role of magnetoelastic coupling in nuclear magnets, especially in copper. Such interactions are important in electronic systems (Kötzler, 1984) but are usually assumed vanishingly small for nuclear spins. The authors find that, when spin-spin interactions are neglected, the quadrupolar energy transforms the fcc crystal of copper to a lattice with noncubic symmetry at $T_c\approx 0.06$ nK. The transition is similar to the Jahn-Teller effect (Gehring and Gehring, 1975). Therefore, magnetostrictive energy of copper is 2–3 orders of magnitude smaller than spin-spin interactions. Siemensmeyer and Steiner emphasize, however, that their estimate is based on conservative values of the shielding and antishielding factors. As a result, magnetostrictive energy could be even 2 orders of magnitude higher, thus becoming significant in comparison with spin-spin interactions. The authors also discuss effects due to the external magnetic field and uniaxial stress caused by the weight of the sample itself. Effects due to distance dependence of spin-spin interactions, i.e., exchange striction, are found negligible in comparison with magnetoelastic coupling with quadrupolar forces.

Lindgård (1992) has studied the role of lattice dynamics in the calculation of exchange interactions. He finds that zero-point lattice vibrations give rise to substantial corrections in some of the exchange parameters, in comparison with values calculated assuming a rigid lattice. The argument is based on the large separation of energy scales for the electronic, lattice, and nuclear systems. The nuclei see the average of phonon fluctuations, whereas the electronic system mediating the exchange interaction can adjust to them. Using the free-electron range function for the RK interaction [see Eq. (64)], Lindgård estimates that the nearest-neighbor J_1 is not modified, whereas J_2 and J_3 are reduced by 20% and 50%, respectively.

B. Mean-field theory of magnetic ordering

1. Basic equations

We rewrite the Hamiltonian of the spin system [see Eq. (1)] as

$$\mathcal{H}=-\tfrac{1}{2}{\sum_{i,j}}' \mathbf{I}_i \underline{A}_{ij}\mathbf{I}_j-\hbar\gamma\mathbf{B}\cdot\sum_i \mathbf{I}_i, \tag{73}$$

where the 3×3 matrix $\underline{A}_{ij}$ consists of the dipolar and exchange interactions. The prime on the summation sign indicates that the term $i=j$ must be omitted. In the mean-field theory, $\mathcal{H}$ is approximated by

$$\mathcal{H}^{\mathrm{MF}}=-\hbar\gamma\sum_i \mathbf{B}_i\cdot\mathbf{I}_i+\tfrac{1}{2}{\sum_{i,j}}' \langle\mathbf{I}_i\rangle\underline{A}_{ij}\langle\mathbf{I}_j\rangle, \tag{74}$$

where the local field $\mathbf{B}_i$ acting on spin i consists of the external field $\mathbf{B}$ and the field due to interactions with other spins, viz.,

$$\mathbf{B}_i=\mathbf{B}+\sum_j \underline{A}_{ij}\langle\mathbf{I}_j\rangle/(\hbar\gamma). \tag{75}$$

The field $\mathbf{B}_i$ is stationary, unlike the randomly fluctuating local field B_{loc} discussed in Sec. IV.C. The thermal average of a spin operator $\langle\mathbf{I}_i\rangle$ is given by

$$\langle\mathbf{I}_i\rangle=\frac{I\mathbf{B}_i}{|\mathbf{B}_i|}\mathcal{B}_I\left(\frac{\hbar\gamma|\mathbf{B}_i|}{k_{\mathrm{B}}T}\right), \tag{76}$$

where $\mathcal{B}_I(x)$ is the Brillouin function for spin I,

$$\mathcal{B}_I(x)=[(I+\tfrac{1}{2})/I]\coth[(I+\tfrac{1}{2})x]-(1/2I)\coth(x/2), \tag{77}$$

as in Eqs. (25a) and (25b).

If the local fields are known, the energy $E=\langle\mathcal{H}^{\mathrm{MF}}\rangle$ is obtained from

$$E=-\tfrac{1}{2}\hbar\gamma\mathbf{B}\cdot\sum_i\langle\mathbf{I}_i\rangle-\tfrac{1}{2}\hbar\gamma\sum_i \mathbf{B}_i\cdot\langle\mathbf{I}_i\rangle. \tag{78}$$

2. Eigenvalue and other **k**-space equations

We first introduce the Fourier transforms

$$\langle\mathbf{I}(\mathbf{k})\rangle=\frac{1}{N}\sum_i\langle\mathbf{I}_i\rangle\exp(-i\mathbf{k}\cdot\mathbf{r}_i), \tag{79}$$

$$\underline{A}(\mathbf{k})={\sum_j}' \underline{A}_{ij}\exp[-i\mathbf{k}\cdot(\mathbf{r}_i-\mathbf{r}_j)]. \tag{80}$$

The energy per spin and the local field can then be written as

$$E/N=-\hbar\gamma\mathbf{B}\cdot\langle\mathbf{I}(\mathbf{k}=0)\rangle-\tfrac{1}{2}\sum_{\mathbf{k}}\langle\mathbf{I}(-\mathbf{k})\rangle\underline{A}(\mathbf{k})\langle\mathbf{I}(\mathbf{k})\rangle, \tag{81}$$

$$\mathbf{B}_i=\mathbf{B}+\sum_{\mathbf{k}}\underline{A}(\mathbf{k})\langle\mathbf{I}(\mathbf{k})\rangle\cos(\mathbf{k}\cdot\mathbf{r}_i)/(\hbar\gamma). \tag{82}$$

Here we have assumed that the lattice has inversion symmetry.

Further progress can be made by introducing the eigenvalues $\lambda_n(\mathbf{k})$ and eigenvectors $\mathbf{e}_n(\mathbf{k})$ of the Fourier-transformed interaction matrix. These are defined by

$$\underline{A}(\mathbf{k})\mathbf{e}_n(\mathbf{k})=\lambda_n(\mathbf{k})\mathbf{e}_n(\mathbf{k}), \tag{83}$$

where $n=1,2,3$. Taking the $\mathbf{e}_n(\mathbf{k})$'s as the basis vectors, we write

$$E/N=-\hbar\gamma\mathbf{B}\cdot\langle\mathbf{I}(\mathbf{k}=0)\rangle-\tfrac{1}{2}\sum_{\mathbf{k},n}\lambda_n(\mathbf{k})a_n(\mathbf{k})^2, \tag{84}$$

$$a_n(\mathbf{k})=\langle\mathbf{I}(\mathbf{k})\rangle\cdot\mathbf{e}_n(\mathbf{k}). \tag{85}$$

The local fields can be expressed in a similar way,

$$\mathbf{B}_i=\mathbf{B}+\sum_{\mathbf{k},n}\lambda_n(\mathbf{k})a_n(\mathbf{k})\mathbf{e}_n(\mathbf{k})\cos(\mathbf{k}\cdot\mathbf{r}_i)/(\hbar\gamma). \tag{86}$$

These equations provide a general and effective framework for carrying out the mean-field analysis.

3. Ordering vector and the ordering temperature

To obtain the critical temperature in zero field we seek solutions for small $\langle\mathbf{I}_i\rangle$ by linearizing Eq. (76). This is permissible for a continuous transition. One is led to the equation (Kjäldman and Kurkijärvi, 1979)

$$\lambda\langle\mathbf{I}(\mathbf{k})\rangle=\underline{A}(\mathbf{k})\langle\mathbf{I}(\mathbf{k})\rangle \tag{87}$$

with $\lambda=3k_{\mathrm{B}}T_c/I(I+1)$. The problem thus reduces to solving the eigenvalue equation (83). The physical solution corresponds to the largest critical temperature T_c, given by

$$k_{\mathrm{B}}T_c^{\mathrm{MF}}=\tfrac{1}{3}I(I+1)\lambda_{\max}. \tag{88}$$

Here $\lambda_{\max}=\max_{\mathbf{k},n}\{\lambda_n(\mathbf{k})\}$, n takes values $n=1,2,3$, and $\mathbf{k}$ runs over vectors in the first Brillouin zone. The ordering vector is the wave vector $\mathbf{k}$ for which $\lambda_n(\mathbf{k})=\lambda_{\max}$. The direction of the spins below $T=T_c$ is determined by the eigenvector(s) corresponding to $\lambda_{\max}$.

At negative temperatures the situation is reversed. When T approaches zero from the negative side, the first solution to the linearized mean-field equation (87) is found at a wave vector that corresponds to the *minimum* of $\lambda_n(\mathbf{k})$ (Abragam and Goldman, 1982).

The total amplitude of antiferromagnetic order at a wave vector $\mathbf{k}$ can be obtained from a measurement of

the antiferromagnetic Bragg reflection at this **k**. Apart from a constant coefficient, the structure factor $|F_{\rm AF}(\mathbf{k})|^2=|\langle\mathbf{I}(\mathbf{k})\rangle|^2$ [see Eq. (51)].

4. Equal-moment and permanent spin structures

In equal-moment spin structures $|\langle\mathbf{I}_i\rangle|$ is the same for all spins i. This is always the case at $T=0$ as the spins are saturated, provided that there is only a single spin species in the system. At $T=T_c$, however, Eqs. (87) and (88) determine the ordering vector irrespective of whether the moments $|\langle\mathbf{I}_i\rangle|$ are equal or not. At in-between temperatures, the concept of *permanent* spin structures (Villain, 1959; Abragam and Goldman, 1982) is useful. By definition, a spin structure is permanent if the local fields $\mathbf{B}_i$ satisfy

$$\mathbf{B}_i=\lambda\langle\mathbf{I}_i\rangle/\hbar\gamma, \tag{89}$$

where λ is independent of the site. If a spin structure corresponding to the maximum of $\lambda_n(\mathbf{k})$ can be chosen permanent, $\lambda=\lambda_{\max}$ and the structure is stable within the mean-field theory, both at $T=0$ and immediately below $T=T_c$ (Luttinger and Tisza, 1946; Villain, 1959; Abragam and Goldman, 1982; Kumar *et al.*, 1986). In the intermediate-temperature region $0<T<T_c$, the structure is at least metastable, and its Gibbs free energy is lower than that of any other permanent configuration.

A permanent structure is always an equal-moment configuration. An equal-moment structure is permanent if and only if (i) the eigenvalues $\lambda_n(\mathbf{k})$ for all nonzero antiferromagnetic components $\langle\mathbf{I}_n(\mathbf{k})\rangle$, $\mathbf{k}\neq0$, are equal and (ii) the ferromagnetic component $\langle\mathbf{I}(0)\rangle$ depends on the external magnetic field **B** via $\langle\mathbf{I}(0)\rangle=\hbar\gamma\mathbf{B}/(\lambda-\lambda(0))$ (Viertiö and Oja, 1993). From this it follows that the critical field for a permanent spin structure is

$$B_c=I[\lambda-\lambda(0)]/\hbar\gamma. \tag{90}$$

5. Thermodynamics

Thermodynamics is particularly simple for permanent spin structures. The partition function is given by

$$Z^{\rm MF}=\exp\left[-\frac{\beta N}{2}\left(\lambda I^2p^2-\frac{\hbar^2\gamma^2B^2}{\lambda-\lambda(0)}\right)\right]z_I^N(\beta\lambda pI), \tag{91a}$$

where $\beta=(k_{\rm B}T)^{-1}$ and

$$z_I(x)=\sinh[(I+\tfrac{1}{2})x]/\sinh(\tfrac{1}{2}x). \tag{91b}$$

The Gibbs free energy $G=-k_{\rm B}T\ln Z$. From these equations one can derive all thermodynamic functions of the system.

The self-consistent equation for polarization is

$$p(T)=p(T,B)=\mathcal{B}_I(\beta\lambda pI), \tag{92}$$

where the Brillouin function $\mathcal{B}_I$ was given by Eq. (77). Note that p does not depend on B anywhere in the antiferromagnetically ordered region. The temperature dependence of the critical field is

$$B_c(T)=p(T)B_c(T=0), \tag{93}$$

where $B_c(T=0)$ is given by Eq. (90).

The expression for entropy per spin is

$$S=-\beta\lambda I^2p^2+\ln z_I(\beta\lambda pI). \tag{94}$$

Like p, S does not depend on B in the antiferromagnetically ordered (T,B) region (Oja, 1984; Lindgård, 1988a). This means, in particular, that the isentropes are vertical as shown in Fig. 7. Therefore, when the nuclear-spin system is demagnetized into the ordered state, there is no further decrease in the spin temperature.[13]

When fluctuations, which are neglected in the mean-field theory, are taken into account, the above picture changes slightly. It has been predicted that isentropes weakly bend towards higher temperatures when $B\to0$ in the ordered region (Lindgård, 1988a). Similar behavior has been observed in electronic magnets (Garrett, 1951; de Klerk, 1956). The absolute value of the ordered-phase entropy as predicted by mean-field theory is unreliable. The critical entropy at $B=0$ is equal to the entropy at $T=\infty$ owing to neglect of short-range order. At low temperatures, on the other hand, the mean-field theory neglects the entropy carried by spin-wave excitations.

The equation for longitudinal magnetic susceptibility (in SI units) is

$$\chi(T,B)=\mu_0\rho\hbar^2\gamma^2/[\lambda-\lambda(0)], \tag{95}$$

which is constant in the ordered region, resulting in a temperature-independent magnetization $M=\chi B/\mu_0$.

The longitudinal susceptibility in the ordered state, Eq. (95), can also be written as

$$\chi(T,B)=C/[T_c^{\rm MF}-\theta_{\rm W}], \tag{96}$$

where C is the Curie constant (see Table II), $T_c^{\rm MF}$ is the mean-field ordering temperature [Eq. (88)], and the Weiss temperature $\theta_{\rm W}=(R+L-D)C$. Here R is the strength of the exchange interaction [see Eq. (66)], $L=\frac{1}{3}$ is the Lorentz constant, and D is the demagnetization factor along the direction of the external field (see Sec. IV.D). $\theta_{\rm W}$ is related to the eigenvalue $\lambda(0)$, appearing in Eq. (95), by $\frac{1}{3}I(I+1)\lambda(0)=\theta_{\rm W}k_{\rm B}$. Note that the high-$T$ behavior of the susceptibility is given by $\chi=C/(T-\theta_{\rm W})$.

6. Transition from the polarized paramagnetic state to the antiferromagnetic phase

Magnetic ordering was analyzed in Sec. XV.B.3 by linearizing the mean-field equations at the ordering tem-

[13]The fact that the isentropes are vertical in the antiferromagnetically ordered state can also be seen from the thermodynamic relation $(dB/dT)_S=(\partial S/\partial T)_B/(\partial M/\partial T)_B$ by noting that $(\partial S/\partial T)_B>0$ always and that in the present case $(\partial M/\partial T)_B=0$ according to the mean-field theory.

perature. The treatment was limited, however, to zero external field. Although a similar calculation is possible when $B \neq 0$, we follow here another procedure.[14] We describe the transition from the polarized paramagnetic state to the antiferromagnetic phase using the soft-mode theory, which was first employed in this context by Lindgård (1992). His approach was later elaborated by Oja and Viertiö (1993), who analyzed the general properties of a soft-mode transition in a system with anisotropic spin-spin interactions.

The idea of the soft-mode description of a phase transition is the following: The energy needed to excite a spin wave at a wave vector $\mathbf{k}$ in the paramagnetic state is first calculated. At a field in which the excitation energy vanishes, i.e., when the spin wave becomes soft, the paramagnetic state is unstable with respect to antiferromagnetic order characterized by this $\mathbf{k}$ vector. The ordering vector $\mathbf{Q}=\mathbf{k}$ is the one that becomes soft in the highest field.

The starting point for the analysis is obtained from the early work of Holstein and Primakoff (1940). In the polarized state at $T=0$, the excitation energy for a spin wave is

$$\varepsilon_{\mathbf{k}} = \sqrt{C_{\mathbf{k}}^2 - 4|D_{\mathbf{k}}|^2}, \tag{97}$$

where

$$C_{\mathbf{k}} = -\tfrac{1}{2} I[A^{xx}(\mathbf{k}) + A^{yy}(\mathbf{k})] + \hbar\gamma B + IA^{zz}(0),$$

$$D_{\mathbf{k}} = \tfrac{1}{4} I[A^{xx}(\mathbf{k}) - A^{yy}(\mathbf{k}) - 2iA^{xy}(\mathbf{k})]. \tag{98}$$

Here z is the direction of the external magnetic field and $A(\mathbf{k})$ is the Fourier transform of the interaction matrix; see Eq. (80). The scheme for deriving this result is the following (see, for example, p. 43 in Keffer, 1966): The Hamiltonian is rewritten using the spin-deviation operators, higher-order terms than those bilinear in these operators are neglected, and the resulting Hamiltonian is Fourier transformed and finally diagonalized. This procedure yields the normal modes, i.e., spin waves and the corresponding energies.

It is clear from Eq. (97) that in a high enough field all excitation energies $\varepsilon_{\mathbf{k}}$ are positive. For antiferromagnetic interactions, one of the spin-wave energies eventually becomes negative with decreasing B, indicating softening of this particular excitation and instability of the paramagnetic phase.

To analyze the instability, it is convenient to write $\varepsilon_{\mathbf{k}}$ in the form (Oja and Viertiö, 1993)

$$\varepsilon_{\mathbf{k}}^2/I^2 = \det\begin{pmatrix} A^{xx}(\mathbf{k}) - \hbar\gamma B/I - A^{zz}(0) & A^{xy}(\mathbf{k}) \\ A^{xy}(\mathbf{k}) & A^{yy}(\mathbf{k}) - \hbar\gamma B/I - A^{zz}(0) \end{pmatrix}. \tag{99}$$

The determinant vanishes when $\hbar\gamma B/I + A^{zz}(0)$ coincides with an eigenvalue $\tilde{\lambda}(\mathbf{k})$ of

$$\underline{\tilde{A}}(\mathbf{k}) = \begin{pmatrix} A^{xx}(\mathbf{k}) & A^{xy}(\mathbf{k}) \\ A^{xy}(\mathbf{k}) & A^{yy}(\mathbf{k}) \end{pmatrix}. \tag{100}$$

This 2×2 matrix is the xy block of the 3×3 matrix $\underline{A}(\mathbf{k})$ and corresponds to the plane perpendicular to the field direction $\mathbf{z}$. Therefore the soft-mode transition takes place at

$$B_c = I[\tilde{\lambda}_{\max} - \lambda(0)]/\hbar\gamma, \tag{101}$$

where $\lambda(0) = A^{zz}(0)$ and

$$\tilde{\lambda}_{\max} = \mathrm{Max}_{\mathbf{k},n}\{\tilde{\lambda}_n(\mathbf{k})\}. \tag{102}$$

The wave vector $\mathbf{k}$ that yields $\tilde{\lambda}_{\max}$ is defined as $\tilde{\mathbf{Q}}$. Note the similarity between Eq. (101) and the relation valid for permanent spin structures, $B_c = I[\lambda_{\max} - \lambda(0)]/\hbar\gamma$ [see Eq. (90)].

The matrix $\underline{\tilde{A}}(\mathbf{k})$ clearly depends on the direction of the external field. Therefore the eigenvalues $\tilde{\lambda}_n(\mathbf{k})$ can also depend on the direction of $\mathbf{B}$, and so can the ordering vector $\tilde{\mathbf{Q}}$ and the critical field B_c.

A question of particular interest is whether the high-field ordering vector $\tilde{\mathbf{Q}}$ is the same as the zero-field ordering vector $\mathbf{Q}$ which corresponds to the maximum eigenvalue $\lambda_{\max}$ of the 3×3 matrix $\underline{A}(\mathbf{k})$. The high-field soft-mode transition has the following properties (Oja and Viertiö, 1993):

(i) If the largest eigenvalue $\lambda_{\max}$ of $\underline{A}(\mathbf{k})$ is degenerate, the soft-mode transition always takes place for the $B=0$ vector $\mathbf{Q}$. The critical field $B=B_c$ [see Eq. (90)] is independent of the field direction.

(ii) If the largest eigenvalue $\lambda_{\max}$ of $\underline{A}(\mathbf{k})$ is nondegenerate, the soft-mode transition can take place for another ordering vector in addition to the one stable at $B=0$, provided that the anisotropy is strong enough and that its easy axis is not perpendicular to the field. By the easy axis we mean the direction of the eigenvector corresponding to $\lambda_{\max}$. The value of B_c will then be lower than that given by Eq. (90), since $\tilde{\lambda}_{\max} < \lambda_{\max}$. However, if $\mathbf{B}$ is perpendicular to the easy axis, the high-field ordering vector is the same as the one at $B=0$, and B_c is not lowered.

It should be noted, however, that if B_c is strongly suppressed by the anisotropy of the interactions, the transition to the antiferromagnetic state may be of first order. Then the present approach, which is based on the assumption of a continuous transition, does not apply.

7. Ordering in the fcc lattice

Most features important for nuclear ordering in Cu, Ag, and Rh can be described in terms of a model that contains isotropic exchange interactions between nearest (J_1) and next-nearest neighbors (J_2) and dipolar interactions between nearest neighbors [$D_1 = (\mu_0/4\pi)\hbar^2\gamma^2 r^{-3}$]. Performing the lattice sums, we find

[14] The soft-mode and mean-field theories lead to the same prediction for an antiferromagnetic transition at $T=0$ (Oja and Viertiö, 1993).

$$\underline{A}(\mathbf{k})=\begin{pmatrix} J(\mathbf{k})-4D_1[-\frac{1}{2}c_x(c_y+c_z)+c_yc_z] & -6D_1s_xs_y & -6D_1s_xs_z \\ -6D_1s_xs_y & J(\mathbf{k})-4D_1[-\frac{1}{2}c_y(c_x+c_z)+c_xc_z] & -6D_1s_ys_z \\ -6D_1s_xs_z & -6D_1s_ys_z & J(\mathbf{k})-4D_1[-\frac{1}{2}c_z(c_x+c_y)+c_xc_y] \end{pmatrix}, \tag{103}$$

where

$$J(\mathbf{k})=4(J_1-2J_2)(c_xc_y+c_yc_z+c_zc_x)+4J_2(c_x+c_y+c_z)^2-6J_2. \tag{104}$$

Here $c_\alpha=\cos(k_\alpha a)$, $s_\alpha=\sin(k_\alpha a)$, $\alpha=x,y,z$, and the lattice constant is $2a$. The eigenvalue equation can be solved analytically if the $\mathbf{k}$ vector lies in a symmetry direction of the reciprocal lattice (Oja and Viertiö, 1993).

Let us first consider the case of only isotropic interactions, i.e., $D_1=0$. The eigenvalue is then simply $\lambda(\mathbf{k})=J(\mathbf{k})$ and the stable structure is the one that maximizes $J(\mathbf{k})$. Four different kinds of configurations are obtained; these are the principal ordering modes of the fcc system. One of them is the ferromagnetic structure; the three others are antiferromagnetic configurations whose magnetic unit cells are shown in Fig. 110, illustrated for the case when there is only one ordering vector (single-$\mathbf{k}$ structure). It is also possible that the spin configuration is modulated by a superposition of cubic-symmetry-related vectors (multiple-$\mathbf{k}$ structure). Figure 110 shows the unit cell for type-IV ordering as well. It cannot be obtained from the J_1,J_2 model but becomes stable if the nearest-neighbor interaction is sufficiently anisotropic.

The stability regions of the four principal modes of ordering in the J_1J_2 plane are shown in Fig. 87 (Smart, 1966). The J_1/J_2 ratios appropriate for Cu, Ag, and Rh are also indicated. The theoretically calculated values of J_1 and J_2 (Lindgård *et al.*, 1986; Harmon *et al.*, 1992) have been used for Cu and Ag, with all other interactions, including the dipolar force, being neglected. For Rh the experimental J_1 and J_2 were adopted (Hakonen, Vuorinen, and Martikainen, 1993). Type-I ordering is predicted for the three metals at positive temperatures, as illustrated by the open symbols. At negative temperatures, shown by solid symbols, ferromagnetic order was obtained.[15] However, one should note that, at $T<0$, Rh is relatively close to the boundary between ferromagnetic ordering and antiferromagnetism of the second kind. Experiments have shown, in fact, a tendency towards antiferromagnetism in rhodium at $T<0$ (see Sec. X.B).

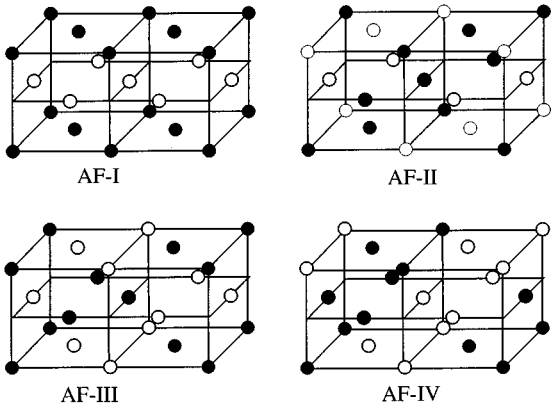

FIG. 110. Magnetic unit cells of the four principal antiferromagnetic configurations in fcc lattices. The respective ordering vectors are (I) $\mathbf{k}=(\pi/a)(1,0,0)$, (II) $\mathbf{k}=(\pi/a)(\frac{1}{2},\frac{1}{2},\frac{1}{2})$, (III) $\mathbf{k}=(\pi/a)(1,\frac{1}{2},0)$, and (IV) $\mathbf{k}=(\pi/a)(\frac{1}{2},\frac{1}{2},0)$. The nuclear-spin directions are opposite in sites marked by ○ and ●, respectively.

The eigenvector equation (87) is trivial for the isotropic model but important when there is some anisotropy. In the case of type-I order, the dipolar energy forces $\langle\mathbf{I}(\mathbf{k})\rangle$, where $\mathbf{k}$ is a type-I ordering vector, to the plane perpendicular to $\mathbf{k}$. Thus type-I systems have easy-plane anisotropy. In contrast, the dipolar energy chooses easy-axis anisotropy for the $(0\ \frac{2}{3}\ \frac{2}{3})$ order. Apart from determining the direction of $\langle\mathbf{I}(\mathbf{k})\rangle$ with respect to $\mathbf{k}$, anisotropic interactions can also be decisive in the selection of the ordering vectors.

The principal kinds of antiferromagnetic structures of fcc systems (see Fig. 110) can easily be chosen permanent when $B=0$. This is because the phase factor $\cos(\mathbf{k}\cdot\mathbf{r}_i)$, where $\mathbf{k}$ is the corresponding ordering vector, takes only values ±1 for the four types of orderings. [For types II, III, and IV the approriate phase factor is $\sqrt{2}\cos(\mathbf{k}\cdot\mathbf{r}_i+\pi/4)$]. The situation is simple, however, only for the single-$\mathbf{k}$ structures depicted in Fig. 110 at $B=0$. In an external field, anisotropic spin-spin interactions in some cases make it impossible to form permanent spin structures (Oja and Viertiö, 1992). The requirement of permanency also imposes severe restrictions on multiple-$\mathbf{k}$ spin configurations.

C. Comparison of measured and calculated magnetic properties of Cu, Ag, and Rh

1. Mean-field T_c and the ordering vector

Kjäldman and Kurkijärvi (1979) were the first to investigate nuclear ordering in a system with dipolar and RK interactions. They assumed the free-electron form for the RK term, Eq. (64), and made their calculation for different strengths of the exchange force by multiply-

[15]Of course, at $T<0$ the exchange constants are the same as at $T>0$. The signs of J_1 and J_2 have been reversed in Fig. 87 at $T<0$ because $\max\{J(\mathbf{k})\}=\min\{-J(\mathbf{k})\}$.

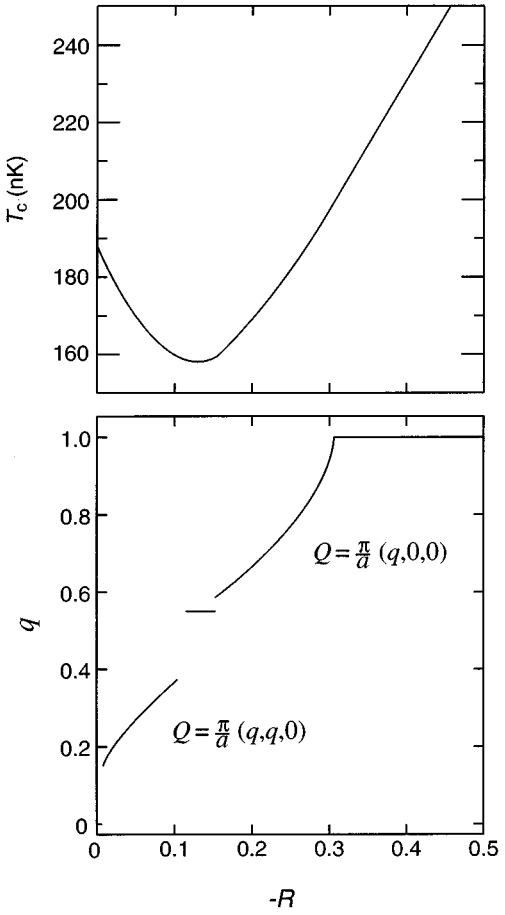

FIG. 111. Magnetic ordering of Cu nuclei as a function of the strength of the RK interaction, which is assumed to have the free-electron form of Eq. (5). Upper frame: Transition temperature. Lower frame: Ordering vector **Q**. For $|R|>0.15$ the spin order has the form $\mathbf{Q}=(\pi/a)(q,0,0)$, whereas $\mathbf{Q}=(\pi/a)(q,q,0)$ for $|R|<0.15$. However, at $R\approx-0.11$, $\mathbf{Q}=(\pi/a)(0.5,0.4,0)$ is found. Modified from Kjäldman and Kurkijärvi (1979) and Huiku *et al.* (1986).

ing the free-electron J_{ij}'s with an overall scaling factor.[16] Figure 111 reproduces their results. For the experimental $R=-0.42$, as determined from the NMR measurements by Ekström *et al.* (1979), $T_c^{\mathrm{MF}}=230$ nK. For $R=-0.37$, which would reproduce the magic-angle spinning NMR measurement of $\Sigma_j J_{ij}^2$ by Andrew *et al.* (1971), T_c^{MF} would be 210 nK. Both mean-field predictions are thus clearly higher than the experimental value $T_{\mathrm{N}}=58$ nK. The predicted ordering vector $\mathbf{Q}=(\pi/a)(1,0,0)$ as observed in both the low- and high-field regions (see Fig. 3).

If data from the band-structure calculations by Lindgård, Wang, and Harmon (1986) are used for the RK interaction, type-I order is again found with $T_c^{\mathrm{MF}}=181$ nK. These authors emphasized, however, that copper

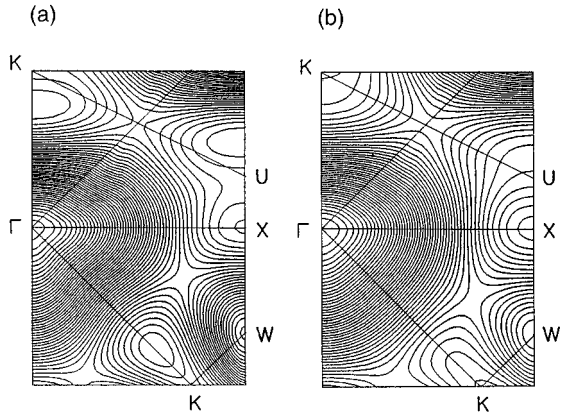

FIG. 112. Contour plots for the eigenvalue $\max_n\{\lambda_n(\mathbf{k})\}$ [see Eq. (83)] of spin-spin interactions in two high-symmetry planes in the reciprocal space of the fcc lattice in copper. The RK-interaction strength parameter $R=-0.26$ and -0.42 in figures (a) and (b), respectively. Maximum eigenvalues were found along the ΓK direction at $\mathbf{k}\approx(\pi/a)(0.6,0.6,0)$ in (a) and at the X point $\mathbf{k}=(\pi/a)(1,0,0)$ in (b). From Lindgård *et al.* (1986).

falls in the region where the RK and dipolar interactions strongly compete. That is, if their theoretical J_{ij}'s were scaled by 20%, from $R=-0.34$ to $R=-0.27$, the ordering vector would move from $\mathbf{Q}=(\pi/a)(1,0,0)$ to an incommensurate $\mathbf{Q}=(\pi/a)(\eta,\eta,0)$ with $\eta\approx0.6$, close to the observed $\eta=\frac{2}{3}$ in low and intermediate fields. This behavior is illustrated in Fig. 112, which shows, in the form of a contour map, $\lambda_n(\mathbf{k})$ on two high-symmetry planes in the reciprocal space. There can be interesting fluctuation effects in a situation when there is, in addition to the global maximum $\lambda_{\max}$, a nearly degenerate local maximum at another **k** vector, as in Fig. 112(a).

When anisotropic exchange forces and relativistic corrections to the RK interaction are included, $\lambda_n(\mathbf{k})$ becomes almost flat along the [100] directions (Oja, Wang, and Harmon, 1989). $\lambda_{\max}$ is found at $\mathbf{Q}=(\pi/a)(0.87,0,0)$, but $\lambda_n(\mathbf{k})$ is only 0.6% lower at $\mathbf{Q}=(\pi/a)(1,0,0)$. Anisotropic exchange interactions thus have a tendency to destabilize type-I ordering. The difference for $\mathbf{Q}=(\pi/a)(\eta,\eta,0)$ is rather small as well, on the order of 10%. Anisotropic interactions also slightly suppress the ordering temperature because T_c^{MF} is decreased to 170 nK, although the absolute value of the exchange constant is increased to $R=-0.37$. A further decrease in T_c should result from increased spin fluctuations along the $[\xi00]$ direction in **k** space.

Experiments (Poitrenaud and Winter, 1964; Oja, Annila, and Takano, 1990; Hakonen and Yin, 1991) and theoretical calculations (Harmon *et al.*, 1992) all show a strong dominance by exchange forces in silver, with $R\approx-2.5$. According to the free-electron picture [see Eq. (5)], the exchange constants J_{ij} of Cu and Ag should be equal, except for a constant coefficient. As a result, type-I ordering was expected (Oja and Kumar, 1987) for silver on the basis of the mean-field calculations by Kjäldman and Kurkijärvi (1979) on copper. Harmon *et al.*, (1992) arrived at the same conclusion using their

[16]The coefficient η of Kjäldman and Kurkijärvi (1979) is related to the R parameter through $R=-0.26\times0.587\eta$ [Eqs. (64) and (66)].

TABLE VI. Summary of mean-field predictions for type-I ordering in Cu, Ag, and Rh at positive spin temperatures, and the corresponding experimental values. The quantities listed are the Néel temperature T_N [Eq. (88)], the critical field $B_c(T=0)$ at zero temperature [Eq. (90)], and the (longitudinal) susceptibility χ of the antiferromagnetic state [Eq. (95)]; χ is independent of T and B within the mean-field theory. The experimental χ refers to its value at $T=T_N$ and $B=0$ for Cu and Ag, while for Rh we have listed the value at the lowest temperature $T=280$ pK reached so far. χ and B_c are given for zero demagnetization factor.

	Cu		Ag		Rh	
	theory[a]	exp.[b]	theory[c]	exp.[d]	theory[e]	exp.[f]
T_N (nK)	170	58±10	2.34	0.56±0.06	1.5	<0.28±0.06
$B_c(T=0)$ (μT)	417	270±10	140	100±10	101	
χ (SI units)	2.94	3.0	0.321	0.33±0.06	0.404	>0.55

[a]Calculated for exchange constants of Oja, Wang, and Harmon (1989).
[b]From Huiku *et al.* (1986).
[c]Calculated for exchange constants of Harmon, Wang, and Lindgård (1992).
[d]From Hakonen and Yin (1991).
[e]Calculated for exchange constants of Hakonen, Vuorinen, and Martikainen (1993).
[f]From Hakonen, Vuorinen, and Martikainen (1993).

band-structure calculation of J_{ij}. These predictions were confirmed by the neutron-diffraction measurements of Tuoriniemi, Nummila, *et al.* (1995).

At negative temperatures, ordering should proceed into a ferromagnetic state that corresponds to λ_{min} (Abragam and Goldman, 1982; Viertiö and Oja, 1992). This state will be discussed in Sec. XV.H.

2. $B_c(T=0)$ and χ of the ordered state

Table VI summarizes the mean-field predictions and experimental values of T_N, $B_c(T=0)$, and χ for Cu, Ag, and Rh. The calculations were made for type-I ordering at $T>0$. The exchange parameters used for Cu and Ag were taken from first-principles electronic band-structure calculations (Oja *et al.*, 1989; Harmon *et al.*, 1992). For Rh the experimental J_1 and J_2 values were used (see Fig. 87) (Hakonen, Vuorinen, and Martikainen, 1993).

The mean-field prediction for T_N is in clear disagreement with the experiments. This is largely explained by inadequacies of the mean-field theory and will be discussed in Sec. XV.C.3. For predicting magnetic properties such as B_c or χ, the mean-field theory is expected to work much better. The longitudinal susceptibility $\chi_L=\mu_0(dM/dB)$ has been measured in the ordered state only in the case of copper (see Fig. 52), which allows a direct comparison with χ^{MF}. The observed χ_L is not strictly constant as the mean-field prediction requires, but neither is the ordering only of type I. Variations about the mean result are ±14%. The value listed in Table VI is the zero-field susceptibility. In view of these ambiguities the excellent agreement between theory and experiment is partly fortuitous.

Also in the case of Ag, χ^{MF} agrees well with χ^{exp} at $B=0$. Although χ_L has not been measured as a function of the magnetic field, the nearly constant value of the transverse susceptibility at T_N (see Fig. 13 in Hakonen and Yin, 1991) suggests that χ_L behaves similarly as well. That is, according to the mean-field theory as applied to a single-**k** type-I structure, the experimental susceptibility along the external field is equal to χ measured perpendicular to the antiferromagnetic amplitude **d**. Although χ along **d** should be smaller than χ perpendicular to **d**, the difference appears only with decreasing temperature and vanishes at $T=T_N$, so that the susceptibility is isotropic. For the same reason multiple-**k** states at $T=T_N$ should also display isotropic susceptibility of the same amplitude.

For both Cu and Ag, the theoretical B_c is larger than the value extrapolated from measurements at a finite T. The discrepancy is at least partly caused by quantum fluctuations. Although the spin is larger in Cu, quantum effects may reduce $B_c(T=0)$ as much in Cu as in Ag owing to the larger dipolar anisotropy in copper.

Since the ordered state has not been reached in rhodium, we have included in Table VI the susceptibility measured at the lowest temperature produced in the disordered state (Hakonen, Vuorinen, and Martikainen, 1993); $\chi(T=T_N)$ should be larger. While the agreement between experimental and theoretical values of χ is good for Cu and Ag, there is a clear discrepancy in Rh: The measured χ is about 40% larger than the mean-field prediction for the ordered state.

One important feature of the data shown in Table VI is that the magnetic susceptibility for Cu is higher than that for Ag and Rh by almost an order of magnitude. This has nothing to do with the larger magnetic moment of Cu nuclei, as one might at first think. To understand the behavior it is useful to write Eq. (95) in the form

$$\chi^{MF}=1/(\tilde{\lambda}-R-L+D_z), \tag{105}$$

where the magnitudes of the dimensionless R and $\tilde{\lambda}=\lambda/(\mu_0\rho\hbar^2\gamma^2)$ parameters are set by the dipolar energy. If exchange interactions were negligible, χ^{MF} would have a universal value dependent on the crystal structure only but not on the magnitude of the moment or of the spin. If the exchange is large, χ^{MF} is reduced.

Therefore the reason for the relatively small χ in Ag and Rh is that $|R|$ is large in these metals.

Quantum-mechanical corrections neglected in the mean-field theory have the effect, at least when $T=0$, of lowering the susceptibility to less than the value predicted by Eq. (105) (Oguchi, 1960; White *et al.*, 1993). The effect is particularly large for $I=\frac{1}{2}$. For an antiferromagnet with the sodium chloride structure, for example, the correction would be on the order of 20%. Therefore, in Ag as well, the good agreement between theory and experiment for χ may be partly fortuitous.

3. Beyond the mean-field theory

In the first experiments on copper (Ehnholm, Ekström, Jacquinot *et al.*, 1979), no unambiguous signs of ordering were observed down to 50 nK, although the mean-field prediction for T_N was 230 nK (Kjäldman and Kurkijärvi, 1979). This discrepancy inspired a large amount of theoretical work aimed at improving estimates of the ordering temperature as well as predictions for the ordered structure. In addition, detailed comparisons were made with the measured S vs T and χ vs T curves.

Meaningful calculations for the paramagnetic state in zero field are more difficult than those for the ordered state in the sense that the mean-field theory completely fails, for example, in predicting the entropy, because short-range order is neglected. Any realistic calculation of thermodynamic properties in the paramagnetic state at $B=0$ requires, therefore, a fairly sophisticated approach, especially in the interesting range near T_N. Apart from mean-field calculations (Kjäldman and Kurkijärvi, 1979), the various theoretical techniques employed have included spherical model (SM; Kumar *et al.*, 1980; Kjäldman *et al.*, 1981; Lindgård *et al.*, 1986; Harmon *et al.*, 1992), high-temperature expansion (HTE; Niskanen and Kurkijärvi, 1981), linked-cluster expansion (LCE; Niskanen and Kurkijärvi, 1983), and an analysis of the eigenvalue spectrum $[\lambda_n(\mathbf{k})]$ of the interaction matrix (Niskanen *et al.*, 1982).

a. Spherical model

It is useful to review some of the results of the spherical-model calculations (Berlin and Kac, 1952; Mattis, 1985) as applied to copper and silver (Kumar *et al.*, 1980). These results provide insights into fluctuation effects that are ignored in the mean-field theory. The ordering temperature T_c in the spherical model is obtained from

$$I(I+1)=k_B T_c \frac{1}{N}\sum_{\mathbf{k},n} [\lambda_{\max}-\lambda_n(\mathbf{k})]^{-1}. \tag{106}$$

As in the mean-field theory (see Sec. XV.B.3), ordering takes place to a structure corresponding to $\lambda_{\max}=\max_{\mathbf{k},n}\{\lambda_n(\mathbf{k})\}$ through a second-order phase transition. In the spherical model, T_c depends on the whole $\lambda_n(\mathbf{k})$ spectrum, rather than on $\lambda_{\max}$ only as in the mean-field theory. Particularly important is the part of the eigenvalue spectrum near $\lambda=\lambda_{\max}$. From Eq. (106) one can see that if the maximum at $\lambda=\lambda_{\max}$ is flat the $\mathbf{k}$ sum becomes large and T_c decreases. In other words, if there are many low-energy excitations around the minimum-energy configuration, thermal fluctuations will suppress the ordering temperature.

The susceptibility is given by (Kumar *et al.*, 1980)

$$\chi=\mu_0\rho\hbar^2\gamma^2/[\lambda(T)-\lambda(0)], \tag{107}$$

where $\lambda(T)$ is obtained from

$$I(I+1)=k_B T\frac{1}{N}\sum_{\mathbf{k},n} [\lambda(T)-\lambda_n(\mathbf{k})]^{-1}. \tag{108}$$

In the high-temperature limit $\lambda(T)\gg\lambda_{\max}$, and one finds $\lambda(T)=3k_BT/I(I+1)$, which yields the Curie behavior. At $T=T_c^{SM}$, $\lambda(T)=\lambda_{\max}$, and the spherical model gives the mean-field susceptibility [see Eq. (95)] for the ordered state. The expression for the entropy is

$$S/Nk_B=\ln(2I+1) - \frac{1}{2N}\sum_{\mathbf{k},n}\ln\frac{I(I+1)[\lambda(T)-\lambda_n(\mathbf{k})]}{3k_BT}. \tag{109}$$

Kumar and co-workers first employed the spherical model to study the role of fluctuations in copper (Kumar *et al.*, 1980; Kjäldman *et al.*, 1981). It was found that this considerably lowered T_N from the mean-field estimate, even by more than 50%. In these calculations exchange interactions were described by means of the free-electron RK force.

Lindgård *et al.* (1986) have more recently made spherical-model calculations[17] in which the RK interaction was taken from their theoretical electronic band-structure data (see Table IV). They also made comparisons with experiments by multiplying the exchange constants by an overall scaling factor to study the dependence of the results on R, the strength of the RK interaction. They found $T_N=82$ nK for $R=-0.42$. This is quite close to the observed $T_N=58\pm10$ nK. However, as the authors point out, T_N^{SM} is for a second-order transition and should therefore be lower than the observed T_N because fluctuations must induce a first-order phase change above the predicted second-order transition to show consistency with experiments.

Another point that makes the discrepancy between the observed T_N and T_N^{SM} for $R=-0.42$ more serious is that the spherical model has a tendency to overestimate fluctuation effects and therefore to underestimate the ordering temperature. This feature is particularly pronounced for a nearest-neighbor Heisenberg antiferromagnet in an fcc lattice (Heinilä and Oja, 1993b). The spherical model does not predict long-range order at all when $T>0$, although there is long-range type-I order below $T_N=0.45J_1/k_B$ according to Monte Carlo simulations, which, in principle, are accurate (Minor and Giebultowicz, 1988; Diep and Kawamura, 1989; Heinilä and Oja, 1993b).

[17]The correlation theory used by these authors is identical to the spherical model in the limit considered.

The ordering temperature of Ag has been calculated using the spherical model (Harmon, Wang, and Lindgård, 1992) by employing the Ruderman-Kittel exchange constants from band-structure calculations. The result, $T_N^{SM}=1.5$ nK, with the transition to an antiferromagnetic structure of type I, is significantly higher than the measured $T_N=560\pm60$ pK.

b. High-T expansions and other quantum-spin theories

High-temperature expansion (HTE) offers a systematic way to improve the accuracy of predictions for the disordered state. HTE can also account for the quantum nature of spins, which is described by the spherical model in only a trivial way, similarly to the mean-field theory. Padé approximations provide a way of continuing the HTE to lower temperatures and can be used to obtain a reliable estimate of the ordering temperature (Rushbrooke *et al.*, 1974).

Pirnie *et al.* (1966) have reported an HTE analysis of ferromagnetic and antiferromagnetic Heisenberg models with nearest-neighbor and next-nearest-neighbor interactions. The seven leading terms in the high-T expansions for the uniform ($\mathbf{k}=0$) as well as the appropriate staggered ($\mathbf{k}\neq0$)[18] susceptibilities were calculated as a function of I. Divergence of the staggered susceptibility at $T=T_N$ is an indication of a second-order transition to an antiferromagnetic state modulated by the corresponding $\mathbf{k}$ vector. An important observation made by Pirnie *et al.* was that $T_N(I)/T_N^{MF}(I)$ is remarkably spin independent.

For a system interacting through dipole-dipole and the free-electron RK forces, Niskanen and Kurkijärvi (1981) have carried out the (staggered) susceptibility expansion to the fifth term and the specific-heat expansion to the fourth term. Their results showed that the Néel temperature of Cu, with $R=-0.42$, is 180 nK, which is about 20% lower than the mean-field estimate but still clearly higher than the observed T_N.

A compromise between the spherical model and HTE is the linked-cluster expansion (LCE) of Niskanen and Kurkijärvi (1983). The technique can describe quantum spin, and it reduces to the spherical model in the high-density limit for classical spins. In comparison with HTE results for classical and $I=\frac{1}{2}$ Heisenberg models (Rushbrooke *et al.,* 1974), the linked-cluster expansion predicts a much lower ordering temperature. The advantage of LCE, in comparison with the exact HTE, is that the method is better adapted to systems with long-range interactions. For Cu with $R=-0.42$, LCE predicts $T_N=120$ nK (Huiku *et al.,* 1986). Since all calculations systematically show that T_N decreases when $|R|$ is reduced, the main reason for the discrepancy between calculations and the observed $T_N=58\pm10$ nK seems to be that $R=-0.42$ for Cu is too large in absolute magnitude, at least when the free-electron form of the RK interaction is assumed.

c. Monte Carlo simulations

The T_N of Cu has also been obtained from Monte Carlo simulations of classical spins. Three different studies have been reported. The major differences between these computations are in the assumptions made about the exchange interaction. Frisken and Miller (1988a) obtained $T_N=50$ nK using their calculation for the RK interaction (Frisken and Miller, 1986) up to eighth nearest neighbors. Viertiö and Oja (1989, 1990a) found $T_N=65$ nK for a two-nearest-neighbor model and $T_N=33$ nK for a set of longer-range exchange constants, which were slightly modified from those given by the band-structure calculations of Oja, Wang, and Harmon (1989).

In the case of silver, Monte Carlo simulations by Viertiö (1990), which include both dipolar and exchange interactions up to eighth nearest neighbors, yield a transition to the expected type-I structure at $T_N=500$ pK (Oja and Kumar, 1987). This is in good agreement with the measured $T_N=560\pm60$ pK, while the mean-field estimate is considerably higher, $T_N^{MF}=2.3$ nK.

At negative spin temperatures, Monte Carlo simulations (Viertiö and Oja, 1992) again produce good agreement with experiment, $T_C^{MC}=-1.7$ nK while the observed $T_C=-1.9\pm0.4$ nK (Hakonen, Nummila, Vuorinen, and Lounasmaa, 1992). The RK interaction used in these simulations on silver nuclei was obtained from the calculations of Harmon *et al.* (1992) and corresponds to $R=-2.3$.

An important and difficult question is how the quantum nature of spins should be taken into account when Monte Carlo results for classical spins are compared with experimental data. In the Monte Carlo results quoted above, no quantum corrections were made. The simulations were done for classical spins with magnetic moments $\mu=\gamma\hbar I$. An estimate of T_c for the corresponding quantum-spin system can be made using the result obtained from the high-temperature expansions of Pirnie *et al.* (1966), according to which $T_c(I)/T_c^{MF}(I)$ is nearly spin independent for Heisenberg systems in an fcc lattice. In other words, T_c scales approximately with I as predicted by the mean-field theory. Therefore the ordering temperature $T_c(I)$ for a system of quantum spins with moments $\gamma\hbar\mathbf{I}$ can be estimated from

$$T_c(I)=\frac{I+1}{I}T_c^{MC}, \tag{110}$$

where T_c^{MC} is obtained from Monte Carlo simulations on a system of classical spins with dipole moments $|\boldsymbol{\mu}|=\gamma\hbar I$, using the same spin-spin interactions.

In the case of copper, $I=\frac{3}{2}$, the Monte Carlo results quoted above should thus be multiplied by $\frac{5}{3}$, while for silver the multiplier is 3. When this is done, there is almost a factor-of-3 discrepancy between predicted and observed ordering temperatures of silver, both at positive and negative spin temperatures. At $T>0$, the

[18]Staggered susceptibility describes the response to a nonuniform field $\mathbf{B}(\mathbf{r})=\mathbf{B}\exp(i\mathbf{k}\cdot\mathbf{r})$, whereas the ordinary susceptibility gives the response to a uniform, constant field.

$(I+1)/I$-corrected T_N then agrees with the spherical-model result of Harmon *et al.* (1992).

One should note, however, that the $(I+1)/I$ scaling, based on the work of Pirnie *et al.* (1966), is for a second-order phase change although the transition is of first order according to simulations (Viertiö, 1992) and experiments (Hakonen and Yin, 1991). Since T_N for a first-order transition is higher than for a corresponding second-order phase change, the remaining discrepancy is in fact less than a factor of 3. Nevertheless, it seems that there remains a clear disagreement between the theoretical and measured ordering temperatures of silver.

When T_N=33 nK from the Monte Carlo simulations on copper by Viertiö and Oja (1990a) is scaled by $(I+1)/I$, one obtains T_N=55 nK, in excellent agreement with the measured T_N=58±10 nK. Recent simulations by Heinilä and Oja (1995), which include couplings only between three neighboring shells, yield T_N=33 nK when scaled by $(I+1)/I$. The earlier simulations (Frisken and Miller, 1988a; Viertiö and Oja, 1989) give a slightly too high T_N when scaled by $(I+1)/I$. Among these simulations, only the more recent calculations (Viertiö and Oja, 1990a; Heinilä and Oja, 1995) are able to account for type-I as well as type-$(0\ \frac{2}{3}\ \frac{2}{3})$ spin configurations. It seems, therefore, that the near degeneracy of the (1 0 0) and $(0\ \frac{2}{3}\ \frac{2}{3})$ orders enhances spin fluctuations and results in a reduction of T_N. This is consistent with spherical-model calculations by Lindgård *et al.* (1986) and is easy to understand: In the case of a near degeneracy, the eigenvalue $\lambda_n(\mathbf{k})$ must be rather flat in the $\mathbf{k}$ space between the $\mathbf{k}=(\pi/a)(1,0,0)$ and $\mathbf{k}=(\pi/a)(0,\frac{2}{3},\frac{2}{3})$ positions, which is illustrated in Fig. 112(a). As discussed in connection with Eq. (106), fluctuations of $\mathbf{k}$ vectors in this region of the reciprocal lattice will then lower T_N.

Viertiö and Oja (1992) have made Monte Carlo calculations to simulate the adiabatic demagnetization process of nuclear spins in silver using the method developed by Merkulov *et al.* (1988).

4. S and χ of the paramagnetic state

A comparison between the measured and calculated susceptibilities of copper was presented in Fig. 25. It is observed that for $R=-0.42$, both the spherical model and LCE predict a too-large inverse susceptibility. The situation is the opposite for the simple Curie-Weiss approximation, which is included for comparison. Within the spherical model, the measured and calculated χ vs T curves can be fitted well if $|R|$ is changed to $R=-0.28$ (Lindgård *et al.*, 1986). The RK interaction used in LCE was the free-electron approximation, while the band-structure values were employed in the spherical-model calculation. Unfortunately, however, comparisons between theory and experiment for the S vs T and χ vs T curves are not yet available for the most complete set of theoretical exchange interactions, which also include anisotropic coupling (Oja *et al.*, 1989).

Figure 27 shows a comparison with the S vs T curve. Now the LCE prediction with $R=-0.42$ describes the data well down to the ordering temperature. The spherical-model estimate for S is too low. The agreement with the spherical model would improve if a lower R were assumed, but agreement with the linked-cluster expansion would then become worse.

Far less theoretical work has been done to compute the thermodynamic properties of silver above T_N. The susceptibility of Ag, calculated using the spherical model, agrees best with measurements if the strength of the RK interaction is decreased in absolute value from $R=-2.3$ to $R=-1.7$ (Harmon *et al.*, 1992). The S vs T curves of Ag and Rh have been investigated by Hakonen (1994) using Monte Carlo simulations of classical spins.

D. Fluctuation-stabilized type-I spin configurations

1. Continuous degeneracy of the mean-field solution

The most general spin configuration for the fcc type-I order can be written as a superposition of the three wave vectors $\mathbf{k}_1=(\pi/a)(1,0,0)$, $\mathbf{k}_2=(\pi/a)(0,1,0)$, and $\mathbf{k}_3=(\pi/a)(0,0,1)$,

$$\langle \mathbf{I}_i\rangle/I=\mathbf{m}+\sum_{j=1,2,3}\mathbf{d}_j\cos(\mathbf{k}_j\cdot\mathbf{r}_i), \tag{111}$$

where $\mathbf{m}$ is the magnetization, $\mathbf{d}_j$ is the amplitude of the antiferromagnetic modulation, and $\mathbf{k}_j$ is the corresponding wave vector. The structure can hence be a single-$\mathbf{k}$, double-$\mathbf{k}$, or a triple-$\mathbf{k}$ state, and the number of sublattices can vary from 2 to 4.

Dipolar anisotropy fixes the relative directions of $\mathbf{d}_j$ and $\mathbf{k}_j$ by imposing the constraints (Luttinger and Tisza, 1946)

$$\mathbf{d}_j\cdot\mathbf{k}_j=0,\quad j=1,2,3. \tag{112}$$

The origin of this anisotropy can be seen from the eigenvalue equation (87). For simplicity, let us consider the $J_1J_2D_1$ model of Sec. XV.B.7. From Eq. (103) one finds that $A(\mathbf{k}_1)$ is diagonal. The doubly degenerate eigenvalue of the yz block, $\lambda=\lambda_2=\lambda_3=-4J_1+6J_2+4D_1$, is the relevant eigenvalue because $\lambda-\lambda_1=12D_1>0$. Ordering therefore takes place in the plane perpendicular to $\mathbf{k}_1$. The energy scale associated with the anisotropy is large, on the order of the dipolar energy. Numerical calculations give $\lambda_{2,3}-\lambda_1=6.50(\mu_0/4\pi)\rho\hbar^2\gamma^2$ when the dipolar interactions are fully included (Cohen and Keffer, 1955).

Requiring equal moments at the four sublattices, one finds (Kumar *et al.*, 1986)

$$|\mathbf{m}|^2+|\mathbf{d}_1|^2+|\mathbf{d}_2|^2+|\mathbf{d}_3|^2=p^2, \tag{113a}$$

$$\mathbf{m}\cdot\mathbf{d}_1+\mathbf{d}_2\cdot\mathbf{d}_3=0,\quad \mathbf{m}\cdot\mathbf{d}_2+\mathbf{d}_3\cdot\mathbf{d}_1=0,$$

$$\mathbf{m}\cdot\mathbf{d}_3+\mathbf{d}_1\cdot\mathbf{d}_2=0. \tag{113b}$$

Here p is the total sublattice polarization, $|\langle\mathbf{I}_i\rangle|/I$. The structure is permanent if

$$\mathbf{m}(T,\mathbf{B})=\mathbf{B}/B_c(T=0), \tag{114}$$

where

$$B_c(T=0)=I[\lambda_{2,3}-\lambda(0)]/\hbar\gamma. \quad (115)$$

The antiferromagnetic order parameter can have altogether six nonzero components $(d_{1y},d_{1z},d_{2x},d_{2z},d_{3x},d_{3y})$. The four equations, (113a) and (113b), do not fix the solution uniquely; there remains a continuous two-dimensional degeneracy. To single out the ground state one has to consider fluctuation effects.

2. Static susceptibility matrices

Thermodynamics of type-I structures is given by the general results for permanent spin structures, which were discussed in Sec. XV.B.5. In particular, the longitudinal susceptibility in the ordered state,

$$\chi_0\equiv\mu_0\rho\hbar^2\gamma^2/[\lambda_{2,3}-\lambda(0)], \quad (116)$$

is independent of T and $\mathbf{B}$. The value of the full susceptibility matrix $\underline{\chi}(0)$ depends on the actual spin configuration. Calculation of $\underline{\chi}(0)$ is technically rather complicated. Special cases have been treated by Heinilä and Oja (1996).

We consider first a single-$\mathbf{k}$ structure in which the modulation vector $\mathbf{k}_3=(\pi/a)(0,0,1)$ is parallel to the field aligned along a crystalline axis, say [001]. In this case

$$\langle\mathbf{I}_i\rangle/I=(0,0,m)+(0,d_3,0)\cos(\mathbf{k}_3\cdot\mathbf{r}_i), \quad (117)$$

where $m=B/B_c$ and $m^2+d_3^2=p^2$. The static susceptibility is

$$\underline{\chi}(0)=\begin{pmatrix}\chi_0 & 0 & 0\\ 0 & \chi_{yy} & 0\\ 0 & 0 & \chi_0\end{pmatrix}, \quad (118)$$

where

$$\chi_{yy}/\chi_0=\frac{B_{\rm D}B_{\rm c}\,p^2(1-\tau)+B_0^2\lambda\,\tau/[\lambda_{2,3}-\lambda(0)]}{B_{\rm D}B_{\rm c}\,p^2(1-\tau)+(\Omega_\perp/\gamma)^2\lambda\,\tau/[\lambda_{2,3}-\lambda(0)]}. \quad (119)$$

Here

$$B_{\rm D}=(I/\gamma\hbar)(\lambda_{2,3}-\lambda_1) \quad (120)$$

is the anisotropy field for type-I order, and $\tau=\tau(p)$ is a monotonic function of polarization defined by the parametric equation

$$\tau[p(x)]=1-\frac{x}{p(x)}\frac{dp(x)}{dx},\quad p(x)=\mathcal{B}_I(x). \quad (121)$$

In particular, τ assumes the values $\tau(0)=0$ and $\tau(1)=1$. At $B=0$ we find the well-known behavior in which the susceptibility along the staggered magnetization (χ_{yy}) increases from zero at $T=0$ to $\chi_{yy}=\chi_0$ at $T=T_{\rm N}$, whereas the susceptibility perpendicular to the spins is constant (Kittel, 1971).

The above case may be considered, however, as a special case. A more general single-$\mathbf{k}$ structure is obtained in a finite field that is not parallel to the ordering vector. The spin configuration can be described by

$$\frac{\langle\mathbf{I}_i\rangle}{I}=\frac{\mathbf{B}_0}{B_c}+d\frac{\mathbf{B}_0\times\mathbf{k}}{|\mathbf{B}_0\times\mathbf{k}|}\cos(\mathbf{k}\cdot\mathbf{r}_i), \quad (122)$$

where $m^2+d^2=p^2$. Here $\mathbf{k}$ is one of the three type-I ordering vectors, namely, $(\pi/a)(1,0,0)$, $(\pi/a)(0,1,0)$, or $(\pi/a)(0,0,1)$. For this structure, Heinilä and Oja (1996) have found a completely isotropic susceptibility. More precisely, $\underline{\chi}(0)=\chi_0\underline{I}$. The same $\underline{\chi}(0)$ has been found for a triple-$\mathbf{k}$ state, defined by Eq. (140). For more details, consult the original paper.

According to the above results for a single-$\mathbf{k}$ state, $\underline{\chi}(0)$ behaves in a discontinuous fashion when the structure of Eq. (122) is demagnetized to zero field. It was suggested that this is connected with a reorientation transition in low fields, which is similar to a spin-flop transition.

3. Overview of fluctuation mechanisms

Several mechanisms can lift the continuous, two-dimensional degeneracy that the mean-field theory predicts for the various type-I fcc antiferromagnets:

(i) Thermal fluctuations.
(ii) Quantum fluctuations.
(iii) "Quenched-in randomness" brought about by the presence of different moments, in the case of a two-isotope system.
(iv) Defects. They also act as quenched-in randomness.
(v) Magnetoelastic forces.

Much theoretical work has been devoted to the first two possibilities, the selection of the ground state by fluctuations. For type-I fcc antiferromagnets with isotropic interactions, the spin-wave calculation of Oguchi *et al.* (1985) first showed that quantum fluctuations favor a single-$\mathbf{k}$ structure instead of, for example, a triple-$\mathbf{k}$ configuration. Effects due to dipolar anisotropy as well as configurations caused by the external magnetic field were first discussed by Viertiö and Oja (1987), who also employed spin-wave theory. The same problems were later investigated by Lindgård (1988a, 1988b), using perturbation theory, and more recently by Heinilä and Oja (1993a). The effects of thermal fluctuations have been studied by employing Monte Carlo simulations (Frisken and Miller, 1988a; Frisken, 1989; Viertiö and Oja, 1989; Viertiö, 1990), spin-wave theory (Viertiö and Oja, 1989), Ginzburg-Landau theory (Oja and Viertiö, 1987), and thermodynamic-perturbation theory (Heinilä and Oja, 1994a).

The multitude of various studies reflects the delicate nature of the problem. In the case of copper, an additional complication is caused by competition between the dipolar and RK interactions. There were several discrepancies among the early theoretical investigations, but now it seems that recent studies by Heinilä and Oja (1993a) have clarified the situation. For this reason we shall focus mainly on their work. We shall first discuss thermal fluctuations, which are intuitively more obvious than the corresponding quantum phenomena. It turns

out that, at least to the leading order, thermal and quantum fluctuations stabilize the same spin structures.

Before we continue, however, we shall briefly comment on the last three possibilities. Following the discussion by Henley (1987), an *ad hoc* argument has been proposed according to which the presence of two isotopes in Cu and Ag is less important for the selection of the ground state than, for example, quantum fluctuations (Oja and Viertiö, 1987). Systematic Monte Carlo simulations so far have not been performed to investigate this question.

In copper, with $I=\frac{3}{2}$, the most important consequence of various defects is probably the quadrupolar interaction that arises if there are distortions from cubic symmetry. The strength of the quadrupolar force near several substitutional impurities has been investigated by NMR experiments (Rowland, 1960). In heat-capacity measurements of high-purity polycrystalline copper at millikelvin temperatures, an extra contribution to the heat capacity of a pure system has been observed and attributed to quadrupolar interactions near impurities and lattice imperfections (Gloos *et al.*, 1988). One can conclude, however, that at least the salient features of nuclear ordering in copper are not related to defects because the main characteristics of the data do not depend on a particular sample.

Siemensmeyer and Steiner (1992) have investigated the importance of magnetoelastic coupling between nuclear spins and the lattice. They find that magnetoelastic energy due to quadrupolar forces can be significant in the selection of the ground state among degenerate type-I structures.

4. Thermal fluctuations

Heinilä and Oja (1994a) have recently investigated the selection of the ground state in type-I fcc antiferromagnets by thermal fluctuations. They made use of the so-called thermodynamic perturbation theory (Landau and Lifshitz, 1980), which, in this context, is identical to the spin-wave theory for classical spins. Although this approach is limited to low temperatures, it is valuable because it gives a simple expression for the leading ground-state selection term.

In order to describe fluctuations about the $T=0$ configuration for a spin at site i, it is useful to introduce a local coordinate frame $(\mathbf{e}_x^i,\mathbf{e}_y^i,\mathbf{e}_z^i)$ where $\mathbf{e}_z^i$ is parallel to the equilibrium direction. The spin vectors can be written as

$$\begin{aligned}\mathbf{I}_i &= I[\mathbf{e}_z^i\cos\theta_i+\sin\theta_i(\mathbf{e}_x^i\cos\phi_i+\mathbf{e}_y^i\sin\phi_i)] \\ &= \mathbf{e}_z^i(I-|\alpha_i|^2)+(I-|\alpha_i|^2/2)^{1/2}(\alpha_i^*\mathbf{e}_+^i+\alpha_i\mathbf{e}_-^i),\end{aligned} \quad (123)$$

where the complex quantities α_i are defined in terms of the polar angles as $\alpha_i=I^{1/2}e^{i\phi_i}(1-\cos\theta_i)^{1/2}=u_i+iv_i$ and $\mathbf{e}_\pm^i=2^{-1/2}(\mathbf{e}_x^i\pm i\mathbf{e}_y^i)$. This is the classical analog of the Holstein-Primakoff transformation. The usefulness of Eq. (123) relies on the fact that $\sin\theta_i d\phi_i d\theta_i \propto du_i dv_i$. Retaining only the parts bilinear in α_i and α_i^*, we rewrite the Hamiltonian of Eq. (73) as $\mathcal{H}=\mathcal{H}_0+\mathcal{H}_1$ with

$$\mathcal{H}_0 = E_0+\lambda I\sum_i \alpha_i^*\alpha_i, \quad (124)$$

$$\mathcal{H}_1 = -\tfrac{1}{2}I\sum_{i,j}{}' \{\mathbf{e}_+^i\underline{A}_{ij}\mathbf{e}_+^j\alpha_i^*\alpha_j^*+\mathbf{e}_+^i\underline{A}_{ij}\mathbf{e}_-^j\alpha_i^*\alpha_j+\text{c.c.}\}, \quad (125)$$

where $E_0=-\frac{1}{2}N\lambda I^2$ and λ is related to the site-independent local field through $B_{\text{loc}}=\lambda I/(\hbar\gamma)$ [see Eq. (89)]. The Gibbs free energy can be expanded with respect to $\mathcal{H}_1$ in the form

$$G\approx G_0-\langle\mathcal{H}_1^2\rangle/(2k_BT), \quad (126)$$

where G_0 is the free energy associated with $\mathcal{H}_0$ and

$$\langle\mathcal{H}_1^2\rangle\propto\int\prod_i [du_i dv_i\exp[-\lambda I(u_i^2+v_i^2)/k_BT]\mathcal{H}_1^2, \quad (127)$$

up to a normalization factor. Extension of integration over the whole complex plane also includes the unphysical states $|\alpha_i|^2>2I$ of the conventional spin-wave theories. Owing to this defect the analysis applies to the low-temperature region only. One obtains (Heinilä and Oja, 1994a)

$$G = E_0-TS_0-Nk_BT\ln(T/T_0)-\frac{k_BT}{2\lambda^2}\times\sum_{i,j}{}' \{|\mathbf{e}_+^i\underline{A}_{ij}\mathbf{e}_+^j|^2+|\mathbf{e}_+^i\underline{A}_{ij}\mathbf{e}_-^j|^2\}, \quad (128)$$

where S_0 and T_0 are constants. This result is an estimate of the lowest-order spin-wave free energy. When the classical ground state at $T=0$ has infinite degeneracy, Eq. (128) can be used to find the configuration favored by thermal effects.

5. Quantum fluctuations

Quantum fluctuations can be treated in the same way as thermal fluctuations. Now the variables α_i^* and α_i of the previous section simply become the bosonic creation and annihilation operators for spin deviations, $a_i^\dagger$ and a_i. In the second-order perturbation theory, the energy at $T=0$ is $E=E_0+\Delta E$, where (Heinilä and Oja, 1993a)

$$\Delta E = -\frac{I}{4\lambda}\sum_{i,j}{}' |\mathbf{e}_+^i\underline{A}_{ij}\mathbf{e}_+^j|^2. \quad (129)$$

This expression is only slightly different from the corresponding term causing ground-state selection by thermal fluctuations, Eq. (128). Heinilä and Oja (1994a) have found that, apart from unimportant constants, the ground-state selection is the same for thermal and quantum fluctuations if the interactions are isotropic. The same may also be true when the interactions are anisotropic, but a rigorous proof is lacking. At least in all special cases investigated by Heinilä and Oja it was found that quantum and thermal fluctuations favor the same spin structures.

Perturbation theory is less accurate than the linear spin-wave theory which was used previously to discuss the ground state of nuclear magnets (Viertiö and Oja, 1987). The transparency of perturbation theory, together with the fact that nearest-neighbor correlations are by far the most important for lifting the degeneracy, makes it a reasonable approach to the ground-state problem, as has been emphasized by Lindgård (1988a).

6. Isotropic spin-spin interactions

Before discussing the ground-state spin configurations of anisotropic fcc antiferromagnets, it is useful to consider the isotropic Hamiltonian,

$$\mathcal{H}=-\tfrac{1}{2}{\sum_{i,j}}' J_{ij}\mathbf{I}_i\cdot\mathbf{I}_j-\hbar\gamma\mathbf{B}\cdot\sum_i \mathbf{I}_i. \tag{130}$$

In this case the direction of the magnetic field with respect to the crystalline axes has no influence.

The free energy of Eq. (128), describing thermal fluctuations, becomes (Heinilä and Oja, 1994a)

$$G=E_0-TS_0-Nk_{\mathrm{B}}T\,\ln(T/T_0)-\frac{k_{\mathrm{B}}T}{4\lambda^2}\times{\sum_{i,j}}' J_{ij}^2[1+I^{-4}(\mathbf{I}_i\cdot\mathbf{I}_j)^2], \tag{131}$$

while the correction to the ground-state energy due to quantum fluctuations is (Long, 1989; Larson and Henley, unpublished; Heinilä and Oja, 1993a)

$$\Delta E=-\frac{NIJ_1^2}{8\lambda}\left[10-16m^2+I^{-4}\sum_{a>b}(\mathbf{I}_a\cdot\mathbf{I}_b)^2\right], \tag{132}$$

where a and b denote summation over the four sublattices. These two expressions show that both quantum and thermal fluctuations favor the spin configuration that maximizes $\Sigma_{i,j}(\mathbf{I}_i\cdot\mathbf{I}_j)^2$. Thus fluctuations tend to stabilize collinear spin arrangements.

The ground-state selection term $\Sigma_{i,j}(\mathbf{I}_i\cdot\mathbf{I}_j)^2$ was, in fact, first proposed by Henley (1987, 1989), who used a somewhat different derivation. His interpretation of the result is that fluctuations of a fixed-length spin j generate random exchange fields $\delta\mathbf{B}_i=J_{ij}\delta\mathbf{I}_j$ which, to leading order, are perpendicular to the equilibrium direction of $\mathbf{I}_j$. If the equilibrium spin structure is collinear, $\delta\mathbf{B}_i$ is perpendicular to $\langle\mathbf{I}_i\rangle$. Spin i can then lower its energy by relaxing towards the direction of the fluctuating field.

The evolution of the spin structure with the externally applied field has been investigated by Heinilä and Oja (1993a). The results are illustrated in Fig. 113. In zero field the stable structure is a single-**k** state with sublattice spin directions $\mathbf{I}_1=\mathbf{I}_2=-\mathbf{I}_3=-\mathbf{I}_4$. At low B, spins cant towards the field to match $\mathbf{m}=\mathbf{B}/B_c$ as required by Eq. (114). There is a transition at $m=B/B_c=0.407$ from a single-**k** configuration to a triple-**k** state. In the latter structure at $0.407<m<0.5$ [see Fig. 113(b)], spins in the three sublattices are tilted towards the field so that two of them have the same spin direction; the spins in the fourth sublattice are nearly opposite to the external

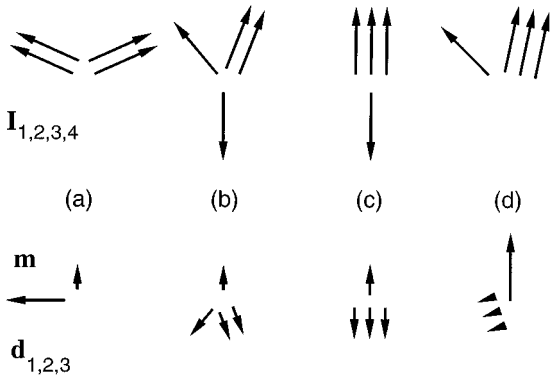

FIG. 113. Isotropic, type-I fcc antiferromagnet in an external magnetic field. Directions of the spins in the four sublattices $\mathbf{I}_1$–$\mathbf{I}_4$ are indicated. $\mathbf{d}_1$–$\mathbf{d}_3$ are the corresponding amplitudes of the antiferromagnetic modulation, and $\mathbf{m}$ is the magnetization [see Eq. (111)]. The external field points upwards. (a) $B=0.40B_c$; (b) $B=0.41B_c$; (c) $B=0.5B_c$; (d) $B=0.9B_c$. From Heinilä and Oja (1993a).

field. At $B=B/B_c=0.5$, a collinear structure is again possible, with $\mathbf{I}_1=\mathbf{I}_2=\mathbf{I}_3=-\mathbf{I}_4$ and parallel to **B**. In the triple-**k** structure at $m\geq 1/2$, depicted in Figs. 113(c) and 113(d), there are three sublattices in which spins have the same direction. In the triple-**k** states of Figs. 113(b)–113(d), the spins in the four sublattices are always coplanar.

The evolution of the ground state with an external magnetic field has also been investigated by Monte Carlo simulations (Heinilä and Oja, 1994b) which, in principle, yield the exact solution for classical spins. These simulations were made for the Hamiltonian of Eq. (130) assuming an antiferromagnetic nearest-neighbor exchange interaction, $J_1<0$, and a weak ferromagnetic next-nearest-neighbor interaction $J_2=-0.1J_1$. The spins were taken as unit vectors. The results were characterized by the parameters

$$p_\perp^2=\sum_{j=1}^{3}\{(\mathbf{d}_j)_x^2+(\mathbf{d}_j)_y^2\}, \tag{133a}$$

$$p_\parallel^2=\sum_{j=1}^{3}(\mathbf{d}_j)_z^2, \tag{133b}$$

where the z axis is along **B**. The behavior of $p_\perp^2$ and $p_\parallel^2$ at $T=0.6|J_1|/k_{\mathrm{B}}$ is illustrated in Fig. 114 for two simulations, one for an increasing and the other for a decreasing field. The simulated sample consisted of $N=4096$ spins, and periodic boundary conditions were imposed.

From the figure one can identify the low-field structure of purely transversal modulation. At $B_\uparrow\approx 5|J_1|/(\hbar\gamma)$, a discontinuous transition takes place to a collinear configuration with purely parallel antiferromagnetism; note the quite large hysteresis. At $B\approx 6|J_1|/(\hbar\gamma)$, there is a continuous transition to a structure with mixed parallel and perpendicular modulations. Finally, the critical field to the paramagnetic state is $B_c\approx 8|J_1|/(\hbar\gamma)$ at $T_{\mathrm{N}}=0.6|J_1|/k_{\mathrm{B}}$. The low-field

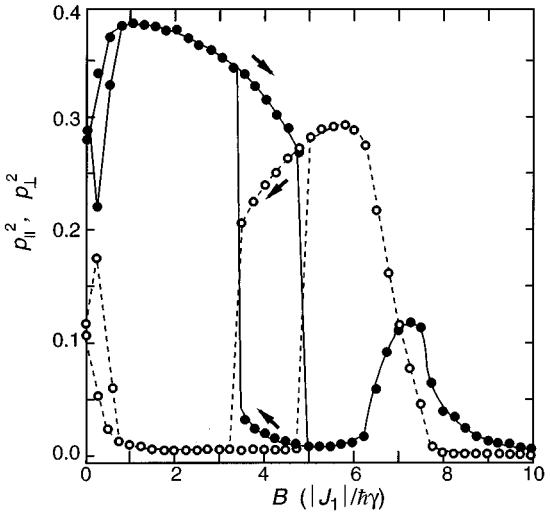

FIG. 114. Field evolution of an isotropic, type-I fcc antiferromagnet, as given by Monte Carlo simulations. Total parallel $p_\parallel^2$ (○) and transversal $p_\perp^2$ (●) antiferromagnetic modulations at $T=0.6|J_1|/k_B$ are shown. The arrows indicate directions of field changes. From Heinilä and Oja (1994b).

perpendicular phase can be identified as the structure in Fig. 113(a) and the parallel configuration as the up-up-up-down state in Fig. 113(c). The behavior of parallel and perpendicular modulations in high fields are in agreement with Fig. 113(d).

These simulations were carried out at a temperature $T=0.6|J_1|/k_B$, which is very close to the corresponding zero-field Néel temperature $T_N=0.68|J_1|/k_B$. A low-T ground-state analysis, based on maximizing $\Sigma_{i,j}(\mathbf{I}_i\cdot\mathbf{I}_i)^2$, therefore works remarkably well in a region where one might expect changes from the low-T behavior.

7. Anisotropic spin-spin interactions with an easy plane

Ground-state selection has been investigated quite extensively for anisotropic models because of its relevance to nuclear ordering, particularly in copper. The first theoretical studies were made by Viertiö and Oja (1987), who used the linear spin-wave theory to calculate the quantum-mechanical correction to the ground-state energy, viz.,

$$E=E_0+\sum_{\mathbf{k}}\left[E_{\mathbf{k}}+\sum_{\alpha}\tfrac{1}{2}\hbar\omega_{\mathbf{k},\alpha}\right], \tag{134}$$

where $E_{\mathbf{k}}$ is a structure-dependent term, $\hbar\omega_{\mathbf{k},\alpha}$ is the spin-wave energy, and α is an index of the mode. The Hamiltonian consisted of the complete, infinite-range dipolar interaction and the free-electron RK coupling. Magnetic phase diagrams were calculated as a function of B, the direction of $\mathbf{B}$ with respect to the crystalline axes, and R, the strength of the RK interaction. Owing to the extensive computing time requirements it was not possible to perform a complete search of the ground state in the whole degenerate, two-dimensional parameter space. Instead, an ansatz for the ground state was made by choosing trial spin configurations of particularly high symmetry with respect to $\mathbf{B}$ and the crystalline directions. The $B=0$ spin structures of Viertiö and Oja are shown in Fig. 115. For strong exchange, the ground state is a single-$\mathbf{k}$ configuration as was already found by Oguchi *et al.* (1985). When the dipolar interaction is sufficiently strong, i.e., when $|R|<0.55$, the ground state is a double-$\mathbf{k}$ structure.

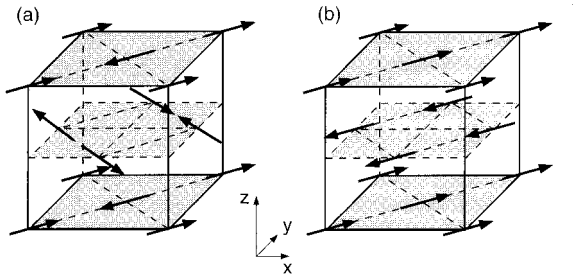

FIG. 115. Ground-state spin configurations in zero external magnetic field assuming dipolar and free-electron RK interactions: (a) $|R|<0.55$; (b) $|R|>0.55$. From Viertiö and Oja (1987).

The problem was further investigated by Lindgård (1988a, 1988b), who introduced the perturbation approach for studying quantum fluctuations. The method was technically simpler than the spin-wave calculation and yet contained the essential physics. Another useful simplifying approximation of Lindgård was to focus the analysis on the nearest-neighbor interaction, which is the most important quantity in the ground-state selection. At $B=0$, his results agreed with spin-wave calculations. Considerable differences between the two approaches were found, however, in an external field. This obscured the theoretical situation although Lindgård's results provided a possible explanation for the three phases observed in the susceptibility measurements of a copper single crystal (Huiku *et al.*, 1986).

Heinilä and Oja (1993a) have recently repeated the perturbation calculation of the ground state using the same approximation as Lindgård. The two sets of results were clearly different for $\mathbf{B}\|[110]$ and in the high-field region for $\mathbf{B}\|[001]$. Since a careful examination (Heinilä and Oja, 1993a) of the discrepancies clearly shows that Lindgård's results are partly erroneous, we have chosen to present here only the phase diagrams of Heinilä and Oja.

Monte Carlo simulations have also been performed to investigate the magnetic phase diagrams of copper and silver (Frisken and Miller, 1988a; Frisken, 1989; Viertiö and Oja, 1989; Viertiö, 1990). These results are valuable as they provide, in principle, an accurate result for the ground state of classical spins. The delicate nature of the problem presents several numerical difficulties. The relaxation times in the simulations can be very long, as there are typically several local minima of free energy. The long range of the interactions also makes the calculations demanding in terms of CPU time. These reasons have strongly limited the range of fields and exchange constants that have been investigated numerically.

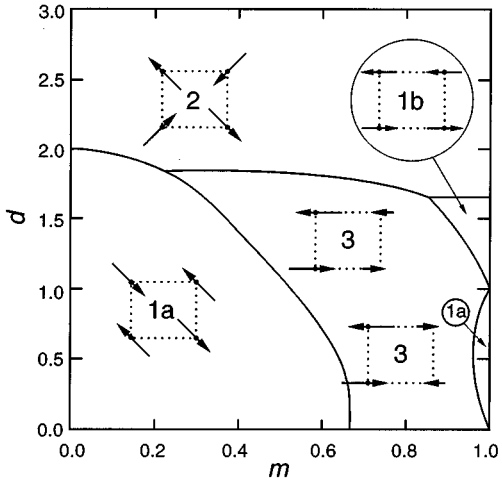

FIG. 116. Phase diagram for easy-plane type-I fcc antiferromagnets in a magnetic field oriented along the [001] crystalline direction. Horizontal axis is the magnetization $m=B/B_c$, and the vertical axis is $d=3D_1/(D_1-J_1)$, where D_1 and J_1 are the nearest-neighbor dipolar and exchange interactions, respectively. The various spin configurations have been illustrated by projection diagrams with labels indicating the number of **k**-vectors in the structure. From Heinilä and Oja (1993a).

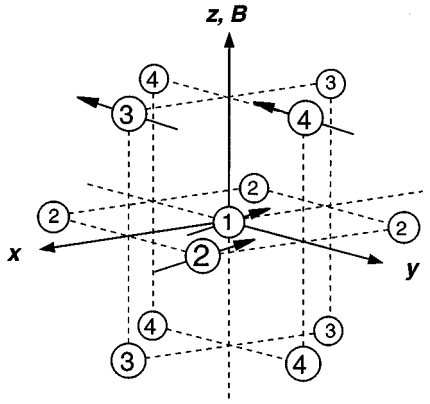

FIG. 117. Enumeration of the four sublattices in type-I fcc antiferromagnets. Spins $\langle \mathbf{I}_i \rangle$ at sites i with the same label are equal. The spin vectors illustrate a single-**k** structure.

a. B‖[001]

The phase diagram resulting from the quantum-mechanical perturbation calculation by Heinilä and Oja (1993a) is shown in Fig. 116. The coordinates in the figure are the magnetization $m=B/B_c$ and the parameter $d=3D_1/(D_1-J_1)$ expressing the strength of the nearest-neighbor dipolar interaction $D_1=(\mu_0/4\pi)\hbar^2\gamma^2 r^{-3}$ over the exchange force J_1. All possible type-I spin structures with easy-plane anisotropy [see Eqs. (112) and (113)] were included in the calculation. The diagram contains four different phases. They are labeled according to the number of nonzero $\mathbf{d}_j$ vectors. The single-**k** and double-**k** phases **1a**, **1b**, and **2** are described by spin projections on a plane perpendicular to **B**. The effect of the magnetic field is only to alter the length of every spin projection in the same way. For a triple-**k** structure, however, the projection diagram can depend on B. The descriptions of the triple-**k** states **3** in Fig. 116 are, therefore, only schematic.

The spin configurations were obtained from Eq. (111) where the vectors $\mathbf{d}_j$ have the following expressions:

$$\textbf{1a}: \quad \mathbf{d}_3=\frac{p_{\mathrm{AF}}}{\sqrt{2}}(\mathbf{e}_x+\mathbf{e}_y), \tag{135a}$$

$$\textbf{1b}: \quad \mathbf{d}_1=p_{\mathrm{AF}}\mathbf{e}_y . \tag{135b}$$

$$\textbf{2}: \quad \begin{cases} \mathbf{d}_1=(p_{\mathrm{AF}}/\sqrt{2})\mathbf{e}_y , \\ \mathbf{d}_2=(p_{\mathrm{AF}}/\sqrt{2})\mathbf{e}_x . \end{cases} \tag{135c}$$

$$\textbf{3}: \quad \begin{cases} \mathbf{d}_1=p_{\mathrm{AF}}\sin\theta\,\cos\phi\,\mathbf{e}_y , \\ \mathbf{d}_2=p_{\mathrm{AF}}\sin\theta\sin\,\phi\,\mathbf{e}_z , \\ \mathbf{d}_3=p_{\mathrm{AF}}\cos\theta\,\mathbf{e}_y . \end{cases} \quad \tan\phi=-\frac{p_{\mathrm{AF}}}{m}\cos\theta, \tag{135d}$$

Here $p_{\mathrm{AF}}=\sqrt{1-m^2}$.

Along the lines $d=0$, $d=1$, and $m=1/2$ the triple-**k** state **3** takes a particularly symmetric form,

$$\begin{cases} \mathbf{d}_1=\mathbf{d}_3=[m(1-m)]^{1/2}\mathbf{e}_y , \\ \mathbf{d}_2=(m-1)\mathbf{e}_z . \end{cases} \tag{136}$$

The spins in the four sublattices are [see Eq. (111)]

$$\begin{cases} \mathbf{I}_1/I=2[m(1-m)]^{1/2}\mathbf{e}_y+(2m-1)\mathbf{e}_z , \\ \mathbf{I}_2/I=\mathbf{e}_z , \\ \mathbf{I}_3/I=-2[m(1-m)]^{1/2}\mathbf{e}_y+(2m-1)\mathbf{e}_z , \\ \mathbf{I}_4=\mathbf{I}_2 , \end{cases} \tag{137}$$

where the subscripts 1–4 refer to Fig. 117. Spins in two of the sublattices are parallel to the field, whereas spins in the other two tilt towards the field when **B** is increased. This structure is the intermediate-field triple-**k** state found earlier by Lindgård (1988a).[19] One should note, however, that far from the lines $d=0$, $d=1$, and $m=1/2$ phase **3** differs considerably from this symmetric form. Moreover, a separate analysis must be performed in the limit $d=0$, as will be discussed in the context of Fig. 119.

The results in Fig. 116 are in fairly good agreement with the earlier spin-wave calculation of Viertiö and Oja (1987), except for structure **3**, which was not investigated in their work. In comparison with the earlier perturbation calculation of Lindgård (1988a) there is good overall agreement for $m<0.8$ except for the fact that the triple-**k** structure does not generally have the symmetric form of Eq. (137), as he found. In high fields, $m>0.8$, there are considerable differences. This field region is particularly important because of the possibility of making comparisons with neutron-diffraction data on copper.

Frisken and Miller (1988a) have performed Monte Carlo simulations to investigate the magnetic phase dia-

[19]Lindgård used the symbol $\overset{\downarrow\uparrow}{oo}$ for the structure.

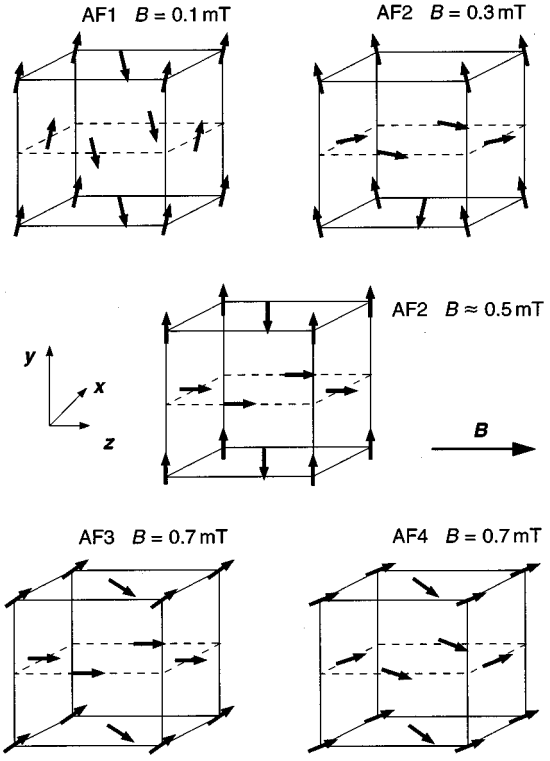

FIG. 118. Predicted spin order for copper in different applied magnetic fields as given by the Monte Carlo simulations of Frisken and Miller (1988a). In all cases the ordering is confined to the yz plane.

gram of copper. A special effort was made to obtain as reliable results as possible. The long-range dipolar and exchange interactions were included up to eighth-nearest neighbors, thereby considering 140 spins. The indirect exchange interaction was obtained from their previous electronic band-structure calculation (Frisken and Miller, 1986). These authors found the ordered spin configurations as a function of B, applied along the [001] crystalline axis. Their results are shown in Fig. 118. There are four separate spin configurations, denoted by AF1–AF4. The low- and high-field phases are two-sublattice structures, whereas AF2 and AF3 are four-sublattice states. The division of the total antiferromagnetic order into transverse and longitudinal components seemed compatible with spin arrangements deduced from static susceptibility measurements of a copper single crystal (Huiku *et al.*, 1986). Later neutron-diffraction experiments showed, however, that in low and intermediate fields copper nuclei display $(0\ \frac{2}{3}\ \frac{2}{3})$ order as well.

Nevertheless, it is interesting to compare the results of Frisken and Miller (1988a) with the calculations by Heinilä and Oja (1993a) for the type-I structure. The ordering vector in the single-**k** configurations AF1 and AF4 of Frisken and Miller is along the field, as it is for state **1a** of Eq. (135a). AF2 falls in the general class of triple-**k** states [see Eq. (135d)], while AF3 refers to the symmetric triple-**k** spin configuration of Eq. (136). Since the nearest-neighbor interaction assumed by Frisken and Miller corresponds to $d=1.59$, the perturbation calculation would yield, according to Fig. 116, the evolution scheme **1a**→**3**→**1b** with increasing field. Thus the high-field structure and the detailed form of the triple-**k** state are different.

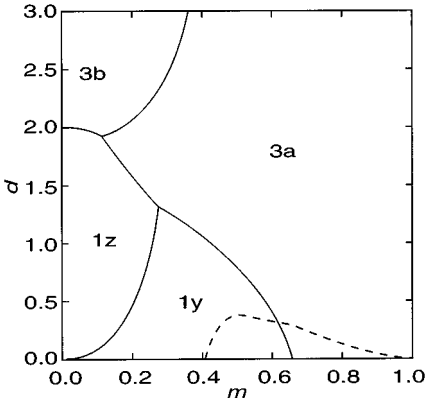

FIG. 119. Phase diagram for easy-plane type-I fcc antiferromagnets, when the magnetic field is in the [110] direction, as a function of $m=B/B_c$ and $d=3D_1/(D_1-J_1)$. Below the broken line quantum effects tend to stabilize the triple-**k** structure of Figs. 113(b)–113(d) in an $I=\frac{1}{2}$ system. From Heinilä and Oja (1993a).

Viertiö and Oja (1989) have also made Monte Carlo simulations of nuclear ordering in copper. Dipolar interactions with nearest and next-nearest neighbors were included in addition to exchange interactions with $J_1/k_B=-12.5$ nK and $J_2/k_B=5.6$ nK. Three structures were obtained with increasing field, applied along the [001] crystalline axis, namely, **1b**, **2**, and **1b**. Since the nearest-neighbor interaction used in these simulations corresponds to $d=2.01$, there is again some but not complete agreement with the perturbation calculation of Fig. 116. As the d parameter of copper is around 2, rather small changes in the interaction constants can affect the predicted ground-state selection.

Viertiö (1992) has made extensive Monte Carlo simulations of nuclear ordering in silver. For the [001] field alignment, she found a **1a** → **3** transition in intermediate fields, in agreement with Heinilä and Oja (1993a). In very small fields, $B\approx 0.1B_c$, Viertiö predicted that phase **1a** is unstable against another single-**k** state with the ordering vector perpendicular to **B**.

b. B‖[110]

Heinilä and Oja (1993a) have used the perturbation approach to study the ground state for the [110] field alignment. The resulting phase diagram is shown in Fig. 119.

It was found that the stable triple-**k** structures in this field direction have the general form

$$\textbf{3b}:\quad \begin{cases} \mathbf{m}=m(\mathbf{e}_x+\mathbf{e}_y)/\sqrt{2}, \\ \mathbf{d}_1=d_{1z}\mathbf{e}_z, \\ \mathbf{d}_2=d_{2z}\mathbf{e}_z, \\ \mathbf{d}_3=d_{3x}\mathbf{e}_x+d_{3y}\mathbf{e}_y, \end{cases} \tag{138}$$

where $m=B/B_c$. A special case is the more symmetric configuration

$$\textbf{3a}: \quad \begin{cases} d_{1z}=d_{2z}=[m(1-m)]^{1/2}, \\ d_{3x}=d_{3y}=(m-1)/\sqrt{2} \end{cases} \tag{139}$$

predicted previously by a spin-wave calculation (Viertiö and Oja, 1987).

Structure **3a** is similar to the symmetric form of configuration **3** [see Eq. (137)] found for $\mathbf{B}\|[001]$: it is a four-sublattice triple-**k** state in which spins in the two sublattices are parallel to the field for all $B<B_c$, viz.,

$$\textbf{3a}: \quad \begin{cases} \mathbf{I}_1/I=(2m-1)(\mathbf{e}_x+\mathbf{e}_y)/\sqrt{2}+2[m(1-m)]^{1/2}\mathbf{e}_z, \\ \mathbf{I}_2/I=(2m-1)(\mathbf{e}_x+\mathbf{e}_y)/\sqrt{2}-2[m(1-m)]^{1/2}\mathbf{e}_z, \\ \mathbf{I}_3/I=(1/\sqrt{2})(\mathbf{e}_x+\mathbf{e}_y), \\ \mathbf{I}_4=\mathbf{I}_3. \end{cases} \tag{140}$$

The sublattices 1–4 are defined in Fig. 117. In particular, configurations **3a** and **3** [see Eq. (136)] are identical in the isotropic limit $d=0$, as they should be, because the coupling between the spin directions and the crystalline axes then vanishes. Structure **3a** is illustrated in Fig. 3(d). Note, however, that the field in the figure is in the [011] rather than the [110] direction.

When $B=0$, configuration **3b** reduces to structure **2** [see Eq. (135c)]. The transition in a low intermediate field between **3b** and **3a** is discontinuous.

Finally, in the lower left corner of Fig. 119 the single-**k** structures **1z** and **1y** are stable. For these configurations the nonzero vectors $\mathbf{d}_j$ are given by

$$\textbf{1z}: \quad \mathbf{d}_3=(p_{\mathrm{AF}}/\sqrt{2})(\mathbf{e}_x-\mathbf{e}_y), \tag{141a}$$

$$\textbf{1y}: \quad \mathbf{d}_2=p_{\mathrm{AF}}\mathbf{e}_z, \tag{141b}$$

where $p_{\mathrm{AF}}=\sqrt{1-m^2}$. In zero field **1z** is identical with **1a** [see Eq. (135a)] and **1y** is the same as **1b**.

The results of Fig. 119 are in fairly good agreement with the spin-wave calculation by Viertiö and Oja (1987, 1989), but there is a clear disagreement with the earlier perturbation calculation of Lindgård (1988b, 1990).

In the $d\to 0$ limit the results for the anisotropic model should be identical with those found in the isotropic case. The reason (Heinilä and Oja, 1993a) why this is not so in the diagrams of Figs. 116 and 119 is that the limit $d\to 0$ is artificial in the sense that the conditions of Eq. (112) caused by the anisotropy of the interactions are still required. As a result, part of the triple-**k** structures are excluded from the analysis although single-**k** and double-**k** states are essentially included. For example, the triple-**k** phase of the isotropic model at $m=\frac{1}{2}$ [see Fig. 113(c)] violates the constraints $\mathbf{d}_j\cdot\mathbf{k}_j=0$ of an easy-plane system for all field alignments and therefore cannot be stable in the presence of an appreciable dipolar anisotropy.

When the anisotropy is weak the ground state obtained for the fully isotropic interaction is approximately correct, and spin configurations of the isotropic model reach into the (m,d) phase diagram of the anisotropic model for small d (Heinilä and Oja, 1993a). Exactly how far they extend depends on the relative magnitude of quantum-mechanical fluctuations, which favor the triple-**k** phase of the isotropic model, and on the dipolar anisotropy energy, which is a classical quantity. The phase boundary in the (m,d) plane depends, therefore, on the spin I.

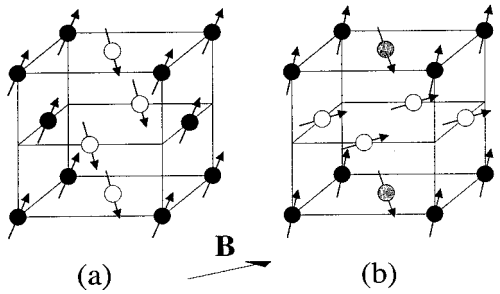

FIG. 120. Equilibrium spin configurations of silver in a magnetic field oriented along the [110] crystalline direction as given by Monte Carlo simulations at $T=0.17$ nK. In low fields, $B<0.4B_c$ a single-**k** state (**1y**) is predicted; in high fields, $B>0.4B_c$, a triple-**k** state (**3a**) is suggested. The arrows indicate the directions of nuclear magnetic moments $-\gamma h\mathbf{I}_i$. From Viertiö, 1990.

According to estimates by Heinilä and Oja (1993a), in the region below the broken line in Fig. 119, quantum fluctuations stabilize the triple-**k** state of Figs. 113(b)–113(d). The region collapses towards the line $d=0$ in the (m,d) diagram with increasing I. For a given m, the quantity d along the phase boundary of this region is approximately proportional to I^{-1}. The boundary of the quantum-fluctuation-stabilized phase depends only weakly on the field direction. It has been left out of Fig. 116 for clarity.

Viertiö (1990) has performed Monte Carlo calculations to investigate nuclear magnetic ordering in silver. As in the simulations of Frisken and Miller (1988a), dipolar and RK interactions were included up to the eighth neighboring shell. The exchange constants were taken from the band-structure calculations of Harmon *et al.* (1992). To distinguish the equilibrium structure from metastable states, Gibbs free energies were calculated for stable and metastable states found in the simulations. This procedure permitted Viertiö (1990) to conclude that the equilibrium configurations are those shown in Fig. 120. In low fields, $B<0.4B_c$, she observed that thermal fluctuations stabilize structure **1y** of Eq. (141b). In high fields, $B>0.4B_c$, phase **3a** corresponding to Eq. (139) was obtained. These results were in good agreement with earlier, less extensive Monte Carlo simulations by Viertiö and Oja (1989).

The Monte Carlo results can be compared with the perturbation calculation illustrated in Fig. 119 by noting that the nearest-neighbor interaction assumed by Viertiö (1990) corresponds to $d=0.75$. There is a discrepancy in low fields since the perturbation calculation predicts a **1z** configuration rather than **1y**. In higher fields the results are in qualitative agreement with each other. Using the perturbation approach to thermal fluctuations,

one finds a similar discrepancy with Monte Carlo results even when the same long-range interactions are employed (Heinilä and Oja, 1994a). One can, therefore, conclude that, at least when thermal fluctuations are considered, the **1z** configuration in low fields is an artifact caused by inadequacies of the perturbation approach. One may expect that the same holds for quantum fluctuations, too, since a spin-wave calculation for silver at $T=0$ (Viertiö and Oja, 1989) agrees well with the Monte Carlo results. In spite of these and possibly some other shortcomings, the perturbation approach remains useful, since it quite effectively provides the correct overall picture.

c. B‖[111]

Fluctuation effects on antiferromagnetic structures with only type-I order have not been investigated as extensively for the [111] field alignment as for the [001] and [110] directions. The reason is that the latter two high-symmetry alignments were first studied in measurements using copper single crystals (Huiku *et al.*, 1986; Jyrkkiö, Huiku, Lounasmaa *et al.*, 1988). When experiments were extended to the [111] direction (Annila *et al.*, 1992), it was found that in the high-field region there was no type-I order while in low and intermediate fields the $(0\ \frac{2}{3}\ \frac{2}{3})$ modulation was present. These results made it clear that a study of fluctuation effects in type-I structures alone would not be sufficient to determine the magnetic-spin configuration in this field direction. At the same time, however, such a study might be useful in revealing why type-I order is unstable only in this field direction. Therefore it is unfortunate that the [111] field alignment has not been investigated in as much detail as the two other high-symmetry directions.

Ground-state selection in the [111] direction for copper and silver has been studied by spin-wave calculations (Viertiö and Oja, 1987, 1989) and by Monte Carlo simulations (Viertiö and Oja, 1989; Viertiö, 1992). In copper the dipolar anisotropy is strong, whereas silver is clearly exchange dominated. The simulations predicted for copper a complicated field evolution: single-**k** $\rightarrow$ triple-**k** (P^{β}_{xy}) $\rightarrow$ single-**k** $\rightarrow$ triple-**k** (P^{γ}_{xy}) $\rightarrow$ single-**k**, while the spin-wave calculation yielded a simpler scheme: triple-**k** (P^{β}_{xy}) $\rightarrow$ triple-**k** (P^{γ}_{xy}). Here P^{β}_{xy} and P^{γ}_{xy} refer to the detailed form of the triple-**k** configuration, as defined in the paper by Viertiö and Oja (1987).

In the case of silver, a single-**k** $\rightarrow$ triple-**k** transition was suggested by Monte Carlo simulations (Viertiö and Oja, 1989), as one would expect on the basis of the completely isotropic model. The predicted triple-**k** state has no special symmetry. In particular, it is not a configuration in which there are two sublattices oriented exactly along the field, as in the structure of Fig. 120 in high fields at $T>0$. Such a spin arrangement could not exist in the [111] field direction owing to dipolar anisotropy. In the spin-wave calculations of Viertiö and Oja (1987, 1989), the ansatz of especially symmetric triple-**k** states has the adverse effect that single-**k** structures occupy too large a portion in the spin-wave-determined phase diagrams when **B**‖[111].

8. Comparison with experiments

One can compare the properties of the predicted spin structures with neutron-diffraction measurements on copper in the high-field region when **B** is along the [001] or the [110] crystalline axes. According to experimental data (Annila *et al.*, 1992) for the [001] field alignment, the (1 0 0) intensity is strong when the field is perpendicular to the respective ordering vector [see Fig. 55(b)] but almost zero when the field is parallel to it [see Fig. 55(a)]. This behavior can be understood, at least qualitatively, if the stable structure in high fields is either **2** or **1b**. For structure **2** [see Eq. (135c)], the reflections perpendicular to **B**‖[001] are

$$F^2(1,0,0)=F^2(0,1,0)\propto\tfrac{1}{2}(|\mathbf{d}_1|^2+|\mathbf{d}_2|^2)=\tfrac{1}{2}(1-B^2/B_c^2), \tag{142a}$$

while the parallel reflection is

$$F^2(0,0,1)\propto|\mathbf{d}_3|^2=0. \tag{142b}$$

Exactly the same results are obtained for structure **1b** when a domain average is taken over the two equivalent staggered magnetization directions x and y in Eq. 135(b). The neutron-diffraction data are, therefore, in agreement with the spin-wave calculations and Monte Carlo simulations of Viertiö and Oja (1987, 1989) and with the perturbation-theory results of Heinilä and Oja (1993a) ($d\approx 2$ for Cu) but not with the Monte Carlo results of Frisken and Miller (1988a)[20] nor with the previous perturbation calculations of Lindgård (1988a).[21]

Neutron-diffraction results for the [110] field directions, illustrated in Fig. 57, are not so clear cut as those for the [001] directions. The (1 0 0) intensity is observed in high fields for both symmetrically inequivalent field alignments. The data show, however, that the (1 0 0) Bragg peak increases more steeply for **B**‖[1 01] [see Fig. 57(c)] than for **B**‖[011] [Figs. 57(a,b)]. One should be cautioned that the absolute intensities were not reproducible, as is shown by the different, although in principle equivalent, (1 0 0) Bragg intensities in Figs. 57(a) and 57(b). Apart from this problem the observed behavior is at least in qualitative agreement with the high-field configuration's being the triple-**k** structure **3a**, as was predicted by the spin-wave calculations and Monte Carlo simulations of Viertiö and Oja (1987, 1989) and by perturbation-theory results of Heinilä and Oja (1993a). According to Eq. (139), the (1 0 0) and (0 1 0) neutron-diffraction intensities of **3a** are

$$F^2(1,0,0)=F^2(0,1,0)\propto\tfrac{1}{2}(|\mathbf{d}_1|^2+|\mathbf{d}_2|^2)$$
$$=(B/B_c)(1-B/B_c), \tag{143a}$$

when **B**‖[110], and for the Bragg peak at (0 0 1) the intensity is

$$F^2(0,0,1)\propto|\mathbf{d}_3|^2=(1-B/B_c)^2. \tag{143b}$$

[20]Their phase AF4 shows behavior exactly opposite to that actually observed.

[21]His high-field triple-**k** structure would show both perpendicular and longitudinal reflections.

The (0 0 1) reflection should therefore be much weaker than the (1 0 0) and (0 1 0) Bragg peaks in fields slightly below B_c, and its intensity should also increase more slowly with decreasing B. The neutron-diffraction measurements are in disagreement with the perturbation calculations of Lindgård (1988b).[22]

In zero field, the three different type-I modulations should all have the same intensity. It is, however, obvious from Fig. 56 that the direction of **B** during demagnetization affects the domain distribution and therefore makes comparisons with theoretical calculations difficult.

Theoretical phase diagrams for nuclear spins in silver have been compared with experimental results in Sec. IX.C.

E. NMR response of type-I structures

The theory of the NMR response of easy-plane, type-I fcc structures is important for an understanding of nuclear ordering in copper and silver, and possibly in rhodium as well. The subject has been investigated theoretically by Kumar, Kurkijärvi, and Oja (1986) and by Heinilä and Oja (1995, 1996). Their work is based on the vast number of papers on antiferromagnetic resonance in electronic magnets that have been reviewed extensively by Foner (1963), Keffer (1966), and Akhiezer *et al.* (1968). However, there are several complications that hamper direct application of this early work to the present case. Most of the NMR data on copper and silver were measured in zero external field and hence the absorption curves are broad. As the crystal structure is cubic in these metals, there is no single-spin anisotropy in the Hamiltonian, and the positions of the NMR lines are determined by spin-spin interactions and, within the ordered state, by the spin structure. The situation is different in most electronic systems in which antiferromagnetic resonance has been investigated: anisotropy caused by noncubic crystal symmetry and/or magnetoelastic effects is important. In addition, in Cu and Ag one has to deal with the inherent frustration of the fcc lattice.

1. Equations of motion

In the mean-field theory, the spin dynamics is described by

$$\frac{d\langle \mathbf{I}_i \rangle}{dt} = \gamma \langle \mathbf{I}_i \rangle \times \mathbf{B}_i , \tag{144}$$

where $\mathbf{B}_i$ is the local field defined by Eq. (75). The equations of motion for the amplitudes of the type-I modulations $\mathbf{d}_j$ ($j=1,2,3$) and for the magnetization **m** [see Eq. (111)] can be found by Fourier transforming Eq. (144). This yields

$$\frac{1}{\gamma}\frac{d\mathbf{m}}{dt} = \mathbf{m}\times\mathbf{B} - B_{\mathrm{D}} \sum_{j=1,2,3} (\mathbf{d}_j \times \hat{\mathbf{e}}_j)(\hat{\mathbf{e}}_j \cdot \mathbf{d}_j) \tag{145}$$

and

$$\frac{1}{\gamma}\frac{d\mathbf{d}_j}{dt} = \mathbf{d}_j \times (\mathbf{B} - B_c \mathbf{m}) - B_{\mathrm{D}}(\mathbf{m}\times\hat{\mathbf{e}}_j)(\hat{\mathbf{e}}_j\cdot\mathbf{d}_j) - B_{\mathrm{D}}(\mathbf{d}_k\times\hat{\mathbf{e}}_l)(\hat{\mathbf{e}}_l\cdot\mathbf{d}_l) - B_{\mathrm{D}}(\mathbf{d}_l\times\hat{\mathbf{e}}_k)(\hat{\mathbf{e}}_k\cdot\mathbf{d}_k). \tag{146}$$

Indices (j,k,l) in Eq. (146) denote either (1,2,3), (2,3,1), or (3,1,2). The coefficient B_{D} is the anisotropy field for type-I order, defined by Eq. (120). When the dipole-dipole force is the only anisotropic contribution to spin-spin interactions, the tabulated (Cohen and Keffer, 1955) lattice sums yield for an fcc lattice $B_{\mathrm{D}} \approx (\mu_0/4\pi)\rho\gamma I\hbar \times 6.501$.

The anisotropy field B_{D} changes the NMR response in a profound way: the resonance peaks are shifted away from the Larmor frequency. Isotropic spin-spin interactions alone, in a system with only one spin species, cannot cause any shifts from the Larmor position. The nonzero value of B_{D} results from anisotropic spin-spin interactions like the dipolar force or an anisotropic exchange interaction.

An important characteristic of copper and silver is that $B_{\mathrm{D}}>0$. In other words, the anisotropy is such that the antiferromagnetic amplitudes $\mathbf{d}_j$ are confined, in equilibrium, into planes perpendicular to the respective ordering vectors $\mathbf{k}_j$, as is expressed by Eq. (112).

The similarity between these equations of motion and those describing the dynamics of solid ^{3}He and superfluid ^{3}He-A has been discussed by Kumar *et al.* (1986) and by Heinilä and Oja (1996). If only one of the $\mathbf{d}_j$'s is nonzero, Eqs. (145) and (146) are almost identical with those proposed for solid ^{3}He (Cross and Fisher, 1985). The difference is that in ^{3}He it is generally possible to neglect the terms proportional to the dipole-dipole energy in Eq. (146) because they are small. This approximation is not needed, however, when the equations of motion are solved to first order in the excitation field, since these terms disappear anyway. Equations (145) and (146) also have much in common with the Leggett (1974) equations of superfluid ^{3}He-A if we identify his $\hat{\mathbf{l}}$ and **d** with our $\hat{\mathbf{e}}_1$ and $\mathbf{d}_1$. Spin dynamics of ^{3}He-A resembles, however, a uniaxial antiferromagnet with an easy axis along $\hat{\mathbf{l}}$ and therefore the corresponding $B_{\mathrm{D}}<0$.

2. Resonances

The linear response can be calculated by considering small deviations from the equilibrium configuration. We assume that a field $\mathbf{B}(t)=\mathbf{B}_0+\mathbf{B}_1(t)$ is applied to the system and expand the spin vectors in leading orders of B_1: $\mathbf{m}(t)=\mathbf{m}^{(0)}+\mathbf{m}^{(1)}(t)+O(B_1^2)$ and similarly for $\mathbf{d}_j(t)$. Our aim is to solve for the quantity $\mathbf{m}^{(1)}(t)$, which is of first order in $\mathbf{B}_1(t)$. One obtains from Eq. (146)

$$\frac{1}{\gamma}\frac{d}{dt}(\hat{\mathbf{e}}_j\cdot\mathbf{d}_j) = (\hat{\mathbf{e}}_j\times\mathbf{d}_j^{(0)})\cdot(\mathbf{B}_1 - B_c\mathbf{m}^{(1)}) + O(B_1^2). \tag{147}$$

Combination of this result with Eq. (145) yields

[22] His high-field single-**k** structure would not give rise to the (1 0 0) reflection at all when $\mathbf{B}\|[011]$.

$$\frac{1}{\gamma}\frac{d^2\mathbf{m}^{(1)}}{dt^2}=\mathbf{m}^{(0)}\times\frac{d\mathbf{B}_1}{dt}-\mathbf{B}_0\times\frac{d\mathbf{m}^{(1)}}{dt}-\gamma B_{\mathrm{D}} \times\sum_{j=1,2,3}(\mathbf{d}_j^{(0)}\times\hat{\mathbf{e}}_j)(\hat{\mathbf{e}}_j\times\mathbf{d}_j^{(0)})\cdot(\mathbf{B}_1-B_{\mathrm{c}}\mathbf{m}^{(1)}). \tag{148}$$

Introducing the Fourier transformation $f(\omega)=(2\pi)^{-1}\int_{-\infty}^{\infty}f(t)\exp(i\omega t)dt$ and noting that $\mathbf{M}_1(\omega)=\rho\gamma I\hbar\mathbf{m}^{(1)}(\omega)$ and $M_1^{\mu}(\omega)=\Sigma_{\nu}\chi^{\mu\nu}(\omega)B_1^{\nu}(\omega)/\mu_0$ one finds, if $\omega\neq 0$ (Heinilä and Oja, 1996),

$$\underline{\chi}_{\mathrm{H}}(\omega)/\chi_0=[\underline{\Upsilon}(\omega)-\underline{I}\omega^2/\gamma B_{\mathrm{c}}]^{-1}\underline{\Upsilon}(\omega), \tag{149}$$

where

$$\underline{\Upsilon}(\omega)=\gamma B_{\mathrm{D}}\sum_{j=1,2,3}(\hat{\mathbf{e}}_j\times\mathbf{d}_j^{(0)})(\hat{\mathbf{e}}_j\times\mathbf{d}_j^{(0)}) -i\omega\sum_{j=1,2,3}(\mathbf{m}^{(0)}\times\hat{\mathbf{e}}_j)\hat{\mathbf{e}}_j. \tag{150}$$

The subscript H of $\underline{\chi}_{\mathrm{H}}(\omega)$ in Eq. (149) emphasizes that the above calculation gives only the nondissipative part of $\underline{\chi}(\omega)$, since the right-hand side of Eq. (149) makes up a Hermitian matrix. The dissipative part is absent because there is no relaxation mechanism in the equations of motion.

Exactly at the resonant frequencies we must add the missing dissipation. The full dynamic susceptibility can be written as

$$\underline{\chi}(\omega)/\chi_0=\frac{1}{2}\sum_{\alpha}\frac{\underline{\Lambda}_{\alpha}}{1-\omega/(\Omega_{\alpha}-i\Gamma_{\alpha})} +\frac{1}{2}\sum_{\alpha}\frac{\underline{\Lambda}_{\alpha}^{*}}{1+\omega/(\Omega_{\alpha}+i\Gamma_{\alpha})}+\frac{\underline{\Lambda}_0}{1-i\omega/\Gamma_0}, \tag{151}$$

where Ω_{α} are resonant frequencies and the Hermitian matrices Λ_{α} are resonant amplitudes. In Eq. (149), $\underline{\chi}_{\mathrm{H}}(\omega)$ is the Hermitian part of the expression in the limit $\Gamma_{\alpha}\to+0$ when $\omega\neq 0$.

The third term in Eq. (151) describes absorption at zero frequency. Its physical meaning can be illustrated by considering the response to a small steplike change in the external field. When the zero-frequency resonance has, for example, the Lorentzian form, the system reacts via a process in which the magnetization relaxes exponentially towards a new equilibrium value, and the relaxation time is essentially the inverse of the linewidth at the $\omega=0$ resonance. The processes that contribute to zero-frequency absorption are those that involve a change in the spin-spin interaction energy but no change in the Zeeman energy. For NMR measurements of the $\omega=0$ resonance, see Anderson (1962).

With zero-frequency resonance, and in general with low-field experiments, one should look for resonances in $\underline{\chi}(\omega)/\omega$ rather than in $\underline{\chi}(\omega)$. The quantity $\chi''(\omega)/\omega$, where $\chi''(\omega)$ is the imaginary part of a diagonal component of $\underline{\chi}(\omega)$, is often called the form function. For example, in the paramagnetic state in zero field, $\chi''(\omega)/\omega$ peaks at $\omega=0$ if the temperature is well above T_c. This peak can be called the zero-frequency resonance.

Kramers-Kronig relations provide an equation between resonant amplitudes $\underline{\Lambda}_{\alpha}$ and the static susceptibility,

$$\underline{\chi}(0)/\chi_0=\sum_{\alpha}\mathrm{Re}\{\underline{\Lambda}_{\alpha}\}, \tag{152}$$

where $\chi_0=\mu_0\rho\gamma I\hbar/B_c$ [see Eq. (116)]. Equation (152) decomposes the static susceptibility matrix into contributions of various resonances Ω_{α}, making it possible to calculate the amplitude of the zero-frequency absorption once the amplitudes of other resonances, as well as $\underline{\chi}(0)$, are known. Static susceptibility matrices of several type-I structures were discussed in Sec. XV.D.2.

As an important example, we consider a single-**k** structure when the external field is not along the ordering vector. The equation of the configuration is given by Eq. (122). It turns out that $\underline{\chi}(\omega)$ can be expressed using the angle θ between $\mathbf{B}_0$ and $\mathbf{k}$ as the only parameter. One obtains two resonant frequencies Ω_+ and Ω_- given by

$$\Omega_{\pm}^2=\tfrac{1}{2}\{\omega_0^2+\gamma^2B_0^2\pm\sqrt{(\omega_0^2-\gamma^2B_0^2)^2+4\gamma^2B_0^2\omega_0^2\cos^2\theta}\}, \tag{153}$$

where $\omega_0^2=(B_{\mathrm{D}}/B_{\mathrm{c}})\gamma^2(p^2B_{\mathrm{c}}^2-B_0^2)$. This result was found for antiferromagnetically ordered solid ^{3}He by Osheroff *et al.* (1980) and later for metallic fcc nuclear magnets (Kumar *et al.*, 1986). A practical difference is that ω_0 has a strong field dependence in nuclear magnets but can be taken as a constant in solid ^{3}He.

The amplitudes of the two resonances of Eq. (153) were calculated by Heinilä and Oja (1996). These authors also showed that the two amplitudes satisfy $\Sigma_{\alpha}\mathrm{Re}\{\underline{\Lambda}_{\alpha}\}=\underline{I}$. As the static susceptibility of the single-**k** state of Eq. (122) is simply $\underline{\chi}(0)=\chi_0\underline{I}$ (see Sec. XV.D.2), the spectral sum rule of Eq. (152) does not leave any room for zero-frequency absorption. The situation is different, however, for a single-**k** structure at $B=0$ or for a single-**k** state in a field when $\mathbf{B}_0\|\mathbf{k}$ [see Eq. (117)]. Zero-frequency absorption is predicted.

As an application, one can study how well the resonance frequencies of a single-**k** state can explain the positions of the antiferromagnetic NMR peaks that were observed by Hakonen and co-workers (Hakonen and Yin, 1991; Hakonen, Yin, and Nummila, 1991). Such a comparison has been made by Heinilä and Oja (1996). To account for the fact that a polycrystalline sample was used in the NMR measurements, it was assumed that, among the three possibilities, the single-**k** structure for which the ordering vector maximizes $(\mathbf{k}_j\cdot\mathbf{B}_0)^2$ is stabilized in each field alignment. The assumption is supported by the neutron-diffraction data of Tuoriniemi, Nummila, *et al.* (1995) as well as by most of the theoretical predictions (Viertiö and Oja, 1989; Viertiö, 1990, 1992; Heinilä and Oja, 1993a, 1996). According to Eq. (153), the antiferromagnetic resonances form two bands, $|\omega|\leq\min\{\gamma B_0,\omega_0\}$ and $\max\{\gamma B_0,\omega_0\}\leq|\omega|\leq\sqrt{\gamma^2B_0^2+\omega_0^2}$,

when the direction of $\mathbf{B}_0$ is varied with respect to the crystalline axes. Their calculated average frequencies have been plotted in Fig. 71 assuming a sublattice polarization $p=0.7$. There is rather good agreement. It seems, therefore, that the observed resonances can be interpreted in terms of a single magnetically ordered phase with a single-**k** structure. The same conclusion was reached by Hakonen and co-workers.

3. Simulation of spin dynamics

Heinilä and Oja (1995, 1996) have recently presented a numerical calculation of the full NMR absorption curve of a classical spin system. Their technique applies equally well to ordered and disordered systems. The method is similar to the procedures employed in the calculation of the dynamic structure factor (Wysin and Bishop, 1990; Chen and Landau, 1994). Since the method is, in principle, accurate for classical spins, it can be used to assess the validity of the mean-field equation-of-motion analysis.

NMR response can be obtained from the autocorrelation matrix

$$\underline{C}(t)=\frac{1}{N}\langle[\mathbf{M}(t_0+t)-\langle\mathbf{M}\rangle][\mathbf{M}(t_0)-\langle\mathbf{M}\rangle]\rangle, \tag{154}$$

where $\mathbf{M}=\Sigma_i\mathbf{I}_i/I$ is the total spin. According to the linear-response theory (Kubo and Tomita, 1954), $\underline{C}(t)$ is related to the dynamic susceptibility through

$$\underline{\chi}(\omega)=\frac{1}{k_B T}[\underline{C}(t=0)+i\omega\underline{C}(\omega)], \tag{155}$$

where

$$\underline{C}(\omega)=\int_0^\infty \underline{C}(t)e^{i\omega t}dt. \tag{156}$$

The NMR response can be calculated numerically by using Monte Carlo simulations to produce a set of spin states. The time dependence of $\underline{C}(t)$ is then obtained by solving the equations of motion [Eq. (144)]. For more details, see the papers by Heinilä and Oja (1995, 1996).

As an example, the NMR response of a system with $N=12^3$ spins, modeling copper nuclei, was investigated. The simulations revealed a first-order transition to a type-I antiferromagnet at $T=T_N^{MC}$. The spin structure was a single-**k** state with spins along a crystalline axis, illustrated on the right-hand side of Fig. 4. The calculated NMR absorption curves are presented in Fig. 121. The results show the presence of two antiferromagnetic resonance peaks below T_N^{MC}.

The mean-field analysis presented in Sec. XV.E.2 predicts only a single antiferromagnetic resonance at a finite frequency for this single-**k** state. The peak can be identified with the high-f absorption signal, and it is similar to conventional antiferromagnetic resonance. The peak at a low but finite f can be understood as an artificial zero-frequency resonance of the mean-field calculation. The failure of the theory is caused by a hidden symmetry in the mean-field Hamiltonian [Eq. (74)],

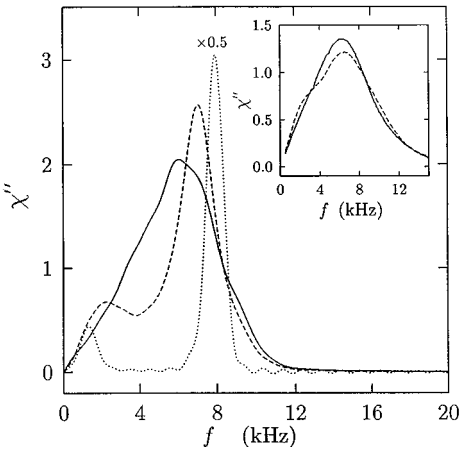

FIG. 121. Theoretically calculated zero-field NMR absorption $\chi''_{xx}(f)$ in the paramagnetic phase at $T=1.14T_N^{MC}$ (solid line), and in the antiferromagnetic state at $T=0.86T_N^{MC}$ (dashed line). Data for $T=0.09T_N^{MC}$ (dotted line) have been divided by 2, and the peaks on this curve are nearly δ functions for the frequency resolution used in the computations. These results are averages over different orientations of the crystal axes, namely, $\chi''_{xx}(f)=\mathrm{Tr}\{\mathrm{Im}\{\chi(f)\}\}/3$. The inset shows experimental spectra of Huiku *et al.* (1986). More data are presented in Fig. 32. All results are in SI units. From Heinilä and Oja (1995).

which results in a continuously degenerate manifold of type-I states, as was discussed in Sec. XV.D. This degeneracy is lifted by thermal fluctuations—the kind of "order-by-disorder" effect discussed by Villain *et al.* (1980)—and the single-**k** state with spins parallel to a crystalline axis is stabilized. In the dynamic susceptibility, the order-by-disorder phenomenon is seen as a shift of spectral intensity from $f=0$ to a finite frequency.[23] Therefore the anisotropy associated with the low-f peak is distinctly different from that of the upper peak.

As is implied by the theoretical curve at $T=0.09T_N^{MC}$ (dotted line in Fig. 121), the width of the simulated resonance peaks tends to zero as T approaches zero. In a real system, however, narrowing of the peaks at low temperatures is limited by quantum fluctuations.

The theoretical line shapes can be compared with the measured NMR data of Huiku *et al.* (1986) on Cu. The experimental spectra are shown in the inset of Fig. 121. The calculated paramagnetic line shape is in good agreement with experiments except for the too rapid falloff at high frequencies. The measured spectrum displays two resonances in the antiferromagnetic state, in agreement with the simulations. The difference between the antiferromagnetic and paramagnetic states is, however, much smaller in the experiment than in the simulation. This could result from the coexistence of antiferromagnetic and paramagnetic domains during the measure-

[23] An analogous phenomenon is the disappearance of a gap in the acoustic magnon dispersion relation at zero wave vector in the frustrated electronic magnet $Ca_3Fe_2Ge_3O_{12}$ (Gukasov *et al.*, 1988).

ment, since a suitable linear combination of the calculated paramagnetic and antiferromagnetic spectra closely reproduces the experimental line shape.

F. (0 $\frac{2}{3}$ $\frac{2}{3}$) order

Neutron-diffraction measurements of copper by Annila *et al.* (1990) revealed, for the first time ever, ordering associated with the $\mathbf{k}=(\pi/a)(0,\frac{2}{3},\frac{2}{3})$ modulation vector in an fcc system. Theoretical studies were crucial in this discovery. First-principles electronic band-structure calculations by Lindgård, Wang, and Harmon (1986) had shown that ordering vectors of the form $\mathbf{k}=(0,\eta,\eta)$ are almost degenerate in energy with type-I modulation vectors in copper. Moreover, Lindgard (1988a) had predicted[24] that this type of order would be stable in the intermediate-field region, exactly as was found in the experiments.

The knowledge of the ordering vector alone does not, however, yield the magnetic structure. The actual spin configurations with (0 $\frac{2}{3}$ $\frac{2}{3}$) order have been investigated in extensive mean-field calculations by Viertiö and Oja (1990a, 1990b, 1993). Their work has been remarkably successful in explaining and predicting the properties of spin structures with (0 $\frac{2}{3}$ $\frac{2}{3}$) order. Our discussion below mostly draws from their papers.

1. Principal features of the (0 $\frac{2}{3}$ $\frac{2}{3}$) spin configurations

Analysis of the so-called permanent spin configurations, which were introduced in Sec. XV.B.4, has been essential in the study of spin structures with (0 $\frac{2}{3}$ $\frac{2}{3}$) order. The concept of permanent configurations, combined with the eigenvalue and eigenvector calculations, very effectively explains the principal features of the (0 $\frac{2}{3}$ $\frac{2}{3}$) order.

a. Easy-axis anisotropy

The (0 $\frac{2}{3}$ $\frac{2}{3}$) order is associated with easy-axis anisotropy. This is seen, for example, by solving the eigenvalue equation (103) in the $J_1J_2D_1$ approximation, i.e., when there are exchange interactions between the nearest and next-nearest neighbors and dipolar interactions between nearest neighbors. For $\mathbf{k}=(\pi/a)(0,\frac{2}{3},\frac{2}{3})$ one finds the following eigenvalues and eigenvectors:

$$\lambda_1=-3J_1-3D_1, \quad \hat{\mathbf{e}}_1=(1,0,0), \tag{157a}$$

$$\lambda_2=-3J_1+6D_1, \quad \hat{\mathbf{e}}_2=(1/\sqrt{2})(0,1,-1), \tag{157b}$$

$$\lambda_3=-3J_1-3D_1, \quad \hat{\mathbf{e}}_3=(1/\sqrt{2})(0,1,1). \tag{157c}$$

Note that J_2 does not enter into these equations. The nearest-neighbor exchange interaction in copper is antiferromagnetic with $J_1/k_B\approx-12$ nK, while the dipolar coupling $D_1/k_B=(\mu_0/4\pi)\hbar^2\gamma^2r^{-3}/k_B=25$ nK. Therefore λ_2 is clearly larger than λ_1 and λ_3, and the spin modulation associated with the (0 $\frac{2}{3}$ $\frac{2}{3}$) order is along the eigenvector $\hat{\mathbf{e}}_2=(1/\sqrt{2})(0,1,-1)$. The corresponding anisotropy energy is, indeed, very large because the difference of the eigenvalues is on the order of k_BT_N. The (0 $\frac{2}{3}$ $\frac{2}{3}$) order can therefore be classified as antiferromagnetism with an easy axis.

The important difference between anisotropy of this sort and the structure found in traditional easy-axis antiferromagnets is that the anisotropy axis is dictated by the ordering vector rather than by the lattice. Because of the cubic symmetry in copper, there are altogether 12 different but symmetrically equivalent ordering vectors. These are the vectors in the star of $\mathbf{k}=(\pi/a)(0,\frac{2}{3},\frac{2}{3})$ (see Fig. 54), namely, $\pm(\pi/a)(0,\frac{2}{3},\pm\frac{2}{3})$, $\pm(\pi/a)(\frac{2}{3},0,\pm\frac{2}{3})$, and $(\pi/a)(\frac{2}{3},\pm\frac{2}{3},0)$. As the axes associated with ordering vectors $\pm\mathbf{k}$ are equivalent, there are altogether six possible easy axes. The presence of an external magnetic field however, breaks, the degeneracy between the vectors in the star.

b. Up-up-down structure

A simple example illustrates the general ideas. Let us consider the single-**k** configuration

$$\mathbf{I}_i/I=\frac{m}{\sqrt{2}}(0,-1,1)+\frac{d_1}{\sqrt{2}}(0,-1,1)\cos\left[\frac{\pi}{a}(0,\tfrac{2}{3},\tfrac{2}{3})\cdot\mathbf{r}_i\right], \tag{158}$$

where $d_1=-\frac{4}{3}$ and $m=\frac{1}{3}$; the structure is illustrated in Fig. 3(c). It is a three-sublattice configuration in which all spins have the saturation value $|\langle\mathbf{I}_i\rangle|=I$. The net magnetization sums up to $I/3$ per spin. The antiferromagnetic amplitude, $\mathbf{d}_1=(d_1/\sqrt{2})(0,-1,1)$, is along the easy axis of the ordering vector $\mathbf{k}=(\pi/a)(0,\frac{2}{3},\frac{2}{3})$. This structure therefore seems a plausible candidate for the ground state at $T=0$ in a field aligned along the [01 1] direction. Exactly at $B=B_c/3$ the local fields at all spin sites are equal, and the structure is permanent. Then, according to Sec. XV.B.4, if $\lambda_2(0,\frac{2}{3},\frac{2}{3})$ is the largest eigenvalue, the up-up-down configuration minimizes the energy and is indeed the ground state.

c. Superposition with type-I order

In fields lower than $B=B_c/3$ the system would like to decrease its magnetization from $m=\frac{1}{3}$. Owing to the easy-axis anisotropy of the (0 $\frac{2}{3}$ $\frac{2}{3}$) order, there is no way to decrease m continuously while, at the same time, increasing the (0 $\frac{2}{3}$ $\frac{2}{3}$) component. Viertiö and Oja (1990a) suggested that the system then makes a linear combination of the best and the second-best solutions: When the field is lowered below $B_c/3$, the whole up-up-down pattern of Fig. 3(c) is reduced to decrease m, and the overall length of the spin vectors is conserved by superposing the up-up-down pattern with an up-down configuration, i.e., type-I modulation, in a perpendicular direction. One possible spin structure is then the one described in Fig. 3(b).

When the field is reduced all the way to $B=0$ there is only type-I order left, as is shown by Fig. 3(a). The whole scenario can be described by using the equation

[24]According to Heinilä and Oja (1993a), the prediction was based, however, on an erroneous calculation, as explained in Sec. XV.F.3.

$$\mathbf{I}_i/I=\frac{m}{\sqrt{2}}(0,1,-1)+\frac{d_1}{\sqrt{2}}(0,1,-1)\cos\left[\frac{\pi}{a}(0,\tfrac{2}{3},\tfrac{2}{3})\cdot\mathbf{r}_i\right]+\frac{d_2}{\sqrt{2}}(0,1,1)\cos\left[\frac{\pi}{a}(1,0,0)\cdot\mathbf{r}_i\right], \quad (159)$$

where $d_1=-4m$ and $d_2^2=1-9m^2$. One can prove that this is the ground state under the following two assumptions: (i) $\lambda_{\max}=\lambda_2(0,\frac{2}{3},\frac{2}{3})=\lambda_{2,3}(1,0,0)$ and (ii) $\lambda_2(0,\frac{2}{3},\frac{2}{3})$ is larger than $\lambda_{2,3}(1,0,0)$ by an infinitesimally small amount.

One feature of Eq. (159), which is worth noting, is that the amplitude of the $(0\ \frac{2}{3}\ \frac{2}{3})$ component is proportional to the field. This particular type of antiferromagnetism is therefore *induced* by the field.

*d. Construction of multiple-***k** *structures*

Viertiö and Oja (1993) have derived equations that can be used to construct, in a general field direction, single-**k** and double-**k** spin configurations with only $(0\ \frac{2}{3}\ \frac{2}{3})$ order. The double-**k** structures can be written as

$$\mathbf{I}_i/I=\mathbf{d}_1\cos(\mathbf{k}_1\cdot\mathbf{r}_i)+\mathbf{d}_2\cos(\mathbf{k}_2\cdot\mathbf{r}_i)+\mathbf{m}, \quad (160)$$

where $\mathbf{k}_1$ and $\mathbf{k}_2$ are vectors in the star of $\mathbf{k}=(\pi/a)(\frac{2}{3},\frac{2}{3},0)$. The amplitudes of the antiferromagnetic modulations $\mathbf{d}_1$ and $\mathbf{d}_2$ lie along the easy directions of the respective ordering vectors $\mathbf{k}_1$ and $\mathbf{k}_2$ (see Sec. XV.F.1a). The magnetization is given by $\mathbf{m}=\mathbf{B}/B_c$ where $B_c=I[\lambda_2(0,\frac{2}{3},\frac{2}{3})-\lambda(0)]/\hbar\gamma$.

At fcc lattice sites, the phase factor $\mathbf{k}\cdot\mathbf{r}_i$ takes the values $2\pi/3$, $4\pi/3$, and 2π, yielding $\cos(\mathbf{k}\cdot\mathbf{r}_i)=-\frac{1}{2}$, $-\frac{1}{2}$, and 1, respectively. There are four sublattices with spins $(\mathbf{d}_1+\mathbf{d}_2+\mathbf{m})$, $(\mathbf{d}_1-\frac{1}{2}\mathbf{d}_2+\mathbf{m})$, $(-\frac{1}{2}\mathbf{d}_1+\mathbf{d}_2+\mathbf{m})$, and $(-\frac{1}{2}\mathbf{d}_1-\frac{1}{2}\mathbf{d}_2+\mathbf{m})$. In zero field, $\mathbf{m}=0$ and it is clearly impossible to find amplitudes $\mathbf{d}_1$ and $\mathbf{d}_2$ such that the four spin vectors would have equal lengths. However, at certain values and directions of the external field, the induced magnetization perfectly compensates for the mismatch.

The analysis is performed at $T=0$ for simplicity. Let us define $\mathbf{m}=\mathbf{m}_\parallel+\mathbf{m}_\perp$, where $\mathbf{m}_\parallel$ is the component of magnetization in the plane determined by $\mathbf{d}_1$ and $\mathbf{d}_2$. The spins are saturated at $\mathbf{I}_i=I$ when the following conditions are satisfied:

$$\mathbf{d}_1\cdot\mathbf{d}_2=0,$$
$$\mathbf{m}_\parallel=-\frac{1}{4}(\mathbf{d}_1+\mathbf{d}_2),$$
$$9m_\parallel^2+m_\perp^2=1. \quad (161)$$

According to the first condition, the only possible double-**k** structure is of the type $\mathbf{d}_1\|(1,1,0)$ and $\mathbf{d}_2\|(1,-1,0)$, with ordering vectors $\mathbf{k}_1=(\pi/a)(\frac{2}{3},-\frac{2}{3},0)$ and $\mathbf{k}_2=(\pi/a)(\frac{2}{3},\frac{2}{3},0)$. The second condition of Eqs. (161) gives the correction $\mathbf{m}_\parallel$, which is needed to make the moments equal. There may be, perpendicular to the plane spanned by $\mathbf{d}_1$ and $\mathbf{d}_2$, an additional component of magnetization $\mathbf{m}_\perp$, the value of which is determined by the third condition.

In the case of a single-**k** structure, $\mathbf{d}_2=0$, the above equations reduce to $\mathbf{m}_\parallel=-\frac{1}{4}\mathbf{d}_1$ and $9m_\parallel^2+m_\perp^2=1$. It is clear that for a fixed direction of the external field, $\mathbf{d}_1$ must have a component along **B**. Otherwise, antiferromagnetic solutions are not found.

A similar analysis can be made for a superposition structure in which $\mathbf{k}_1$ is a vector in the star of $\mathbf{k}=(\pi/a)(\frac{2}{3},\frac{2}{3},0)$ and $\mathbf{k}_2$ is one of the three type-I ordering vectors. There are then four sublattices with spins $(\mathbf{d}_1+\mathbf{d}_2+\mathbf{m})$, $(\mathbf{d}_1-\mathbf{d}_2+\mathbf{m})$, $(-\frac{1}{2}\mathbf{d}_1+\mathbf{d}_2+\mathbf{m})$, and $(-\frac{1}{2}\mathbf{d}_1-\mathbf{d}_2+\mathbf{m})$. At $T=0$, $\mathbf{I}_i=I$ and the following conditions must be satisfied:

$$\mathbf{d}_1\cdot\mathbf{d}_2=0,$$
$$\mathbf{d}_2\cdot\mathbf{m}=0,$$
$$\mathbf{m}_\parallel=-\frac{1}{4}\mathbf{d}_1,$$
$$9m_\parallel^2+m_\perp^2+d_2^2=1. \quad (162)$$

From the first condition and from the easy-axis anisotropy of type-I order, it follows that if $\mathbf{d}_1\|(1,1,0)$, then $\mathbf{d}_2\|(1,-1,0)$ or $\|(0,0,1)$. The corresponding ordering vectors are $\mathbf{k}_1=(\pi/a)(\frac{2}{3},-\frac{2}{3},0)$ and $\mathbf{k}_2=(\pi/a)(0,0,1)$ in the former case, and $\mathbf{k}_2=(\pi/a)(1,0,0)$ or $(\pi/a)(0,1,0)$ in the latter. In a general field direction, in which $|m_x|$, $|m_y|$, and $|m_z|$ are all nonequal and nonzero, it is then impossible to satisfy simultaneously the second equation, and a double-**k** superposition structure does not exist. Once there is some symmetry in the field alignment, for example, if $\mathbf{m}\|[\alpha\alpha\beta]$, a superposition solution can be found.

In the high-symmetry field directions, it is possible to find more complex, permanent multiple-**k** structures that superimpose the $(0\ \frac{2}{3}\ \frac{2}{3})$ and $(1\,0\,0)$ orders. Viertiö and Oja (1993) have constructed, for the [100] and [011] field alignments, quadruple-**k** spin configurations that are simultaneously modulated by one $(0\ \frac{2}{3}\ \frac{2}{3})$ ordering vector and by the three type-I vectors.

2. Theoretical spin structure versus experiments on copper

Neutron-diffraction measurements on copper by Annila *et al.* (1992), in which **B** was aligned along the various crystalline high-symmetry directions, revealed clear selection rules for the three type-I reflections and the twelve cubic-symmetry-related $(0\ \frac{2}{3}\ \frac{2}{3})$ reflections (see Fig. 59). These selection rules provided crucial tests for the theoretically calculated spin configurations, as we discussed in Sec. XV.D.8 for type-I configurations. In the case of the $(0\ \frac{2}{3}\ \frac{2}{3})$ order, the observed selection rules provide even more tests of the spin structures. The experimentally determined selection rules are in complete agreement with the theoretical predictions of Viertiö and Oja (1990a, 1990b). Their equations for the actual spin configurations will be given below.

a. B‖[011]

When the external field is aligned along the [011] crystalline axis, there are three nonequivalent ordering vectors in the star of $\mathbf{k}_2=(\pi/a)(\frac{2}{3},\frac{2}{3},0)$. The use of Eq. (161) yields the following permanent single-**k** structures:

$$\mathbf{k}_1=(\pi/a)(0,\tfrac{2}{3},-\tfrac{2}{3}),\quad \mathbf{d}_1=-\frac{4}{3\sqrt{2}}(0,1,1), \tag{163}$$

at $B=B_c/3$, and

$$\mathbf{k}_1=(\pi/a)(\tfrac{2}{3},0,\tfrac{2}{3}),\quad \mathbf{d}_1=-\frac{2}{\sqrt{6}}(1,0,-1), \tag{164}$$

at $B=B_c/\sqrt{3}$. Solutions similar to the latter can be obtained for the symmetrically equivalent ordering vectors $\mathbf{k}=(\pi/a)(\frac{2}{3},0,-\frac{2}{3})$, $(\pi/a)(\frac{2}{3},\frac{2}{3},0)$, and $(\pi/a)(\frac{2}{3},-\frac{2}{3},0)$. For $\mathbf{k}=(\pi/a)(0,\frac{2}{3},\frac{2}{3})$, a permanent single-**k** solution does not exist.

Equation (161) also yields the double-**k** structure

$$\mathbf{k}_1=(\pi/a)(\tfrac{2}{3},\tfrac{2}{3},0),\quad \mathbf{d}_1=\frac{2}{\sqrt{6}}(1,-1,0),$$

$$\mathbf{k}_2=(\pi/a)(\tfrac{2}{3},-\tfrac{2}{3},0),\quad \mathbf{d}_2=-\frac{2}{\sqrt{6}}(1,1,0) \tag{165}$$

at $B=B_c/\sqrt{5}$.

The above configurations are permanent only at discrete values of **B**. In other fields it may be energetically advantageous to combine the $(0\ \frac{2}{3}\ \frac{2}{3})$ modulation with a suitable amount of type-I order, as was discussed in Sec. XV.F.1c. This is possible for the single-**k** structure of Eq. (163), as was demonstrated by Eq. (159) and in Fig. 3. The actual spin arrangement may be more complex, however. It is easy to see that one can superpose yet another type-I modulation with the configuration given by Eq. (159), namely, $(d_3,0,0)\cos[(\pi/a)(0,1,0)\cdot\mathbf{r}_i]$, where d_3 and d_2 are now obtained from $d_2^2+d_3^2=1-9m^2$. Furthermore, it turns out that it is possible to add even a third type-I modulation, $\mathbf{k}=(\pi/a)(0,0,1)$, but the equation for the spin configuration then becomes very complicated indeed.

The use of Eq. (162) shows that it is impossible to superimpose type-I order with the single-**k** configuration of Eq. (164) to construct a permanent double-**k** structure.

The analytical solutions for spin arrangements by superposition are exact within the mean-field theory only when $\lambda_{\max}=\lambda_2(0,\frac{2}{3},\frac{2}{3})=\lambda_{2,3}(1,0,0)$. Most of the degeneracy associated with the ground state is removed by the assumption that $\lambda_2(0,\frac{2}{3},\frac{2}{3})$ is larger than $\lambda_{2,3}(1,0,0)$ by an infinitesimally small amount. The ground state is then the one that maximizes the $(0\ \frac{2}{3}\ \frac{2}{3})$ order. This leaves, however, some degeneracy in the spin system. A unique ground state can be found by considering fluctuation effects as was the case with pure type-I order. In addition, one has to take into account that the assumption $\Delta\lambda\equiv\lambda_2(0,\frac{2}{3},\frac{2}{3})-\lambda_{2,3}(1,0,0)\rightarrow+0$ cannot be exactly valid in a real system, and one has to accept a positive but small $\Delta\lambda$. One may consider this as an extra source of fluctuations to the ideal case $\Delta\lambda\equiv\lambda_2(0,\frac{2}{3},\frac{2}{3})-\lambda_{2,3}(1,0,0)\rightarrow+0$. Monte Carlo simulations (Viertiö and Oja, 1990a) have given evidence that the stable structure is a configuration in which the $\mathbf{k}_1=(\pi/a)(0,\frac{2}{3},-\frac{2}{3})$ ordering vector is superimposed on $\mathbf{k}_3=(\pi/a)(0,1,0)$. The reason for illustrating in Fig. 3(b) the combination structure with the $\mathbf{k}_2=(\pi/a)(1,0,0)$ ordering vector is that this configuration is easier to visualize.

TABLE VII. Summary of theoretical selection rules for the $(0\ \frac{2}{3}\ \frac{2}{3})$ order. From Viertiö and Oja (1990a, 1990b, 1993).

Alignment	$\mathbf{k}(\pi/a)$	Stability region
B‖[100]	$\pm(0,\frac{2}{3},\pm\frac{2}{3})$	not stable
	$\pm(\frac{2}{3},0,\pm\frac{2}{3})$	$0\leqslant B\leqslant B_c/\sqrt{5}$
	$\pm(\frac{2}{3},\pm\frac{2}{3},0)$	$0\leqslant B\leqslant B_c/\sqrt{5}$
B‖[011]	$\pm(0,\frac{2}{3},\frac{2}{3})$	not stable
	$\pm(0,\frac{2}{3},-\frac{2}{3})$	$0\leqslant B\leqslant B_c/3$
	$\pm(\frac{2}{3},0,\pm\frac{2}{3})$	$B_c/\sqrt{5}$, $B_c/\sqrt{3}$
	$\pm(\frac{2}{3},\pm\frac{2}{3},0)$	$B_c/\sqrt{5}$, $B_c/\sqrt{3}$
B‖[111]	$\pm(0,\frac{2}{3},\frac{2}{3})$	not stable
	$\pm(0,\frac{2}{3},-\frac{2}{3})$	$0\leqslant B\leqslant\sqrt{3/19}B_c$
	$\pm(\frac{2}{3},0,\frac{2}{3})$	not stable
	$\pm(\frac{2}{3},0,-\frac{2}{3})$	$0\leqslant B\leqslant\sqrt{3/19}B_c$
	$\pm(\frac{2}{3},\frac{2}{3},0)$	not stable
	$\pm(\frac{2}{3},-\frac{2}{3},0)$	$0\leqslant B\leqslant\sqrt{3/19}B_c$

Information on the stability of the various ordering vectors has been collected into Table VII. Comparison with the observed selection rules, which were summarized in Fig. 59, shows that there is complete agreement between theory and experiment: Only the predicted (Viertiö and Oja, 1990a, 1990b) ordering vectors were observed in measurements (Annila *et al.*, 1992). In addition, when **B**‖[011], the eight mutually equivalent vectors[25] $\mathbf{k}=\pm(\pi/a)(\frac{2}{3},0,\pm\frac{2}{3})$ and $\pm(\pi/a)(\frac{2}{3},\pm\frac{2}{3},0)$ have their maximum intensities in higher fields than the $\mathbf{k}=\pm(\pi/a)(0,\frac{2}{3},-\frac{2}{3})$ vector.

The observed field dependence of the (1 0 0) and the $(0\ \frac{2}{3}\ \frac{2}{3})$ Bragg reflections has been compared with calculations (Viertiö and Oja, 1990a). The theoretical magnetic structure factors $|\mathbf{I}(\mathbf{k})|^2$ are presented in Fig. 122 in terms of a contour diagram in the B-T plane. According to Eq. (51), $|\mathbf{I}(\mathbf{k})|^2$ is proportional to the intensity of the Bragg peak, but experimental difficulties make it exceedingly hard to obtain an accurate value for the proportionality constant. Measurements of relative intensities are, however, very interesting as such because the

[25]Viertiö and Oja associated these ordering vectors with the double-**k** configuration of Eq. (165) in their 1990a paper. The structure was then thought to be nonpermanent. Only later (1993) did the authors notice that the structure is, in fact, a permanent one. In their 1990a paper, the structure was called a 4-**k** state rather than 2-**k** because ±**k**'s were counted separately. The single-**k** configuration of Eq. (164) was found only in the 1993 paper.

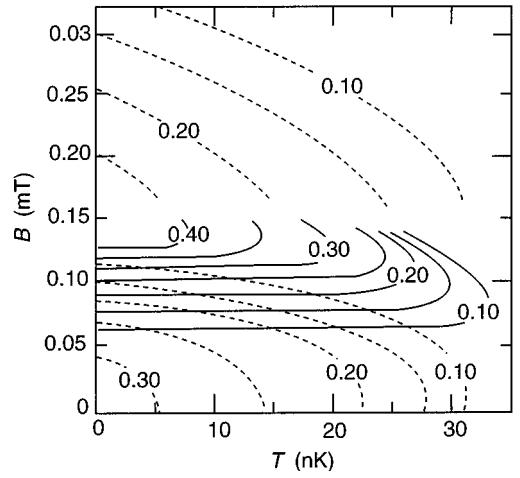

FIG. 122. Contour diagrams of the magnetic structure factor $|\mathbf{I}(0,\frac{2}{3},\frac{2}{3})|^2$ (solid lines) and the averaged (1 0 0) structure factor $\frac{1}{3}[|\mathbf{I}(1,0,0)|^2+|\mathbf{I}(0,1,0)|^2+|\mathbf{I}(0,0,1)|^2]$ (dashed lines) in the temperature vs magnetic field plane for $\mathbf{B}\|[011]$. The results were obtained in a simulated warmup during a Monte Carlo run. Compare with the experimental diagram shown in Fig. 3. From Viertiö and Oja (1990a).

contour diagram has a rich structure.

There is clearly a good resemblance between the theoretical and experimental (see Fig. 3) diagrams. In high fields, only (1 0 0) order has been found. In intermediate fields, there is an abrupt transition between the (1 0 0) state and a structure with only $(0\,\frac{2}{3}\,\frac{2}{3})$ order. When the field is lowered further the intensity of the $(0\,\frac{2}{3}\,\frac{2}{3})$ reflection decreases while the (1 0 0) peak increases. Finally, at $B=0$, only (1 0 0) order exists. The theoretical contour diagram reproduces well the two different kinds of transitions between the $(0\,\frac{2}{3}\,\frac{2}{3})$ and (1 0 0) structures: The transition is gradual in low fields and quite abrupt in high fields.

There are several matters, however, that one should pay attention to when making a comparison. First, the horizontal axis in the experimental phase diagram is the warmup time t rather than the absolute temperature. There has to be a monotonically increasing relationship between t and T so that the topology of the two diagrams should be the same. Another important point is the way in which the theoretical diagram was constructed. $|\mathbf{I}(\mathbf{k})|^2$ was obtained from a Monte Carlo simulation by heating the ground state in small temperature steps. The initial configuration was the combination structure of Eq. (159) in fields $B<B_c/3$, but with the $\mathbf{k}_3=(\pi/a)(0,1,0)$ ordering vector rather than $\mathbf{k}_2=(\pi/a)(1,0,0)$. In fields $B>B_c/3$, the initial configuration was the type-I structure **3a** [see Eq. (139)].

The largest discrepancy between the experimental and theoretical structure-factor diagrams occurs in fields $B=0.12$–0.16 mT, where a gap develops upon warming between the contours for the $(0\,\frac{2}{3}\,\frac{2}{3})$ and (1 0 0) Bragg peaks. Viertiö and Oja (1990a) suggested that this is due to the fact that another structure, with $\pm(\frac{2}{3}\;0\;\pm\frac{2}{3})$ and $\pm(\frac{2}{3}\;\pm\frac{2}{3}\;0)$ Bragg reflections, is stable in this field region (see the previous footnote). Subsequent experimental results, summarized in Table VII, were in accord with the suggestion. Apart from the double-**k** structure of Eq. (165), another plausible candidate for the stable structure in the region of the gap is the single-**k** structure of Eq. (164).

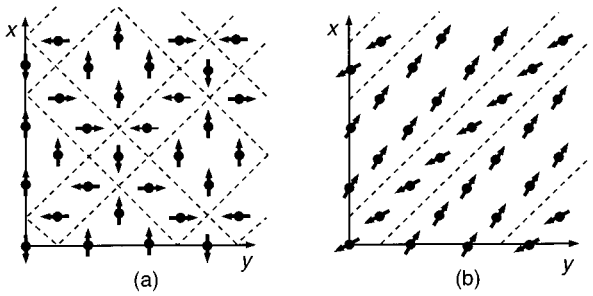

FIG. 123. Spin structures in the AF1 and AF2 phases of copper when the external magnetic field is aligned along a crystallographic axis, here the [100] direction. The corresponding experimental diagram is illustrated in Fig. 1. Only spins in one crystallographic plane have been shown: (a) AF1 phase in fields $B<B_c/3$ as given by Eq. (166); (b) AF2 in $B_c/3<B<B_c/\sqrt{5}$ [see Eq. (167)]. From Viertiö and Oja (1990a).

b. B‖[100]

Permanent spin structures with $(0\,\frac{2}{3}\,\frac{2}{3})$ order have been predicted for $\mathbf{B}\|[100]$ as well (Viertiö and Oja, 1990a, 1990b). In this field direction, too, it is possible to construct structures that superimpose the $(0\,\frac{2}{3}\,\frac{2}{3})$ and (1 0 0) orders when $\lambda_2(0,\frac{2}{3},\frac{2}{3})=\lambda_{2,3}(1,0,0)$. In these spin configurations the $(0\,\frac{2}{3}\,\frac{2}{3})$ order is uniquely determined, whereas the (1 0 0) order is continuously degenerate: various combinations of $\mathbf{k}=(\pi/a)(1,0,0)$, $(\pi/a)(0,1,0)$, and $(\pi/a)(0,0,1)$ modulations are possible. In the equations below, the particular solutions that maximize the Bragg intensities at positions (0 1 0) and (0 0 1) have been chosen (Viertiö and Oja, 1993), since neutron-diffraction measurements (Annila *et al.*, 1992) showed that these reflections are much stronger than the one at (1 0 0) after demagnetization with $\mathbf{B}\|[100]$, as illustrated in Fig. 56.

In fields $0<B<B_c/3$ the permanent spin structure that maximizes $(0\,\frac{2}{3}\,\frac{2}{3})$ order is the triple-**k** configuration

$$\begin{aligned}
&\mathbf{k}_1=(\pi/a)(\tfrac{2}{3},\tfrac{2}{3},0),\quad \mathbf{d}_1=\frac{d_1}{\sqrt{2}}(1,-1,0),\\
&\mathbf{k}_2=(\pi/a)(-\tfrac{2}{3},\tfrac{2}{3},0),\quad \mathbf{d}_2=\frac{d_2}{\sqrt{2}}(1,1,0),\\
&\mathbf{k}_3=(\pi/a)(0,1,0),\quad \mathbf{d}_3=d_3(0,0,1),\\
&d_1=d_2=-2\sqrt{2}m,\\
&d_3=\pm\sqrt{1-9m^2}.
\end{aligned}\tag{166}$$

The structure is illustrated in Fig. 123(a). Viertiö and Oja (1990a) identified this spin configuration with the experimentally observed low-field phase AF1 in Fig. 1.

In fields $B_c/3<B<B_c/\sqrt{5}$ one finds the quadruple-**k** structure

$$\mathbf{k}_1=(\pi/a)(\tfrac{2}{3},\tfrac{2}{3},0),\quad \mathbf{d}_1=\frac{d_1}{\sqrt{2}}(1,-1,0),$$

$$\mathbf{k}_2=(\pi/a)(0,0,1),\quad \mathbf{d}_2=\frac{d_2}{\sqrt{2}}(1,1,0),$$

$$\mathbf{k}_3=(\pi/a)(0,1,0),\quad \mathbf{d}_3=d_3(0,0,1),$$

$$\mathbf{k}_4=(\pi/a)(1,0,0),\quad \mathbf{d}_4=d_4(0,0,1), \tag{167}$$

$$d_1=-2\sqrt{2}m,$$

$$d_2=\frac{1}{\sqrt{2}}(m-\sqrt{2-9m^2}),$$

$$d_3=\pm[\tfrac{1}{2}m(\sqrt{2-9m^2}-m)]^{1/2},$$

$$d_4=d_3.$$

This configuration is illustrated in Fig. 123(b). The structure was associated with the experimentally observed intermediate-field phase AF2.

In fields above $B_c/\sqrt{5}$, the ordered spin configuration AF3 should be the type-I structure with two ordering vectors [see Eq. (135c)], as was discussed in Sec. XV.D.7a. The stability regions of the various ordering vectors have been summarized in Table VII. Comparison with observed selection rules of Fig. 59 again shows complete agreement.

With the above identification of the three experimentally found phases in this field direction (see Fig. 1), the transitions AF1↔AF2 and AF2↔AF3 are of first order as observed. Even the absolute values for the transition fields at $T=0$ are in good agreement with experiment: For the exchange constants, which were used in the Monte Carlo simulations of Viertiö and Oja (1990a), one finds $B_c/3=0.13$ mT and $B_c/\sqrt{5}=0.18$ mT, while the measured values are 0.12 mT and 0.17 mT, respectively.

c. B∥[111]

Permanent spin configurations with $(0\ \frac{2}{3}\ \frac{2}{3})$ order have been constructed for **B**∥[111], too (Viertiö and Oja, 1990a, 1990b). In this case, there are no permanent double-**k** structures but a single-**k** solution was found at $B=\sqrt{3/19}B_c$. The ordering vector is perpendicular to the field; it is either $\pm(\pi/a)(0,\frac{2}{3},-\frac{2}{3})$, $\pm(\pi/a)(\frac{2}{3},0,-\frac{2}{3})$, or $\pm(\pi/a)(\frac{2}{3},-\frac{2}{3},0)$. These modulations are all equivalent when the field is exactly along the [111] direction. The other six $(0\ \frac{2}{3}\ \frac{2}{3})$ ordering vectors do not yield permanent solutions. These theoretical selection rules are in agreement with the measurements (see Fig. 59).

In fields $0<B<\sqrt{3/19}B_c$, the single-**k** structure can be superimposed with (1 0 0) order, viz.,

$$\mathbf{k}_1=(\pi/a)(0,\tfrac{2}{3},-\tfrac{2}{3}),\quad \mathbf{d}_1=\frac{d_1}{\sqrt{2}}(0,1,1),$$

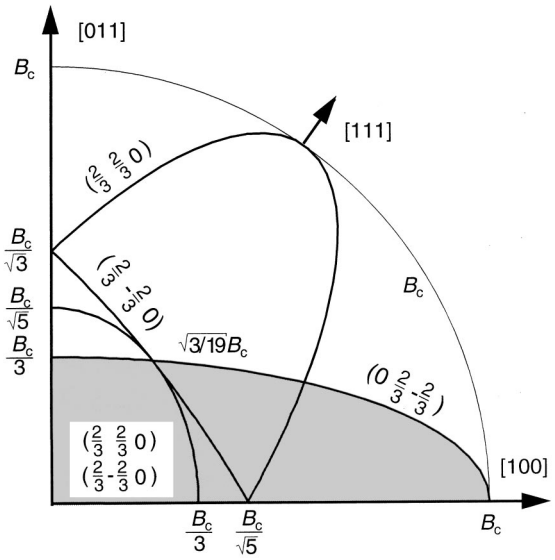

FIG. 124. Permanent spin configurations of copper with $(0\ \frac{2}{3}\ \frac{2}{3})$ order as functions of the external magnetic field in the plane $B_y=B_z$. The structures exist along the heavy curves with the particular ordering vector(s) indicated. The field values (in units of B_c) for the high-symmetry directions are indicated. In the shaded region, $(0\ \frac{2}{3}\ -\frac{2}{3})$ and (1 0 0) orders are superimposed. The thin B_c curve shows the critical field for antiferromagnetic order. From Viertiö and Oja (1993).

$$\mathbf{k}_2=(\pi/a)(1,0,0),\quad \mathbf{d}_2=\frac{d_2}{\sqrt{2}}(0,1,-1), \tag{168}$$

$$d_1=-8m/\sqrt{6},$$

$$d_2=\pm\sqrt{1-19m^2/3}.$$

d. Other field directions

Viertiö and Oja (1993) have constructed all permanent spin configurations with one or two $(\frac{2}{3}\ \frac{2}{3}\ 0)$ ordering vectors when the external magnetic field is applied in the plane $B_y=B_z$. The results of this calculation are illustrated in Fig. 124. In the shaded region, there exists a double-**k** configuration that can be obtained from Eq. (162) by a superposition of $\mathbf{k}_1=(\pi/a)(0,\frac{2}{3},-\frac{2}{3})$ and $\mathbf{k}_2=(\pi/a)(1,0,0)$ ordering vectors. Along the [011] and [100] field directions, the above mentioned quadruple-**k** superposition structures exist as well.

3. Stability of $(0\ \frac{2}{3}\ \frac{2}{3})$ modulation versus type-I order

There has been some controversy about the origin of the $(0\ \frac{2}{3}\ \frac{2}{3})$ order in copper. The question has been whether this modulation is stabilized by fluctuation effects beyond the mean-field theory, or whether the spin-spin interactions are such that the $(0\ \frac{2}{3}\ \frac{2}{3})$ order results already from the mean-field theory. The latter possibility would require that the indirect exchange interactions differ by some 10 to 20% from their calculated and measured values.

Although an ordering vector of type $\mathbf{k}=(\pi/a)(\eta,\eta,0)$ was a possibility in the mean-field calculations, which assumed the free-electron model for the RK interaction (Kjäldman and Kurkijärvi, 1979; Oja and Kumar, 1984), this ordering became a serious alternative for the modulation vector of copper only with the first-principles electronic-band-structure calculations of the RK interaction by Lindgård, Wang, and Harmon (1986). Their study predicted that the ordering vector should be of type I, as was thought previously, but also showed that, if the strength of the RK interaction was somewhat reduced, the type-I ordering vector should become unstable against the $\mathbf{k}=(\pi/a)(\eta,\eta,0)$ order rather than the $\mathbf{k}=(\pi/a)(\eta,0,0)$ modulation, as was predicted by the free-electron model (see Figs. 111 and 112).

In the first neutron-diffraction measurements on copper by Jyrkkiö, Huiku, Lounasmaa *et al.* (1988), the type-I Bragg reflection was found in the low- and high-field regions when $\mathbf{B}\|[01\,1]$; in intermediate fields the Bragg intensity was almost zero. Soon afterwards, theoretical calculations of Lindgård (1988a, 1988b) showed that there are two different single-**k** states, **1z** and **1y** [see Eqs. (141)], in this field direction, with a transition at $B\approx 0.3B_c$. According to Lindgård, quantum fluctuations stabilize a $\mathbf{k}=(\pi/a)(\eta,\eta,0)$ phase in the field region between the **1z** and **1y** states. This prediction explained the low intensity of the type-I reflection in intermediate fields and was consistent with the $(0\ \frac{2}{3}\ \frac{2}{3})$ Bragg reflection found in later neutron-diffraction experiments of Annila *et al.* (1990). In a more recent paper, Lindgård (1990) confirmed that the $(0\ \frac{2}{3}\frac{2}{3})$ order is, indeed, favored by quantum fluctuations.

Different results were obtained, however, in the recent work by Heinilä and Oja (1993a). They noticed that Lindgård's calculation of the ground-state energies for type-I structures was partly incorrect. According to Heinilä and Oja, perturbation theory predicts the type-I structures **3b** and **3a** for copper ($d=2$) when $\mathbf{B}\|[011]$ (see Fig. 119) rather than **1z** and **1y**. Furthermore, these authors found that quantum fluctuations favor type-I order rather than the $(0\ \frac{2}{3}\ \frac{2}{3})$ modulation. At least in the important case of $B=B_c/3$, for which measurements show that the $(0\ \frac{2}{3}\ \frac{2}{3})$ Bragg peak has its maximum intensity, the perturbation calculation of Heinilä and Oja predicts, in the case of complete degeneracy $\lambda_{2,3}(1,0,0)=\lambda_2(0,\frac{2}{3},\frac{2}{3})$, that quantum fluctuations favor the **3a** structure rather than the up-up-down configuration of $(0\ \frac{2}{3}\ \frac{2}{3})$ order. This work therefore gives support to the idea advocated earlier by Viertiö and Oja (1990a, 1990b, 1993), who explained the observed stability of the $(0\ \frac{2}{3}\ \frac{2}{3})$ order by starting from the assumption that the exchange interactions are such that the eigenvalue for $\mathbf{k}=(\pi/a)(0,\frac{2}{3},\frac{2}{3})$ is, in fact, larger than that for a type-I ordering vector.

The problem that remains is that the eigenvalue for the $(0\ \frac{2}{3}\ \frac{2}{3})$ spin configuration is 10% lower than that for type-I order according to first-principles band-structure calculations (Lindgård *et al.*, 1986; Oja *et al.*, 1989). Since the 10% difference in the two eigenvalues is within the estimated uncertainty of the calculated exchange parameters, there is no serious discrepancy. Nevertheless, refined computations of exchange interactions in copper would be of value.

According to band-structure calculations made so far, several exchange parameters seem to be important in deciding the relative stability of the $(0\ \frac{2}{3}\ \frac{2}{3})$ and $(1\,0\,0)$ orders, since their energies are so close to each other. It would be particularly important to narrow down error margins for the isotropic interactions between the nearest and the third-nearest neighbors. Anisotropic exchange parameters between nearest neighbors are significant, too, as well as other isotropic interactions even up to the sixth-nearest neighbors.

4. Superposition structure or a mixed state of $(0\ \frac{2}{3}\ \frac{2}{3})$ and $(1\,0\,0)$ domains

One of the main features of the neutron-diffraction data on copper is that in a wide-field region, approximately from $B=0.02$ to 0.06 mT, both $(0\ \frac{2}{3}\ \frac{2}{3})$ and $(1\,0\,0)$ orders are present simultaneously. There are two interpretations of this fact. First, there can be superposition of $(0\ \frac{2}{3}\ \frac{2}{3})$ and $(1\,0\,0)$ orders in a single magnetic domain, as was discussed in Sec. XV.F.1c. Without theoretical support, such a complicated spin configuration might appear unlikely. Second, the ordered spin system can be a mixture of two different kinds of domains, namely, one with $(0\ \frac{2}{3}\ \frac{2}{3})$ order and the other with $(1\,0\,0)$ modulation. It was stressed by the experimentalists (Annila *et al.*, 1990, 1992) that measured data cannot distinguish between these two possibilities.

Assuming tentatively the second alternative, Annila *et al.* interpreted their data as a first-order transition between $(0\ \frac{2}{3}\ \frac{2}{3})$ and $(1\,0\,0)$ orders at $B\approx 0.06$ mT, with large hysteresis effects. The $(0\ \frac{2}{3}\ \frac{2}{3})$ Bragg reflection in fields below $B=0.06$ mT would then result from metastable domains. The relaxation time to thermodynamic equilibrium would have to be longer than the warmup time caused by spin-lattice relaxation.

If the possibility of a superposition structure is accepted, as is suggested by theoretical calculations (Viertiö and Oja, 1990a, 1990b, 1993), there is no need to assume large hysteresis effects. The simultaneous presence of $(0\ \frac{2}{3}\ \frac{2}{3})$ and $(1\,0\,0)$ orders is thereby explained, as shown by the good agreement between the theoretical and the experimental structure-factor diagrams (Figs. 3 and 122). Annila *et al.* (1990, 1992) conclude that a superposition structure is possible particularly in the field region from $B=0.02$ to 0.05 mT, where the temporal behavior of the $(0\ \frac{2}{3}\ \frac{2}{3})$ and $(1\,0\,0)$ Bragg reflections is similar, as shown by Fig. 46(b). Although this is a compelling argument, it should be noted that, according to Monte Carlo simulations (Fig. 122), the T dependence of the two Bragg reflections is different. Therefore the superposition structure could, in principle, be stable also in fields higher than 0.05 mT.

In very low fields, below 0.02 mT, the intensity of the $(0\ \frac{2}{3}\ \frac{2}{3})$ Bragg reflection rapidly decreases, as is shown by curve (d) in Fig. 45. Depending on the nature of the $(0\ \frac{2}{3}\ \frac{2}{3})$ order in fields above 0.02 mT, this behavior sug-

gests that the superposition structure becomes unstable or, alternatively, that the $(0\ \frac{2}{3}\ \frac{2}{3})$ domains disappear.

There are some measurements that could be useful in deciding between the superposition structure or a mixed state. One possibility relies on the fact that Eqs. (162) show that it is impossible to construct, in a general field direction $\mathbf{B}\|[\alpha\ \beta\ \gamma]$ where $|\alpha|$, $|\beta|$, and $|\gamma|$ are all different and nonzero, a permanent double-**k** spin structure that would superimpose the $(0\ \frac{2}{3}\ \frac{2}{3})$ and $(1\ 0\ 0)$ orders. It is likely that more complicated, permanent multiple-**k** spin configurations do not exist either. On the other hand, a superposition structure is predicted for the cubic high-symmetry field directions. One would then expect that, for a suitable general field alignment, the behavior of the $(0\ \frac{2}{3}\ \frac{2}{3})$ and $(1\ 0\ 0)$ reflections in low intermediate fields would be different from their behavior in high-symmetry directions.

Another possibility is to perform NMR measurements on a single-crystal specimen. A careful analysis of the NMR line shape might help in deciding between the two possibilities (Heinilä and Oja, 1995).

5. Related electronic magnets

The simultaneous presence of two different kinds of ordering vectors is a rare occurrence. Moreover, a period of three is rather unusual in ordered spin structures. The purpose of this section is to draw attention to some electronic magnets sharing these properties in the hope that this will result in a better understanding of these systems.

In $TbMn_2$, which crystallizes in the C15 cubic Laves phase, the Mn atoms are distributed on the vertices of regular tetrahedra, which, in turn, are packed in a diamond arrangement sharing vertices. A high degree of frustration arises for the Mn antiferromagnetism, leading to complicated magnetic structures (Ballou *et al.*, 1988). Neutron-diffraction measurements have revealed that the low-temperature magnetic phase of $TbMn_2$ is metastable and poised between magnetic configurations with propagation vectors $(\frac{2}{3}\ \frac{2}{3}\ 0)$ and $(\frac{1}{2}\ \frac{1}{2}\ \frac{1}{2})$, respectively (Ballou *et al.*, 1992). Experiments have also shown that these reflections depend on the external magnetic field in an interesting way.

A period-of-three modulation has also been found for $USb_{0.9}Te_{0.1}$ in which the U atoms occupy fcc sites. Neutron-diffraction experiments have shown that, in the low-temperature phase, the ordering vectors $\pm(\pi/a)(\frac{2}{3},0,0)$, $\pm(\pi/a)(0,\frac{2}{3},0)$, and $\pm(\pi/a)(0,0,\frac{2}{3})$, as well as a ferromagnetic component, are present simultaneously (Rossat-Mignod *et al.*, 1979).

Tripling of the magnetic unit cell along one crystalline axis has been observed in $MnSe_2$ (Hastings *et al.*, 1959). Mn atoms occupy fcc sites in this compound having a pyrite structure. The antiferromagnetic state displays the ordering vectors $(\pi/a)(\frac{1}{3},0,1)$ and $(\pi/a)(0,1,0)$. The type-I component in this case is the third harmonic of the fundamental ordering vector $(\pi/a)(\frac{1}{3},0,1)$. The role of anisotropic interactions in $MnSe_2$ has been discussed theoretically (Heinilä and Oja, 1994c).

Finally, we comment on the up-up-down configuration predicted for copper in a field $B=B_c/3$ when $\mathbf{B}\|[011]$ [see Fig. 3(c)]. A similar configuration with the propagation vector along a cubic axis has been found in calculations on *Ising* systems for certain nearest and next-nearest neighbor interactions (Binder *et al.*, 1981). The nature of this structure, however, is different from that for vector spins.

Experimentally, an up-up-down spin configuration has been observed in EuSe, which is an fcc system (Griessen *et al.*, 1971, and references therein). In contrast to copper, magnetoelastic energies play a significant role in the behavior of this compound.

G. High-field phase of copper when B‖[111]

Neutron-diffraction measurements of Annila *et al.* (1992) on copper showed unexpectedly that in fields $B=0.17-0.25$ mT, applied along the [111] crystalline direction, no antiferromagnetic $(1\ 0\ 0)$ Bragg peak was observed (see Fig. 58), although it was found for the [100] and [011] field directions. Neither was there any $(0\ \frac{2}{3}\ \frac{2}{3})$ structure present. Several other ordering vectors were searched for but with negative results, as was described in Sec. VII.J. A number of theoretical calculations have been performed to explain the absence of the $(1\ 0\ 0)$ order and to predict the actual spin configuration.

1. A (*h k l*) structure

Assuming that the soft-mode theory, presented in Sec. XV.B.6, may be used to describe the transition from the polarized phase to the ordered state, Oja and Viertiö (1992, 1993) have predicted the form of the ordering vector for the as-yet-unknown $\mathbf{B}\|(1,1,1)$ phase. First, $\lambda_{\max}$ must be obtained for a vector other than $\mathbf{k}=(\pi/a)(1,0,0)$. Otherwise the transition would always take place at a type-I vector for all field alignments, since $\lambda_{2,3}(\pi/a,0,0)$ is degenerate. Clearly, $\lambda_{\max}$ must be a unique eigenvalue. The corresponding eigenvector **e** should not be perpendicular to any of the three [100] directions so that type-I order could be stable in these field alignments. Therefore $e_x\neq 0, e_y\neq 0$, and $e_z\neq 0$. For the same reason, **e** should not be perpendicular to any of the six [110] directions. Thus $|e_x|\neq|e_y|$, $|e_x|\neq|e_z|$, and $|e_y|\neq|e_z|$. The eigenvector corresponding to the unknown ordering vector **Q** is thus of most general form. Using group-theoretical arguments or direct calculations, one can show that **Q** itself has to be of the most general form, namely, $\mathbf{Q}=(h,k,l)$, with $|h|$, $|k|$, and $|l|$ all unequal and nonzero.

a. Model Hamiltonian

A $\mathbf{Q}=(h,k,l)$ type of ordering vector may seem too complicated for an fcc system. Viertiö and Oja (1993), however, have performed extensive numerical calculations to demonstrate that such an ordering vector is, at least in principle, a real possibility. As the first step, theoretical spin-spin interactions in copper were altered to produce a model that would favor ordering at a **Q**=

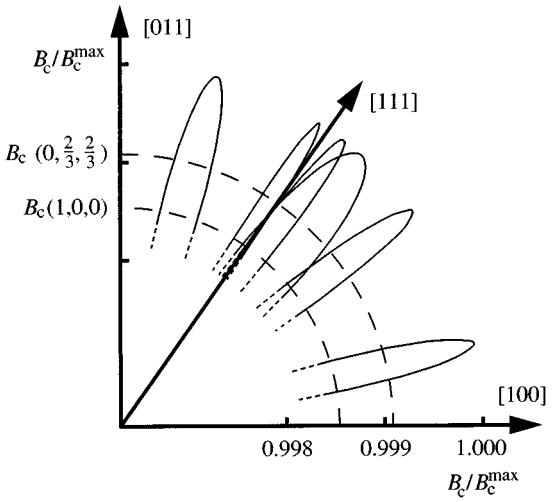

FIG. 125. Critical fields B_c for antiferromagnetic structures in copper, with ordering vectors in the star of $\mathbf{Q}=(\pi/a)(\frac{2}{3},\frac{1}{2},\frac{1}{6})$, as a function of the external-field direction in the plane $B_y=B_z$. The six "finger"-shaped curves represent critical fields for the various cubic-symmetry related vectors. The broken lines with labels (1,0,0) and $(0,\frac{2}{3},\frac{2}{3})$ show B_c's for the corresponding ordering vectors. The scale is $B_c^{max}=0.37$ mT. The resolution has been enhanced greatly as shown by the values on the horizontal axis. From Oja and Viertiö (1993).

(h,k,l) type vector. Modifications of the exchange constants were arbitrary except for the fact that changes were kept within limits that are reasonable in view of the state-of-the-art band-structure calculations of exchange interactions (Lindgård *et al.*, 1986; Oja *et al.*, 1989). It turned out to be possible to construct, using interactions between spins up to the ninth-nearest-neighboring shell, a Hamiltonian for which the following two inequalities hold:

$$\lambda_{max}=\lambda_{max}(\tfrac{2}{3},\tfrac{1}{2},\tfrac{1}{6})\gtrsim\lambda_2(0,\tfrac{2}{3},\tfrac{2}{3})\gtrsim\lambda_{2,3}(1,0,0). \qquad (169)$$

Here, the set of **k**-vectors has been restricted to those compatible with a system of $12^3/2=864$ spins in an fcc lattice, which is the reason that **Q** assumes the rational value $\mathbf{Q}=(\pi/a)(\frac{2}{3},\frac{1}{2},\frac{1}{6})$. The inequalities for $\lambda_2(0,\frac{2}{3},\frac{2}{3})$, which is the relevant eigenvalue for the $(0\ \frac{2}{3}\ \frac{2}{3})$ order, are needed to explain the interplay of the $(0\ \frac{2}{3}\ \frac{2}{3})$ and (1 0 0) modulations in intermediate fields.

The interaction constants that produce this situation were tabulated in the paper of Viertiö and Oja (1993). When they were compared with the calculated exchange constants of Oja, Wang, and Harmon (1989), it was found that the largest absolute change occurred in the nearest-neighbor interaction, which was enhanced by 18%. The modified values are thus reasonable in the sense that they fall within the error bars of the first-principles calculations and within the uncertainty of the various experiments probing exchange constants.

For the modified interactions, the soft-mode transition takes place to a $\mathbf{Q}=(\pi/a)(\frac{2}{3},\frac{1}{2},\frac{1}{6})$ state in fields aligned close to the [111] crystalline direction, as shown by Fig. 125. Whereas in the [011] and [100] field alignments, B_c for a type-I structure is higher than for a $\mathbf{Q}=(\pi/a)(\frac{2}{3},\frac{1}{2},\frac{1}{6})$ configuration. An additional complication arises from the fact that $B_c(0,\frac{2}{3},\frac{2}{3})$ is higher than $B_c(1,0,0)$. However, a suitable 2° misalignment of the field away from the plane $B_y=B_z$ stabilizes type-I modulation over the $(0\ \frac{2}{3}\ \frac{2}{3})$ order in the [011] and [100] field alignments, as observed.

b. *Interplay of the (h k l), (0 2/3 2/3), and (1 0 0) modulations*

Since the soft-mode theory applies only along the phase boundary $B=B_c$, several questions could not be answered. To obtain more information on the actual spin configurations and the magnetic phase diagram of copper nuclei, Viertiö and Oja (1993) performed numerical mean-field calculations in the antiferromagnetically ordered region, for different alignments and strengths of the external magnetic field.

The stable spin configurations were determined by numerical iteration of the mean-field equations. The processes started from various initial configurations made of several combinations of the three modulations $(\frac{2}{3}\ \frac{1}{2}\ \frac{1}{6})$, $(0\ \frac{2}{3}\ \frac{2}{3})$, and (1 0 0). The iterations were continued until a self-consistent solution was found. At every step, one of the 864 spins was randomly chosen, and a new direction and value was assigned to it according to Eqs. (75)–(77). The temperature was fixed at 140 nK=0.83 T_N^{MF} which corresponds to the sublattice polarization $|\langle\mathbf{I}_i\rangle|/I=0.61$.

At each field point, 7–9 different initial configurations were tried. Typically 5–7 inequivalent final states were found, and the stable structure was extracted from the metastable ones by comparing their Gibbs free energies. The phase diagram as a function of the field was then constructed in the plane $B_y=B_z$. The result turned out to be very complex. Altogether 17 ordered phases were found. The magnetic phase diagram deduced from these calculations is presented in Fig. 126.

The ordering vectors of the different phases have been sorted out in Table VIII. The phases are labeled by A, B, and/or C to show that the structure contains $(\frac{2}{3}\ \frac{1}{2}\ \frac{1}{6})$, $(0\ \frac{2}{3}\ \frac{2}{3})$, or (1 0 0) orders, respectively. It can be seen that most of the phases are complicated superposition structures of two different types of ordering vectors. For information on the modulation amplitudes, we refer the reader to the original publication (Viertiö and Oja, 1993).

In high fields, close to the [111] direction, phases A_1–A_4 contain only $(\frac{2}{3}\ \frac{1}{2}\ \frac{1}{6})$ type modulations. This is different from the [100] and [011] field directions, in which the (1 0 0) order, combined with the $(\frac{2}{3}\ \frac{1}{2}\ \frac{1}{6})$ modulation, appears up to B_c. The results are in agreement with the neutron-diffraction measurements of Annila *et al.* (1992).

The simulations revealed some interesting nonlinear effects that were not anticipated on the basis of the linear soft-mode analysis. In particular, exactly in the [100] and [011] field directions, soft-mode analysis predicted that the $(0\ \frac{2}{3}\ \frac{2}{3})$ order would become stable at higher fields than the (1 0 0) order. The simulations showed,

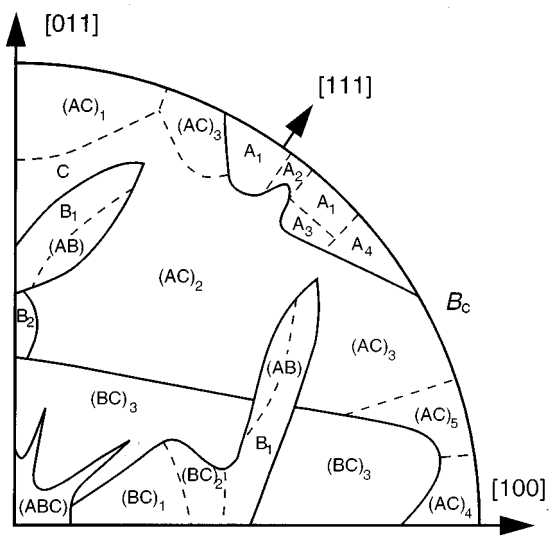

FIG. 126. Magnetic phase diagram of nuclear spins in copper at $T=0.83T_N^{MF}$ in the plane $B_y=B_z$, as given by numerical mean-field simulations of Viertiö and Oja (1993). The diagram consists of 17 phases, which are labeled by A, B, and/or C to show that the structure contains $(\frac{2}{3}\ \frac{1}{2}\ \frac{1}{6})$, $(0\ \frac{2}{3}\ \frac{2}{3})$, and/or (1 0 0) order, respectively. For clarity, similar phases have been grouped into larger units using heavy lines for their boundaries; other borders are indicated with dashed curves. The particular ordering vectors in the stars of the $(\frac{2}{3}\ \frac{1}{2}\ \frac{1}{6})$, $(0\ \frac{2}{3}\ \frac{2}{3})$, and (1 0 0) modulations are listed in Table VIII.

however, that the stable structure combines (1 0 0) and $(\frac{2}{3}\ \frac{1}{2}\ \frac{1}{6})$ modulations but not the $(0\ \frac{2}{3}\ \frac{2}{3})$ component.

Studies of metastable states also produced some interesting and possibly important features. A pure $(\frac{2}{3}\ \frac{1}{2}\ \frac{1}{6})$ state is not even metastable in high fields when $\mathbf{B}\|[100]$ or $\mathbf{B}\|[011]$. In contrast, the pure high-field (1 0 0) structure was found to be metastable in the [100] and [011] directions but unstable in the [111] direction.

There is a discrepancy between the theoretical and experimental phase diagrams of Figs. 126 and 61 in small and zero fields. Although the fundamental ordering vectors in the (ABC) phase are $(\pi/a)(\frac{1}{6},\frac{2}{3},\frac{1}{2})$ and $(\pi/a)(0,1,0)$, the structure also contains some $\mathbf{k}=(\pi/a)(\frac{2}{3},\frac{2}{3},0)$ order at zero field, even though the measured intensity of this Bragg peak vanished at $B=0$. There are two ways to resolve this discrepancy. It is possible that the first-order transitions $(BC)_1\rightarrow$ (ABC) and $(BC)_3\rightarrow$ (ABC) (see Fig. 126) do not take place during the experimental time scale, so that phases $(BC)_1$ and $(BC)_3$, which are formed when B is lowered to zero during adiabatic demagnetization, are metastable at $B=0$. The structures $(BC)_1$ and $(BC)_3$ in zero field become pure (1 0 0) states, which are indeed metastable according to the simulations. Another possibility is that the $(\pi/a)(\frac{2}{3},\frac{2}{3},0)$ component is just the third harmonic of the two fundamental modulations $(\pi/a)(\frac{1}{6},\frac{2}{3},\frac{1}{2})$ and $(\pi/a)(0,1,0)$. The appearance of the $(\frac{2}{3}\ \frac{2}{3}\ 0)$ order at $B=0$ could therefore be due solely to the particular value $\mathbf{k}=(\pi/a)(\frac{1}{6},\frac{2}{3},\frac{1}{2})$, yielding λ_{max} in the simulations. If the maximum eigenvalue were located at another $\mathbf{k}=(h,k,l)$, the third harmonic component

TABLE VIII. Ordering vectors for the theoretical spin structures illustrated in Fig. 126. Most phases can have different domains, but only one is listed; others are obtained by the appropriate symmetry transformations, for instance, by exchanging the y and z components of the ordering vectors. From Viertiö and Oja (1993).

Phase	Ordering vectors $\mathbf{k}(\pi/a)$
A_1	$(\frac{1}{6},\frac{2}{3},\frac{1}{2})$ & $(\frac{1}{2},\frac{2}{3},\frac{1}{6})$
A_2	$(\frac{2}{3},\frac{1}{2},\frac{1}{6})$
A_3	$(\frac{2}{3},\frac{1}{2},\frac{1}{6})$ & $(\frac{2}{3},\frac{1}{6},\frac{1}{2})$
A_4	$(\frac{2}{3},\frac{1}{2},-\frac{1}{6})$ & $(\frac{1}{6},\frac{2}{3},\frac{1}{2})$
B_1	$(\frac{2}{3},\frac{2}{3},0)$
B_2	$(\frac{2}{3},\frac{2}{3},0)$ & $(\frac{2}{3},-\frac{2}{3},0)$
C	(1,0,0) & (0,1,0) & (0,0,1)
(ABC)	$(\frac{1}{6},\frac{2}{3},\frac{1}{2})$ & $(\frac{2}{3},\frac{2}{3},0)$ & (0,1,0) or $(\frac{1}{2},\frac{2}{3},-\frac{1}{6})$ & $(0,\frac{2}{3},-\frac{2}{3})$ & (0,1,0) or $(\frac{2}{3},-\frac{1}{6},\frac{1}{2})$ & $(\frac{2}{3},-\frac{2}{3},0)$ & (1,0,0)
(AB)	$(\frac{2}{3},\frac{2}{3},0)$ & $(\frac{1}{6},\frac{2}{3},\frac{1}{2})$
$(AC)_1$	$\left\{\begin{matrix}(\frac{1}{2},\frac{2}{3},-\frac{1}{6})\\(\frac{1}{2},-\frac{2}{3},\frac{1}{6})\\(\frac{1}{2},-\frac{1}{6},\frac{2}{3})\\(\frac{1}{2},\frac{1}{6},-\frac{2}{3})\end{matrix}\right\}$ & & (1,0,0)
$(AC)_2$	$\left\{\begin{matrix}(\frac{1}{2},\frac{2}{3},\frac{1}{6})\\(\frac{1}{2},-\frac{2}{3},-\frac{1}{6})\\(\frac{1}{2},\frac{1}{6},\frac{2}{3})\\(\frac{1}{2},-\frac{1}{6},-\frac{2}{3})\end{matrix}\right\}$ & & (1,0,0) when $B_x\leqslant B_y$
$(AC)_2$	$\left\{\begin{matrix}(\frac{2}{3},\frac{1}{6},\frac{1}{2})\\(-\frac{2}{3},-\frac{1}{6},\frac{1}{2})\\(\frac{1}{6},\frac{2}{3},\frac{1}{2})\\(-\frac{1}{6},-\frac{2}{3},\frac{1}{2})\end{matrix}\right\}$ & & (0,0,1) when $B_x\geqslant B_y$
$(AC)_3$	$\left\{\begin{matrix}(\frac{2}{3},-\frac{1}{6},\frac{1}{2})\\(-\frac{2}{3},\frac{1}{6},\frac{1}{2})\\(\frac{1}{6},\frac{2}{3},\frac{1}{2})\\(-\frac{1}{6},-\frac{2}{3},\frac{1}{2})\end{matrix}\right\}$ & & (0,0,1)
$(AC)_4$	$\left\{\begin{matrix}(\frac{1}{6},-\frac{2}{3},\frac{1}{2})\\(-\frac{1}{6},\frac{2}{3},\frac{1}{2})\\(\frac{1}{6},\frac{2}{3},\frac{1}{2})\\(-\frac{1}{6},-\frac{2}{3},\frac{1}{2})\end{matrix}\right\}$ & & (0,0,1)
$(AC)_5$	$(\frac{1}{6},-\frac{2}{3},\frac{1}{2})$ & (1,0,0)
$(BC)_1$	$(\frac{2}{3},\frac{2}{3},0)$ & $(\frac{2}{3},-\frac{2}{3},0)$ & (0,1,0)
$(BC)_2$	$(\frac{2}{3},\frac{2}{3},0)$ & (1,0,0) & (0,1,0) & (0,0,1)
$(BC)_3$	$(0,\frac{2}{3},-\frac{2}{3})$ & (1,0,0)

would not be $(\pi/a)(\frac{2}{3},\frac{2}{3},0)$. Actually, the (ABC) phase would then be of type (AC).

As for quantitive features, the agreement between the phase diagram of Fig. 126 and the neutron-diffraction measurements could be somewhat better. For example, the configurations A_1–A_4 with no (1 0 0) order should extend to lower fields in the [111] direction. There are, however, possible explanations of this discrepancy (Oja and Viertiö, 1993).

In low intermediate fields, the phase diagram of Fig. 126 reproduces the interplay of the $(0\ \frac{2}{3}\ \frac{2}{3})$ and (1 0 0) modulations consistently with the experiments of Annila *et al.* (1990, 1992) and the earlier theoretical calculations of Viertiö and Oja (1990a, 1990b).

All in all, these mean-field results can model the very complicated behavior of copper nuclei in the whole $B_y = B_z$ plane within a single theoretical framework using fixed values of interaction parameters.

c. Criticism

It has been emphasized by Lindgård (1992) that it would be more satisfactory if the [111] phase of copper could be explained using a simpler set of exchange parameters than those employed in the simulations of Viertiö and Oja (1993). However, the first-principles calculations of the spin-spin interactions have shown that the long range of the isotropic Ruderman-Kittel interaction, as well as anisotropic exchange forces, can be important in the selection of the ground state. In fact, the use of a linear theory, together with the constraints obtained from experiments, dictates the most symmetric form $\mathbf{Q}=(h,k,l)$ for the ordering vector. A simpler type of order can emerge only as a result of fluctuations, which are neglected in the linear soft-mode calculation and in the mean-field theory.

Fluctuations might indeed play a decisive role in this problem. For the interactions used in the mean-field calculations of Viertiö and Oja (1993), the energies of the three different types of modulations are very close to each other: The relevant eigenvalues are $\lambda_{\max}(\frac{2}{3},\frac{1}{2},\frac{1}{6})/k_B$=135.57 nK, $\lambda_2(0,\frac{2}{3},\frac{2}{3})/k_B$=135.31 nK, and $\lambda_{2,3}(1,0,0)/k_B$=135.16 nK. Monte Carlo simulations could, of course, take into account thermal fluctuations of classical spins. However, the problem in such simulations would be the presence of several metastable states, and determining the stable structure would be computationally a difficult task. The simulations using mean-field theory did not suffer from this problem since calculation of the Gibbs free energy was straightforward.

It should also be noted that all theoretical work done so far has considered only the conventional, long-range antiferromagnetic order.

In the experiments, on the other hand, one of the important questions is whether the observed behavior relates to equilibrium situations. It is difficult, if not impossible, to fully assure oneself that this is indeed the case. Even for electronic magnets, with several decades shorter time scales, nonequilibrium behavior has been observed in geometrically frustrated systems (Ballou *et al.*, 1992).

2. Other possibilities

The high-field spin structure of copper for $\mathbf{B}\|[111]$ has been studied by Lindgård (1992). He, too, employed the soft-mode theory. A detailed comparison between his results and the calculations of Oja and Viertiö (1993) is difficult because Lindgård reported in his brief paper only the final numerical results.

Lindgård (1992) found that the wave vector of the spin-wave excitation, which softens in the paramagnetic state, is (i) the type-I vector $(\pi/a)(1,0,0)$, $(\pi/a)(0,1,0)$, or $(\pi/a)(0,0,1)$ when $\mathbf{B}\|[001]$ or $\mathbf{B}\|[110]$, and (ii) $\mathbf{k}=(t+\delta,t-\delta,0)$ with $t\sim(\frac{2}{3})(\pi/a)$ and $\delta\sim 0.05(\pi/a)$ when $\mathbf{B}\|[111]$. These results conflict, however, with some analytical properties of the soft-mode transition discussed in Sec. XV.B.6, and they cannot be reproduced from this theory (for further details, see Oja and Viertiö, 1993). Although the results of Lindgård were promising in the sense that they were consistent with neutron-diffraction data and provided an interesting prediction to be tested by future experiments, it seems that his results are erroneous.

Testing the prediction of a $\mathbf{Q}=(h,k,l)$ type ordering vector is very difficult, since it is not practical to scan through the whole reciprocal space. For experimentalists it would therefore be desirable for the order to show up in a more accessible, high-symmetry direction of the $\mathbf{k}$ space. This, together with the critical remarks on the $(h\ k\ l)$ order presented in the previous section, has been the motivation for other theoretical suggestions.

One proposal (Oja and Viertiö, 1992) is based on the idea that the lock-in mechanism that stabilizes the $(0\ \frac{2}{3}\ \frac{2}{3})$ order at a commensurate $\mathbf{k}$ vector in low and intermediate fields is not operational in high fields. This is plausible in view of some observations on electronic magnets, namely, that a commensurate order → incommensurate order → disorder sequence is often found with increasing T, when the low-T ordering vector is not at the zone boundary (see, for example, Rossat-Mignod *et al.*, 1979). When copper nuclei enter the high-field [111] phase, they are necessarily near the ordering temperature. By examining the energy eigenvalues, Oja and Viertiö concluded that incommensuration is most likely to occur for a $\mathbf{k}$ vector of the form $\mathbf{k}=(\pi/a)(\delta,\frac{2}{3}+\epsilon,\frac{2}{3}+\epsilon)$. In fact, a local, but not the global, maximum of $\lambda_n(\mathbf{k})$ is obtained at $\mathbf{k}=(\pi/a)(0, 0.55, 0.55)$, making the $[0\,\eta\,\eta]$ direction most promising, as is illustrated by Fig. 112. Neutron-diffraction measurements testing this possibility have not as yet been performed (see Sec. VII.J).

It has also been suggested that the high-field [111] structure of copper could be a spiral configuration with the ordering vector along the field direction (Oja and Viertiö, 1992; Viertiö and Oja, 1993). Such a proposal faces difficulties in low fields and requires a near degeneracy of three completely different types of ordering vectors. In addition, the calculated exchange interactions would have to be off by tens of percent.

Siemensmeyer and Steiner (1992) have suggested that magnetoelastic energy due to quadrupolar moments of

copper nuclei is important in the selection of the stable spin structure in the high-field region.

H. Ferromagnetic ordering at $T<0$

Ferromagnetic ordering at negative temperatures for a spin system interacting through the dipolar and exchange interactions, as in silver (see Hakonen, Nummila, Vuorinen, and Lounasmaa, 1992), has been analyzed theoretically by Viertiö and Oja (1992). Their work follows the earlier treatments of nuclear-spin systems of insulators in a rotating coordinate frame (Abragam and Goldman, 1982). There are, however, some important differences between the two cases owing to the fact that only the truncated part of the dipolar interaction is important for insulators.

At $T<0$, the system orders into a state that corresponds to the minimum eigenvalue $\lambda_n(\mathbf{k})$, provided that this state is permanent. The minimum value can be obtained in the limit $\mathbf{k}\rightarrow 0$ (see, for example, Kumar *et al.*, 1985),

$$\lambda_{\min}\equiv\lambda_1(\mathbf{k}\rightarrow 0)=(-\tfrac{2}{3}+R)\mu_0\hbar^2\gamma^2\rho, \tag{170a}$$

$$\mathbf{e}_1(\mathbf{k}\rightarrow 0)=\hat{\mathbf{k}}. \tag{170b}$$

The limiting values are to be taken at an infinitesimally small but nonzero $\mathbf{k}$. Exactly at $\mathbf{k}=0$, the eigenvalue $\lambda_\mu(0)=(L-D_\mu+R)\mu_0\hbar^2\gamma^2\rho$ depends on the shape of the sample.

For an infinite plate perpendicular to the z direction, $D_x=D_y=0$ and $D_z=1$, so that $\lambda_1(\mathbf{k}\rightarrow 0)$ coincides with $\lambda_z(0)$. Therefore a $\mathbf{k}=0$ state of uniform magnetization along the z direction is stable.[26]

For all other sample shapes $\lambda_1(\mathbf{k})$ is discontinuous at $\mathbf{k}=0$, and the maximum eigenvalue is obtained for a vanishingly small but nonzero $|\mathbf{k}|$. Physically, this means that the sample breaks into domains that can be described by a quasipermanent spin structure, which is a superposition of modulations with small $\mathbf{k}$-vectors (Abragam and Goldman, 1982). In contrast to the situation in dielectrics, the directions of $\mathbf{k}$ and $\langle\mathbf{I}(\mathbf{k})\rangle$ in a metal are not restricted by the external magnetic field (Viertiö and Oja, 1992). This results in a wide variety of stable structures.

1. Domain configurations

Let us consider the case of two types of domains with spins $\langle\mathbf{I}_i\rangle=\mathbf{I}_A$ in domains of type A and $\langle\mathbf{I}_i\rangle=\mathbf{I}_B$ in domains of type B. Three possible two-domain configurations in silver at $T<0$ have been illustrated in Fig. 127. There are xN and $(1-x)N$ spins in domains A and B, respectively. It is useful to express $\mathbf{I}_A$ and $\mathbf{I}_B$ in terms of a static and an oscillating part,

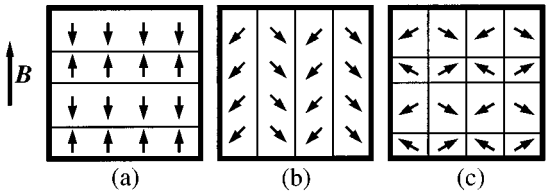

FIG. 127. Three degenerate domain configurations of silver nuclei at $T<0$ in a magnetic field $\mathbf{B}$ pointing upwards. Modified from Viertiö and Oja (1992).

$$\mathbf{I}_{A,B}=\mathbf{I}_{\rm av}+\mathbf{I}'_{A,B}, \tag{171}$$

where

$$\mathbf{I}_{\rm av}=\langle\mathbf{I}(\mathbf{k}=0)\rangle=x\mathbf{I}_A+(1-x)\mathbf{I}_B \tag{172}$$

is the magnetization, apart from a constant coefficient. The oscillating parts are

$$\mathbf{I}'_A=\sum_{\mathbf{k}\neq 0}\langle\mathbf{I}(\mathbf{k})\rangle\exp(i\mathbf{k}\cdot\mathbf{r}_{i\in A})=(1-x)(\mathbf{I}_A-\mathbf{I}_B), \tag{173}$$

$$\mathbf{I}'_B=\sum_{\mathbf{k}\neq 0}\langle\mathbf{I}(\mathbf{k})\rangle\exp(i\mathbf{k}\cdot\mathbf{r}_{i\in B})=-x(\mathbf{I}_A-\mathbf{I}_B). \tag{174}$$

The local fields acting on spins in the two domains are

$$\mathbf{B}_{i\in A}=\mathbf{B}_0+[\lambda_z(0)\mathbf{I}_{\rm av}+\lambda_1(\mathbf{k}\rightarrow 0)\mathbf{I}'_A]/(\hbar\gamma), \tag{175}$$

$$\mathbf{B}_{i\in B}=\mathbf{B}_0+[\lambda_z(0)\mathbf{I}_{\rm av}+\lambda_1(\mathbf{k}\rightarrow 0)\mathbf{I}'_B]/(\hbar\gamma), \tag{176}$$

where the static external field $\mathbf{B}_0=B_0\mathbf{z}$. Here we have made use of Eq. (75) and the assumption that the width of the domains is large in comparison with the lattice parameter, so that only small $\mathbf{k}$-vectors are relevant (see p. 490 in Abragam and Goldman, 1982). There should, however, be many domains in the sample. We have further assumed that the oscillating component of the domain magnetization, proportional to $\mathbf{I}_A-\mathbf{I}_B$, is aligned along the direction of modulation, i.e., the nonzero wave vectors $\mathbf{k}$ in Eqs. (173) and (174). This selects the coefficients $\lambda_1(\mathbf{k}\rightarrow 0)$ which multiply $\mathbf{I}'_{A,B}$ in the expressions for the local fields.

For a constant entropy and magnetic field, the stable state corresponds to a maximum of the magnetic enthalpy E. The entropy is constant if $|\mathbf{I}_A|=|\mathbf{I}_B|$ =constant. The stable states can be found by maximizing the enthalpy with respect to the division parameter x and the directions of $\mathbf{I}_A$ and $\mathbf{I}_B$. Viertiö and Oja (1992) derived an equation for E by using Eq. (78) and the expressions for the local fields $\mathbf{B}_{i\in A}$ and $\mathbf{B}_{i\in B}$. It is more convenient, however, to make use of Eq. (84). Assuming that $\mathbf{I}_{\rm av}$ is along the external field, and neglecting all contributions from domain walls, we obtain

$$E/N=-\hbar\gamma B_0 I_{\rm av}-\tfrac{1}{2}[\lambda(0)-\lambda_1(\mathbf{k}\rightarrow 0)]I_{\rm av}^2 -\tfrac{1}{2}\lambda_1(\mathbf{k}\rightarrow 0)I^2p^2. \tag{177}$$

[26]It is interesting that for a purely dipolar system in an fcc lattice $\lambda_{\max}$ is also obtained at $\mathbf{k}\rightarrow 0$: $\lambda_{2,3}(\mathbf{k}\rightarrow 0)=\mu_0\hbar^2\gamma^2\rho/3$, with $\mathbf{e}_2,\mathbf{e}_3\perp\mathbf{k}$. The ferromagnetic state is therefore stable at $T>0$ as well as at $T<0$, but the domain structures differ because of the different relative orientations of $\langle\mathbf{I}(\mathbf{k})\rangle$ and $\mathbf{k}$. Dipolar ferromagnetic ordering in an fcc lattice has recently been investigated experimentally by Roser and Corruccini (1990) in several $Cs_2NaR(NO_2)_6$ rare-earth salts, and theoretically by Bouchaud and Zérah (1993).

We have here made use of the sum rule

$$I_{\rm av}^2+\sum_{\mathbf{k}\neq 0}|\langle\mathbf{I}(\mathbf{k})\rangle|^2=I^2p^2, \tag{178}$$

where p is the polarization and $|\mathbf{I}_A|=|\mathbf{I}_B|=pI$. The maximum of E is found by requiring $\partial E/\partial x=(\partial E/\partial I_{\rm av})(\partial I_{\rm av}/\partial x)=0$. The nontrivial solution yields the magnetization

$$\mathbf{M}=\hbar\gamma\rho\mathbf{I}_{\rm av}=-\mathbf{B}_0/[\mu_0(1-D_z)]. \tag{179}$$

It should be noted that **M** is antiparallel to the external field in order to maximize E. The domain structure is stable below

$$B_c=\mu_0\hbar\gamma\rho Ip(1-D_z). \tag{180}$$

In this sense there is a ferromagnetic transition in a nonvanishing external field.

The above equations yield local fields $\mathbf{B}_i=\lambda_1(\mathbf{k}\rightarrow 0)\langle\mathbf{I}_i\rangle/(\hbar\gamma)$; here $|\langle\mathbf{I}_i\rangle|=pI$ where p is obtained from Eq. (76). Thus the magnitude of the local fields and spins is indeed constant, as was assumed at the beginning of the calculation. Hence the solutions obtained by maximizing E correspond to the stable state.

For the domain configuration illustrated in Fig. 127(a), the magnetization depends on the relative volumes of the two types of domains. When the external field is increased, the domains with magnetizations antiparallel to the field grow at the expense of those with parallel magnetizations. The equilibrium **M** of Eq. (179) corresponds to the relative volume of domains A expressed by

$$x=\tfrac{1}{2}(1+B_0/B_c). \tag{181}$$

This kind of domain structure has been found in dielectric nuclear magnets both theoretically (Abragam and Goldman, 1982) and experimentally. Neutron-diffraction measurements by Roinel *et al.*. (1980) revealed the presence of ferromagnetic domains in the form of thin slices, approximately 20-Å thick, perpendicular to the external field.

Figures 127(b) and 127(c) show configurations that do not exist in dielectrics in the rotating frame. In the structure of Fig. 127(b), spins adjust to the external field simply by canting, and no movement of domain walls is necessary. In this case, the relative volumes of the two domains are always equal, i.e., $x=\frac{1}{2}$. The structure in Fig. 127(c) is a superposition of the patterns (a) and (b). Spins can adjust to the external field both by canting and by domain-wall movement. It is also possible to have a domain-modulation in the third Cartesian direction.

According to Viertiö and Oja (1992), the general characteristics of domain structures at $T<0$ are that the tangential component of magnetization is always continuous and the normal component changes sign at a domain boundary. The opposite is true at positive spin temperatures.

2. Demagnetization into the domain state

The enthalpy per spin for the domain configurations of Fig. 127 is given by

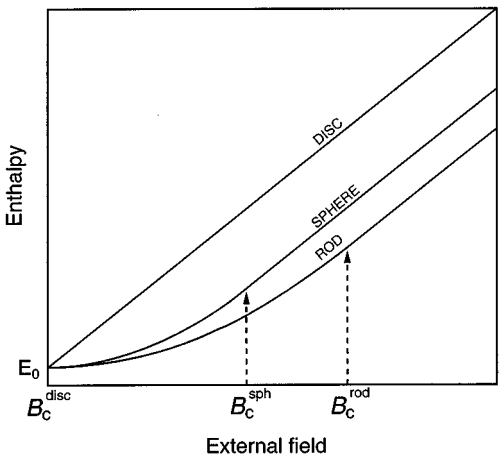

FIG. 128. Magnetic enthalpy for samples of different shapes (infinite disc normal to **B**, sphere, and an infinitely long rod with its axis along **B**) in an external magnetic field at $T=-0$. Domains are created below the respective critical fields $B_c^{\rm disc}=0$, $B_c^{\rm rod}=\mu_0\hbar\gamma\rho I$, and $B_c^{\rm sph}=\frac{2}{3}B_c^{\rm rod}$.

$$E/N=\tfrac{1}{2}B^2/[\mu_0\rho(1-D_z)]-\tfrac{1}{2}\lambda_1(\mathbf{k}\rightarrow 0)I^2p^2. \tag{182}$$

Figure 128 shows how E depends on the external field for samples with different shapes. It is obvious that formation of domains makes it possible for, say, a sphere-shaped specimen to mimic the most advantageous sample shape at $T<0$, namely, an infinite plate perpendicular to the external field.

Since the local fields have a constant value for the domain states, the structures are permanent (see Sec. XV.B.4). It then follows, similarly to the type-I fcc antiferromagnets (see Sec. XV.B.5 and Fig. 7), that the lines of constant entropy are vertical in the (T,B) region corresponding to the domain state.

Although the three domain configurations of Fig. 127 are all degenerate in E, the processes that are needed to create them during demagnetization are very different. As illustrated in Fig. 129, the sample can be demagnetized into the domain state of Fig. 127(b) by continuous canting of the spins. The situation is completely different for the two other domain configurations illustrated in Fig. 127. In case (a), when the system is demagnetized below B_c, domains with magnetizations completely opposite to the rest of the sample should be created to maximize E. Nucleation of such domains is likely to be a slow process. Adjustment to the external field for domain configuration (a) is also much more difficult than

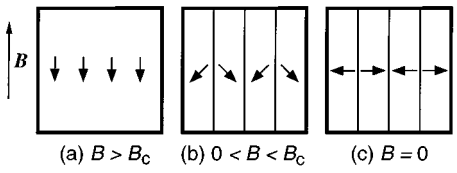

FIG. 129. Spin directions during demagnetization into a domain state. For explanations, see text. Modified from Viertiö and Oja (1992).

for state (b) because movement of domain walls is certainly a slower process than canting of individual spins. Similarly, we expect that configuration (c) suffers from a slow nucleation, although the problem is not so severe as for the state (a). We conclude that domain configuration (b) is the most likely to be present in experiments.

If the spins are indeed ordered in the domain pattern of Fig. 127(b), it should be possible to reverse **B** with no hysteresis (Viertiö and Oja, 1992). This is in agreement with measurements on silver that did not show any hysteresis while the field direction across the ferromagnetically ordered region was slowly reversed (Hakonen, Nummila, Vuorinen, and Lounasmaa, 1992).

3. Comparison with experimental data on silver

The ferromagnetic nuclear-spin structure in silver at $T<0$ has been investigated using Monte Carlo simulations (Viertiö and Oja, 1992). In these calculations the demagnetization factors were chosen as $D_x=D_y=0$ and $D_z=1$ to imitate the equilibrium inside a single domain. The spin-spin interactions were summed up to the eighth neighboring cell. Simulations found ferromagnetic ordering along the z axis above $T=T_C=-1.7$ nK. Adiabatic demagnetization was also simulated, whereby a critical initial polarization $p_c=30\%$ for ferromagnetic ordering was obtained. This is clearly lower than the observed $p_c=(49\pm5)\%$, although the theoretical T_C is in good agreement with the measured $T_C=-(1.9\pm0.4)$ nK.

These Monte Carlo simulations were made for classical spins with magnetic moments $\mu=\gamma\hbar I$. Since nuclear spins in silver have $I=\frac{1}{2}$, the assumption of a classical spin is a severe approximation. As we discussed in Sec. XV.C.3c, a rule of thumb for taking into account this difference is to multiply the simulated T_C by the factor $(I+1)/I$. This leads, however, to almost a factor-of-3 discrepancy between the theoretical and observed T_C's of silver.

Unlike the ordering temperature, static magnetic susceptibility is expected to be rather insensitive to I. The simulations and the mean-field theory both reproduced the measured result for the transversal susceptibility; the corresponding three values fall between $\chi=-0.9$ and $\chi=-1.1$.

XVI. SUMMARY AND FUTURE PROSPECTS

A. Copper

The magnetic phase diagram of copper is summarized in Fig. 130 on the basis of experimental and theoretical studies. The $(0\ \frac{2}{3}\ \frac{2}{3})$ and (1 0 0) spin configurations have been investigated in detail by neutron-diffraction measurements and by theoretical calculations. The general trend is that the (1 0 0) order is found in low and high fields while the $(0\ \frac{2}{3}\ \frac{2}{3})$ spin configuration is stable in intermediate fields. An important exception however, is, the high-field configuration for the $\mathbf{B}\|[111]$ alignment, where no (1 0 0) order has been found. This remains an

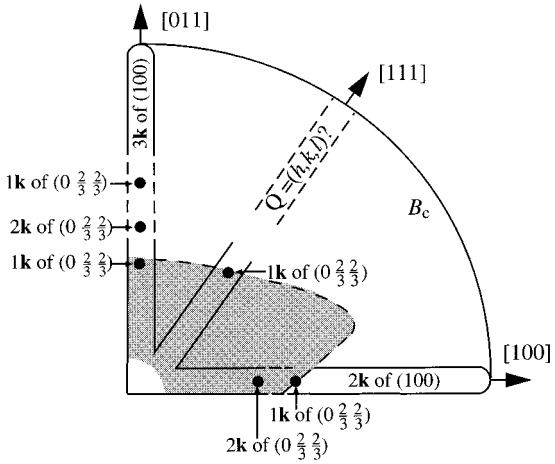

FIG. 130. Magnetic phase diagram of copper nuclei in the plane $B_y=B_z$. The illustration is based on a combination of neutron-diffraction data and theoretical calculations. The gray area corresponds to fields in which the $(0\ \frac{2}{3}\ \frac{2}{3})$ and (1 0 0) orders exist simultaneously. The form of this region is tentative. The ordering vector $\mathbf{Q}=(h,k,l)$ is only one of several possibilities.

open question although several suggestions have been made, including, in particular, an ordering vector of the form $\mathbf{Q}=(h,k,l)$, with $|h|$, $|k|$, and $|l|$ all unequal and nonzero. Another possibility is an incommensuration of the $\mathbf{k}=(\pi/a)(0,\frac{2}{3},\frac{2}{3})$ ordering vector along the $[0\,\eta\,\eta]$ direction.

In the high-field regions for the [011] and [100] field alignments, neutron-diffraction data were consistent with the theoretically predicted triple-**k** and double-**k** type-I structures. In low and intermediate fields, alignment of **B** with respect to the crystalline axes had a dramatic effect on the stability of various cubic-symmetry-related $(0\ \frac{2}{3}\ \frac{2}{3})$ Bragg reflections. The fact that the measurements completely agreed with theoretical selection rules adds confidence to the calculated spin configurations. In low intermediate fields, measurements found simultaneous $(0\ \frac{2}{3}\ \frac{2}{3})$ and (1 0 0) orders, which seemed to be the result of superposition of the two ordering vectors in a single magnetic domain. The proposal must still be confirmed experimentally. For field alignments somewhat off the [100] direction it is possible that a superposition structure extends to relatively high fields, as sketched in Fig. 130.

B. Other simple metals

The magnetic phase diagram of silver was summarized in Fig. 4. The observation of antiferromagnetism at positive temperatures and ferromagnetism at negative temperatures provides an excellent illustration of basic principles of statistical physics. At $T>0$, the type-I ordering vector has been found in recent neutron-diffraction measurements (Tuoriniemi, Nummila *et al.*, 1995). New information on ordered spin structures for different alignments of the field will soon be available. The dis-

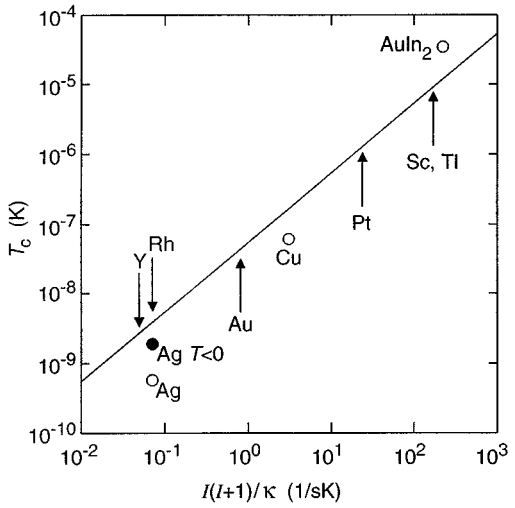

FIG. 131. Observed nuclear-ordering temperatures of silver, copper, and $AuIn_2$ vs $I(I+1)/\kappa$; I is the spin, and κ is the Korringa constant. The line $T_c=5\times10^{-8}$ K [I(I+1)/κ] sK is only a guide for the eye. The solid circle represents the absolute value of the Curie temperature of silver at $T<0$. The values for $I(I+1)/\kappa$ in several other nuclear-spin systems have been indicated as well.

crepancy between theoretical and observed ordering temperatures, both at $T>0$ and $T<0$, warrants further investigations.

The obvious next goal in studies on rhodium is to observe nuclear-spin ordering.

The origin of the high ferromagnetic ordering temperature of ^{115}In in $AuIn_2$ is a subject of considerable interest. To further substantiate the presence of a large exchange interaction, it might be useful to study exchange merging of the NMR lines of ^{115}In and ^{113}In as has been done in thallium. Electronic band-structure calculations of exchange forces are very much in order. The importance of magnetoelastic coupling between nuclear spins and the lattice should be further investigated as has been discussed by Siemensmeyer and Steiner (1992).

There are several other simple metals for which one can expect important progress in the study of nuclear ordering. These include, for example, gold, thallium, scandium, platinum, and yttrium. The presence of magnetic impurities, even at the level of one-ppm, is a problem in several of these materials and poses serious materials-science challenges. To estimate the ordering temperature in these metals one may assume that T_c is determined by the Ruderman-Kittel mechanism. According to the free-electron picture, the strength of the Ruderman-Kittel interaction is approximately proportional to the inverse of the Korringa constant κ (see, for example, Oja and Kumar, 1987; Slichter, 1990; Herrmannsdörfer and Pobell, 1995). One expects then that, within an order of magnitude, $T_c\approx I(I+1)/\kappa$, where I is the spin. The observed T_c's of copper, silver, and $AuIn_2$ display such a dependence, as shown in Fig. 131. A rough estimate of the ordering temperature in Au, Rh, Tl, Sc, Pt, and Y can be obtained on the basis of their $I(I+1)/\kappa$ parameters, which are indicated in the figure as well.

C. Temperature records

Usually as a by-product of their research, ultralow-temperature physicists are, from time to time, drawing closer to their elusive goal of achieving the absolute zero. Figure 132 (see p. 58) illustrates the progress during the last 25 years. What has been achieved depends on the substance that has been refrigerated.

^3He is an important subject of research at ultralow temperatures. This includes the superfluid liquid, dilute mixtures of ^3He and ^4He, and solid ^3He. Superfluid ^3He has been refrigerated below 100 μK by the group of George Pickett at Lancaster University (Carney *et al.*, 1989), and more recently by the group of Frank Pobell at the University of Bayreuth (König, Betat, and Pobell, 1994) and by Bunkov and Fisher (1995) at Grenoble. Dilute solutions have been cooled to 100 μK by the Osaka team (Oh *et al.*, 1994) and by the group at Bayreuth (König, Betat, and Pobell, 1994). Solid ^3He has been refrigerated to temperatures around 30–40 μK by groups at Tokyo, Osaka, and Nagoya (Takano *et al.*, 1985; Yano *et al.*, 1990; Suzuki, Kondo *et al.*, 1991; Okamoto *et al.*, 1994).

Metals offer another important category of specimens that have been studied at ultralow temperatures. Conduction-electron temperatures in copper of about 10 μK and below have been measured by the groups of Pobell (Gloos *et al.*, 1988) and Pickett (Enrico *et al.*, 1994). In Helsinki, nuclear spins have been cooled to 280 pK in rhodium, while the "hot" record at negative nuclear temperatures is -750 pK (see Sec. X.A). Spontaneous spin ordering has been observed at 560 pK for antiferromagnetism and at -1.9 nK for ferromagnetism in silver (see Sec. VIII).

The newest entry into the race for low-temperature records is Bose-Einstein condensation in gaseous assemblies of several alkaline atoms. Researchers at the National Institute of Standards and Technology in Boulder, together with their colleagues at the University of Colorado, first reported Bose-Einstein condensation in rubidium atoms near a temperature of 170 nanokelvin (Anderson *et al.*, 1995). The progress in this field has been very rapid since this breakthrough (Culotta, 1995).

ACKNOWLEDGMENTS

Preparation of this review was financially supported by the Academy of Finland. We express our gratitude to our colleagues Pertti Hakonen, Marko Heinilä, Kim Lefmann, Kaj Nummila, Hanna Viertiö-Oja, Reko Vuorinen, and Juha Tuoriniemi for several useful discussions. We have also benefitted from comments by Yuriy Bunkov, Georg Eska, George Pickett, Frank Pobell, Martti Salomaa, Haruhiko Suzuki, Michael Steiner, and Yasumasa Takano. We are indebted to Harri Colerus, Ursula Holmström, Tauno Knuuttila, and Juha Martikainen for help in preparing the illustrations. Finally, we

thank the anonymous referees for their useful and detailed comments on the manuscript.

REFERENCES

Aalto, M. I., P. M. Berglund, H. K. Collan, G. J. Ehnholm, R. G. Gylling, and O. V. Lounasmaa, 1972, ''Nuclear spin-lattice relaxation of the Zeeman and the spin-spin systems in copper between 1 and 17 mK,'' Physica **61**, 314–320.

Abragam, A., 1961, *The Principles of Nuclear Magnetism* (Clarendon, Oxford).

Abragam, A., 1987, ''Ordering nuclear spins,'' Proc. R. Soc. London, Ser. A **412**, 255–268.

Abragam, A., and M. Goldman, 1982, *Nuclear Magnetism: Order and Disorder* (Clarendon, Oxford).

Abragam, A., J. F. Jacquinot, M. Chapellier, and M. Goldman, 1973, ''Absortion lineshape of highly polarized nuclear spin systems,'' J. Magn. Reson. **10**, 322–346.

Abragam, A., and W. G. Proctor, 1958, ''Spin temperature,'' Phys. Rev. **109**, 1441–1458.

Akai, K., and H. Ishii, 1994, ''Electronic specific heat in metallic Van Vleck paramagnets,'' Phys. Rev. B **49**, 275–284.

Akhiezer, A. I., V. G. Bar'yakhtar, and S. V. Peletminskii, 1968, *Spin Waves* (North-Holland, Amsterdam).

Alloul, H., and C. Froidevaux, 1967, ''Nuclear-magnetic-resonance spin echoes in alloys,'' Phys. Rev. **163**, 324–335.

Al'tshuler, S. A., 1966, ''Use of substances containing rare-earth ions with even number of electrons to obtain infralow temperatures,'' Pis'ma Zh. Éksp. Teor. Fiz. **3**, 180–183 [Sov. Phys. JETP Lett. **3**, 112–115 (1966)].

Anderson, A. G., 1962, ''Nuclear spin absortion spectra in solids,'' Phys. Rev. **125**, 1517–1527.

Anderson, M. H., J. R. Ensher, M. R. Matthews, C. E. Wieman, and E. A. Cornell, 1995, ''Observation of Bose-Einstein condensation in a dilute atomic vapor,'' Science **269**, 198–201.

Anderson, P. W., 1973, ''Resonating valence bonds: A new kind of insulator?'' Mater. Res. Bull. **8**, 153–160.

Andres, K., and E. Bucher, 1968, ''Observation of hyperfine-enhanced nuclear magnetic cooling,'' Phys. Rev. Lett. **21**, 1221–1223.

Andres, K., and E. Bucher, 1972, ''Nuclear cooling in $PrCu_6$,'' J. Low Temp. Phys. **9**, 267–289.

Andres, K., E. Bucher, J. P. Maita, and A. S. Cooper, 1972, ''Observation of cooperative nuclear magnetic order in $PrCu_2$ below 54 mK,'' Phys. Rev. Lett. **28**, 1652–1655.

Andres, K., E. Bucher, P. H. Schmidt, J. P. Maita, and S. Darack, 1975, ''Nuclear-induced ferromagnetism below 50 mK in the Van Vleck paramagnet $PrCu_5$,'' Phys. Rev. B **11**, 4364–4372.

Andres, K., E. Hagn, E. Smolic, and G. Eska, 1975, ''A $PrCu_6$ cryostat for nuclear orientation experiments down to 2.7 mK,'' J. Appl. Phys. **46**, 2752–2759.

Andres, K., and O. V. Lounasmaa, 1982, ''Recent progress in nuclear cooling,'' Prog. Low Temp. Phys. **8**, 221–287.

Andrew, E. R., 1973, ''NMR in rapidly-rotated metals,'' in *Proceedings of the XVII Congress Ampère,* edited by V. Hovi (North-Holland, Amsterdam), pp. 18–32.

Andrew, E. R., J. L. Carolan, and P. J. Randall, 1971, ''Measurement of the Ruderman-Kittel interaction for copper,'' Phys. Lett. A **37**, 125–126.

Andrew, E. R., and W. S. Hinshaw, 1973, ''Indirect nuclear interaction coupling constants for metallic copper,'' Phys. Lett. A **43**, 113–114.

Angerer, U., and G. Eska, 1984, ''Nuclear demagnetization of thallium,'' Cryogenics **53**, 515–521.

Annila, A. J., K. N. Clausen, P.-A. Lindgård, O. V. Lounasmaa, A. S. Oja, K. Siemensmeyer, M. Steiner, J. T. Tuoriniemi, and H. Weinfurter, 1990, ''Nuclear order in copper: New type of antiferromagnetism in an ideal fcc system,'' Phys. Rev. Lett. **64**, 1421–1424.

Annila, A. J., K. N. Clausen, A. S. Oja, J. T. Tuoriniemi, and H. Weinfurter, 1992, ''Neutron-diffraction studies of the nuclear magnetic phase diagram of copper,'' Phys. Rev. B **45**, 7772–7788.

Asada, T., K. Terakura, and T. Jarlborg, 1981, ''An analysis of the spin-lattice relaxation of cubic transition metals,'' J. Phys. F **11**, 1847–1857.

Ashcroft, N. W., and N. D. Mermin, 1976, *Solid State Physics* (Holt, Rinehart, and Winston, New York).

Babcock J., J. Kiely, T. Manley, and W. Weyhmann, 1979, ''Nuclear magnetic ordering in $PrCu_6$,'' Phys. Rev. Lett. **43**, 380–383.

Bacon, F., J. A. Barclay, W. D. Brewer, D. A. Shirley, J. E. Templeton, 1972, ''Temperature-independent spin-lattice relaxation time in metals at very low temperatures,'' Phys. Rev. B **5**, 2397–2409.

Ballou, R., P. J. Brown, J. Deportes, A. S. Markosyan, and B. Ouladdiaf, 1992, ''Exchange frustration and metastability of the magnetic structure of $TbMn_2$,'' J. Magn. Magn. Mater. **104–107**, 935–936.

Ballou, R., J. Deportes, R. Lemaire, and B. Ouladdiaf, 1988, ''Mn magnetism and magnetic structures in RMn_2,'' J. Appl. Phys. **63**, 3487–3489.

Bardeen, J., 1937, ''An improved calculation of the energies of metallic Li and Na,'' J. Chem. Phys. **6**, 367–371.

Bäuml, W., G. Eska, and W. Pesch, 1994, ''NMR in metals at low temperatures with particular emphasis on the finite skin depth,'' Physica B **194–196**, 321–322.

Benoit, A., J. Bossy, J. Flouquet, and J. Schweizer, 1985, ''Magnetic diffraction in solid ^{3}He,'' J. Phys. (Paris) Lett. **46**, 923–927.

Benoit, A., J. Flouquet, J. L. Genicon, and J. Palleau, 1981, ''Magnetic ordering in $PrCu_5$ by neutron diffaction,'' Physica B **108**, 1103–1104.

Benoit, A., J. Flouquet, D. Rufin, and J. Schweizer, 1982a, ''Magnetic transition of solid ^{3}He observed by polarized neutrons,'' J. Phys. (Paris) Lett. **43**, 431–436.

Benoit, A., J. Flouquet, D. Rufin, and J. Schweizer, 1982b, ''Thermometry at very low temperatures with polarized neutrons; application to the search for the ^{3}He magnetic structure,'' J. Phys. (Paris) Colloq. **43**, C7, 311–316.

Berglund, P. M., H. K. Collan, G. J. Ehnholm, R. G. Gylling, and O. V. Lounasmaa, 1972, ''The design and use of nuclear orientation thermometers employing ^{54}Mn and ^{60}Co nuclei in ferromagnetic hosts,'' J. Low Temp. Phys. **6**, 357–383.

Berlin, T. H., and M. Kac, 1952, ''The spherical model of a ferromagnet,'' Phys. Rev. **86**, 821–835.

Betts, D. S., 1976, *Refrigeration and Thermometry below One Kelvin* (Sussex University Press, London).

Binder, K., J. L. Lebowitz, M. K. Phani, and M. H. Kalos, 1981, ''Monte Carlo study of the phase diagrams of binary alloys with face centered cubic lattice structure,'' Acta Metall. **29**, 1655–1665.

Binder, K., and A. P. Young, 1986, ''Spin glasses: Experimental facts, theoretical concepts, and open questions,'' Rev. Mod. Phys. **58**, 801–976.

Bloembergen, N., and T. J. Rowland, 1955, "Nuclear spin exchange in solids: Tl^{203} and Tl^{205} magnetic resonance in thallium and thallic oxide," Phys. Rev. **97**, 1679–1698.

Bloembergen, N., S. Shapiro, P. S. Pershan, and J. O. Artman, 1959, "Cross-relaxation in spin systems," Phys. Rev. **114**, 445–459.

Bloembergen, N., and S. Wang, 1954, "Relaxation effects in para-and ferromagnetic resonance," Phys. Rev. **93**, 72–83.

Bouchaud, J. P., and P. G. Zérah, 1993, "Dipolar ferromagnetism: A Monte Carlo study," Phys. Rev. B **47**, 9095–9097.

Bouffard, V., C. Fermon, J. F. Gregg, J. F. Jacquinot, and Y. Roinel, 1994, "Nuclear magnetic ordering 'avant toute chose'," in *NMR and More in Honour of Anatole Abragam*, edited by M. Goldman and M. Porneuf (Les Éditions de Physique, Les Ulis), pp. 81–102.

Bradley, D. I., A. M. Guénault, V. Keith, C. J. Kennedy, I. E. Miller, S. G. Mussett, G. R. Pickett, and W. P. Pratt Jr., 1984, "New methods for nuclear cooling into the microkelvin regime," J. Low Temp. Phys. **57**, 359–390.

Bucal, Ch., K. J. Fischer, M. Kubota, R. M. Mueller, and F. Pobell, 1978, "Nuclear demagnetization of PrS and $PrNi_5$," J. Phys. (Paris) **39**, L-457–L-458.

Buchal, C., J. Hanssen, R. M. Mueller, and F. Pobell, 1978, "Platinum wire NMR thermometer for ultralow temperatures," Rev. Sci. Instrum. **49**, 1360–1361.

Bucal, Ch., R. M. Mueller, F. Pobell, M. Kubota, and H. R. Folle, 1982, "Superconductivity investigations of Au-In alloys at ultralow temperatures," Solid State Commun. **42**, 43–47.

Buchal, C., F. Pobell, R. M. Mueller, M. Kubota, and J. R. Owers-Bradley, 1983, "Superconductivity of rhodium at ultralow temperatures," Phys. Rev. Lett. **50**, 64–67.

Buishvili, L. L., and N. P. Fokina, 1994, "Cross relaxation in weak magnetic fields at ultralow spin temperatures," Zh. Éksp. Teor. Fiz. **106**, 627–632 [Sov. Phys. JETP **79**, 344–346 (1994)].

Buishvili, L. L., D. A. Kostarov, and N. P. Fokina, 1994, "Merging-splitting and suppression-enhancement in magnetic resonance lines of highly polarized exchange-coupled nonequivalent spins," Zh. Eksp. Teor. Fiz. **106**, 1477–1488 [J. Expt. Theor. Phys. **79**, 799–894 (1994)].

Bunkov, Yu. M., 1989, "Superconducting aluminium heat switch prepared by diffusion welding," Cryogenics **29**, 938–939.

Bunkov, Yu. M., and S. Fisher, 1995, "NMR in superfluid ^{3}He at very low temperatures," J. Low Temp. Phys. **101**, 123–134.

Carney J. P., A. M. Guénault, G. R. Pickett, and G. F. Spencer, 1989, "Extreme nonlinear damping of the quasiparticle gas in superfluid ^{3}He-B in the low-temperature limit," Phys. Rev. Lett. **62**, 3042–3045.

Casimir, H. B. G., and F. K. Du Pré, 1938, "Note on the thermodynamic interpretation of paramagnetic relaxation phenomena," Physica **5**, 507–511.

Chamberlin, R. V., L. A. Moberly, and O. G. Symko, 1979, "High-sensitivity magnetic resonance by SQUID detection," J. Low Temp. Phys. **35**, 337–347.

Chapellier, M., M. Goldman, V. H. Chau, and A. Abragam, 1969, "Production et observation d'un état antiferromagnétique nucléaire," C.R. Acad. Sci. **268**, 1530–1533.

Chapellier, M., M. Goldman, V. H. Chau, and A. Abragam, 1970, "Production and observation of a nuclear antiferromagnetic state," J. Appl. Phys. **41**, 849–853.

Chapman, A. C., P. Rhodes, and E. F. Seymour, 1957, "The effect of eddy currents on nuclear magnetic resonance in metals," Proc. Phys. Soc. London **70**, 345–360.

Chen, K., and D. P. Landau, 1994, "Spin-dynamics study of the dynamic critical behavior of the three-dimensional classical Heisenberg ferromagnet," Phys. Rev. B **49**, 3266–3274.

Clausen, K. N., 1991, "Neutron scattering at nK temperatures," Neutron News **2**, 25–28.

Cohen, M. H., and F. Keffer, 1955, "Dipolar sums in the primitive cubic lattices," Phys. Rev. **99**, 1128–1134.

Cross, M. C., and D. S. Fisher, 1985, "Magnetism in solid ^{3}He: confrontation between theory and experiment," Rev. Mod. Phys. **57**, 881–921.

Culotta, E., 1995, "A new form of matter unveiled," editorial article in Science **270**, 1902–1903.

De Jongh, L. J., and A. R. Miedema, 1974, "Experiments on simple magnetic model systems," Adv. Phys. **23**, 1–260.

De Klerk, D., 1956, "Adiabatic demagnetization," in *Encyclopedia of Physics* (Springer, Berlin), Vol. 15, pp. 38–209.

Deimling, M., H. Brunner, J. P. Colpa, K. P. Dinse, and K. H. Hausser, 1980, "Microwave-induced optical nuclear polarization (MI-ONP)," J. Magn. Reson. **39**, 185–202.

Demco, D. E., J. Tegenfeldt, and J. S. Waugh, 1975, "Dynamics of cross relaxation in nuclear magnetic double resonance," Phys. Rev. B **11**, 4133-4151.

Diep, H. T., and H. Kawamura, 1989, "First-order phase transition in the fcc Heisenberg antiferromagnet," Phys. Rev. B **40**, 7019–7022.

Domb, C., and A. R. Miedema, 1964, "Magnetic transitions," in *Progress in Low Temperature Physics,* edited by C. J. Gorter (North-Holland, Amsterdam), Vol. 4, pp. 296–343.

Ebert, H., H. Winter, and J. Voitländer, 1984, "Nuclear spin lattice relaxation rates of Ag in AgPd and Cu in CuPd," J. Phys. F **14**, 2433–2442.

Ehnholm, G. J., J. P. Ekström, J. F. Jacquinot, M. T. Loponen, O. V. Lounasmaa, and J. K. Soini, 1979, "Evidence for nuclear antiferromagnetism in copper," Phys. Rev. Lett. **42**, 1702–1705.

Ehnholm, G. J., J. P. Ekström, J. F. Jacquinot, M. T. Loponen, O. V. Lounasmaa, and J. K. Soini, 1980, "NMR studies on nuclear ordering in metallic copper below 1 5 K," J. Low Temp. Phys. **39**, 417–450.

Ehnholm, G. J., J. P. Ekström, M. T. Loponen, and J. K. Soini, 1979, "Transversal SQUID NMR," Cryogenics **19**, 673–678.

Ehrlich, A. C., 1974, "Oxygen annealing of silver for obtaining low electrical resistivity: technique and interpretation," J. Mater. Sci. **9**, 1064–1072.

Ekström, J. P., J. F. Jacquinot, M. T. Loponen, J. K. Soini, and P. Kumar, 1979, "Nuclear spin interaction in copper: NMR at high polarization and in low fields," Physica B **98**, 45–52.

Enrico, M. P., S. N. Fisher, A. M. Guénault, I. E. Miller, and G. R. Pickett, 1994, "Temperature dependence of the nuclear spin-lattice relaxation time in copper metal to below 10 μK," Phys. Rev. B **49**, 6339–6342.

Eska, G., 1989, "Nonlinear spin dynamics and nuclear ordering: Tl metal as an example," in *Symposium on Quantum Fluids and Solids—1989*, AIP Conference Proceedings No. 194, edited by G. G. Ihas and Y. Takano (AIP, New York), pp. 316–327.

Eska, G., and E. Schuberth, 1987, "NMR behavior of Tl metal at very low temperatures," Jpn. J. Appl. Phys. Suppl. **26-3**, 435–436.

Eska, G., E. Schuberth, and B. Turrell, 1986, "Nuclear spin-lattice relaxation of thallium at low temperatures," Phys. Lett. A **115**, 413–416.

Fickett, F. R., 1974, "Oxygen annealing of copper: A review," Mater. Sci. Eng. **14**, 199–210.

Foner, S. 1963, "Antiferromagnetic and ferrimagnetic resonance," in *Magnetism*, edited by G. T. Rado and H. Suhl (Academic, New York), Vol. I, pp. 383–447.

Frisken, S. J., 1989, Ph.D. Thesis (University of New South Wales).

Frisken, S. J., and D. J. Miller, 1986, "Realistic calculation of the indirect-exchange interaction in metals," Phys. Rev. Lett. **57**, 2971–2974.

Frisken, S. J., and D. J. Miller, 1988a, "Monte Carlo study of antiferromagnetic nuclear ordering in Cu," Phys. Rev. Lett. **61**, 1017–1020.

Frisken, S. J., and D. J. Miller, 1988b, "Indirect-exchange interaction in copper," Phys. Rev. B **37**, 10884–10886.

Froidevaux, C., and M. Weger, 1964, "Direct measurement of the Ruderman-Kittel interaction in platinum alloys," Phys. Rev. Lett. **12**, 123–125.

Garrett, C. G. B., 1951, "Experiments with an anisotropic magnetic crystal at temperatures below 1K," Proc. R. Soc. London, Ser. A **206**, 242–257.

Gehring, G. A. and K. Z. Gehring, 1975, "Co-operative Jahn-Teller effects," Rep. Prog. Phys. **38**, 1–89.

Genicon, J. L., J. L. Tholence, and R. Tournier, 1978, "Nuclear induced ferromagnetism in $PrCu_5$," J. Phys. (Paris) Colloq. **39**, C6, 798–799.

Gloos, K., R. König, P. Smeibidl, and F. Pobell, 1990, "Anomalous nuclear magnetic properties of ^{115}In in $AuIn_2$," Europhys. Lett. **12**, 661–666.

Gloos, K., P. Smeibidl, C. Kennedy, A. Singsaas, P. Sekowski, R. M. Mueller, and F. Pobell, 1988, "The Bayreuth nuclear demagnetization refrigerator," J. Low Temp. Phys. **73**, 101–136.

Gloos, K., P. Smeibidl, and F. Pobell, 1991, "Nuclear spin–electron coupling of copper at microkelvin temperatures," Z. Phys. B **82**, 227–231.

Goldman, M., 1970, *Spin Temperature and Nuclear Magnetic Resonance in Solids* (Clarendon, Oxford).

Greywall, D. S., 1985, "^{3}He melting-curve thermometry at millikelvin temperatures," Phys. Rev. B **31**, 2675–2683.

Griessen, R., M. Landolt, and H. R. Ott, 1971, "A new antiferromagnetic phase in EuSe below 1.8 K," Solid State Commun. **9**, 2219–2223.

Griffiths, J. H. E., J. Owen, J. G. Park, and M. F. Partridge, 1959, "Exhange interactions in antiferromagnetic salts of iridium I. Paramagnetic resonance experiments," Proc. R. Soc. London, Ser. A **250**, 84–96.

Gukasov, A. G. Th. Brückel, B. Dorner, V. P. Plakhty, W. Prandl, E. F. Shender, and O. P. Smirnov, 1988, "Quantum exchange magnon gap in an antiferromagnetic with dynamically interacting spin subsystems," Europhys. Lett. **7**, 83.

Gylling, R. G., 1971, "Construction and operation of a nuclear refrigeration cryostat," Acta Polytech. Scand. Ph. **81**, xx–xx.

Hakonen, P. J., 1993, "Nuclear magnetic ordering in silver at positive and negative spin temperatures," Phys. Scr. **T49**, 327–332.

Hakonen, P. J., 1994, "Calculation of nuclear-spin entropy in silver and rhodium at positive and negative temperatures using Monte Carlo simulations," Phys. Rev. B **49**, 15363–15365.

Hakonen, P. J., and O. V. Lounasmaa, 1994, "Negative absolute temperatures: 'Hot' spins in spontaneous magnetic order," Science **265**, 1821–1825.

Hakonen, P. J., O. V. Lounasmaa, and A. S. Oja, 1991, "Spontaneous nuclear magnetic ordering in copper and silver at nano and picokelvin temperatures," J. Magn. Magn. Mater. **100**, 394–412.

Hakonen, P. J., K. K. Nummila, and R. T. Vuorinen, 1992, "Spin dynamics in highly polarized silver at negative absolute temperatures," Phys. Rev. B **45**, 2196–2200.

Hakonen, P. J., K. K. Nummila, R. T. Vuorinen, and O. V. Lounasmaa, 1992, "Observation of nuclear ferromagnetic ordering in silver at negative nanokelvin temperatures," Phys. Rev. Lett. **68**, 365–368.

Hakonen, P. J., and R. T. Vuorinen, 1992, "Nuclear ferromagnetic ordering in silver at negative nanokelvin temperatures," J. Low Temp. Phys. **89**, 177–186.

Hakonen, P. J., R. T. Vuorinen, and J. E. Martikainen, 1993, "Nuclear antiferromagnetism in rhodium metal at positive and negative nanokelvin temperatures," Phys. Rev. Lett. **70**, 2818–2821.

Hakonen, P. J., R. T. Vuorinen, and J. E. Martikainen, 1994, "Anomalous spin-lattice relaxation in dilute *Rh*Fe at positive and negative nanokelvin temperatures," Europhys. Lett. **25**, 551–556.

Hakonen, P. J., and S. Yin, 1991, "Investigations of nuclear magnetism in silver down to picokelvin temperatures. II," J. Low Temp. Phys. **85**, 25–64.

Hakonen, P. J., S. Yin, and O. V. Lounasmaa, 1990, "Nuclear magnetism in silver at positive and negative absolute temperatures in the low nanokelvin range," Phys. Rev. Lett. **64**, 2707–2710.

Hakonen, P. J., S. Yin, and K. K. Nummila, 1991, "Phase diagram and NMR studies of antiferromagnetically ordered polycrystalline silver," Europhys. Lett. **15**, 677–682.

Harmon, B. N., and X.-W. Wang, 1987, "Comment on 'Realistic calculation of the indirect-exchange interaction in metals'," Phys. Rev. Lett. **59**, 379.

Harmon, B. N., X.-W. Wang, and P.-A. Lindgård, 1992, "Calculation of the Ruderman-Kittel interaction and the nuclear magnetic ordering in silver," J. Magn. Magn. Mater. **104–107**, 2113–2115.

Hastings, J. M., N. Elliott, and L. M. Corliss, 1959, "Antiferromagnetic structures of MnS_2, $MnSe_2$, and $MnTe_2$," Phys. Rev. **115**, 13–17.

Heinilä, M. T., and A. S. Oja, 1993a, "Selection of the ground state in type-I fcc antiferromagnets in an external magnetic field," Phys. Rev. B **48**, 7227–7237.

Heinilä, M. T., and A. S. Oja, 1993b, "Long-range order produced by the interaction between spin waves in classical fcc Heisenberg models," Phys. Rev. B **48**, 16514–16523.

Heinilä, M. T., and A. S. Oja, 1994a, "Breaking of degeneracy in classical Heisenberg antiferromagnets," Physica B **194–196**, 237–238.

Heinilä, M. T., and A. S. Oja, 1994b, "Isotropic type I fcc antiferromagnet in an external field," Physica B **194–196**, 239–240.

Heinilä, M. T., and A. S. Oja, 1994c, "Anisotropic magnetic nearest-neighbor exchange interaction in the pyrite structure: $MnTe_2$, MnS_2, and $MnSe_2$," Phys. Rev. B **49**, 11995– 12002.

Heinilä, M. T., and A. S. Oja, 1994d, "Simulation study of NMR lineshapes in a classical nuclear spin system with two isotopes," Phys. Rev. B **50**, 15843–15851.

Heinilä, M. T., and A. S. Oja, 1995, "First-principles calculation of antiferromagnetic NMR absorption curves," Phys. Rev. B **52**, R6967–R6970.

Heinilä, M. T., and A. S. Oja, 1996, "Magnetic resonance of type-I fcc antiferromagnets," Phys. Rev. B **54**, 9275–9287.

Henley, C. L., 1987, "Ordering by disorder: ground-state selection in fcc vector antiferromagnets," J. Appl. Phys. **61**, 3962–3964.

Henley, C. L., 1989, "Ordering due to disorder in a frustrated vector antiferromagnet," Phys. Rev. Lett. **62**, 2056–2059.

Herrmannsdörfer, T., and F. Pobell, 1995, "Spontaneous nuclear ferromagnetic ordering of In nuclei in $AuIn_2$: Part I: Nuclear specific heat and nuclear susceptibility," J. Low Temp. Phys. **100**, 253–279.

Herrmannsdörfer, T., P. Smeibidl, B. Schröder-Smeibidl, and F. Pobell, 1995, "Spontaneous nuclear ferromagnetic ordering of In in $AuIn_2$," Phys. Rev. Lett. **74**, 1665–1668.

Herrmannsdörfer, T., H. Uniewski, and F. Pobell, 1994a, "Nuclear ferromagnetic ordering of ^{141}Pr in the diluted Van Vleck paramagnets $Pr_{1-x}Y_xNi_5$," Phys. Rev. Lett. **72**, 148–151.

Herrmannsdörfer, T., H. Uniewski, and F. Pobell, 1994b, "Nuclear ferromagnetic ordering of ^{141}Pr in the diluted Van Vleck paramagnets $Pr_{1-x}Y_xNi_5$," J. Low Temp. Phys. **97**, 189–211.

Hobden, M. V., and N. Kurti, 1959, "Experiments on nuclear cooling," Philos. Mag. **4**, 1092–1095.

Holstein, T., and H. Primakoff, 1940, "Field dependence of the intrinsic domain magnetization of a ferromagnet," Phys. Rev. **58**, 1098–1113.

Huiku, M. T., 1984, "Nuclear magnetism in copper at nanokelvin temperatures and in low external magnetic fields," Physica B **126**, 51–61.

Huiku, M. T., T. A. Jyrkkiö, J. M. Kyynäräinen, M. T. Loponen, O. V. Lounasmaa, and A. S. Oja, 1986, "Investigations of nuclear antiferromagnetic ordering in copper at nanokelvin temperatures," J. Low Temp. Phys. **62**, 433–487.

Huiku, M. T., T. A. Jyrkkiö, J. M. Kyynäräinen, A. S. Oja, and O. V. Lounasmaa, 1984, "Phase diagram for spontaneous nuclear magnetic ordering in copper," Phys. Rev. Lett. **53**, 1692–1695.

Huiku, M. T., T. A. Jyrkkiö, and M. T. Loponen, 1983, "Experimental curves of entropy and susceptilibity versus temperature for copper nuclear spins down to the ordered state," Phys. Rev. Lett. **50**, 1516–1519.

Huiku, M. T., and M. T. Loponen, 1982, "Observation of a magnetic phase transition in the nuclear spin system of metallic copper at nanokelvin temperatures," Phys. Rev. Lett. **49**, 1288–1291.

Huiku, M. T., M. T. Loponen, T. A. Jyrkkiö, J. M. Kyynäräinen, A. S. Oja, and J. K. Soini, 1984, "Impurities and the anomalous spin-lattice relaxation in copper at submillikelvin temperatures," in *Proceedings of the 17th International Conference on Low Temperature Physics*, edited by U. Eckern *et al.* (North-Holland, Amsterdam), pp. 133–134.

Huiku, M. T., and J. K. Soini, 1983, "Further studies of nuclear ordering in metallic copper," J. Low Temp. Phys. **50**, 523–543.

Huiskamp, W. J., and O. V. Lounasmaa, 1973, "Ultralow temperatures—how and why," Rep. Prog. Phys. **36**, 423–496.

Ishii, H., and S. Aoyama, 1991, "Quantum effect in enhanced nuclear magnets," Prog. Theor. Phys. Suppl. **106**, 109–117.

Ishimoto, H., N. Nishida, T. Furubayashi, M. Shinohara, Y. Takano, Y. Miura, and K. Ono, 1984, "Two-stage nuclear demagnetization refrigerator reaching 27 μK," J. Low Temp. Phys. **55**, 17– 31.

Jauho, P., and P. V. Pirilä, 1970, "Spin-lattice relaxation of nuclei due to electrons at very low temperatures," Phys. Rev. B **1**, 21–24.

Jeener, J., H. Eisendrath, and R. Van Steenwinkel, 1964, "Thermodynamics of spin systems in solids," Phys. Rev. **133**, 478A–490A.

Jensen, J., and A. R. Mackintosh, 1991, *Rare Earth Magnetism* (Clarendon, Oxford).

Jyrkkiö, T. A., M. T. Huiku, K. N. Clausen, K. Siemensmeyer, K. Kakurai, and M. Steiner, 1988, "Calibration and applications of polarized neutron thermometry at milli- and microkelvin temperatures," Z. Phys. B **71**, 139–148.

Jyrkkiö, T. A., M. T. Huiku, O. V. Lounasmaa, K. Siemensmeyer, K. Kakurai, M. Steiner, K. N. Clausen, and J. K. Kjems, 1988, "Observation of nuclear antiferromagnetic order in copper by neutron diffraction at nanokelvin temperatures," Phys. Rev. Lett. **60**, 2418–2421.

Jyrkkiö, T. A., M. T. Huiku, K. Siemensmeyer, and K. N. Clausen, 1989, "Neutron diffraction studies of nuclear magnetic ordering in copper," J. Low Temp. Phys. **74**, 435–473.

Karaki, Y., M. Kubota, and H. Ishimoto, 1994, "Specific heat of indium below 1 mK," Physica B **194–196**, 461–462.

Karimov, Yu. S., and I. F. Shchegolev, 1961, "Nuclear magnetic resonance in metallic thallium," Zh. Éksp. Teor. Fiz. **41**, 1082–1090 [Sov. Phys. JETP **14**, 772–778 (1962)].

Kasevich, M., and S. Chu, 1992, "Laser cooling below a photon recoil with three-level atoms," Phys. Rev. Lett. **69**, 1741–1744.

Kasuya, T., 1956, "A theory of metallic ferro-and antiferromagnetism on Zener's model," Prog. Theor. Phys. **16**, 45–57.

Kawarazaki, S., N. Kunitomi, J. R. Arthur, R. M. Moon, W. G. Stirling, and K. A. McEwen, 1988, "Evidence for nuclear-spin order in double-hcp praseodymium by neutron diffraction," Phys. Rev. B **37**, 5336–5341.

Keffer, F., 1966, "Spin waves," in *Handbuch der Physik* (Springer, Berlin) Vol. 18/2, pp. 1–273.

Kittel, C., 1968, "Indirect exchange interactions in metals," in Solid State Physics, Vol. **22** (Academic, New York), pp. 1–26.

Kittel, C., 1971, *Introduction to Solid State Physics* (Wiley, New York).

Kjäldman, L. H., P. Kumar, and M. T. Loponen, 1981, "Nuclear magnetism in metals: Thermodynamics and magnetic resonance," Phys. Rev. B **23**, 2051–2059.

Kjäldman, L. H., and J. Kurkijärvi, 1979, "Antiferromagnetic ordering of Cu-nuclei," Phys. Lett. A **71**, 454–456.

Knoll, G., 1968, *Radiation Detection and Measurement* (Wiley, New York).

Koester, L., and H. Rauch, 1981, *Summary of Neutron Scattering Lengths*, IAEA Contract 2517/RB.

Koike, Y., H. Suzuki, S. Abe, Y. Karaki, M. Kubota, and H. Ishimoto, 1995, "Ferromagnetic nuclear spin order of scandium," J. Low Temp. Phys. **101**, 617–622.

Kolac, M., B. S. Neganov, and S. Sahling, 1985, "Low temperature heat release from copper: Ortho-para conversion of hydrogen," J. Low Temp. Phys. **59**, 547–559.

Komori, K., T. Goto, and S. Kobayashi, 1986, "Depolarization of nuclear magnetization in aluminum small particles at low temperature," J. Phys. Soc. Jpn. **55**, 2133–2136.

König, R., A. Betat, and F. Pobell, 1994, "Refrigeration and thermometry of liquid ^{3}He-^{4}He mixtures in the ballistic regime," J. Low Temp. Phys. **97**, 311–333.

Korringa, J., 1950, "Nuclear magnetic relaxation and resonance line shift in metals," Physica **16**, 601–610.

Kötzler, J., 1984, "On the possibility of fluctuation-driven first-order transitions," Z. Phys. B **55**, 119–129.

Kubo, R., and K. Tomita, 1954, "A general theory of magnetic resonance absorption," J. Phys. Soc. Jpn. **9**, 888–919.

Kubota, M., K. J. Fischer, and R. M. Mueller, 1987, "Nonferromagnetic nuclear magnetic ordering in metallic hyperfine enhanced nuclear magnet PrSe," Jpn. J. Appl. Phys. Suppl. **26-3**, 427–428.

Kubota, M., H. R. Folle, C. Buchal, R. M. Mueller, and F. Pobell, 1980, "Nuclear magnetic ordering in $PrNi_5$ at 0.4 mK," Phys. Rev. Lett. **45**, 1812–1815.

Kubota, M., R. M. Mueller, C. Buchal, H. Chocholacs, J. R. Owers-Bradley, and F. Pobell, 1983, "Evidence for moment fluctuation effects in the metallic nuclear magnet $PrNi_5$," Phys. Rev. Lett. **51**, 1382–1385.

Kubota, M., R. M. Mueller, and K. J. Fischer, 1984, "Study of magnetic ordering in metallic Pr compounds: Is simplest candidate PrS?," in *Proceedings of the 17th International Conference on Low Temperature Physics*, edited by U. Eckern *et al.* (North-Holland, Amsterdam), pp. 15–16.

Kumar, P., J. Kurkijärvi, and A. S. Oja, 1985, "Phase diagram for spontaneous nuclear magnetic ordering in copper," Phys. Rev. B **31**, 3194–3195.

Kumar, P., J. Kurkijärvi, and A. S. Oja, 1986, "Nuclear magnetism in a metal," Phys. Rev. B **33**, 444–449.

Kumar, P., M. T. Loponen, and L. H. Kjäldman, 1980, "Spin-density-wave fluctuations in copper nuclear spins," Phys. Rev. Lett. **44**, 493–496.

Kurkijärvi, J., 1984, "Magnetic ordering of the nuclear spins in metallic copper at nanokelvin temperatures and low applied fields," Physica B **127**, 317–321.

Kurti, N., 1978, "From Cailletet and Pictet to microkelvin," Cryogenics **18**, 451–458.

Kurti, N., 1982, "From the first mist of liquid oxygen to nuclear ordering: anecdotes from the history of refrigeration," Physica **B-C109-110**, 1737–1752.

Kurti, N., F. N. Robinson, F. E. Simon, and D. A. Spohr, 1956, "Nuclear cooling," Nature **178**, 450–453.

Landau, L. D., and E. M. Lifshitz, 1980, *Statistical Physics*, Part I (Pergamon, London).

Lefmann, K., 1995, "Nuclear magnetic ordering in silver," Ph.D. Thesis, University of Copenhagen, Risø National Laboratory Report R-850(EN).

Lefmann, K., J. T. Tuoriniemi, K. K. Nummila, and A. Metz, 1996, "Neutron thermometry on polarized silver nuclei at sub-microkelvin spin temperatures," Z. Phys. B (in press).

Leggett, A. J., 1974, "The spin dynamics of an anisotropic Fermi superfluid (^{3}He?)," Ann. Phys. **85**, 11–55.

Leib, J., M. Huebner, S. Götz, Th. Wagner, and G. Eska, 1995, "NMR-investigations on thallium-samples of high spin-polarization," J. Low Temp. Phys. **101**, 253–258.

Lindelof, P. E., I. E. Miller, and G. R. Pickett, 1975, "Nuclear cooperative ordering in single-crystal praseodymium at low temperatures," Phys. Rev. Lett. **35**, 1297–1299.

Lindgren, I., and A. Rosen, 1974a, "Relativistic self-consistent-field calculations with application to atomic hyperfine interaction. I. Relativistic self-consistent fields. II. Relativistic theory of atomic hyperfine interaction," Case Stud. At. Phys. **4**, 93–196.

Lindgren, I., and A. Rosen, 1974b, "Relativistic self-consistent-field calculations with application to atomic hyperfine interaction. III. Comparison between theoretical and experimental hyperfine-structure results," Case Stud. At. Phys. **4**, 197–298.

Lindgård, P.-A., 1988a, "Theory of adiabatic nuclear magnetic ordering in Cu," Phys. Rev. Lett. **61**, 629–632.

Lindgård, P.-A., 1988b, "Theory of the nuclear magnetic ordering in Cu in a field," J. Phys. (Paris) Colloq. **49**, C8, 2051–2052.

Lindgård, P. A., 1990, "Theory of a new type of antiferromagnetism in the ideal fcc system of Cu," J. Magn. Magn. Mater. **90-91**, 138–140.

Lindgård, P. A., 1992, "Vibrationally reduced magnetic interactions in Cu and the magnetic ordering in a magnetic field," J. Magn. Magn. Mater. **104–107**, 2109–2110.

Lindgård, P. A., X. W. Wang, and B. N. Harmon, 1986, "Calculation of the Ruderman-Kittel interaction and magnetic ordering in copper," J. Magn. Magn. Mater. **54–57**, 1052–1054.

Long, M. W., 1989, "Effects that can stabilise multiple spin-density waves," J. Phys., Condens. Matter **1**, 2857–2874.

Loponen, M. T., R. C. Dynes, V. Narayanamurti, and J. P. Garno, 1981, "Observation of time-dependent specific heat in amorphous SiO_2," Phys. Rev. Lett. **45**, 457–460.

Lounasmaa, O. V., 1974, *Experimental Principles and Methods below 1 K* (Academic, London).

Lounasmaa, O. V., 1989, "Nuclear magnetic ordering at nanokelvin temperatures," Phys. Today **42**, 26–33.

Lounasmaa, O. V., P. Hakonen, K. Nummila, R. Vuorinen, and J. Martikainen, 1994, "Negative nanokelvin temperatures in the nuclear spin systems of silver and rhodium metals," Physica B **194–196**, 291–292.

Luttinger, J. M., and L. Tisza, 1946, "Theory of dipole interaction in crystals," Phys. Rev. **70**, 954–964; **72**, 257(E).

Marks, J., W. Th. Wenckebach, and N. J. Poulis, 1979, "Magnetic ordering of proton spins in $Ca(OH)_2$," Physica B **96**, 337–340.

Martikainen, J., 1993, "Nuclear magnetic susceptibility measurements in rhodium," Diploma Thesis (in Finnish), Helsinki University of Technology.

Mattis, D. C., 1985, *The Theory of Magnetism*, Vol. 2 (Springer, Heidelberg).

McEwen, K. A., and W. G. Stirling, 1989, "Search for nuclear spin polarisation in praseodymium," Physica B **156–157**, 754–755.

Meredith, D. J., G. R. Pickett, and O. G. Symko, 1973, "Application of a SQUID magnetometer to NMR at low temperatures," J. Low Temp. Phys. **13**, 607–615.

Merkulov, I. A., Yu. I. Papava, V. V. Ponomarenko, and S. I. Vasiliver, 1988, "Monte Carlo simulation and theory in Gaussian approximation of a phase in the nuclear spin system of a solid," Can. J. Phys. **66**, 135–144.

Miki, T., M. Yanaka, M. Nakagawa, D. Kim, O. Ishikawa, T. Hata, H. Ishii, and T. Kodama, 1992, "Electrical resistivity anomaly at the nuclear magnetic ordering in a Van Vleck paramagnet $PrCu_6$," Phys. Rev. Lett. **69**, 375–378.

Miller, D. J., and S. J. Frisken, 1988, "Calculation of the indirect-exchange interaction between nuclear spins in Cu and Ag," J. Appl. Phys. **64**, 5630–5632.

Minor, W., and T. M. Giebultowicz, 1988, "Studies of fcc Heisenberg antiferromagnets by Monte Carlo simulation on large spin arrays," J. Phys. (Paris) Colloq. **49**, C8, 1551–1552.

Moon, R. M., T. Riste, and W. C. Koehler, 1969, "Polarization analysis of thermal-neutron scattering," Phys. Rev. **181**, 920–931.

Moyland, P. L., P. Kumar, J. Xu, and Y. Takano, 1993, "Coupling of the Larmor precession to the correlated motion of pairs of nuclear spins in noble metals," Phys. Rev. **48**, 14020–14022.

Moyland, P. L., T. Lang, J. Xu, E. D. Adams, G. R. Stewart, and Y. Takano, 1995, "Magnetic susceptibility measurements in $PrBe_{13}$," J. Low Temp. Phys. **101**, 641–643.

Mueller, R. M., C. Buchal, H. R. Folle, M. Kubota, and F. Pobell, 1980, "A double-stage nuclear demagnetization refrigerator," Cryogenics **20**, 395–407.

Muething, K., G. G. Ihas, and J. Landau, 1977, "Metallic thermal connectors for use in nuclear refrigeration," Rev. Sci. Instrum. **48**, 906–909.

Murao, T., 1971, "Magnetism of a 'Nuclei plus electrons' system," J. Phys. Soc. Jpn. **31**, 683–690.

Murao, T., 1972, "Magnetism of a 'Nuclei plus electrons' system. II," J. Phys. Soc. Jpn. **33**, 33–38.

Murao, T., 1981, "Magnetism of a nucleus-electron complex system in the vicinity of the threshold," J. Phys. Soc. Jpn. **50**, 3240–3244.

Narath, A., A. T. Fromhold Jr, and E. D. Jones, 1966, "Nuclear spin relaxation in metals: rhodium, palladium, and silver," Phys. Rev. **144**, 428–435.

Nicklow, R. M., R. M. Moon, S. Kawarazaki, N. Kunitomi, H. Suzuki, T. Ohtsuka, and Y. Morii, 1985, "Nuclear spin ordering observed by neutron diffraction," J. Appl. Phys. **57**, 3784–3788.

Niinikoski, T. O., 1988, "The principles of detection of dark matter based on non-resolved fluctuations of excitations in solids," Ann. Phys. (Paris) **13**, 143–150.

Niskanen, K. J., L. H. Kjäldman, and J. Kurkijärvi, 1982, "Ordered phases of the combinated Ruderman-Kittel and dipole-dipole interaction on different lattices and their stability," J. Low Temp. Phys. **49**, 241–249.

Niskanen, K. J., and J. Kurkijärvi, 1981, "The transition temperature of Cu nuclei to an ordered state," J. Phys. C **14**, 5517–5522.

Niskanen, K. J., and J. Kurkijärvi, 1983, "Linked cluster expansion for quantum spins," J. Phys. A **16**, 1491–1504.

Nummila, K. K., J. T. Tuoriniemi, R. T. Vuorinen, K. Lefmann, A. Metz, and F. B. Rasmussen, 1997, "Neutron diffraction studies of nuclear magnetic ordering in silver," Phys. Rev. B (to be published).

Oguchi, T., 1960, "Theory of spin-wave interactions in ferro- and antiferromagnetism," Phys. Rev. **117**, 117–123.

Oguchi, T., H. Nishimori, and Y. Taguchi, 1985, "The spin wave theory in antiferromagnetic Heisenberg model on face centered cubic lattice," J. Phys. Soc. Jpn. **54**, 4494–4497.

Oh, G.-H., Y. Ishimoto, T. Kawae, M. Nakagawa, O. Ishikawa, T. Hata, and T. Kodama, 1994, "Cooling of ^{3}He-^{4}He dilute solution down to 97 μK. Thermal boundary resistance between dilute solution and metal powder," J. Low Temp. Phys. **95**, 525–546.

Oja, A. S., 1984, "Magnetic ordering of copper nuclei," Diploma Thesis (in Finnish), Helsinki University of Technology.

Oja, A. S., 1987, "Nuclear magnetism in metals," Phys. Scr. **T19**, 462–468.

Oja, A. S., 1991, "Nuclear magnetic ordering in copper and silver at nanokelvin temperatures," Physica B **169**, 306–315.

Oja, A. S., A. J. Annila, and Y. Takano, 1988, "Resplitting of exchange-merged NMR absorption lines at high spin polarizations," Phys. Rev. B **38**, 8602–8608.

Oja, A. S., A. J. Annila, and Y. Takano, 1990, "Cross relaxation by single spin flips in silver at nanokelvin temperatures," Phys. Rev. Lett. **65**, 1921–1924.

Oja, A. S., A. J. Annila, and Y. Takano, 1991, "Investigations of nuclear magnetism in silver down to picokelvin temperatures. I," J. Low Temp. Phys. **85**, 1–24.

Oja, A. S., and P. Kumar, 1984, "Helical structures of nuclear spins in a metal," Physica B **126**, 451–452.

Oja, A. S., and P. Kumar, 1987, "Indirect nuclear spin interactions and nuclear ordering in metals," J. Low Temp. Phys. **66**, 155–167.

Oja, A. S., and H. E. Viertiö, 1987, "Magnetically ordered structures of nuclear spins in fcc metals," Jpn. J. Appl. Phys. **26-3**, 441–442.

Oja, A. S., and H. E. Viertiö, 1992, "Nuclear magnetic ordering in copper: the spin structure in the high-field phase at $\mathbf{B}\|[111]$," J. Magn. Magn. Mater. **104–107**, 908– 910.

Oja, A. S., and H. E. Viertiö, 1993, "Antiferromagnets with anisotropic spin-spin interactions: Stability of the zero-field structure in an external field," Phys. Rev. B **47**, 237–253.

Oja, A. S., X.-W. Wang, and B. N. Harmon, 1989, "First-principles study of the conduction-electron-mediated interactions between nuclear spins in copper metal," Phys. Rev. B **39**, 4009–4021.

Okamoto, T., H. Fukuyama, H. Akimoto, H. Ishimoto, and S. Ogawa, 1994, "Direct demagnetization cooling of high-density solid ^{3}He," Phys. Rev. Lett. **72**, 868–871.

Osheroff, D. D., M. C. Cross, and D. S. Fisher, 1980, "Nuclear antiferromagnetic resonance in solid ^{3}He," Phys. Rev. Lett. **44**, 792–795.

Pershan, P. S., 1960, "Cross relaxation in LiF," Phys. Rev. **117**, 109–116.

Pickett, G. R., 1988, "Microkelvin physics," Rep. Prog. Phys. **51**, 1295–1340.

Pirnie, K., P. J. Wood, and J. Eve, 1966, "On high temperature susceptibilities of Heisenberg model ferromagnetics and antiferromagnetics," Mol. Phys. **11**, 551–577.

Pobell, F., 1982, "The quest for ultralow temperatures: What are the limitations?" Physica B **109-110**, 1485–1498.

Pobell, F., 1988, "La quête du zéro absolu," Recherche **19**, 784–789.

Pobell, F., 1992a, *Matter and Methods at Low Temperatures* (Springer, Berlin).

Pobell, F., 1992b, "Nuclear refrigeration and thermometry at microkelvin temperatures," J. Low Temp. Phys. **87**, 635–649.

Pobell, F., 1994, "Nuclear magnetic ordering in metals," Physica B **197**, 115–123.

Poitrenaud, J., 1967, "Resonance magnetique nucléaire dans le rubidium et le cesium métalliques," J. Phys. Chem. Solids **28**, 161–170.

Poitrenaud, J., and J. M. Winter, 1964, "Resonance nucléaire dans l'argent métallique," J. Phys. Chem. Solids **25**, 123– 127.

Pollack, L., E. N. Smith, J. M. Parpia, and R. C. Richardson, 1992, "Novel low-temperature cross relaxation in nuclear quadrupole resonance," Phys. Rev. Lett. **69**, 3835–3838.

Price, D. L., and K. Sköld, 1986, "Introduction to neutron scattering," in *Neutron Scattering: Methods of Experimental Physics*, edited by K. Sköld and D. L. Price (Academic, London), Vol. 23, Part A, pp. 1–98.

Provotorov, B. N., 1962, "Quantum statistical theory of cross relaxation," Zh. Éksp. Teor. Fiz. **42**, 882–888 [Sov. Phys. JETP **15**, 611–614 (1962)].

Purcell, E. M., and R. V. Pound, 1951, "A nuclear spin system at negative temperature," Phys. Rev. **81**, 279–280.

Ramakrishnan, S., and G. Chandra, 1993, "Nuclear magnetism in metals and alloys," in *Selected Topics in Magnetism*, Frontiers in Solid State Sciences, No. 2, edited by L. C. Gupta and M. S. Multani (World Scientific, Singapore), pp. 409–441.

Ramsey, N. F., 1956, "Thermodynamics and statistical mechanics at negative absolute temperatures," Phys. Rev. **103**, 20–28.

Richardson, R. C., and E. N. Smith, 1988, *Experimental Techniques in Condensed Matter Physics at Low Temperatures* (Addison Wesley, New York).

Rivier, N., and V. Zlatic, 1972, "Temperature dependence of the resistivity due to localized spin fluctuations (Part I)," J. Phys. F **2**, L87–L92; **2**, "Temperature dependence of the resistivity due to localized spin fluctuations II–Coles alloys," L99–L104.

Rodak, M. I., 1971, "Behavior of a system of spins close in frequency and coupled by cross relaxation," Zh. Éksp. Teor. Fiz. **61**, 832–842 [Sov. Phys. JETP **34**, 443–448 (1972)].

Roger, M., J. H. Hetherington, and J. M. Delrieu, 1983, "Magnetism in solid ^{3}He," Rev. Mod. Phys. **55**, 1–64.

Roinel, Y., G. L. Bachella, O. Avenel, V. Bouffard, M. Pinot, P. Roubeau, P. Mériel, and M. Goldman, 1980, "Neutron diffraction study of nuclear magnetic ordered phases and domains in lithium hydride," J. Phys. (Paris) Lett. **41**, 123–125.

Roinel, Y., V. Bouffard, G. L. Bacchella, M. Pinot, P. Mériel, P. Roubeau, O. Avenel, M. Goldman, and A. Abragam, 1978, "First study of nuclear antiferromagnetism by neutron diffraction," Phys. Rev. Lett. **41**, 1572–1574.

Roinel, Y., V. Bouffard, C. Fermon, M. Pinot, F. Vigneron, G. Fournier, and M. Goldman, 1987, "Phase diagrams of ordered nuclear spins in LiH: a new phase at positive temperature?" J. Phys. (Paris) **48**, 837–845.

Roser, M. R., and L. R. Corruccini, 1990, "Dipolar ferromagnetic order in a cubic system," Phys. Rev. Lett. **65**, 1064–1067.

Roshen, W. A., and W. F. Saam, 1980, "Effect of Kondo impurities on the Korringa relaxation time," Phys. Rev. B **22**, 5495–5500.

Roshen, W. A., and W. F. Saam, 1982, "More exact field dependence of nuclear spin relaxation of the host metal in the Kondo systems," Phys. Rev. B **26**, 2644–2647.

Rossat-Mignod, J., P. Burlett, O. Vogt, and G. H. Lander, 1979, "Magnetization and neutron scattering studies of multiaxial magnetic ordering in $USb_{0.9}Te_{0.1}$," J. Phys. C **12**, 1101–1112.

Rowland, T. J., 1960, "Nuclear magnetic resonance in copper alloys. Electron distribution around solute atoms," Phys. Rev. **119**, 900–912.

Ruderman, M. A., and C. Kittel, 1954, "Indirect exchange coupling of nuclear magnetic moments by conduction electrons," Phys. Rev. **96**, 99–102.

Rushbrooke, G. S., G. A. Baker, and P. J. Wood, 1974, "Heisenberg model," in *Phase Transitions and Critical Phenomena*, edited by C. Domb and M. S. Green (Academic, New York), Vol. 3, pp. 245–356.

Ryhänen, T., H. Seppä, R. Ilmoniemi, and J. Knuutila, 1989, "SQUID magnetometers for low-frequency applications," J. Low Temp. Phys. **76**, 287–386.

Schermer, R. I., and M. Blume, 1968, "Polarization effects in slow-neutron scattering. III. Nuclear polarization," Phys. Rev. **166**, 554–561.

Schmid, D., 1973, "Nuclear magnetic double resonance–Principles and applications in solid state physics," in Springer Tracts of Modern Physics **68** (Springer, Berlin/Heidelberg), pp. 1–75.

Schröder-Smeibidl, B., P. Smeibidl, G. Eska, and F. Pobell, 1991, "Nuclear specific heat of thallium," J. Low Temp. Phys. **85**, 311–320.

Schwark, M., F. Pobell, W. P. Halperin, C. Buchal, J. Hanssen, M. Kubota, and R. M. Müller, 1983, "Ortho-para conversion of hydrogen in copper as origin of time dependent heat leaks," J. Low Temp. Phys. **53**, 685–694.

Shibata, F., and Y. Hamano, 1982, "Spin relaxation in metals at very low temperatures," Solid State Commun. **44**, 921–925.

Shigematsu, T., K. Morita, Y. Fujii, T. Shigi, M. Nakamura, and M. Yamaguchi, 1992, "Investigation of annealing effects of ultra pure copper," Cryogenics **32**, 913–915.

Siemensmeyer, K., K. Kakurai, M. Steiner, T. A. Jyrkkiö, M. T. Huiku, and K. N. Clausen, 1990, "Neutron scattering investigation of the ordered state of the nuclear spins in Cu at 60 nK," J. Appl. Phys. **67**, 5433–5435.

Siemensmeyer, K., and M. Steiner, 1992, "Magnetostrictive and quadrupolar anisotropy in nuclear magnetic fcc systems," Z. Phys. B **89**, 305–311.

Slichter, C. P., 1990, *Principles of Magnetic Resonance* (Springer-Verlag, Berlin), pp. 219–246.

Smart, J. B., 1966, *Effective Field Theories of Magnetism* (Saunders, Philadelphia).

Smeibidl, P., B. Schröder-Smeibidl, and F. Pobell, 1994, "Spin lattice relaxation measurements on Cu at very low temperatures," Physica B **194–196**, 337–338.

Smythe, W. R., 1950, *Static and Dynamic Electricity* (McGraw-Hill, New York).

Soini, J. K., 1982, "Further studies of nuclear ordering in metallic copper," Helsinki University of Technology Report TKK-F-A471.

Soulen, R. J., and R. B. Dove, 1979, *Standard Reference Material 768, Superconductive Thermometric Fixed Point Device (0.015 K–0.208 K)*, US National Bureau of Standards.

Steiner, M., 1985, "Neutron scattering studies of nuclear orientation in the μK range," in *Neutron Scattering in the Nineties* (IAEA report), pp. 185–190.

Steiner, M., 1990, "The use of the spin-dependent scattering length: New areas and improved techniques for neutron-scattering," Phys. Scr. **42**, 367–384.

Steiner, M., 1993, "Nuclear magnetic order: Use of spin dependent amplitudes," Internat. J. Mod. Phys. B **7**, 2909–2944.

Steiner, M., L. Bevaart, Y. Ajiro, A. J. Millhouse, K. Ohlhoff, G. Rahn, H. Dachs, U. Scheer, and B. Wanklyn, 1981, "Observation of hyperfine-enhanced nuclear polarisation in CoF_2 by means of neutron diffraction," J. Phys. C **14**, L597–L602.

Steiner, M., A. Metz, K. Siemensmeyer, O. V. Lounasmaa, J. T. Tuorinemi, K. K. Nummila, R. T. Vuorinen, K. N. Clausen, K. Lefmann, and F. B. Rasmussen, 1996, "Neutron diffraction determination of the nuclear spin ordering in Cu and Ag at nano- and subnano-K temperatures," J. Appl. Phys. **79**, 5078–5080.

Steiner, M., K. Siemensmeyer, K. D. Ohlhoff, G. Rahn, M. Kubota, and S. M. Smith, 1986, "A polarized neutron diffraction study of nuclear polarization and order in $HoVo_4$," J. Magn. Magn. Mater. **54–57**, 1333–1334.

Suzuki, H., Y. Koike, Y. Karaki, M. Kubota, and H. Ishimoto, 1994, "Nuclear spin order in Sc metal," Physica B **194–196**, 249–250.

Suzuki, T., H. Kondo, H. Yano, S. Abe, Y. Miura, and T. Mamiya, 1991, "Zeeman-exchange relaxation time of h.c.p. solid ^{3}He near the nuclear ordering temperature," Europhys. Lett. **16**, 467– 471.

Symko, O. G., 1969, "Nuclear cooling using copper and indium," J. Low Temp. Phys. **1**, 451–467.

Takano, Y., N. Nishida, Y. Miura, H. Fukuyama, H. Ishimoto, S. Ogawa, T. Hata, and T. Shigi, 1985, "Magnetization of hcp solid ^{3}He," Phys. Rev. Lett. **55**, 1490–1493.

Tuoriniemi, J. T., 1995, "Neutron Experiments on Nuclear Magnetism in Copper and Silver," Ph.D. Thesis (Helsinki University of Technology).

Tuoriniemi, J. T., K. Lefmann, K. K. Nummila, and A. Metz, 1995, "Neutron studies of highly polarized silver nuclei at nanokelvin spin temperatures," Helsinki University of Technology Report TKK-F-A744.

Tuoriniemi, J. T., K. K. Nummila, K. Lefmann, R. T. Vuorinen, and A. Metz, 1996, "Neutron thermometry applied to magnetization and spin-lattice relaxation measurements on silver nuclei," Z. Phys. B (to be published).

Tuoriniemi, J. T., K. K. Nummila, R. T. Vuorinen, O. V. Lounasmaa, A. Metz, K. Siemensmeyer, M. Steiner, K. Lefmann, K. N. Clausen, and F. B. Rasmussen, 1995, "Neutron experiments on antiferromagnetic nuclear order in silver at picokelvin temperatures," Phys. Rev. Lett. **75**, 3744–3747.

Urbina, C., J. F. Jacquinot, and M. Goldman, 1982, "Rotating transverse helical nuclear ordering," Phys. Rev. Lett. **48**, 206–209.

Urbina, C., J. F. Jacquinot, and M. Goldman, 1986, "Rotating transverse nuclear helimagnetism in CaF_2: I. Prediction and experimental study," J. Phys. C **19**, 2275–2297.

Van der Zon, C. M., G. D. Van Velzen, and W. Th. Wenckebach, 1990, "Nuclear magnetic ordering in $Ca(OH)_2$. III. Experimental determination of the critical temperature," J. Phys. (Paris) **51**, 1479–1488.

Van Kesteren, H. W., W. Th. Wenckebach, and J. Schmidt, 1985, "Production of high, long-lasting, dynamic proton polarization by way of photoexcited triplet states," Phys. Rev. Lett. **55**, 1642–1644.

Van Vleck, J. H., 1937, "The influence of dipole-dipole coupling on the specific heat and susceptibility of a paramagnetic salt," J. Chem. Phys. **5**, 320–337.

Van Vleck, J. H., 1948, "The dipolar broadening of magnetic resonance lines in crystals," Phys. Rev. **74**, 1168–1183.

Van Vleck, J. H., 1957, "The concept of temperature in magnetism," Nuovo Cimento Suppl. **6**, 1081–1100.

Veuro, M. C., 1978, "A double bundle nuclear demagnetization refrigerator for cooling ^{3}He," Acta Polytech. Scand. Ph. **122**.

Viertiö, H. E., 1990, "Thermally stabilized stuctures of the nuclear spin system in silver," Phys. Scr. **T33**, 168–175.

Viertiö, H., 1992, "Theoretical studies on nuclear magnetic ordering in copper and silver," Ph.D. thesis (Helsinki University of Technology).

Viertiö, H. E., and A. S. Oja, 1987, "Ground state of nuclear spins in fcc metals," Phys. Rev. B **36**, 3805–3808.

Viertiö, H. E., and A. S. Oja, 1989, "Nuclear magnetism in copper at nanokelvin temperatures," in *Symposium on Quantum Fluids and Solids −1989*, AIP Conference Proceedings No. 194, edited by G. G. Ihas and Y. Takano (AIP, New York), pp. 305–315.

Viertiö, H. E., and A. S. Oja, 1990a, "Nuclear antiferromagnetism in copper: Interplay of $(0,\frac{2}{3},\frac{2}{3})$ and (1,0,0) order," Phys. Rev. B **42**, 6857–6860.

Viertiö, H. E., and A. S. Oja, 1990b, "Nuclear antiferromagnetism in copper: Predictions for spin structures in a magnetic field," Physica B **165–166**, 799–800.

Viertiö, H. E., and A. S. Oja, 1992, "Mean-field calculation and Monte Carlo simulation of ferromagnetic ordering at negative temperatures," J. Magn. Magn. Mater. **104–107**, 915–917.

Viertiö, H. E., and A. S. Oja, 1993, "Interplay of three antiferromagnetic modulations in the nuclear-spin system of copper," Phys. Rev. B **48**, 1062–1076.

Villain, J., 1959, "La structure des substances magnetiques," J. Phys. Chem. Solids **11**, 303–309.

Villain, J., R. Bidaux, J.-P. Carton, and R. Conte, 1980, "Order as an effect of disorder," J. Phys. (Paris) **41**, 1263–1272.

Vuorinen, R., 1992, "Ferromagnetic ordering of silver nuclei at negative absolute temperatures," Diploma Thesis (in Finnish) (Helsinki University of Technology).

Vuorinen, R. T., P. J. Hakonen, W. Yao, and O. V. Lounasmaa, 1995, "Susceptibility and relaxation measurements on rhodium metal at positive and negative spin temperatures in the nanokelvin range," J. Low Temp. Phys. **98**, 449–487.

Webb, R. A., 1977, "New technique for improved low-temperature SQUID NMR measurements," Rev. Sci. Instrum. **48**, 1585–1594.

White, S. J., M. R. Roser, J. Xu, J. T. Van der Noordaa, and L. R. Corruccini, 1993, "Dipolar magnetic order with large quantum spin fluctuations in a diamond lattice," Phys. Rev. Lett. **71**, 3553–3556.

Windsor, C. G., 1986, "Experimental techniques," in *Neutron Scattering: Methods of Experimental Physics*, edited by K. Sköld and D. L. Price (Academic, London), Vol. **23**, Part A, pp. 197–258.

Wolf, D., 1979, *Spin Temperature and Nuclear-Spin Relaxation in Matter* (Clarendon, Oxford).

Wysin, G. M., and A. R. Bishop, 1990, "Dynamic correlations in a classical two-dimensional Heisenberg antiferromagnet," Phys. Rev. B **42**, 810–819.

Yano, H., H. Kondo, T. Suzuki, Y. Minamide, T. Kato, Y. Miura, and T. Mamiya, 1990, "Magnetization and ac susceptibility of hcp solid ^{3}He near the nuclear ordering temperature," Phys. Rev. Lett. **65**, 3401–3404.

Yin, S., and P. J. Hakonen, 1991, "Electron-beam welded Cu-to-Ag joints for thermal contact at low temperatures," Rev. Sci. Instrum. **62**, 1370–1371.

Yosida, K., 1957, "Magnetic properties of Cu-Mn alloys," Phys. Rev. **106**, 893–898.

Zachariassen, W. H., 1967, "A general theory of X-ray diffraction in crystals," Acta Crystallogr. **23**, 558–564.

Zimmermann, J., and G. Weber, 1981, "Thermal relaxation of low-energy excitations in vitreous silica," Phys. Rev. Lett. **46**, 661–664.